INVESTIGATION INTO DIFFERENT TYPES OF SINGLE-PHASE AC/DC CONVERTERS

by
Vahik Babayan-Aghan

A Doctoral Thesis
Submitted in partial fulfilment of the requirements
for the award of
DOCTOR OF PHILOSOPHY
of the
Loughborough University of Technology

December 1995

Supervisors: Mr. J. G. Kettleborough
Professor I. R. Smith
Department of Electronic and Electrical Engineering
Loughbourough University of Technology

This thesis is gratefully dedicated to my parents

Synopsis

The work detailed in the thesis compares the performance of single-phase thyristor bridge converters under different control strategies; considering in particular the efficiency, ac side power factor and harmonic content of the current and voltage waveforms.

Extensive practical investigations were performed, in which analogue and digital control circuits were developed to provide the drive signals necessary for a converter to operate in the different control modes for:

a) A series-connected fully-controlled double thyristor bridge (used mainly in traction applications) operating under sequence control and;

b) A fully controlled single-bridge operating under sequence and conventional control.

A novel pulse-width modulation control strategy was developed for the single-bridge converter, using gate turn-off thyristors as the switching elements, whereby output voltage control is obtained by variation of the modulation index. Turn-on and turn-off signals for the power devices were obtained using an analogue control circuit. The advantages and disadvantages of this switching strategy compared with conventional and sequence control were studied, and results clearly showed that an improved input power factor and lower supply current and load voltage harmonics were all obtained.

Mathematical models for single and double bridge converters operating under sequence and conventional control were developed using tensor techniques. Using these models, computer programmes were written in Fortran 77 on the

University mainframe computer, to assemble automatically and solve the network equations as the converter topology changes. In addition, analytical models were also developed on the assumption that the load current is completely smooth. However, such an assumption is not justifiable with ac-to-dc converters and consequently a novel technique was developed to include the load current ripple in calculating the supply current harmonics. The results obtained are compared with both the computed and experimental ones.

TABLE OF CONTENTS

Page No.

List of Principal Symbols

A_n, B_n	Fourier coefficients of the supply current waveform including the load current ripple.	(A)
a_n, b_n	Fourier coefficients of the supply current waveform.	(A)
a_{nv}, b_{nv}	Fourier coefficients of the load voltage waveform.	(V)
$C^b_{.m}$	Transformation tensor.	
E_b, E_m	Branch and mesh impressed voltage vectors.	(V)
E_{cw}, E_{mw}	Amplitude of the carrier and modulating waveforms.	(V)
e_b	Generated back emf	(V)
i_a, I_a	Instantaneous and mean armature current.	(A)
I^b, I^m	Branch and mesh current vectors.	(A)
i_f, I_f	Instantaneous and mean field current.	(A)
I_n	Supply current nth-harmonic.	(A)
i_s, I_s	Instantaneous and r.m.s. value of the supply current.	(A)
J	Combined moment of inertia of the motor and its coupled load.	(Kg m^2)
K	Generated voltage per unit field current and motor speed.	(Vs/A rad)
L_a, L_f	Inductance of armature and field windings.	(H)
L_{bb}, L_{mm}	Branch and mesh inductance metrices.	(H)
L_s	Source inductance.	(H)
M	Modulation index.	
M_e, M_l	Electromagnetic and load torque.	(Nm)
M_{loss}	Friction and windage torque.	(Nm)
n	Harmonic order.	
p	$\frac{d}{dt}$ operator.	
P.F.	Power Factor.	
R_a, R_f	Resistance of the armature and field windings.	(Ω)
R_{bb}, R_{mm}	Branch and mesh resistance matrices.	(Ω)
R_s	Source resistance.	(Ω)
v_a, V_a	Instantaneous and mean armature voltage.	(V)

V_b, V_m	Branch and mesh voltage vectors.	(V)
v_f, V_f	Instantaneous and mean field voltage.	(V)
v_l, V_l	Instantaneous and mean load voltage.	(V)
V_m	Maximum instantaneous supply voltage.	(V)
V_n	R.M.S. value of the nth-harmonic of the load voltage.	(V)
V_s	Supply voltage.	(V)
X_t	Source reactance.	(Ω)
α	Firing delay angle.	(^{o})
δ	Commutation angle or angle of overlap.	(^{o})
ϕ	Phase displacement angle.	(^{o})
ω_m	Motor speed.	(rad/s)

All other symbols are defined as they appear

CHAPTER 1

Introduction

In the past, dc and single-phase ac commutator type series motors have been the undisputed propulsion units for railway traction purposes. This is primarily because of their ability to meet the five basic requirements of traction applications [1]:

a) Ideal torque-speed characteristic.
b) Sharing of torque between individual motor driven axles.
c) Automatic torque and speed adjustment when encountering different track gradients.
d) Controllability of output torque and speed.
e) Fast response to sudden line voltage variations.

The above requirements are adequately fulfilled by the series motor due to the relationship existing between the armature current and field excitation. Since the field ampere turns are directly proportional to the armature current, a reduction in speed causes an increase in armature current, which in turn increases the field strength. As a result of this increase more torque is generated, leading to a different operating point at a lower speed. This simple but effective feedback system not only prevents overloading of the motor but also provides a fast response to sudden line voltage variations, i.e. the voltage difference between the generated motor emf and the line voltage forces the field strength to the required value and hence reduces current surges to a minimum. However, in addition to its many advantages, the series motor possesses certain disadvantages [1], and as a consequence of the availability of large semiconductor switching devices other types of motor are now being used in railway traction applications. One option is the separately excited dc motor, whereby the field excitation is controlled independently of the armature voltage. However, external control circuits are required to make the machine suitable for traction applications, and these circuits control the armature current under rapidly varying line voltage conditions. Prior to the advent of power thyristors, only Ward-Leonard sets [2] were suitable for this type of duty, but these are large and heavy and are clearly unsuitable for traction applications. Depending upon the type of power supply, either an ac-to-dc converter with natural commutation or a dc-to-dc chopper will offer continuous voltage control with a fast response, which is well suited for control of a separately excited dc traction motor [3]. With either scheme, the performance is improved and regenerative braking, which is not possible with a series motor due to its unstable characteristic as a generator, becomes practical. With a dc power supply, rectifier units are sited in substations at suitable locations along the track, and a chopper on board the locomotive is used to control the motor armature voltage. When an ac power supply is available, controlled ac-to-dc converters are carried on board to vary the motor armature voltage. The two schemes are discussed below.

1.1 Substation Type Rectifier Units

Typically, the substations are supplied by 33kV 3-phase ac, which is transformed down, rectified and supplied to the track, either by an overhead catenary or a third rail, at a voltage ranging from 600V to 3000V dc. The basic requirements have remained unchanged since the mercury-arc era, but with the advent of silicon power diodes there has been substantial progress in rectifier equipment design. The voltage levels commonly used are 750V, 1500V and 3000V with the latter being used almost entirely in main-line systems to maximize the substation spacing. The 750V and 1500V supplies are used predominantly in urban mass-transit or light-rail systems [4,5]. Substation-type rectifier units typically provide a 12-pulse output voltage. This is achieved by a 3-winding transformer having a single primary winding and one star and one delta secondary winding to give the necessary 30^{o} phase displacement between the two secondary voltages. Each secondary winding is connected to a 3-phase bridge rectifier which are then paralleled through an interphase transformer [6]. A 12-pulse rectifier unit can also be obtained by series connection of phase-displaced bridge rectifiers without the need for an interphase transformer [4].

1.2 On-board Rectifier Units

AC fed railway systems have become more attractive since the advent of reliable on-board static ac-to-dc converters, which allow high-voltage (25kV-50kV) single phase transmission at industrial frequencies(50-60Hz) to be exploited [5]. An important design consideration is the harmonic current level in the overhead catenary, which can cause interference with signalling systems in close proximity with the railway line [7]. These supply current harmonics prevent full utilization of the installed capacity, by increasing the rms supply current without delivering any additional power, and also reducing the converter power factor. The harmonics can also cause overheating of power supply components and electrical machines, and may trigger protective devices prematurely. The harmonic content present in the supply current is governed by [8]:

a) The power circuit configuration and the type of control used
b) The converter pulse number.
c) The degree of imbalance in the converter firing circuits.
d) The supply voltage symmetry.
e) The converter firing angle.
f) The commutating reactance.

The commutating reactance of the power transformer prevents instantaneous commutation of load current from the outgoing to the incoming thyristor, and there is a consequent overlap period when the supply is virtually short circuited. The effect of commutation is threefold:

a) It reduces the mean armature voltage.
b) It softens the edges of the supply current waveform, with a marginal improvement in the harmonic content and
c) It severely distorts the transformer secondary voltage waveform, a process that is termed `notching´.

When a power transformer is on-load, there is a phase displacement between the primary and secondary terminal voltages, and consequently the transformer secondary voltage waveform is used as a timing reference in the electronic circuitry which fires the thyristors. Any harmonic distortion on this waveform, such as `notching´, can cause mal-operation and misfiring of the thyristors and to prevent this it is necessary to provide high-performance filters [8]. To improve both the input power factor and the harmonic content of the supply current and load voltage waveforms, it is usual for two or more half-controlled bridges to be connected in series on the dc side [7,9]. However, these cannot provide regeneration and, when this mode of operation is required, fully controlled bridges must be used. The conventional operation of these bridges suffers from several disadvantages when compared with half-controlled converters, such as a higher reactive demand, a low power factor (particularly at low output voltages) and a large ripple in the output voltage [10]. An improved performance is available when sequence control techniques are used, which provide an improved phase-control scheme for operating fully controlled bridges with half-controlled characteristics in both rectification and inversion modes [11,12].

This thesis investigates several types of single phase ac-to-dc converters suitable for railway traction purposes. Single bridge operation under conventional and sequence control and double-bridge operation under sequence control are considered. A pulse-width modulation (PWM) control strategy for a single-bridge converter is also considered, with the output voltage controlled by varying the modulation index of the PWM process [13,14]. With PWM control, the fundamental component of the supply current is co-phasal with the supply voltage, irrespective of the level of output voltage, and this results in a unity input displacement factor [15]. The PWM scheme reduces low-order harmonics [16] but produces high-order sideband harmonics at the switching frequency and its multiples, which can easily be filtered. For traction applications using PWM switching strategies, the switching devices must be able to withstand high voltage and current levels and be capable of easy turn-on and turn-off, and consequently gate turn-off (GTO) thyristors were used as the switching devices.

1.3 Thesis Outline

Chapter 2 outlines the operation of a separately excited dc machine, together with the operation of phase controllers and their characteristics in terms of the input power factor and harmonic content of the supply current and load voltage waveforms. Detailed operation of the PWM controller is also considered.

Chapter 3 presents the design of the series-connected fully controlled double-bridge converter and describes respectively the analogue and digital control circuitry required to produce sequence control for the thyristor switches.

Chapter 4 presents the design of a single-phase fully-controlled PWM bridge converter together with its associated firing pulses to turn-on and turn-off the GTO thyristors in a PWM manner.

Chapter 5 is concerned with mathematical models for phase and PWM controllers. The voltage and current waveforms together with their harmonic spectra are presented and discussed. The harmonic content of the load voltage and current waveforms for phase controllers are calculated using the analytical models developed in Appendix A2 and are compared with the computed results. A novel technique is presented for calculating the harmonic content of the supply current waveforms, which also includes the harmonics injected into the supply by the load current ripple. The results obtained from this technique are compared with computed results.

Chapter 6 presents experimental results for both phase and PWM controllers. A single-phase single-bridge configuration, operating under both conventional and sequence control, and a double-bridge operating under sequence control are considered for the phase controller and a single-bridge is considered for the PWM controller. Results are presented for both rectification and inversion modes, and a detailed comparison is made between different controllers. Analytical results using the models developed in Appendix A2 and chapter 5 are also included and comparisons are made between the experimental and analytical results.

Chapter 7 presents the overall conclusions for the thesis.

CHAPTER 2

DC Motor Speed Control

The separately excited dc motor is often used for variable speed drives, due to the ease with which its speed may be controlled. Section 2.1 presents the equivalent circuit for such a motor and explains the methods by which its speed may be adjusted. The operation of various types of single-phase bridge-connected phase-controller, suitable for motor speed control, is then outlined. The effect of overlap in the controller is examined, and the harmonic content of the supply current and the armature voltage are investigated. The supply power factor for a single-phase system is considered and, finally, the operation of a novel Pulse-Width Modulation (PWM) switching strategy for a bridge-connected converter is described.

2.1 The Separately-excited DC Motor

The equivalent circuit for a separately-excited dc motor, shown in figure 2.1, has six terminal variables. These are the field voltage and current (V_f and I_f), the applied armature voltage and current (V_a and I_a) and the mechanical angular velocity and shaft torque (ω_m and M_L). For an unsaturated machine, the equations relating these variables are [17]:

$$V_f = R_f i_f + L_f \frac{di_f}{dt} \tag{2.1}$$

$$V_a = K i_f \omega_m + R_a i_a + L_a \frac{di_a}{dt} \tag{2.2}$$

$$M_L = M_e - J \frac{d\omega_m}{dt} - M_{loss} \tag{2.3}$$

Where $M_e = KI_fI_a$ is the electromagnetic torque, M_{loss} the friction and windage torque and J the combined moment of inertia of the motor and its coupled load. If any of the quantities i_f, i_a or ω_m are constant, the corresponding time derivative terms in equations (2.1) to (2.3) becomes zero. The steady-state motor speed for a constant armature current is then given by equation (2.2) as:

$$\omega_m = \frac{V_a - R_a I_a}{K I_f} \tag{2.4}$$

which shows that the speed may be controlled by adjustment of either the field current, the armature circuit resistance or the armature terminal voltage.

The lowest motor speed available using field current control occurs at the maximum allowable field current. The highest speed is with low field current and is restricted by armature reaction, which eventually causes either the speed to become unstable or the commutation to deteriorate. Field control provides constant maximum power from the motor [18].

Armature-resistance control [18] is provided by inserting additional resistance in series with the armature, thereby altering the speed-torque relationship and giving the machine a large speed regulation for a small increase in load torque. In addition, the power loss in the resistor is large, especially at low speeds, and consequently this method is not normally used.

Armature-voltage control [18] relies on the fact that a change in this voltage is accompanied by an almost proportionate change in the generated emf and therefore in the motor speed. In the past motor/generator sets were often used to provide the armature voltage supply, but the development of high-power solid-state switching devices has increased considerably the range of possibilities for the precise control of motor speed. The direction of rotation depends on the direction of the armature current relative to the polarity of the main magnetic field, and a reversal of rotation may be achieved by reversing either the armature voltage or the field current.

2.2 Phase-controllers

A single-phase converter using phase-control connects the motor armature to the ac supply for only a portion of each supply half-cycle. Commutation occurs naturally, since the incoming thyristors reverse-bias the outgoing thyristors and turn them off. Consequently commutation circuits are unnecessary, which makes the scheme simple and inexpensive. Phase-controllers are widely used, since they can control the armature voltage smoothly over a wide range. They have however the disadvantage that the supply power factor decreases at lower armature voltages [19].

Section 2.2.1 examines the half-controlled single-bridge connection and sections 2.2.2 to 2.2.5 consider respectively conventional and sequence controlled switching strategies for the single- and double-bridge arrangement.

2.2.1 Half-controlled Bridge

The mean armature voltage of the half-controlled arrangement of figure 2.2(a) never goes negative, irrespective of whether or not the free-wheeling diode D_{FW} is present, and this can be explained by considering the device conduction pattern. After a supply voltage zero, and before say thyristor T_3 is fired, T_1 continues to conduct while the return armature current is transferred from diode D_2 to D_4. A free-wheeling path is provided via T_1 and D_4, which results in zero armature voltage (neglecting device voltage drops) and zero supply current to the bridge. The diode D_{FW} provides a preferential parallel path for the free-wheeling current I_{FW}, enabling the outgoing thyristor to turn off and regain its blocking state [7]. Figure 2.2(b) shows the voltage and current waveforms for this arrangement. The familiar mean armature voltage expression is obtained by setting $\alpha_f=0$ and $\alpha_v=\alpha$ in the general expression derived in Appendix A1, to give:

$$V_a = \frac{1}{2} V_{d0} [1 + \cos \alpha] \qquad (2.5)$$

where $V_{d0} = \frac{2V_m}{\pi}$.

This arrangement is cheaper, maintains a better supply power factor and has a smaller peak-to-peak ripple voltage at the dc terminals than does a conventional controlled bridge rectifier. However, it has the disadvantage that it cannot regenerate.

2.2.2 Conventional Controlled Single-bridge

Conventional control of the bridge configuration shown in figure 2.3(a) is achieved by firing thyristors T_1 and T_2 in each positive half-cycle and T_3 and T_4 in the negative half-cycle of the supply voltage with the same firing delay angle α. The corresponding voltage and current waveforms are shown in figure 2.3(b). As before, the mean armature voltage for continuous load current is obtained by setting $\alpha_v=\alpha_f=\alpha$ in the expression of Appendix A1 to give:

$$V_a = V_{d0} \cos \alpha \tag{2.6}$$

where $V_{d0} = \frac{2V_m}{\pi}$

The disadvantages of this arrangement are the high reactive power demand, the low supply power factor and the high output-voltage ripple [12].

2.2.3 Sequence Controlled Single-bridge

Sequence control of the bridge shown in figure 2.3(a) is achieved by triggering the upper pair of thyristors T_1 and T_3 with a delay angle α_v and the lower pair T_2 and T_4 with an angle α_f [11,12]. The operating range for both α_v and α_f is limited to between 10^o and 160^o, to ensure that there is sufficient voltage for the armature current to commutate between thyristors, as explained later in section 2.3.

The armature voltage is controlled by maintaining α_f at 10^o and varying α_v from 10^o to 160^o (i.e. rectification). Negative voltage is achieved by keeping α_v at 160^o and varying α_f from 10^o to 160^o (i.e. inversion). The voltage and current waveforms for a typical operating condition are shown in figure 2.3(c). The equation for the mean voltage is obtained by setting $\alpha_{v1}=\alpha_{v2}=\alpha_v$ and $\alpha_{f1}=\alpha_{f2}=\alpha_f$ in the expression of Appendix A1. This gives the result which has previously appeared in the literature [11] but without proof,

$$V_a = \frac{1}{2} V_{d0} [\cos \alpha_f + \cos \alpha_v] \qquad (2.7)$$

where $V_{d0} = \frac{2V_m}{\pi}$

The above scheme has the characteristics of a half-controlled bridge rectifier, with the added advantage that it can operate in the inversion mode.

2.2.4 Conventional Controlled Double-bridge

The series connected double-bridge of figure 2.4 may be controlled by either of the two methods explained below.

In the first of these, thyristors $T_1, T_2, \dot{T}_1$ and $\dot{T}_2$ are turned on together in the positive half-cycle of the supply voltage and $T_3, T_4, \dot{T}_3$ and $\dot{T}_4$ in the negative half-cycle, with the same firing delay angle α. The performance and circuit waveforms are identical to those produced by a conventional controlled single-bridge rectifier.

In the second method, conventional control is implemented on each bridge separately; hence two phase-shifters are needed. One of these controls the firing delay angle α_1 of bridge 1 (Br.1) and the other the firing delay angle α_2 of bridge 2 (Br.2). Rectification is obtained by maintaining one bridge at full advance (i.e. either $\alpha_1=10^o$ or $\alpha_2=10^o$) and varying the firing delay angle of the other bridge from 10^o to 160^o. Alternatively, inversion is obtained with one bridge kept at full retard (i.e. either $\alpha_1=160^o$ or $\alpha_2=160^o$) while varying the firing delay angle of the other from 10^o to 160^o.

2.2.5 Sequence Controlled Double-bridge

An alternative method for controlling the output voltage of the double bridge circuit of figure 2.4 is sequence control [12]. Since each bridge employs sequence control independently, four phase-shifters are required to provide the four firing delay angles. Two of these control the firing of the thyristors of bridge 1 with delay angles α_{v1} and α_{f1} and the other two the firing delay angles α_{v2} and α_{f2} of bridge 2.

The converter has two different methods of operation and the four distinct operating zones, defined in table 2.1 in terms of the firing delay angle. With method 1, rectification is obtained by maintaining one bridge at full advance (i.e. either $\alpha_{v1}=\alpha_{f1}=10^o$ or $\alpha_{v2}=\alpha_{f2}=10^o$) while the other is triggered in sequence control. Inversion is achieved by keeping one bridge at full retard (i.e. either $\alpha_{v1}=\alpha_{f1}=160^o$ or $\alpha_{v2}=\alpha_{f2}=160^o$) while the other is again triggered in sequence control. Figures 2.5(a) to (d) shows the voltage and current waveforms for the four different operating zones.

It can be seen from table 2.1 that the main difference between methods 1 and 2 arises when the converter operates in either zone 2 or zone 3. Operation of method 2 causes the armature current to free-wheel through bridges 1 and 2 for part of the supply period, and the transformer copper loss is consequently reduced and a better regulation is obtained. Figures 2.6(a) and (b) show the voltage and current waveforms for operation in zones 2 and 3 respectively.

The mean armature voltage as derived in Appendix A1 for continuous load current is:

$$V_a = \frac{1}{4} V_{d0} \left[\cos \alpha_{f1} + \cos \alpha_{v1} + \cos \alpha_{f2} + \cos \alpha_{v2}\right] \qquad (2.8)$$

Sequence control produces better input distortion and displacement factors compared with that of conventional

Method 1	Method 2	
$\alpha_{v2}=\alpha_{f2}=\alpha_{f1}=10^o$ α_{v1} variable $10^o \rightarrow 160^o$	$\alpha_{v2}=\alpha_{f2}=\alpha_{f1}=10^o$ α_{v1} variable $10^o \rightarrow 160^o$	Zone 1 $\frac{V_a}{2} \rightarrow V_a$
$\alpha_{v2}=\alpha_{f2}=10^o$ α_{f1} variable $10^o \rightarrow 160^o$ $\alpha_{v1}=160^o$	$\alpha_{f1}=\alpha_{f2}=10^o$ α_{v2} variable $10^o \rightarrow 160^o$ $\alpha_{v1}=160^o$	Zone 2 $0 \rightarrow \frac{V_a}{2}$
$\alpha_{v1}=\alpha_{f1}=160^o$ α_{v2} variable $10^o \rightarrow 160^o$ $\alpha_{f2}=10^o$	$\alpha_{v1}=\alpha_{v2}=160^o$ α_{f1} variable $10^o \rightarrow 160^o$ $\alpha_{f2}=10^o$	Zone 3 $0 \rightarrow -\frac{V_a}{2}$
$\alpha_{v1}=\alpha_{f1}=\alpha_{v2}=160^o$ α_{f2} variable $10^o \rightarrow 160^o$	$\alpha_{v1}=\alpha_{f1}=\alpha_{v2}=160^o$ α_{f2} variable $10^o \rightarrow 160^o$	Zone 4 $-\frac{V_a}{2} \rightarrow -V_a$

or

Method 1	Method 2	
$\alpha_{v1}=\alpha_{f1}=\alpha_{f2}=10^o$ α_{v2} variable $10^o \rightarrow 160^o$	$\alpha_{v1}=\alpha_{f1}=\alpha_{f2}=10^o$ α_{v2} variable $10^o \rightarrow 160^o$	Zone 1 $\frac{V_a}{2} \rightarrow V_a$
$\alpha_{v1}=\alpha_{f1}=10^o$ α_{f2} variable $10^o \rightarrow 160^o$ $\alpha_{v2}=160^o$	$\alpha_{f1}=\alpha_{f2}=10^o$ α_{v1} variable $10^o \rightarrow 160^o$ $\alpha_{v2}=160^o$	Zone 2 $0 \rightarrow \frac{V_a}{2}$
$\alpha_{v2}=\alpha_{f2}=160^o$ α_{v1} variable $10^o \rightarrow 160^o$ $\alpha_{f1}=10^o$	$\alpha_{v1}=\alpha_{v2}=160^o$ α_{f2} variable $10^o \rightarrow 160^o$ $\alpha_{f1}=10^o$	Zone 3 $0 \rightarrow -\frac{V_a}{2}$
$\alpha_{v2}=\alpha_{f2}=\alpha_{v1}=160^o$ α_{f1} variable $10^o \rightarrow 160^o$	$\alpha_{v2}=\alpha_{f2}=\alpha_{v1}=160^o$ α_{f1} variable $10^o \rightarrow 160^o$	Zone 4 $-\frac{V_a}{2} \rightarrow -V_a$

Table 2.1 Operating zones and positions of the firing delay angles

Method 1	Method 2	
$\alpha_{v2}=\alpha_{f2}=\alpha_{v1}=10^{o}$ α_{f1} variable $10^{o}\rightarrow160^{o}$	$\alpha_{v2}=\alpha_{f2}=\alpha_{v1}=10^{o}$ α_{f1} variable $10^{o}\rightarrow160^{o}$	Zone 1 $\frac{V_a}{2}\rightarrow V_a$
$\alpha_{v2}=\alpha_{f2}=10^{o}$ α_{v1} variable $10^{o}\rightarrow160^{o}$ $\alpha_{f1}=160^{o}$	$\alpha_{v1}=\alpha_{v2}=10^{o}$ α_{f2} variable $10^{o}\rightarrow160^{o}$ $\alpha_{f1}=160^{o}$	Zone 2 $0\rightarrow\frac{V_a}{2}$
$\alpha_{v1}=\alpha_{f1}=160^{o}$ α_{f2} variable $10^{o}\rightarrow160^{o}$ $\alpha_{f1}=10^{o}$	$\alpha_{f1}=\alpha_{f2}=160^{o}$ α_{v1} variable $10^{o}\rightarrow160^{o}$ $\alpha_{v2}=10^{o}$	Zone 3 $0\rightarrow-\frac{V_a}{2}$
$\alpha_{v1}=\alpha_{f1}=\alpha_{f2}=160^{o}$ α_{f1} variable $10^{o}\rightarrow160^{o}$	$\alpha_{v1}=\alpha_{f1}=\alpha_{f2}=160^{o}$ α_{v2} variable $10^{o}\rightarrow160^{o}$	Zone 4 $-\frac{V_a}{2}\rightarrow-V_a$

or

Method 1	Method 2	
$\alpha_{v1}=\alpha_{f1}=\alpha_{v2}=10^{o}$ α_{f2} variable $10^{o}\rightarrow160^{o}$	$\alpha_{v1}=\alpha_{f1}=\alpha_{v2}=10^{o}$ α_{f2} variable $10^{o}\rightarrow160^{o}$	Zone 1 $\frac{V_a}{2}\rightarrow V_a$
$\alpha_{v1}=\alpha_{f1}=10^{o}$ α_{v2} variable $10^{o}\rightarrow160^{o}$ $\alpha_{f2}=160^{o}$	$\alpha_{v2}=\alpha_{f1}=10^{o}$ α_{f1} variable $10^{o}\rightarrow160^{o}$ $\alpha_{f2}=160^{o}$	Zone 2 $0\rightarrow\frac{V_a}{2}$
$\alpha_{v2}=\alpha_{f2}=160^{o}$ α_{f1} variable $10^{o}\rightarrow160^{o}$ $\alpha_{v1}=10^{o}$	$\alpha_{f1}=\alpha_{f2}=160^{o}$ α_{v2} variable $10^{o}\rightarrow160^{o}$ $\alpha_{v1}=10^{o}$	Zone 3 $0\rightarrow-\frac{V_a}{2}$
$\alpha_{v2}=\alpha_{f2}=\alpha_{f1}=160^{o}$ α_{v1} variable $10^{o}\rightarrow160^{o}$	$\alpha_{v2}=\alpha_{f2}=\alpha_{f1}=160^{o}$ α_{v1} variable $10^{o}\rightarrow160^{o}$	Zone 4 $-\frac{V_a}{2}\rightarrow-V_a$

Table 2.1 Continued

control and consequently a better supply power factor.

2.3 Effect of Overlap

In the previous section, it was assumed that current commutation from one thyristor to the next was instantaneous. However in practice, the supply has both series reactance and resistance and a finite commutation time is required.

The supply reactance is predominantly the leakage reactance of the supply transformer, which is usually much greater than its resistance. It is valid therefore to neglect the supply resistance and to represent the ac supply by a Thêvenin equivalent circuit comprising a voltage source in series with an inductance.

The bridge circuit of figure 2.3(a) operating in sequence control will be used to explain the commutation phenomena. Figure 2.7(a) shows converter voltage and current waveforms, assuming the load to be sufficiently inductive to maintain a constant armature current. The angular period δ, during which both outgoing and incoming thyristors are conducting, is termed the commutation angle or angle of overlap [7,20]. During overlap the load current is the sum of two thyristor currents, and overlap is complete when the current level in the incoming thyristor reaches that of the armature current. An expression for the commutation angle is derived by assuming a circulating current i to flow in the closed path formed by the two conducting thyristors T_1 and T_3 of figure 2.7(b). Ignoring thyristor voltage drops

$$V_m \sin \omega t = L_S \frac{di}{dt} \tag{2.9}$$

where L_S is the source inductance. Rearranging equation (2.9) gives:

$$\int_{\frac{\alpha_v}{\omega}}^{\frac{\alpha_v+\delta_v}{\omega}} V_m \sin \omega t \quad dt = L_s \int_0^{I_a} di \tag{2.10}$$

and after integration

$$I_a = \frac{V_m}{\omega L_s} [\cos \alpha_v \ - \cos(\alpha_v+\delta_v)] \tag{2.11}$$

If the supply source reactance ωL_s is written as X_t, then

$$I_a X_t = V_m [\cos \alpha_v \ - \cos(\alpha_v+\delta_v)] \tag{2.12}$$

or

$$\delta_v = \cos^{-1} [\cos \alpha_v \ - \frac{I_a X_t}{V_m}] - \alpha_v \tag{2.13}$$

Equation 2.13 shows the commutation angle δ_v to be related to both the armature current I_a and the supply source reactance X_t. It depends also on the commutation voltage V_t, which equals the instantaneous load voltage at the instant of firing, as given by equation (2.14), and as this voltage increases δ_v reduces. This phenomena is shown in figure 2.7(c), which is a graphical representation of equation (2.13) for a given armature current and source reactance.

$$V_t = V_m \sin \alpha_v \qquad\qquad 0<\alpha_v>\pi \tag{2.14}$$

The commutation voltage forces the commutation current to decay to zero in the outgoing thyristor and to ensure that there is adequate voltage for this to occur successfully, the operating range for the firing delay angle is limited to between 10° and 160°.

The mean armature voltage derived in Appendix A1 includes the effect of commutation, and shows its significance in reducing the mean armature voltage. The commutation angle δ_f of figure 2.10, due to the lower thyristor pair T_2 and T_4, has no effect on the mean armature voltage during either rectification or inversion, since the armature voltage is already zero due to free-wheeling.

2.4 Harmonic Content of the Supply Current

The r.m.s. value of the nth-harmonic of the supply current for a sequence controlled double-bridge is derived in Appendix A2. For operation in zone 1

$$\frac{I_n}{I_a} = \frac{\sqrt{2}}{n\pi}\sqrt{\frac{5 + 3\cos n(\alpha_{v1} - \alpha_{f1})}{2}} \tag{2.15}$$

and in zone 2

$$\frac{I_n}{I_a} = \frac{\sqrt{2}}{n\pi}\sqrt{\frac{3+2\cos n(\alpha_{v2}-\alpha_{f1})+ 2\cos n(\alpha_{v2}-\alpha_{f1})+ \cos n(\alpha_{v1}-\alpha_{f1})}{2}} \tag{2.16}$$

For a sequence controlled single-bridge

$$\frac{I_n}{I_a} = \frac{2\sqrt{2}}{n\pi}\sqrt{\frac{1 + \cos n(\alpha_v-\alpha_f)}{2}} \tag{2.17}$$

and for a conventional controlled single-bridge

$$\frac{I_n}{I_a} = \frac{2\sqrt{2}}{n\pi} \tag{2.18}$$

Figures 2.8(a) and (b) show the variation of the fundamental and lower-order harmonic current components for the double and single bridges respectively, as given by equations (2.15) to (2.17). For comparative purposes, figure 2.8(b) also includes the harmonics for a conventionally controlled bridge as expressed by equation (2.18). It is evident that these harmonics remain constant, since the shape of the current waveform does not vary with firing delay angle. In contrast, with sequence control the waveform shape changes with the firing delay angle and so does its harmonic content, as shown in figure 2.8. Consequently the r.m.s. supply current with sequence control is lower than with conventional control.

2.5 Harmonic Content of Armature Voltage

The harmonic content of the armature voltage for a sequence controlled double-bridge, assuming continuous armature current, is derived in Appendix A2. The r.m.s. value of the nth-harmonic is:

$$V_n = \sqrt{\frac{a_{nv}^2+b_{nv}^2}{2}} \qquad (2.19)$$

where for a sequence controlled double-bridge a_{nv} and b_{nv} are respectively:

$$a_{nv} = \frac{V_m}{\pi}\left[\frac{1}{n+1}\cos A\cos B - \frac{1}{n-1}\cos C\cos D + \frac{1}{n+1}\cos E\cos F - \frac{1}{n-1}\cos G\cos H\right] \qquad (2.20)$$

and

$$b_{nv} = \frac{V_m}{\pi}\left[\frac{1}{n+1}\sin A\cos B - \frac{1}{n-1}\sin C\cos D + \frac{1}{n+1}\sin E\cos F - \frac{1}{n-1}\sin G\cos H\right] \qquad (2.21)$$

in which

$$A = \frac{(n+1)(\alpha_{f2}+\alpha_{v2})}{2} \qquad (2.22)$$

$$B = \frac{(n+1)(\alpha_{f2}-\alpha_{v2})}{2} \qquad (2.23)$$

$$C = \frac{(n-1)(\alpha_{f2}+\alpha_{v2})}{2} \qquad (2.24)$$

$$D = \frac{(n-1)(\alpha_{f2}-\alpha_{v2})}{2} \qquad (2.25)$$

$$E = \frac{(n+1)(\alpha_{v1}+\alpha_{f1})}{2} \qquad (2.26)$$

$$F = \frac{(n+1)(\alpha_{v1}-\alpha_{f1})}{2} \qquad (2.27)$$

$$G = \frac{(n-1)(\alpha_{v1}+\alpha_{f1})}{2} \qquad (2.28)$$

$$H = \frac{(n-1)(\alpha_{v1}-\alpha_{f1})}{2} \tag{2.29}$$

and for a sequence controlled single-bridge

$$a_{nv} = \frac{V_m}{\pi}\left[\frac{1}{n+1}\cos A - \frac{1}{n-1}\cos C + \frac{1}{n+1}\cos E - \frac{1}{n-1}\cos G\right] \tag{2.30}$$

$$b_{nv} = \frac{V_m}{\pi}\left[\frac{1}{n+1}\sin A - \frac{1}{n-1}\sin C + \frac{1}{n+1}\sin E - \frac{1}{n-1}\sin G\right] \tag{2.31}$$

with

$$A = (n+1)\alpha_f \tag{2.32}$$

$$C = (n-1)\alpha_f \tag{2.33}$$

$$E = (n+1)\alpha_v \tag{2.34}$$

$$G = (n-1)\alpha_v \tag{2.35}$$

and for a conventional controlled single-bridge

$$a_{nv} = \frac{2V_m}{\pi}\left[\frac{1}{n+1}\cos A - \frac{1}{n-1}\cos C\right] \tag{2.36}$$

$$b_{nv} = \frac{2V_m}{\pi}\left[\frac{1}{n+1}\sin A - \frac{1}{n-1}\sin C\right] \tag{2.37}$$

with

$$A = (n+1)\alpha \tag{2.38}$$

$$C = (n-1)\alpha \tag{2.39}$$

Figures 2.9 to 2.11 show the variation of the dc component and the lower-order harmonic voltage components with firing delay angle, for different controllers. These voltage harmonics give rise to harmonic armature currents which contribute to an increase in machine losses. As is evident from the figures, a sequence controlled double-bridge has a lower harmonic content than the other controllers, resulting in a reduced armature current ripple and consequently in a smaller smoothing inductor.

2.6 Supply Power Factor

The general expression for the power factor of a single-phase system is [7,20]:

$$\text{Power Factor} = \frac{\text{Mean Power}}{V_s I_s} \tag{2.40}$$

Where V_s and I_s are the total r.m.s. voltage and current respectively. Assuming that the supply voltage is sinusoidal, with an r.m.s value of V_1, no power is associated with the harmonic current and the mean power is [7],

$$\text{Mean Power} = V_1 I_1 \cos \phi_1 \tag{2.41}$$

where I_1 is the fundamental r.m.s. component of the supply current and ϕ_1 the phase angle between this current and the voltage V_1. Substituting equation (2.41) into (2.40) gives,

$$\text{Power Factor} = \frac{I_1}{I_s} \cos \phi_1 \tag{2.42}$$

in which $\frac{I_1}{I_s}$ is defined as the input distortion factor and $\cos\phi_1$ as the input displacement factor.

The power factor expressions given below for different controllers are derived in Appendix A2:

For a double-bridge operating in zone 1

$$\text{P.F.} = 0.9 \sqrt{\frac{\pi[5 + 3\cos(\alpha_{v1}-\alpha_{f1})]}{6(\alpha_{f1}-\alpha_{v1}) + 8\pi}}$$

$$\cos \tan^{-1}\left(\frac{3\sin \alpha_{f1}+\sin \alpha_{v1}}{3\cos \alpha_{f1}+\cos \alpha_{v1}}\right) \tag{2.43}$$

and in zone 2

$$P.F.=0.9\sqrt{\frac{\pi[3+2\cos(\alpha_{v2}-\alpha_{v1})+2\cos(\alpha_{v2}-\alpha_{f1})+\cos(\alpha_{v1}-\alpha_{f1})]}{8\alpha_{v2}-6\alpha_{v1}-2\alpha_{f1}+8\pi}}$$

$$\cos\tan^{-1}\left(\frac{2\sin\alpha_{v2}+\sin\alpha_{v1}+\sin\alpha_{f1}}{2\cos\alpha_{v2}+\cos\alpha_{v1}+\cos\alpha_{f1}}\right) \qquad (2.44)$$

for a sequence controlled single-bridge

$$P.F. = 0.8\left[\frac{\cos\alpha_v+\cos\alpha_f}{\sqrt{(\pi-\alpha_v+\alpha_f)}}\right] \qquad (2.45)$$

and for a conventionally controlled single-bridge

$$P.F. = 0.9\cos\alpha \qquad (2.46)$$

Figure 2.12 shows the variations of power factor for different controllers, as given by equations (2.43) to (2.46). It is clear that a sequence controlled double-bridge produces a better power factor than either a sequence or a conventional controlled single-bridge. Equation (2.46) shows that the presence of current harmonics causes the power factor to be always less than unity, even when the fundamental component and the input voltage are co-phasal.

2.7 PWM Control Strategy

A PWM control strategy is used for the single-phase bridge of figure 2.13, with gate turn-off thyristors, GTOs, as the switching elements and series diodes, to protect them against reverse voltages. The gate signals to turn-on and turn-off the GTOs in a PWM manner is obtained by comparing a triangular carrier waveform with a full-wave rectified modulating waveform, with the unrectified waveform being in phase with the supply voltage waveform [14]. The widths of the load voltage pulses, and hence output voltage control is achieved by variation of the modulation index M[13,14].

$$M = \frac{E_{mw}}{E_{cw}} \qquad (2.47)$$

Where E_{mw} and E_{cw} are the amplitudes of the modulating and carrier waveforms.

This scheme reduces low-order supply current and load voltage harmonics and consequently substantial savings in the size and cost of the input current filtering and output smoothing inductor compared to that of phase-controllers. However, PWM switching strategy produces high-order supply current and load voltage harmonics located at the switching frequency and multiples of it, but these can easily be filtered. The input fundamental displacement factor and distortion factor are improved by using PWM scheme which results in a power factor higher than that produced by phase-controllers.

A disadvantage with the PWM scheme is the increased switching losses caused by more frequent device switching. In addition, the mean output voltage obtained from the PWM controller is reduced due to the chopping of the output voltage waveform, resulting in a reduction in the maximum output power to below that produced by phase-controllers for a given supply voltage and load current. GTOs are substantially more expensive than conventional thyristors and also the gate drive circuits for GTOs are more complex and consequently more expensive.

2.7.1 Fully-controlled PWM Bridge Converter

Figure 2.13(a) shows a single-phase fully-controlled PWM converter. The circuit waveforms are given in figure 2.13(b) and its operation is explained with reference to figure 2.13(c), which illustrates the gate signals applied to GTOs T_1 to T_4.

The gate signals to turn on T_3 and T_2 and turn off T_4 are applied throughout the positive half-cycle of the supply voltage. However, since T_3 is reversed biased it remains off until it becomes forward biased in the manner explained later.

When T_2 is turned on and T_1 is triggered, the load is connected to the supply via T_1,D_1,D_2 and T_2. When T_1 is turned off, a voltage is induced in the inductance L_a which forward biases D_3 and T_3. Since the gate signal is already applied to T_3 it turns on and provides a free-wheeling path via D_2,T_2,T_3 and D_3 thereby clamping the armature voltage to zero.

Operation of the bridge during a negative half-cycle is the same as that during a positive half-cycle, except that the load is connected to the supply via T_3,D_3,D_4 and T_4 and the free-wheeling path is through D_4,T_4,T_1 and D_1.

Regenerative operation is obtained by altering the gate signals applied to the GTOs T_1 to T_4. The circuit waveforms and the modified gate signals are shown respectively in figures 2.13(d) and (e).

2.7.2 Half-controlled PWM Bridge Converter

Figure 2.14(a) represents the half-controlled bridge arrangement, which can only operate in the rectification mode. Circuit waveforms, together with the gate signals applied to GTOs T_3 and T_2 are given in figures 2.14(b) and (c) respectively.

Operation of the bridge is the same as that explained in the previous section. The load is connected to the supply via D_1,D_2,T_2 and T_3,D_3,D_4 in the positive and negative half-cycle of the supply voltage respectively and the free-wheeling path is through D_4 and D_1.

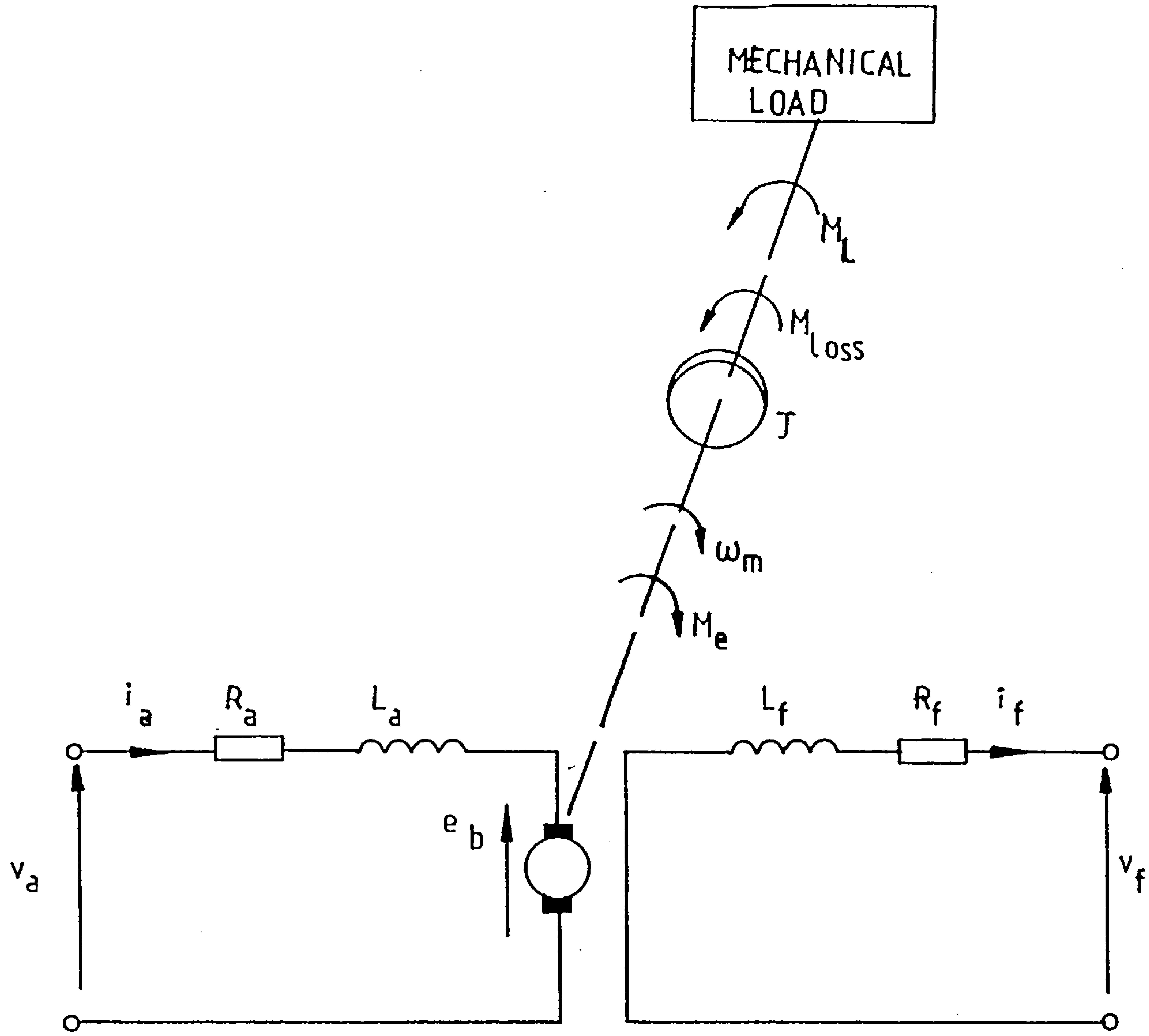

Figure2.1 Equivalent circuit of a dc motor.

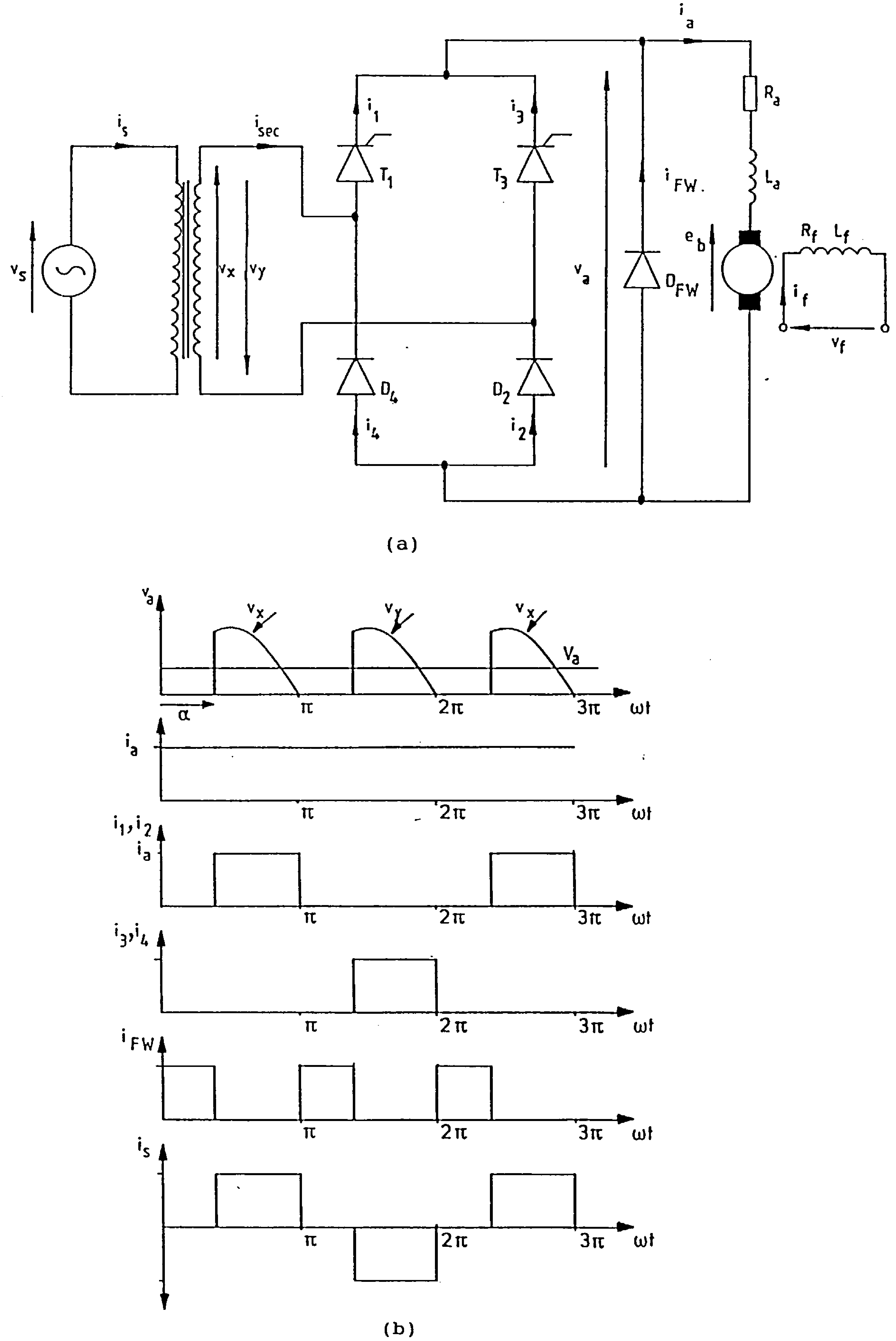

Figure2.2 Half-controlled single-bridge converter.
(a) Connection.
(b) Waveforms.

(a)

(b)

Figure2.3 Fully-controlled single-bridge converter.
(a) Connection.
(b) Waveforms for conventional control.

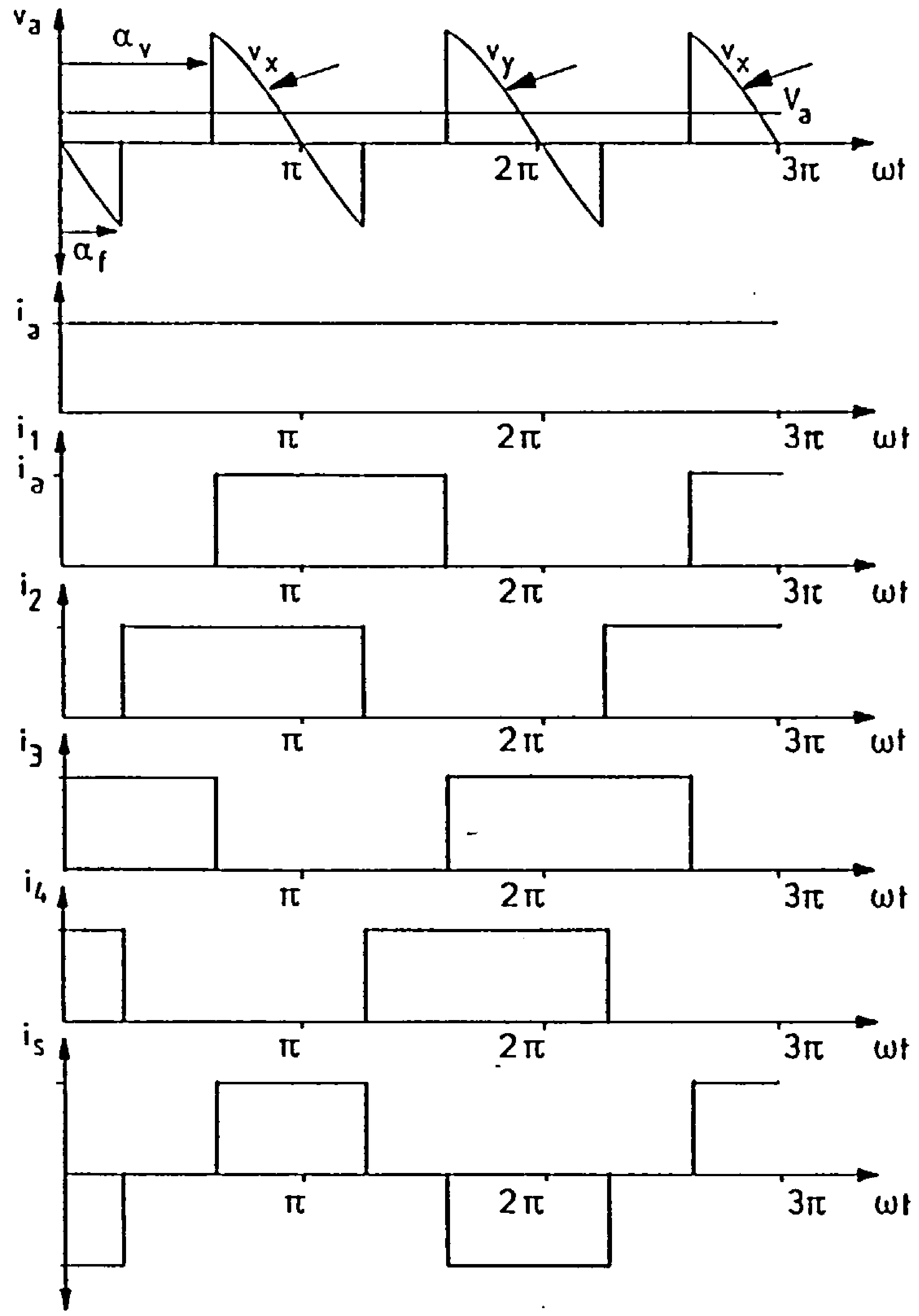

(c)

Figure2.3 Continued.
(c) Waveforms for sequence control.

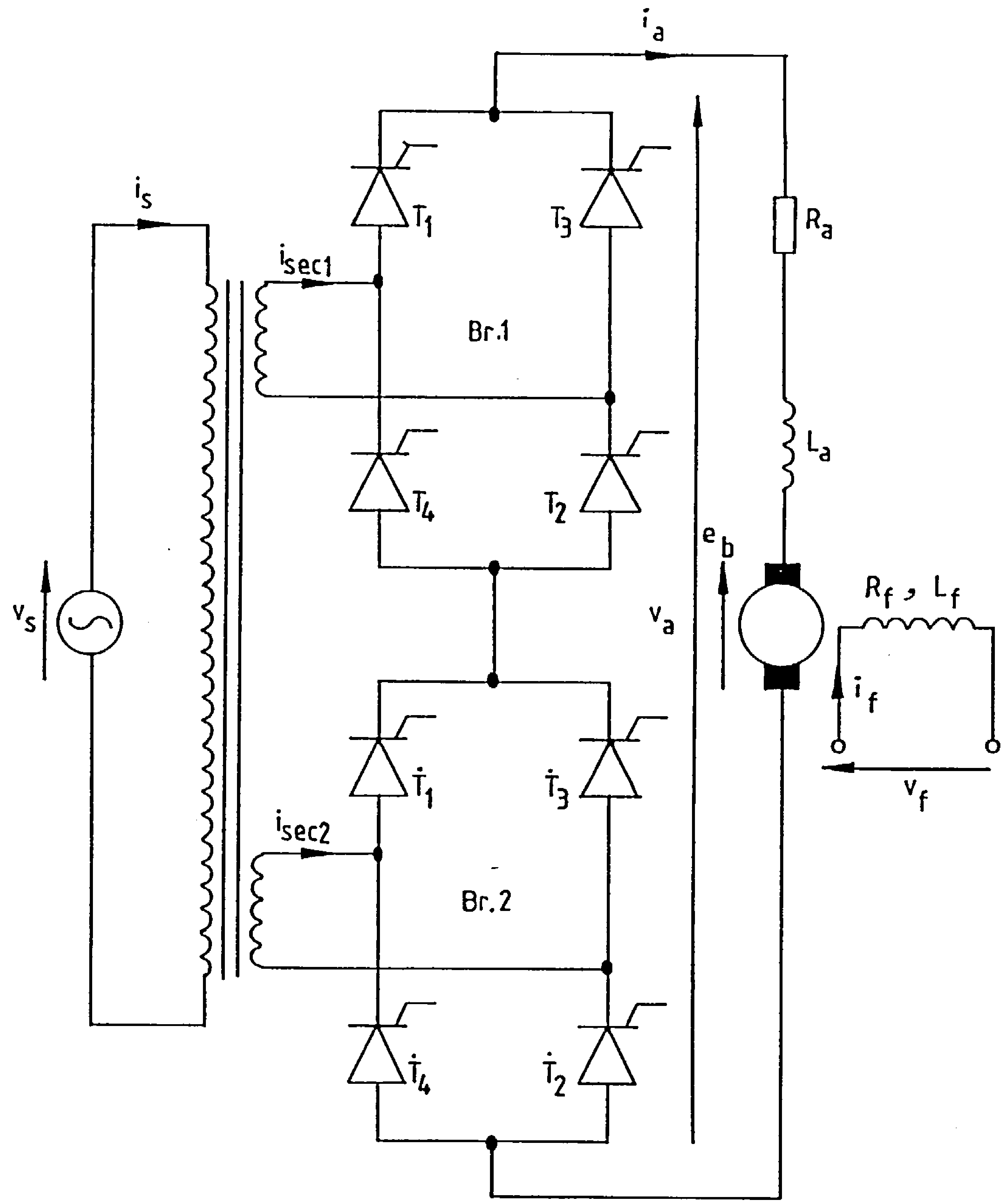

Figure2.4 Fully controlled series connected double-bridge converter.

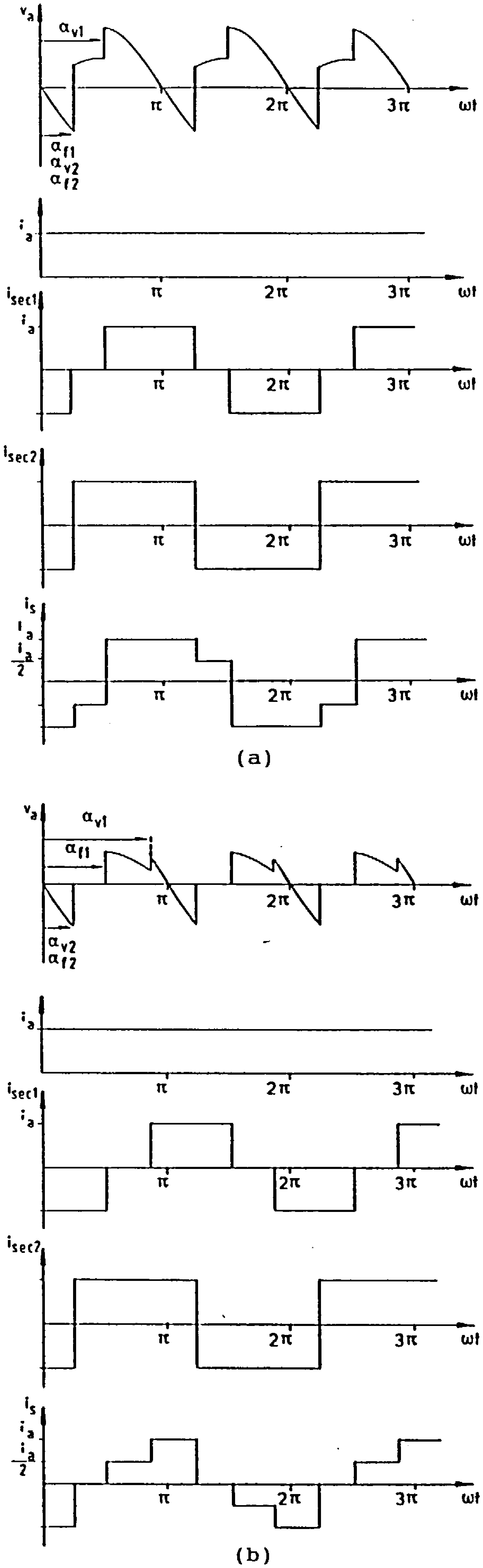

(a)

(b)

Figure2.5(a)to(d) Waveforms for method 1 operation of sequence-controlled double-bridge converter in zones 1 to 4 respectively.

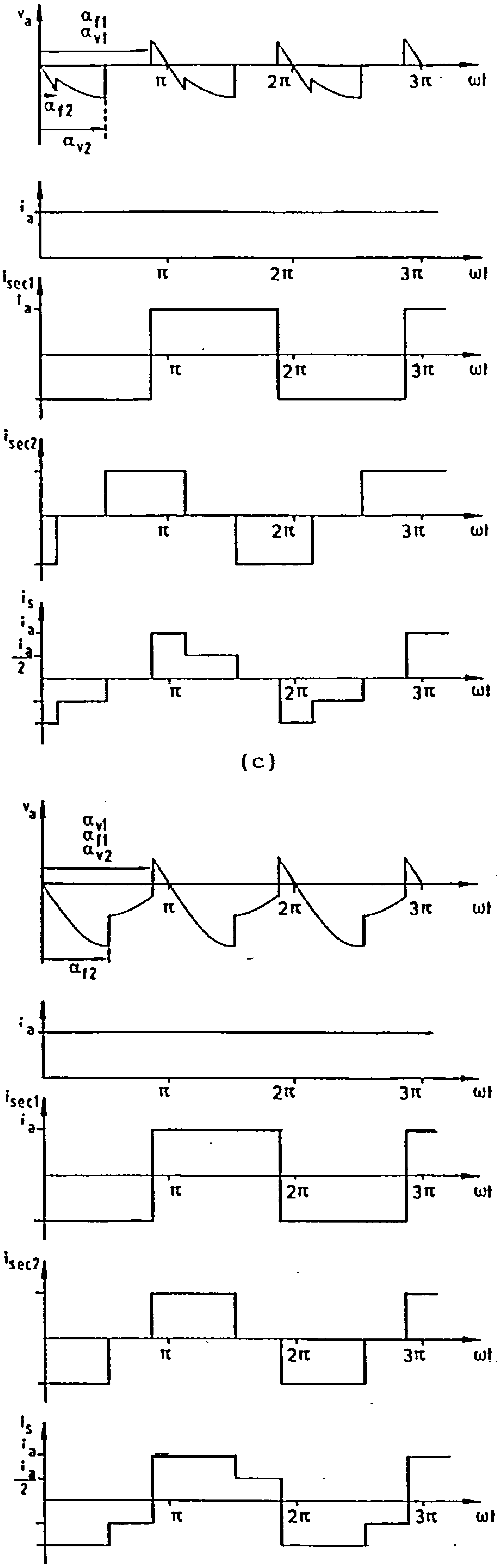

Figure2.5 Continued.

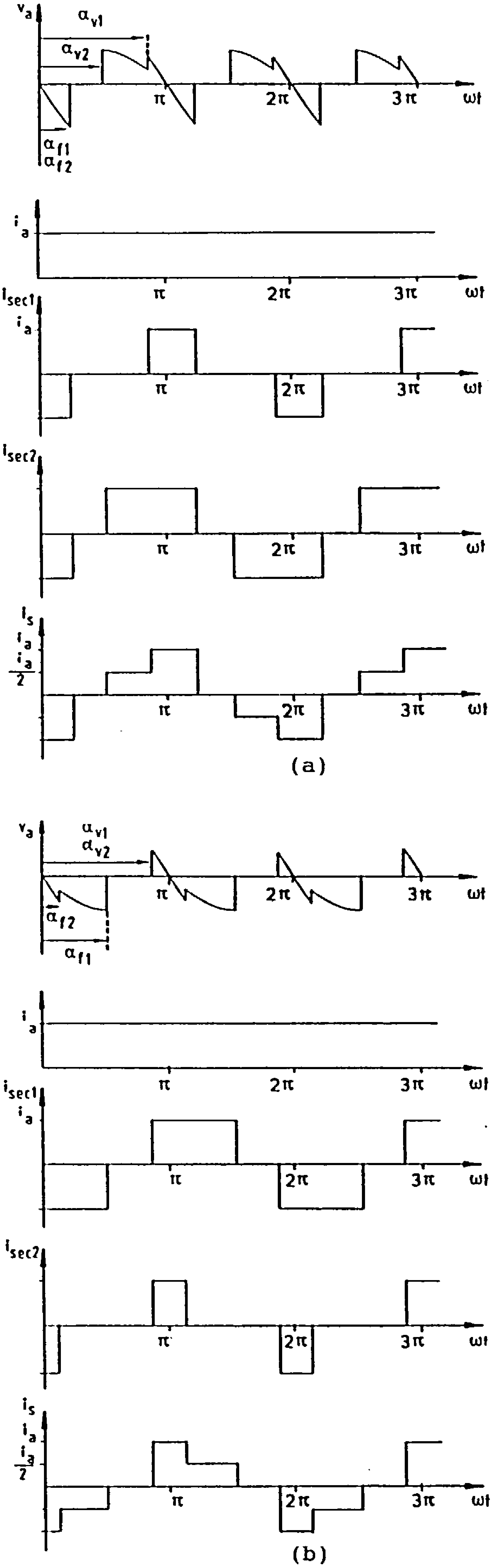

Figure2.6(a)and(b) Waveforms for method 2 operation of sequence-controlled double-bridge converter in zones 2 and 3 respectively.

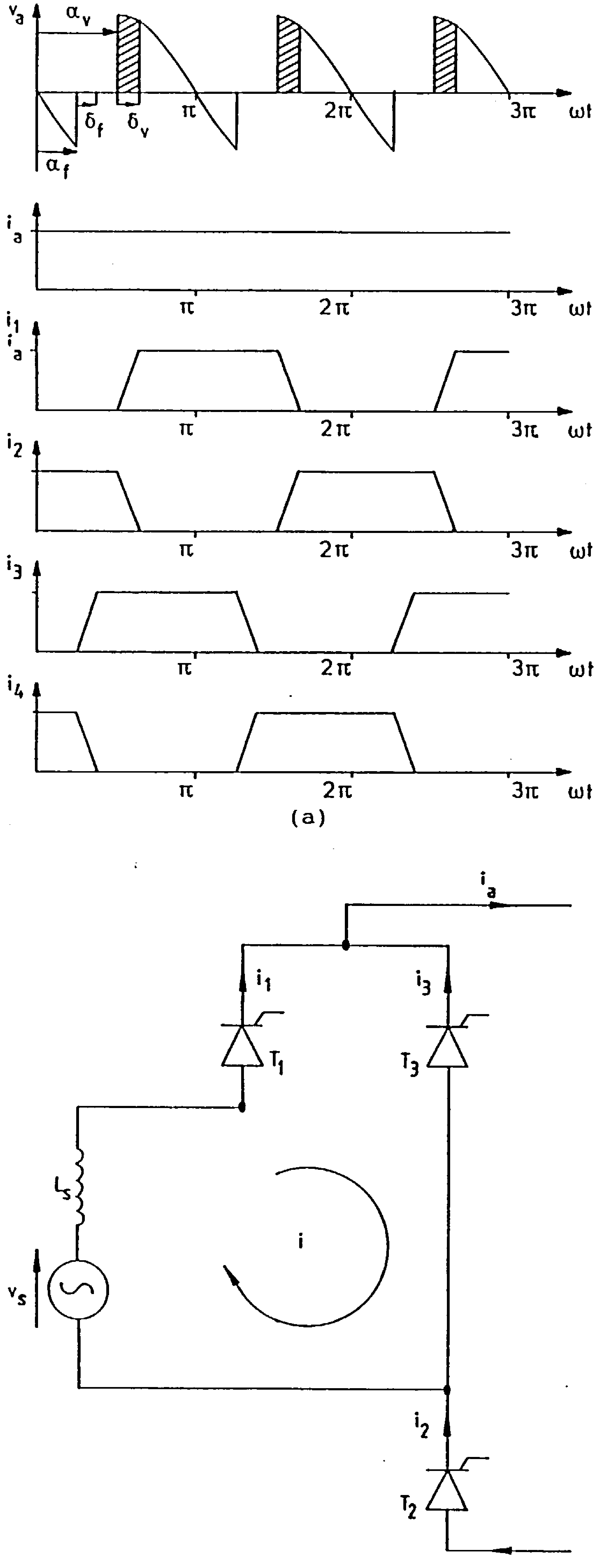

Figure2.7 Commutation in sequence controlled single-bridge converter.
(a) Waveforms.
(b) Equivalent circuit.

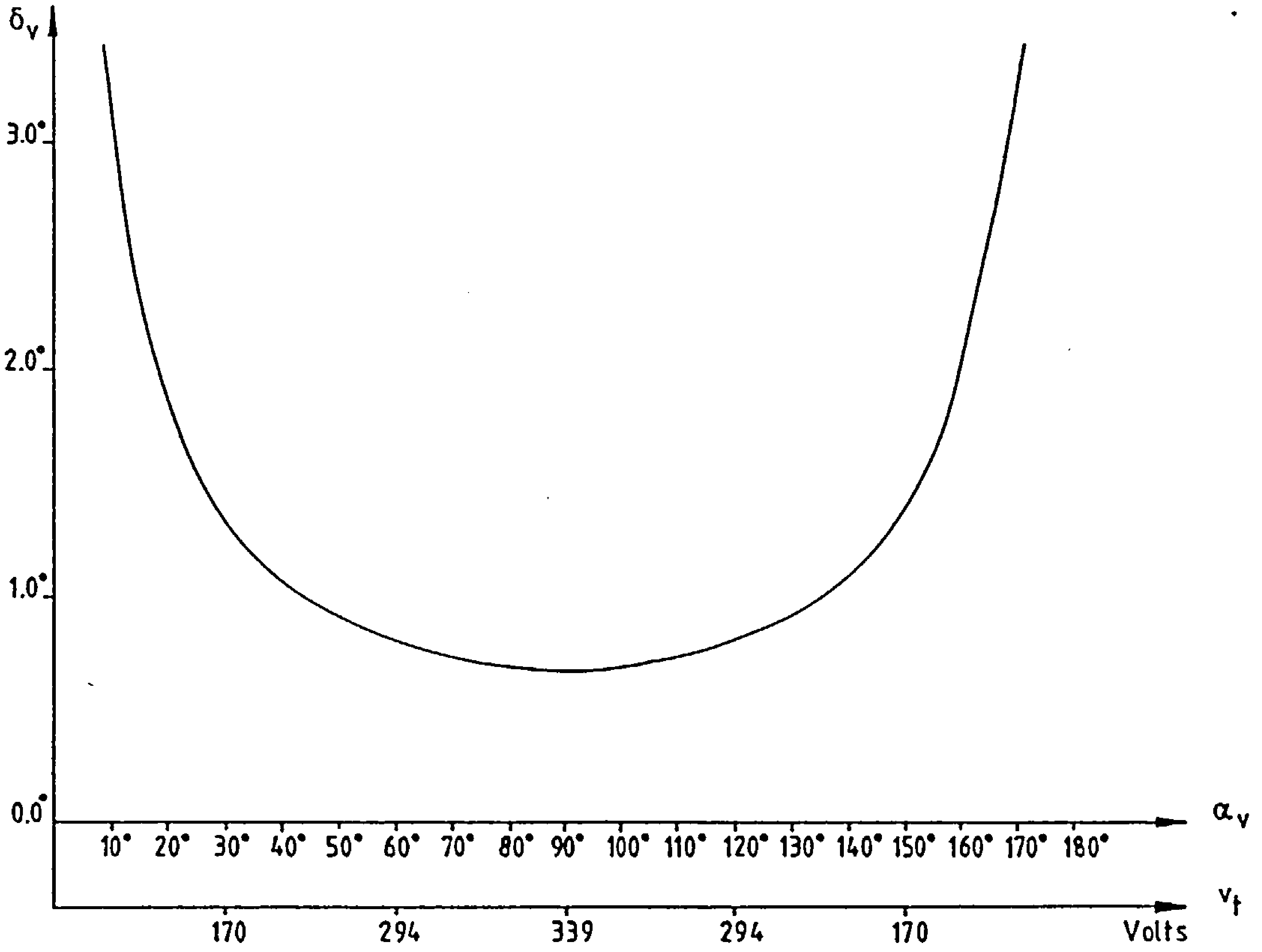

Figure2.7 Continued.
(c) Variation of commutation angle with commutating voltage.

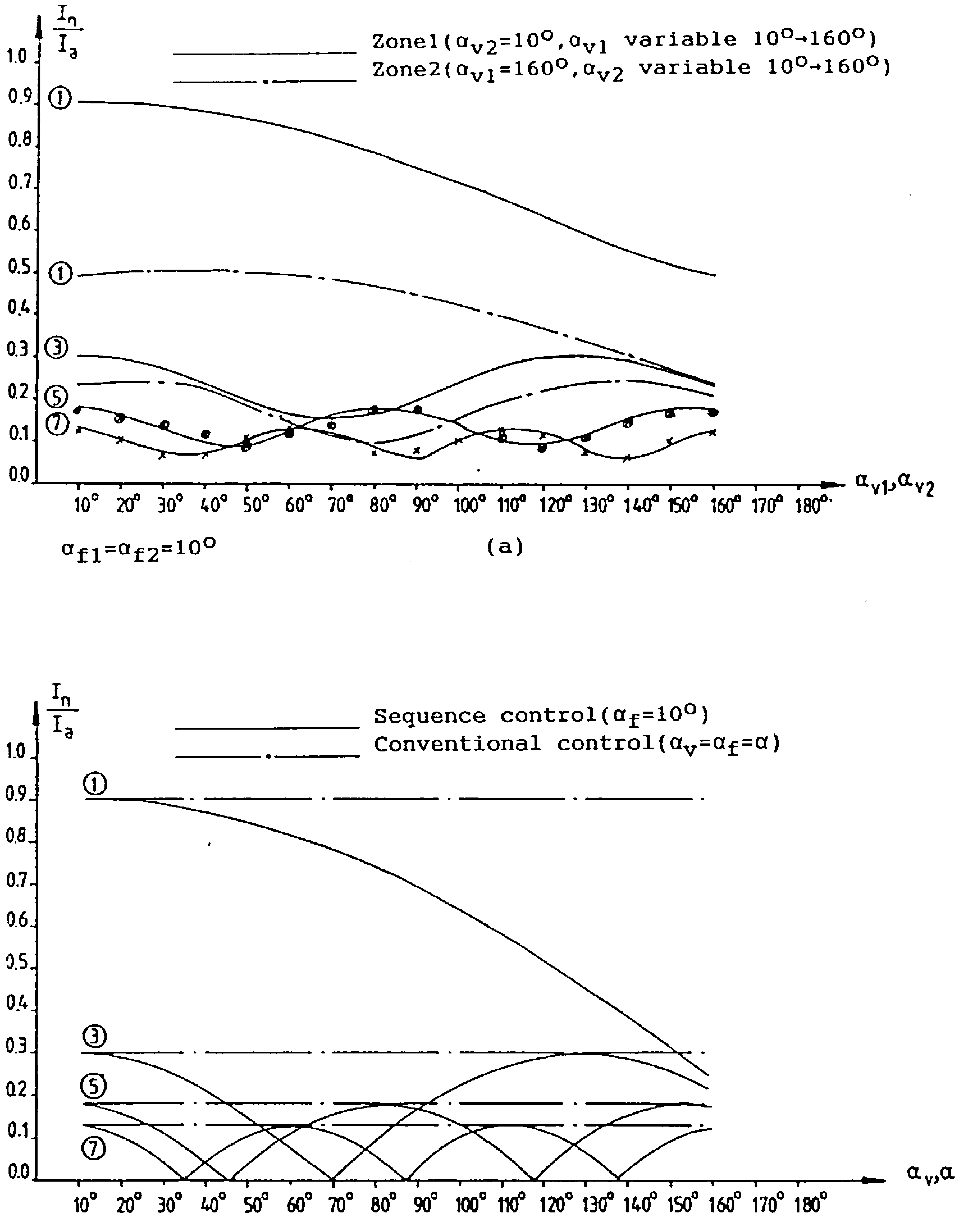

Figure2.8 Supply current harmonics.
(a) Sequence-controlled double-bridge converter.
(b) Sequence and conventional-controlled single-bridge converter.
(Encircled numbers indicate harmonic order)

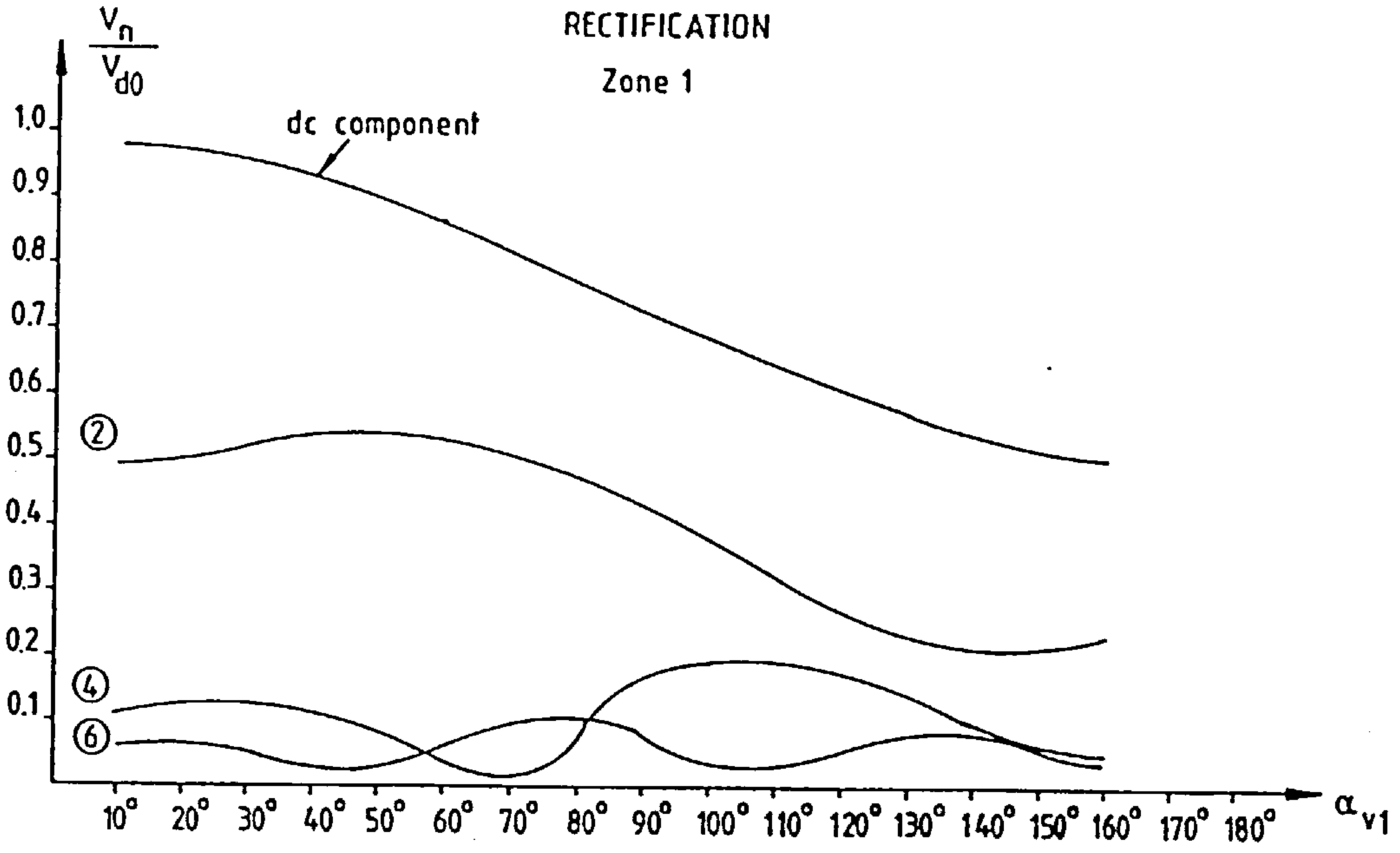

$\alpha_{f1}=\alpha_{f2}=\alpha_{v2}=10^o$ (a)

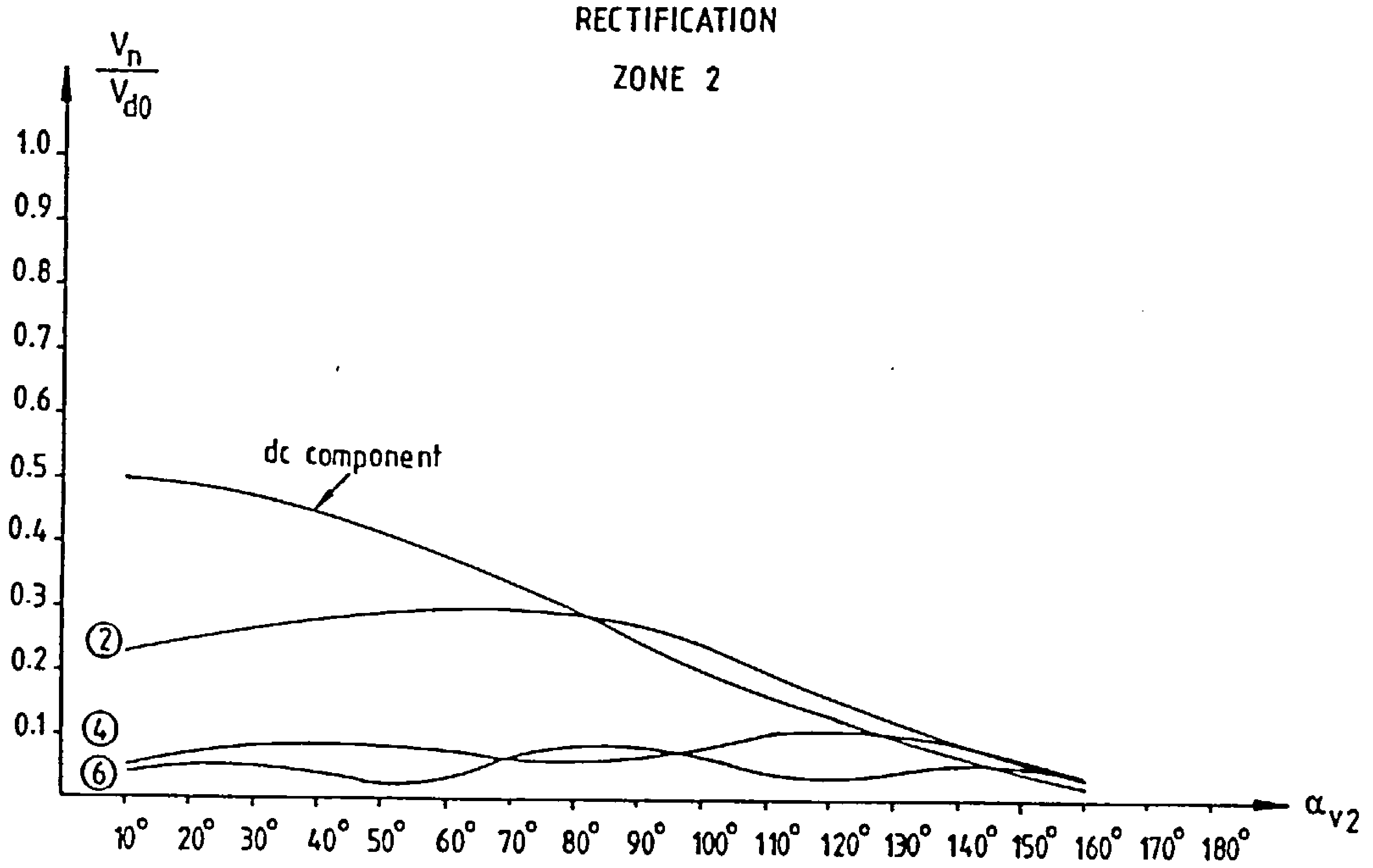

$\alpha_{f1}=\alpha_{f2}=10^o, \alpha_{v1}=160^o$ (b)

Figure2.9(a)to(d) Armature voltage harmonics for sequence-controlled double-bridge converter.
(Encircled numbers indicate harmonic order)

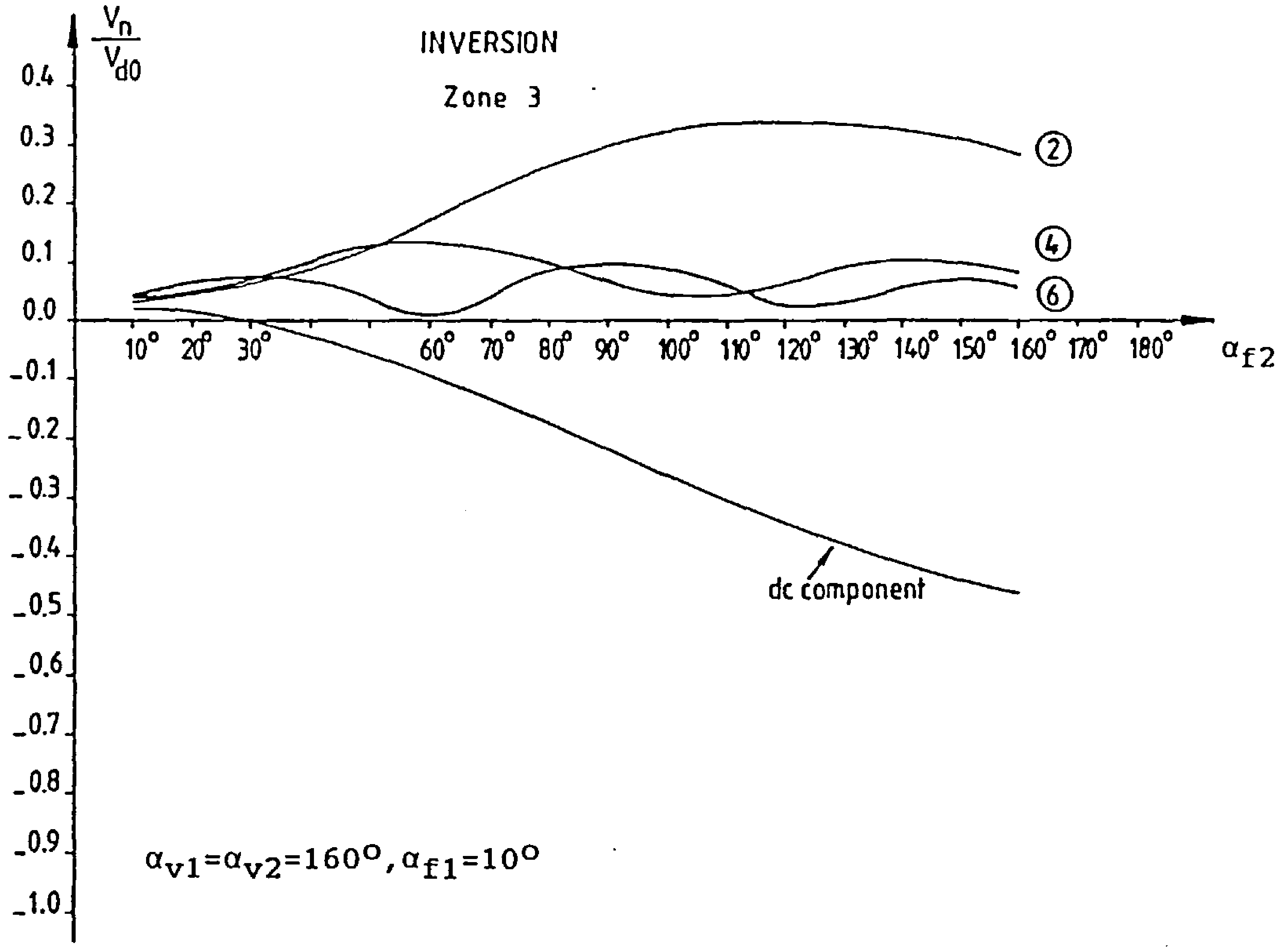

(c)

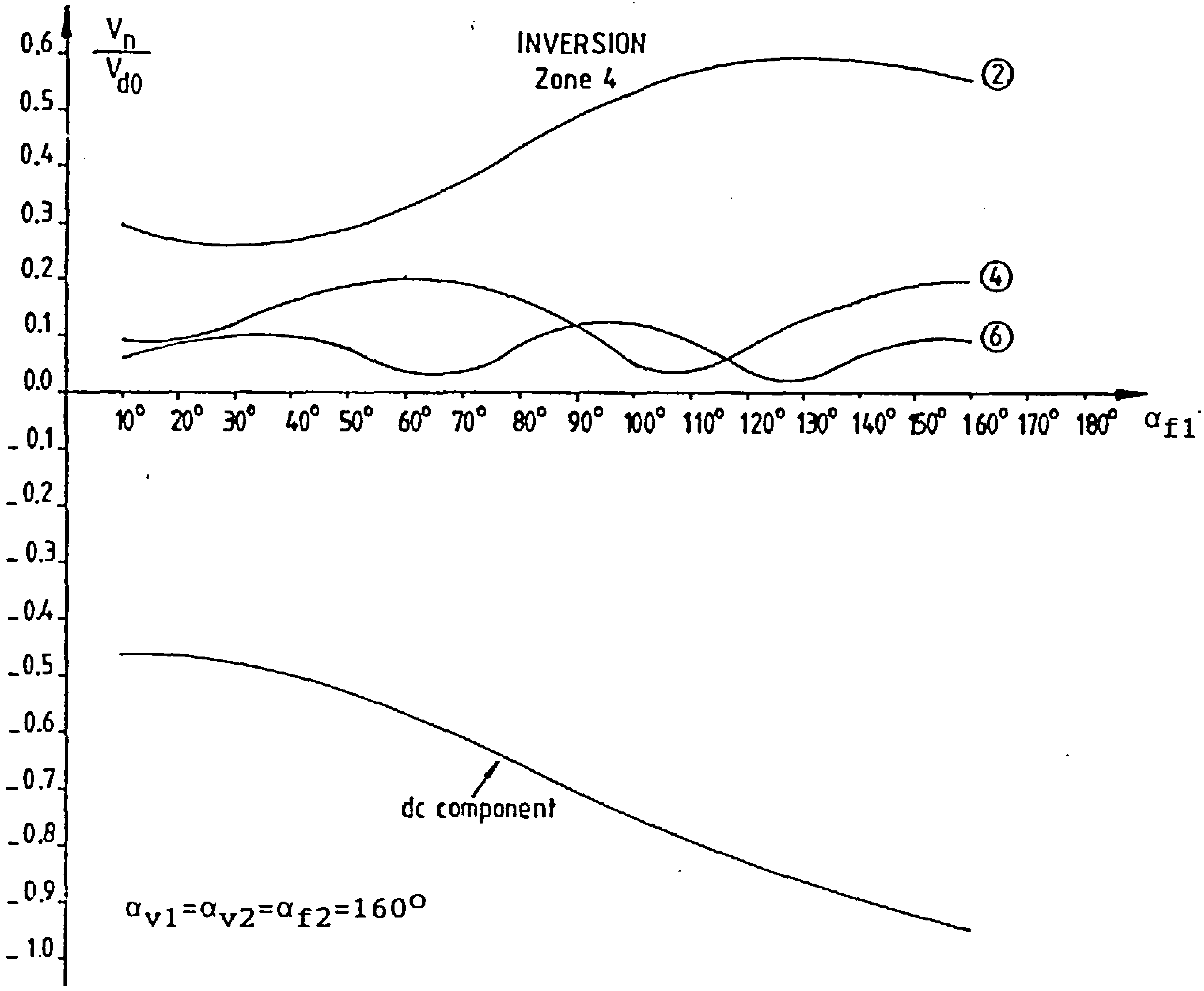

(d)

Figure2.9 Continued.

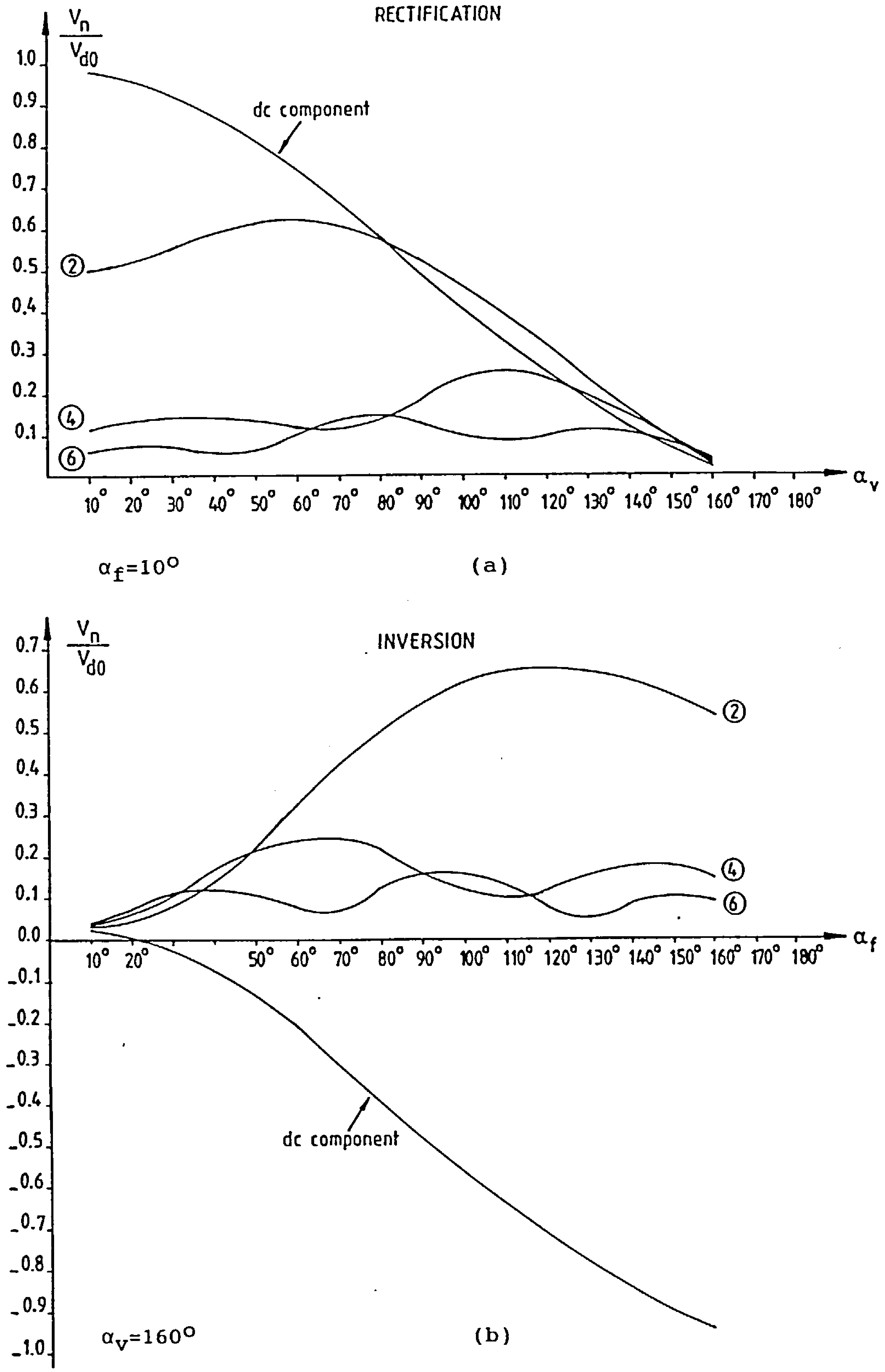

Figure2.10(a)and(b) Armature voltage harmonocs for sequence-controlled single-bridge converter.
(Encircled numbers indicate harmonic order)

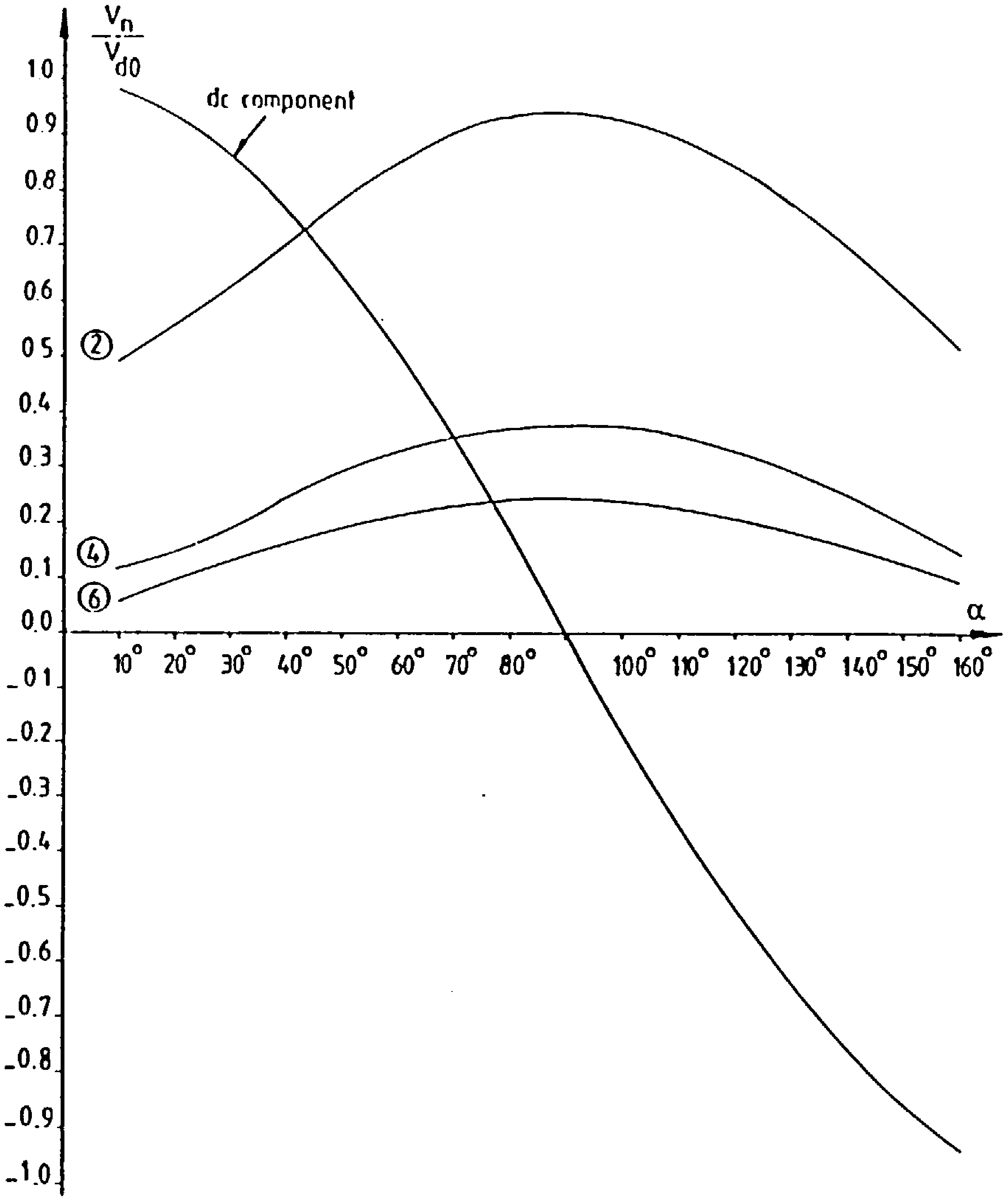

Figure2.11 Armature voltage harmonics for conventional-controlled single-bridge converter.
(Encircled numbers indicate harmonic order)

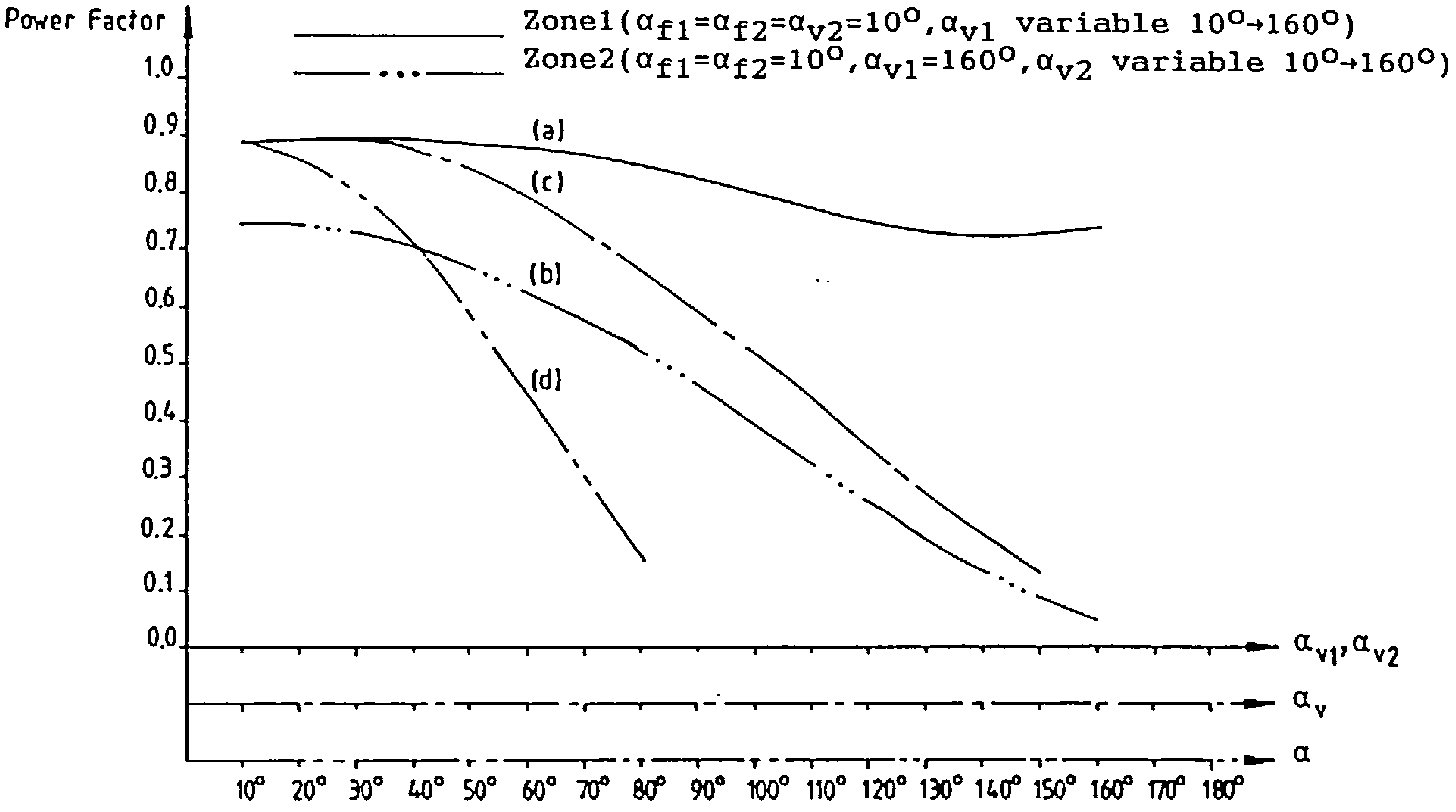

Figure2.12 Power factor variation with firing delay angle.
(a),(b) Sequence-controlled double-bridge converter.
(c) Sequence-controlled single-bridge converter($\alpha_f=10^{o}$).
(d) Conventional-controlled single-bridge converter($\alpha_v=\alpha_f=\alpha$)

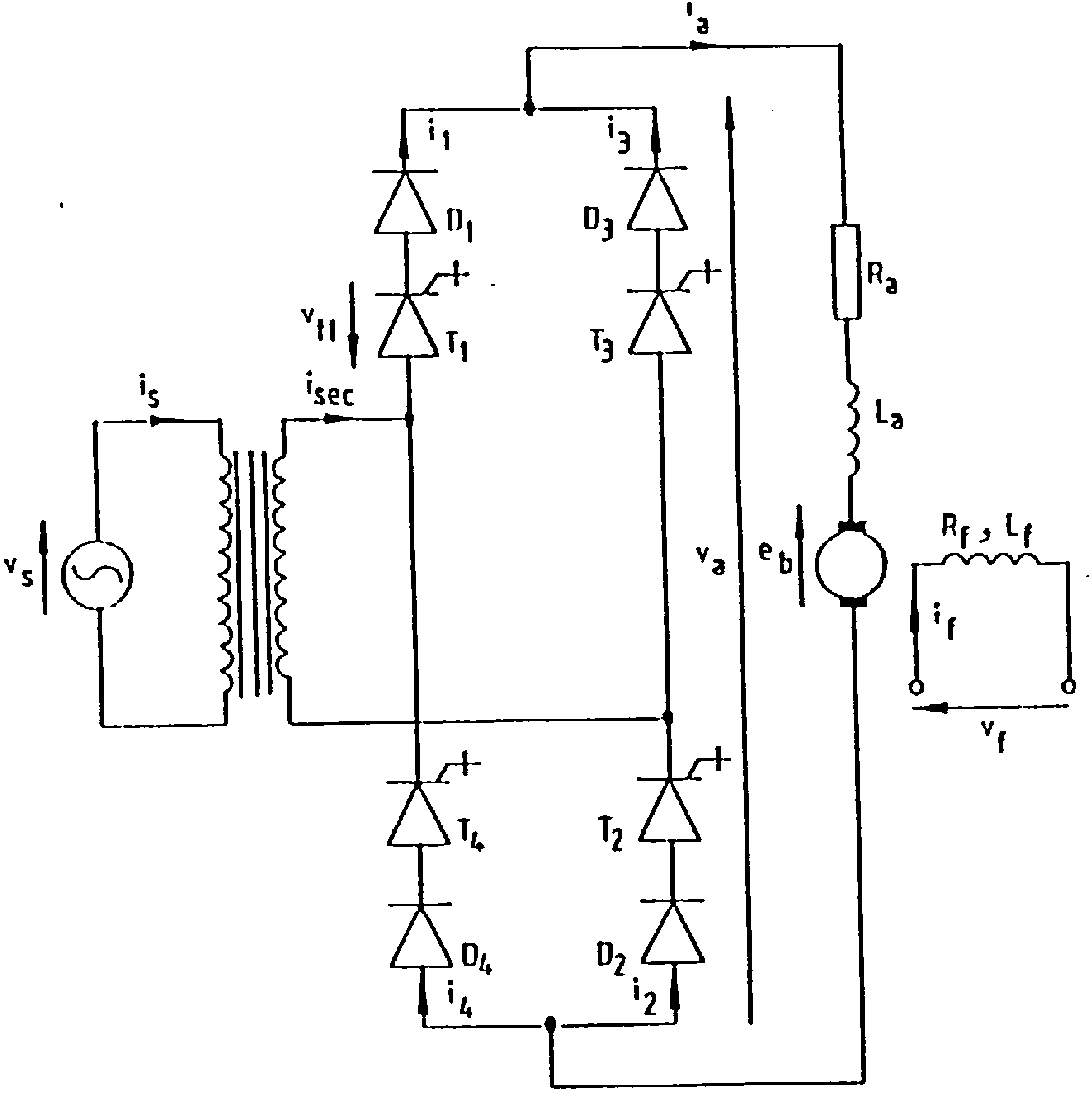

(a)

Figure2.13 Fully-controlled PWM Bridge Converter.
(a) Connection.

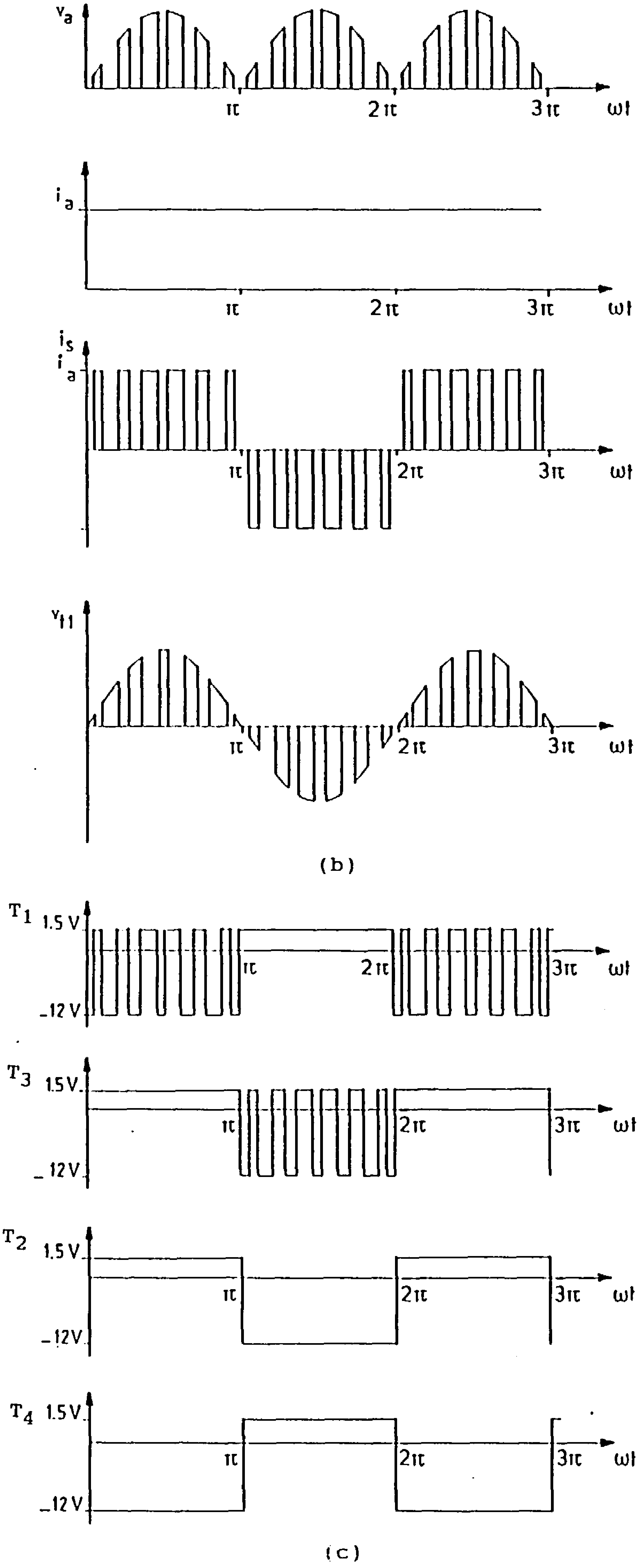

Figure2.13 Continued.
(b) Waveforms for rectification.
(c) Gate signals to GTO thyristors T_1 to T_4.

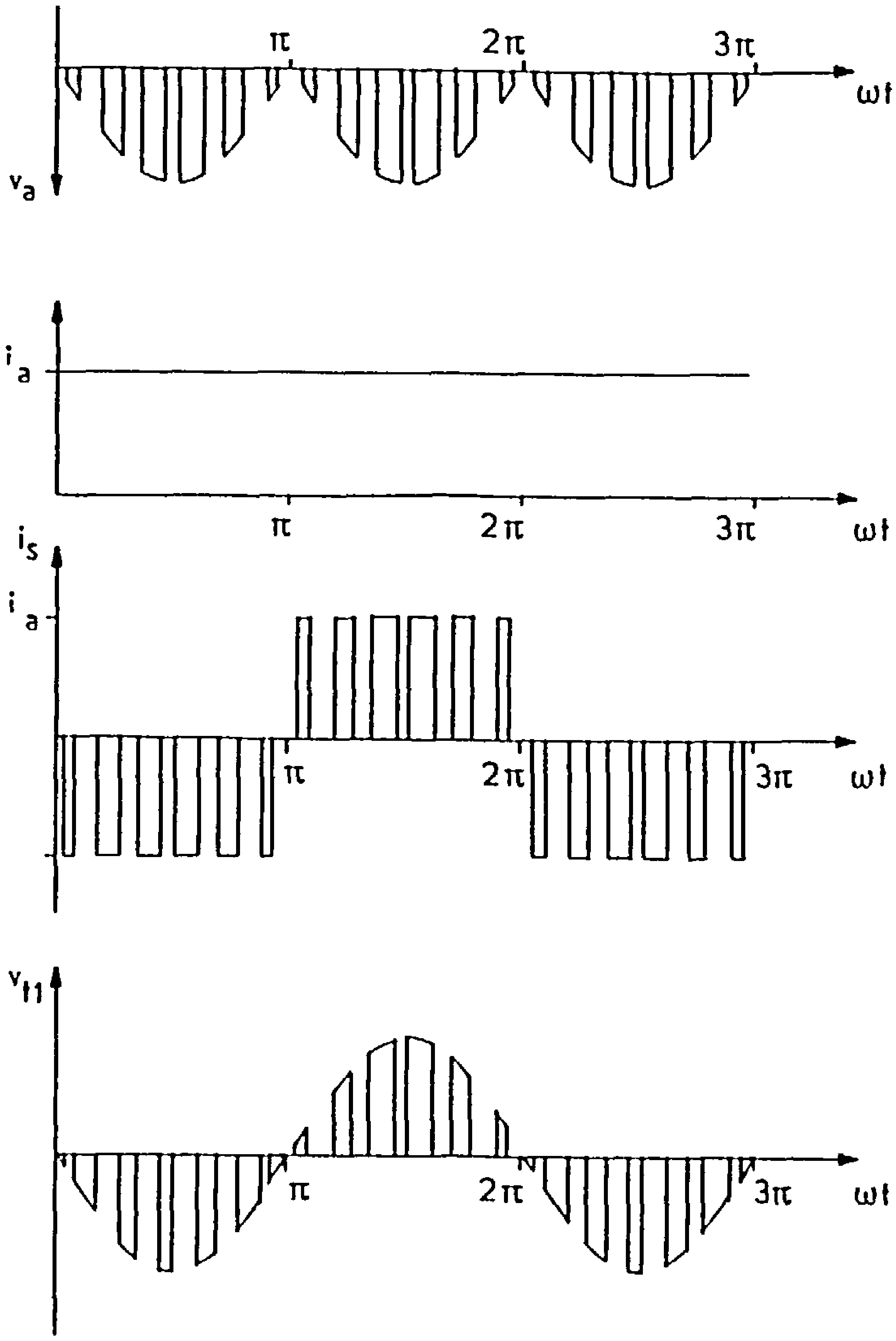

(d)

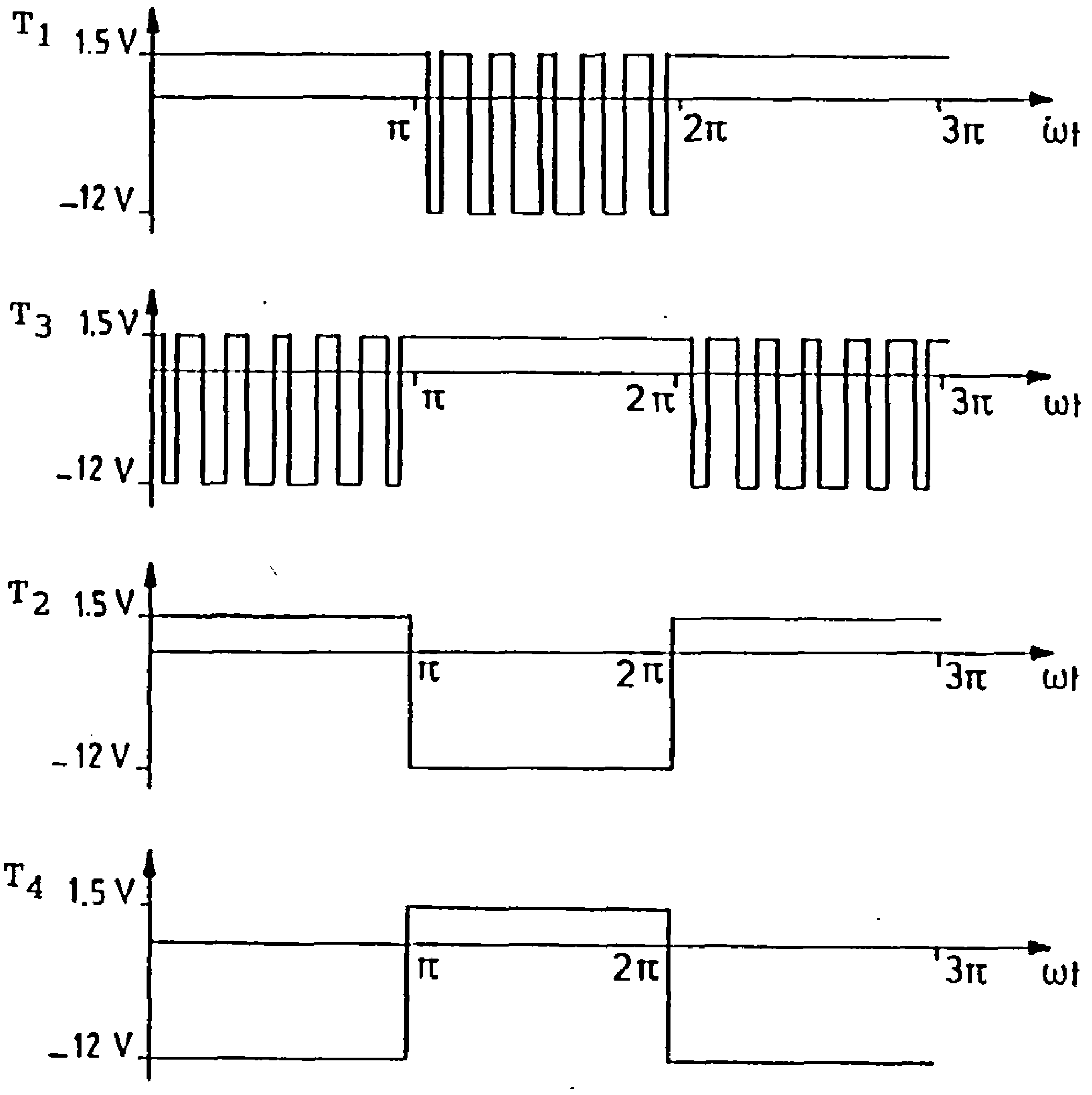

(e)

Figure2.13 Continued.
(d) Waveforms for inversion.
(e) Gate signals to GTO thyristors T_1 to T_4.

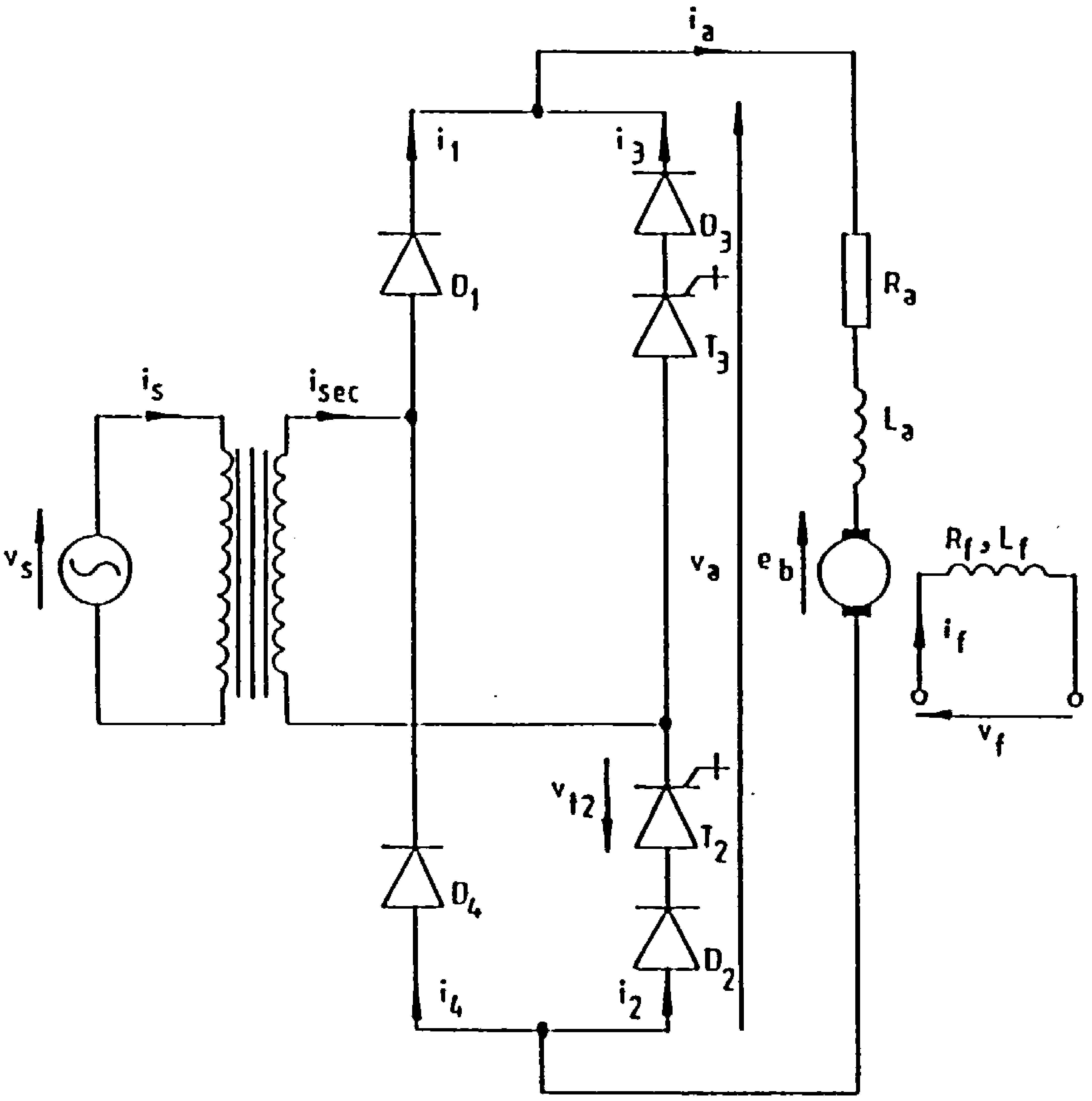

(a)

Figure2.14 Half-controlled PWM Bridge Converter.
(a) Connection.

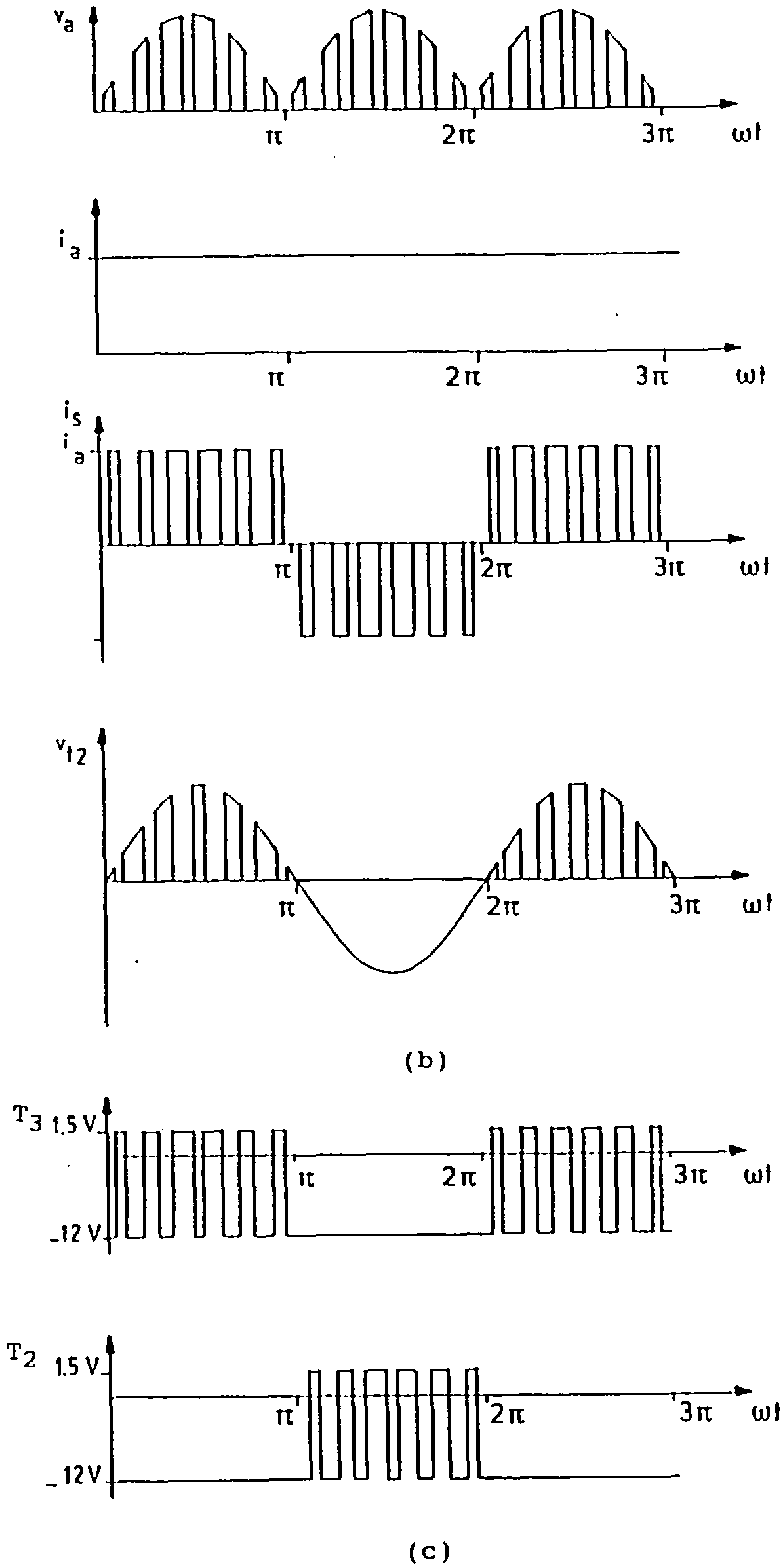

Figure2.14 Continued.
(b) Waveforms.
(c) Gate signals to GTO thyristors T_3 and T_2.

CHAPTER 3

Design of Sequence-Controlled Double-bridge Converter

A schematic diagram for the power circuit of the sequence controlled double-bridge converter described in Chapter 2 is shown in figure 3.1. Each thyristor has a parallel snubber circuit to protect against an excessive rate-of-rise of voltage. The design of the snubber is explained in Appendix A3.

The choice of thyristor, based on the expected load conditions, is discussed in section 3.1. Sections 3.2 and 3.3 describe respectively the analogue and digital control systems required to produce sequence control for the thyristor switching.

3.1 Device Ratings

The voltage and current ratings of the thyristors must be sufficiently in excess of the rated output (200V at 11A) to provide an adequate safety margin in the event of voltage spikes or current surges. On this basis a 1400V, 24A device was chosen. The $\frac{dV}{dt}$ rating of 200V/µs obtained from the device data sheet determines the snubber circuit components and the $\frac{di}{dt}$ rating is not of great significance, since the load is inductive. The selection of the high-speed fuses (FS1 and FS2 of figure 3.1) used for over-current protection is outlined in Appendix A4. The choice of heat sink, which constitutes an important part of the power circuit design, is described in detail in Appendix A5.

3.2 Analogue Control Circuit

The control system shown in block-diagram form in figure 3.2, is powered by stabilized power supplies at 15V, 1A and 30V, 0.5A. The 5V supply for the TTL logic circuits is obtained from an IC type voltage regulator as explained in section 3.2.2.

The control system contains four phase-shift circuits, two to control the firing delay angles α_{v1} and α_{f1} of bridge 1 (Br.1) and two the angles α_{v2} and α_{f2} of bridge 2 (Br.2). The phase-shift circuits could have a full range of control from 0^o to 180^o, to give the maximum range of output voltage control. However, the control range is limited to 10^o and 160^o, as explained earlier in Section 2.3 of Chapter 2. Buffer stages are used to provide sufficient gate current to trigger the thyristors.

3.2.1 Synchronization and Saw-tooth Generator

Synchronization of the thyristor gate drive signals with the supply and generation of the saw-tooth waveform is obtained by means of the circuit of figure 3.3(a), with its waveforms presented in figure 3.3(b). The secondary voltage of transformer TF1 is applied to zero cross-over detectors IC1 and IC2 to obtain the complementary square-waves v_1 and v_2, which in turn are applied to the bases of transistors TR1 and TR2. During negative half-cycles of the square-waves the transistors are non-conducting, and the -3 V input voltages to IC3 and IC4 are integrated to produce the positive ramp waveforms v_4 and v_5. During positive half-cycles of the square-waves the integrator capacitor is discharged and the output is clamped to zero. The two ramp waveforms are added using resistors R_9, R_{10} and R_{11} to provide the required saw-tooth waveform v_6 [22].

3.2.2 Firing Delay Angle Control

The firing delay angles of the two bridges are controlled using the circuit of figure 3.4(a). The saw-tooth waveform v_6 of figure 3.3(b) is applied to the four comparators IC2 to IC5, together with dc levels individually controlled by the variable resistors VR1 to VR4. The 5V supply to these variable resistors and trimming resistors R_l and R_u is obtained from a 7805 voltage regulator (IC1), which also provides the supply to the TTL logic circuits. The resistors R_l and R_u provide the lower and upper limits for the firing delay angles (10^o to 160^o respectively). Resistors R_9 to R_{12} and zener diodes Z_1 to Z_4 eliminate the negative portion of the output signals and clip the positive portion to 4.7V. The resulting output voltage waveform v_1 obtained from IC2 for two different firing delay angles is shown in figure 3.4(b).

3.2.3 Pulse-train Envelope Generator

Direct application of the phase-shift signals to monostables IC10 to IC13 of figure 3.4(a) would produce unstable pulse-train envelopes, due to the slow slew-rate of the operational amplifiers (Motorola MC1741) used in the preceding stages. To overcome this, the phase-shift signals are processed through Schmitt-triggers (IC6 to IC9) and then applied to the monostables. The output voltage waveforms v_2 from IC10 is shown in figure 3.4(c).

3.2.4 Steering and Pulse-train Signal Generator

The firing pulses derived from the monostables are directed to the relevant thyristor using the circuit of figure 3.5(a) with its voltage waveforms at terminals 1 to 8 shown in figure 3.5(b). The complementary square-waves v_2 and v_3 obtained in section 3.2.1 are chopped using the resistor-zener combination, and then ANDed with the firing pulses obtained from the monostables IC10 to IC13 of figure 3.4(a).

The pulse-train method of firing thyristors reduces the gate power dissipation and ensures reliable operation, especially with inductive load conditions [23]. Consequently this technique is implemented as shown in figure 3.6(a), by ANDing control pulses 1 to 8 of figure 3.5(b) with a 10 kHz square-wave derived from the astable multivibrator IC1. The resulting gate signals are shown in figure 3.6(b).

3.2.5 Buffer Stage

The pulse-trains obtained in the previous section are applied to buffer circuits, one of which is shown in figure 3.7. Electrical isolation between power and control circuits is provided by the pulse transformer TF1, the design of which is explained in Appendix A6. The purpose of the back-to-back diode D_1 and zener diode Z_1 is to reset the flux in the transformer core when transistor TR3 turns off. Diode D_2 eliminates the negative portion of the gate voltage, while resistor R_6 connected between the thyristor gate and cathode decreases the possibility of unwanted turn-on due to an excessive rate-of-rise of anode-cathode voltage.

3.3 Digital Control Circuit

A block diagram of the digital controller for varying the firing delay angles is given in figure 3.8. The 8-bit binary number A, defined in table 3.1 in terms of the firing delay angle, is applied to the four octal positive edge-triggered latches IC1 to IC4 shown in figure 3.9. The outputs of these are controlled by push buttons pb1 to pb4, to initiate the desired firing delay angles α_{v1}, α_{f1}, α_{v2} and α_{f2} respectively. The outputs from IC1 to IC4 are compared separately with an 8-bit binary number B, using four comparators. The 4-bit comparators (IC5 to IC12) are cascaded in pairs, as shown in figure 3.9, to provide the four 8-bit comparators. The number B is produced by applying a 25.6 kHz clock signal to two cascaded 4-bit counters IC13 and IC14, to produce a maximum count of 2^8 in 10 ms. The three possible decisions A>B, A=B and A<B are externally available at the three output pins of the comparators. The outputs A>B from IC9 to IC12 are used; which give output waveforms of logic 1 when A>B and logic 0 when A≤B. These waveforms are inverted using IC15 to produce the four firing delay angles α_{v1}, α_{f1}, α_{v2} and α_{f2} respectively.

Synchronization of the counter with the mains supply is achieved using the circuit of figure 3.10(a) with its voltage

Firing Delay Angle, deg	Equivalent Binary Number A
0	0000 0000
10	0000 1110
20	0001 1100
30	0010 1011
40	0011 1000
50	0100 0111
60	0101 0110
70	0110 0011
80	0111 0000
90	1000 0000
100	1000 1110
110	1001 1100
120	1010 1100
130	1011 1001
140	1100 0110
150	1101 0101
160	1110 0000
170	1111 0001
180	1111 1111

Table 3.1 Equivalent binary number for firing delay angle.

waveforms shown in figure 3.10(b). The 240V supply is stepped-down by transformer TF1 and the secondary voltage is applied to two zero cross-over detectors to produce two complementary square-wave voltages. The resistor-zener combinations R_5, Z_1 and R_6, Z_2 eliminate the negative portion of these waveforms and clip the positive portion to 4.7V. The complementary voltages are applied to monostables IC3 and IC4, with corresponding output pulses being fed to the OR-gate IC5. The output from OR-gate v_6 is applied to terminal C of figure 3.9 to reset the count at each zero cross-over of the supply voltage. The steering and pulse-train signal generator circuit is given in figure 3.11(a) and the corresponding voltage waveforms in figure 3.11(b). The buffer stage is the same as that described in section 3.2.5.

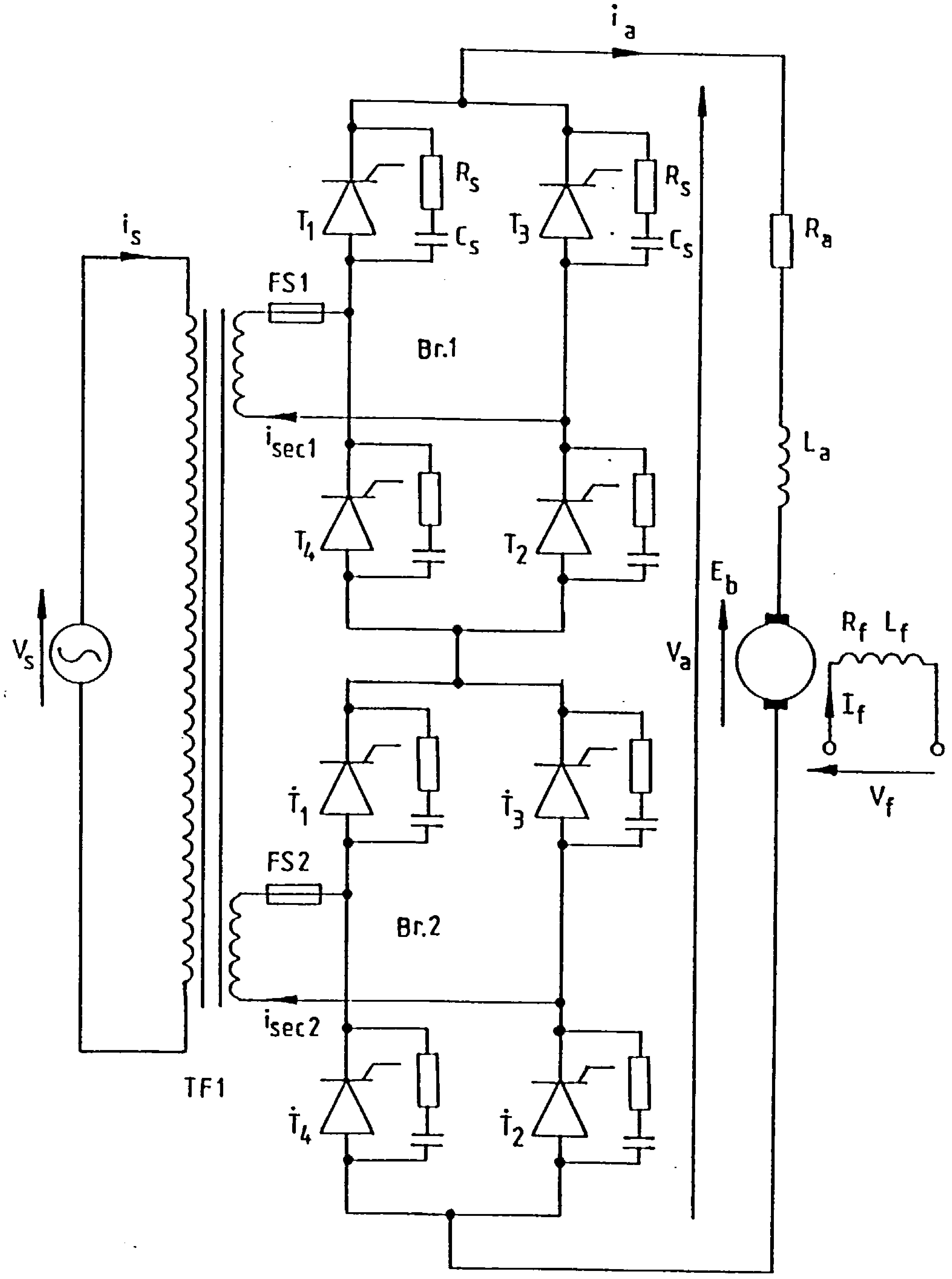

Figure3.1 Fully-controlled series connected double-bridge converter.

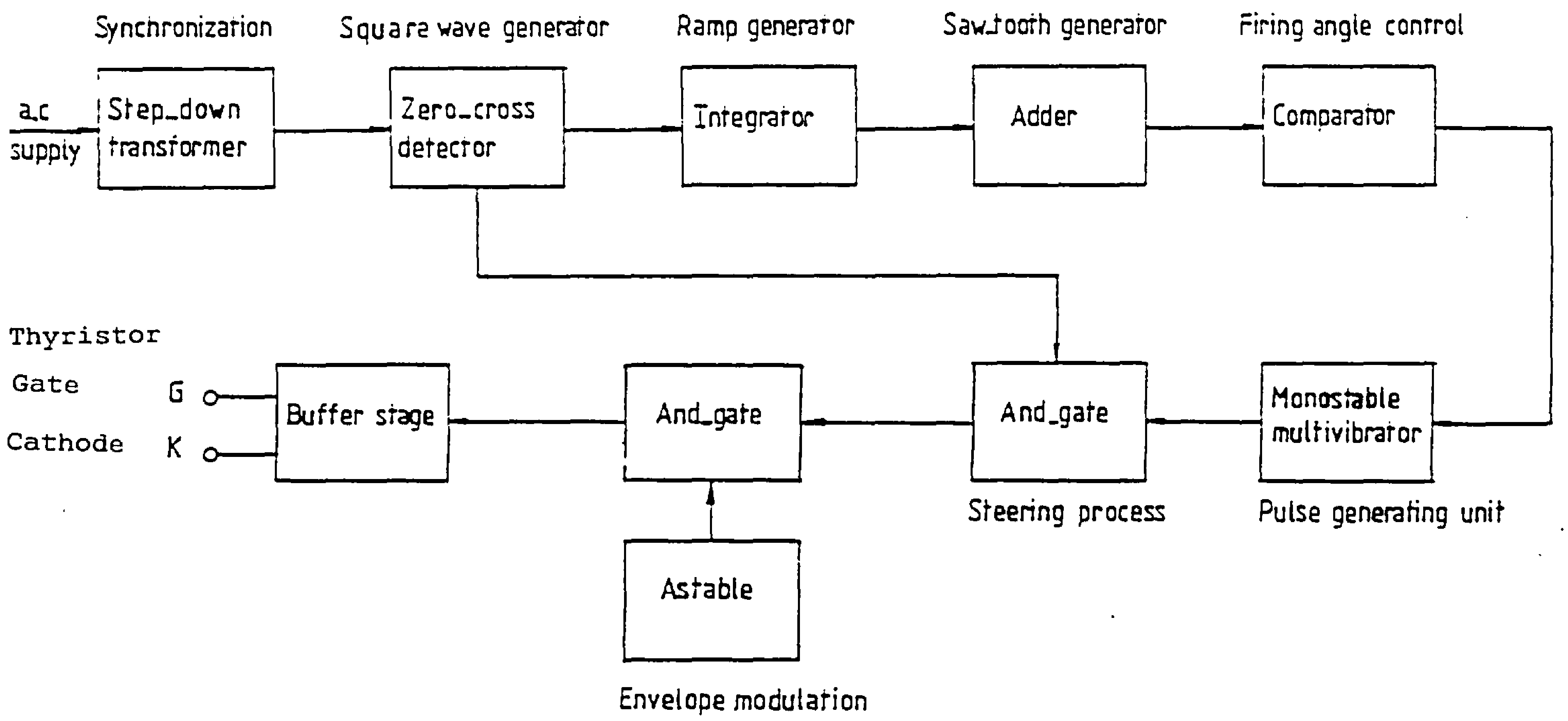

Figure3.2 Block diagram of analogue control system to produce sequence control for thyristor switching.

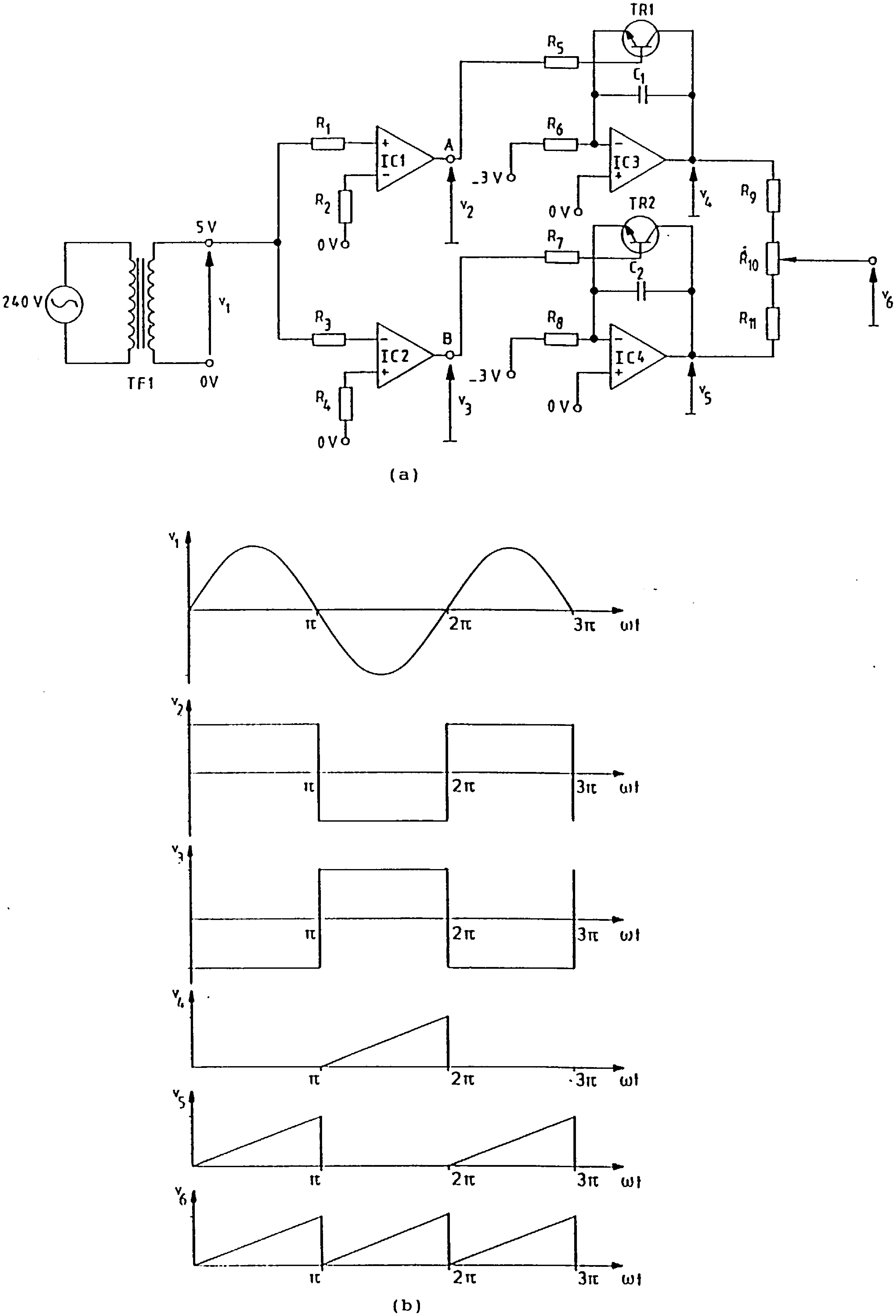

Figure3.3 Synchronization and saw-tooth generator.
(a) Connection.
(b) Waveforms.
(List of components given in Appendix A10)

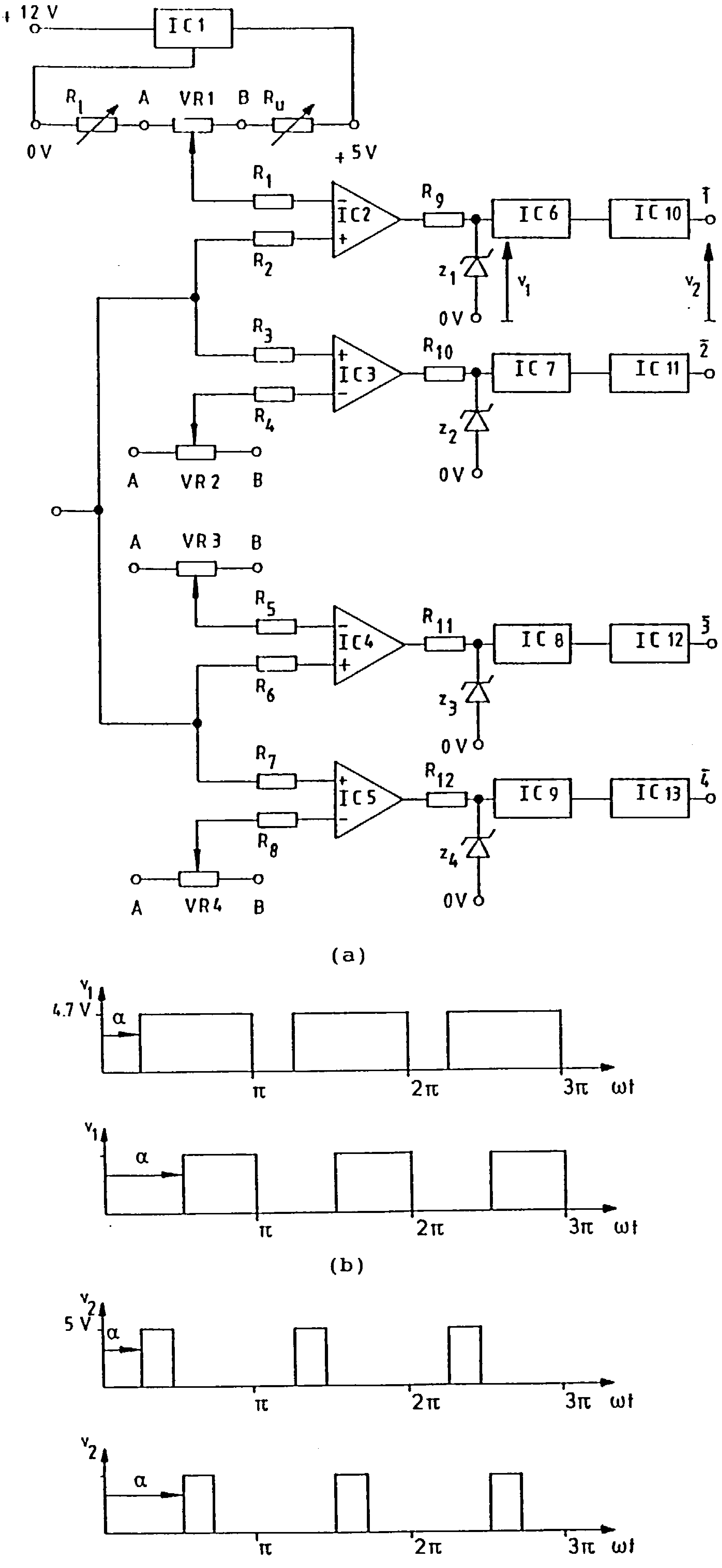

(a)

(b)

(c)

Figure3.4 Firing delay angle control and pulse-train envelope generator.
(a) Connection.
(b) Waveforms of two different firing delay angle.
(c) Waveforms from monostable.
(List of components given in Appendix A10)

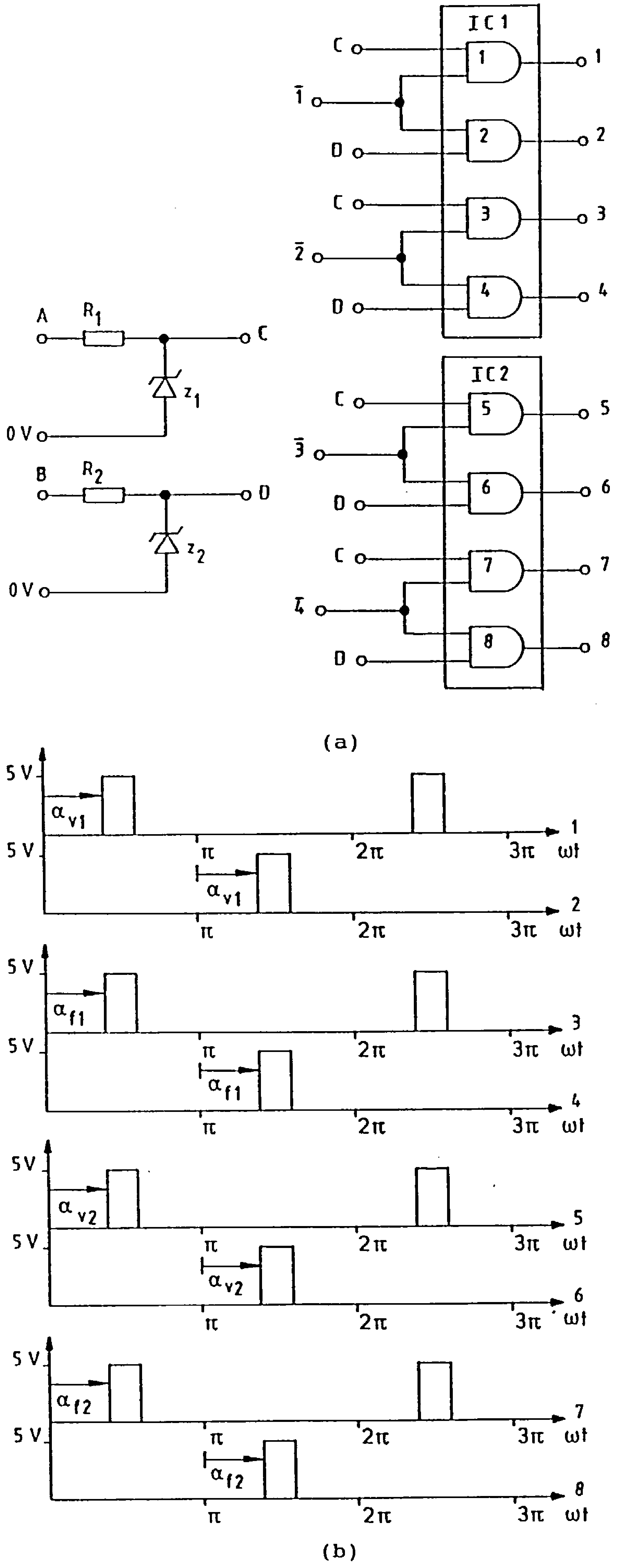

Figure3.5 Circuit diagram of steering process.
(a) Connection.
(b) Waveforms.
(List of components given in Appendix A10)

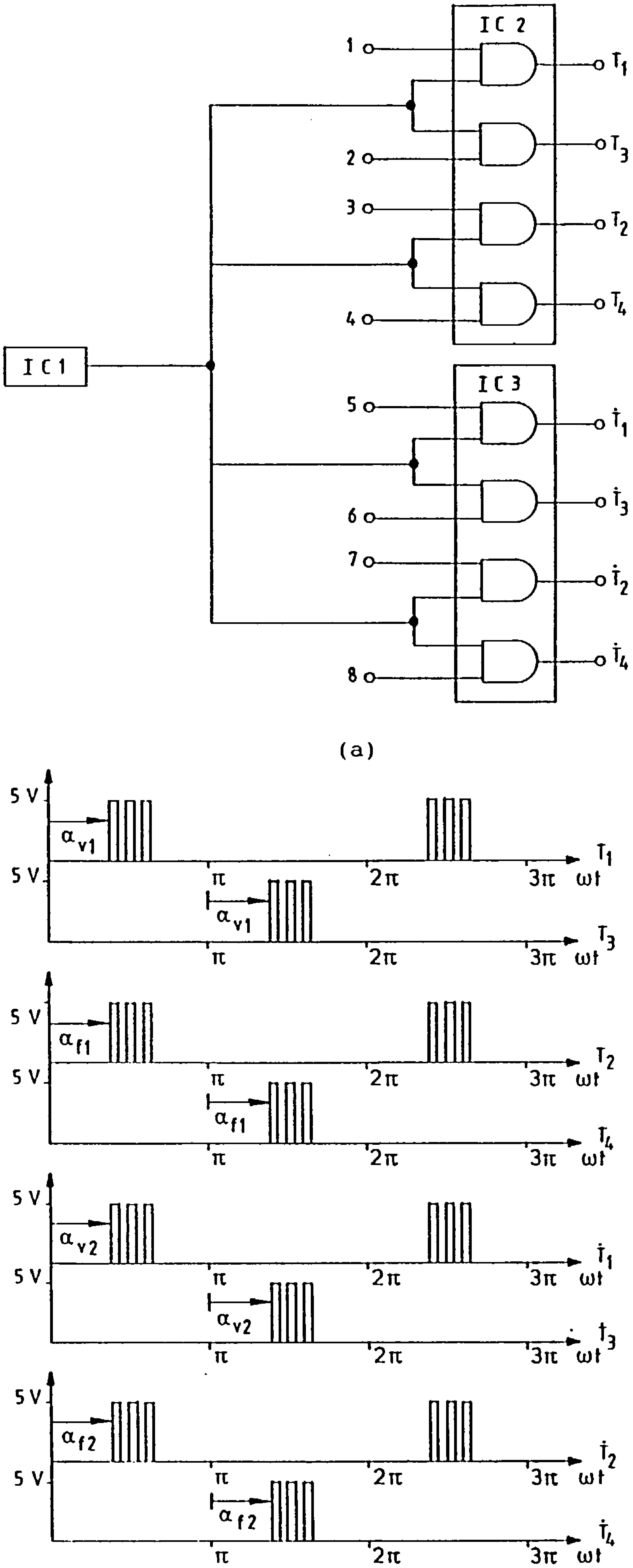

(a)

(b)

Figure3.6 Pulse-train signal generator.
(a) Connection.
(b) Waveforms.
(List of components given in Appendix A10)

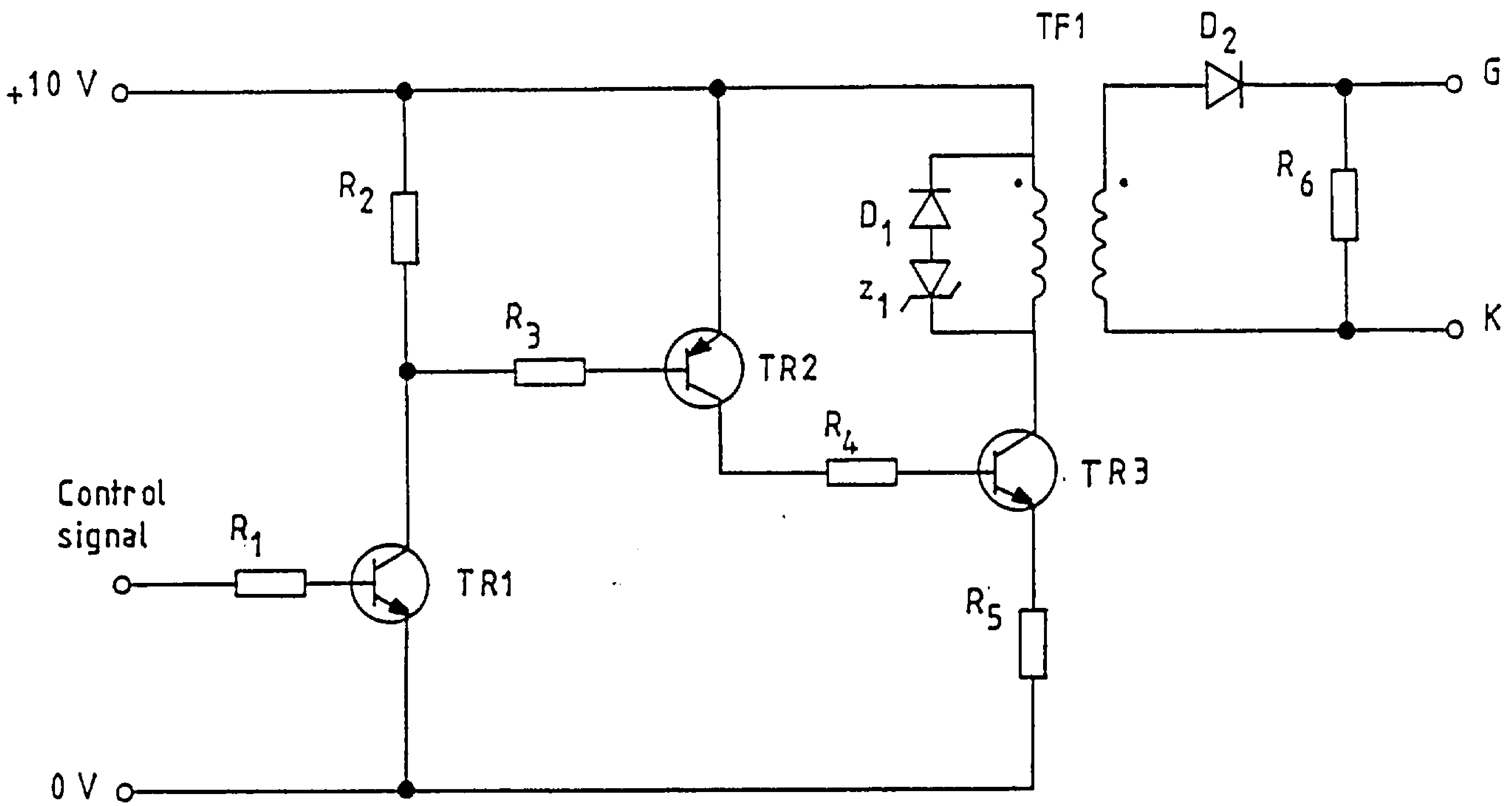

Figure3.7 Pulse amplifier circuit.
(List of components given in Appendix A10)

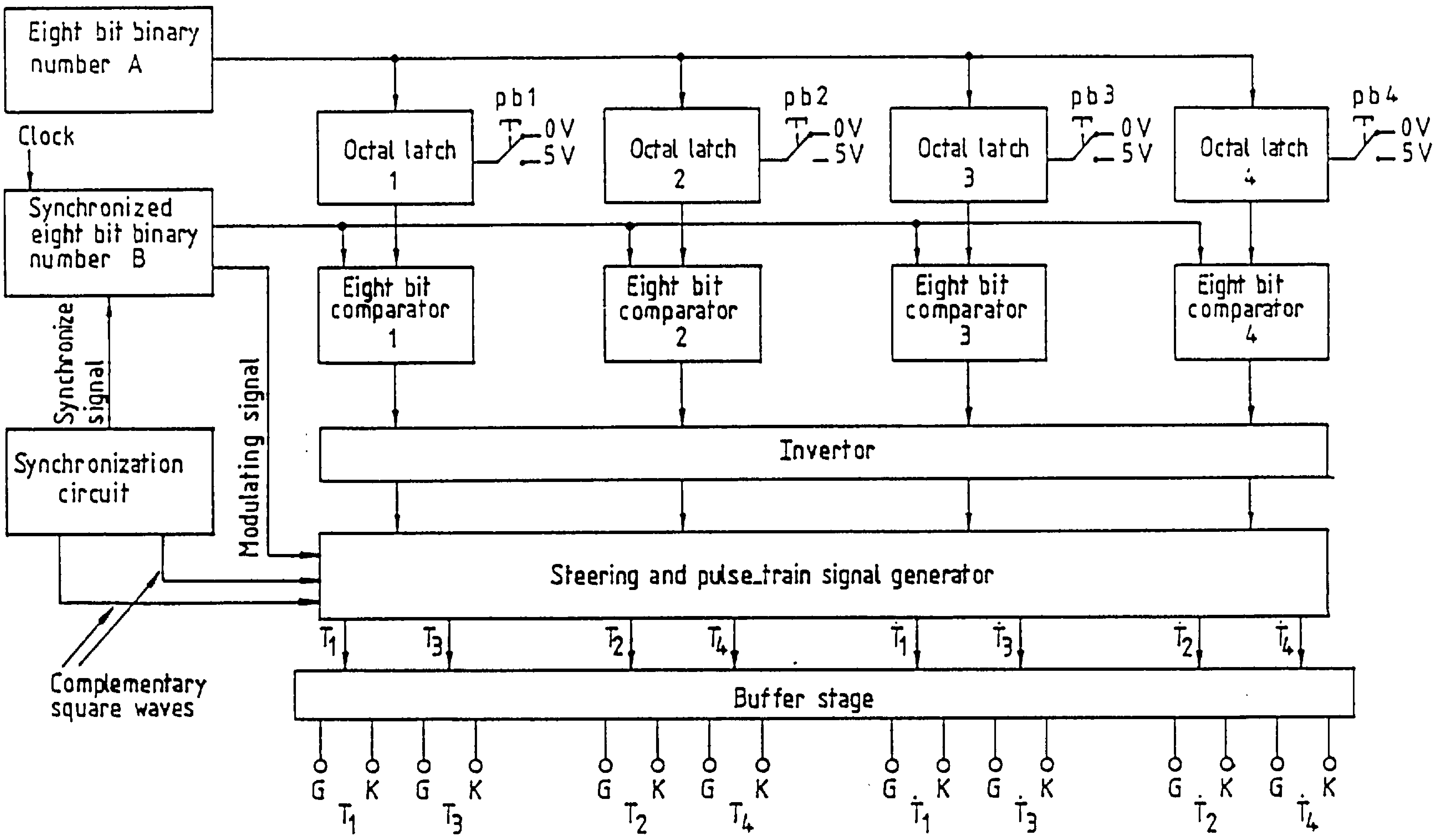

Figure3.8 Block diagram of digital control system to produce sequence control for thyristor switching.

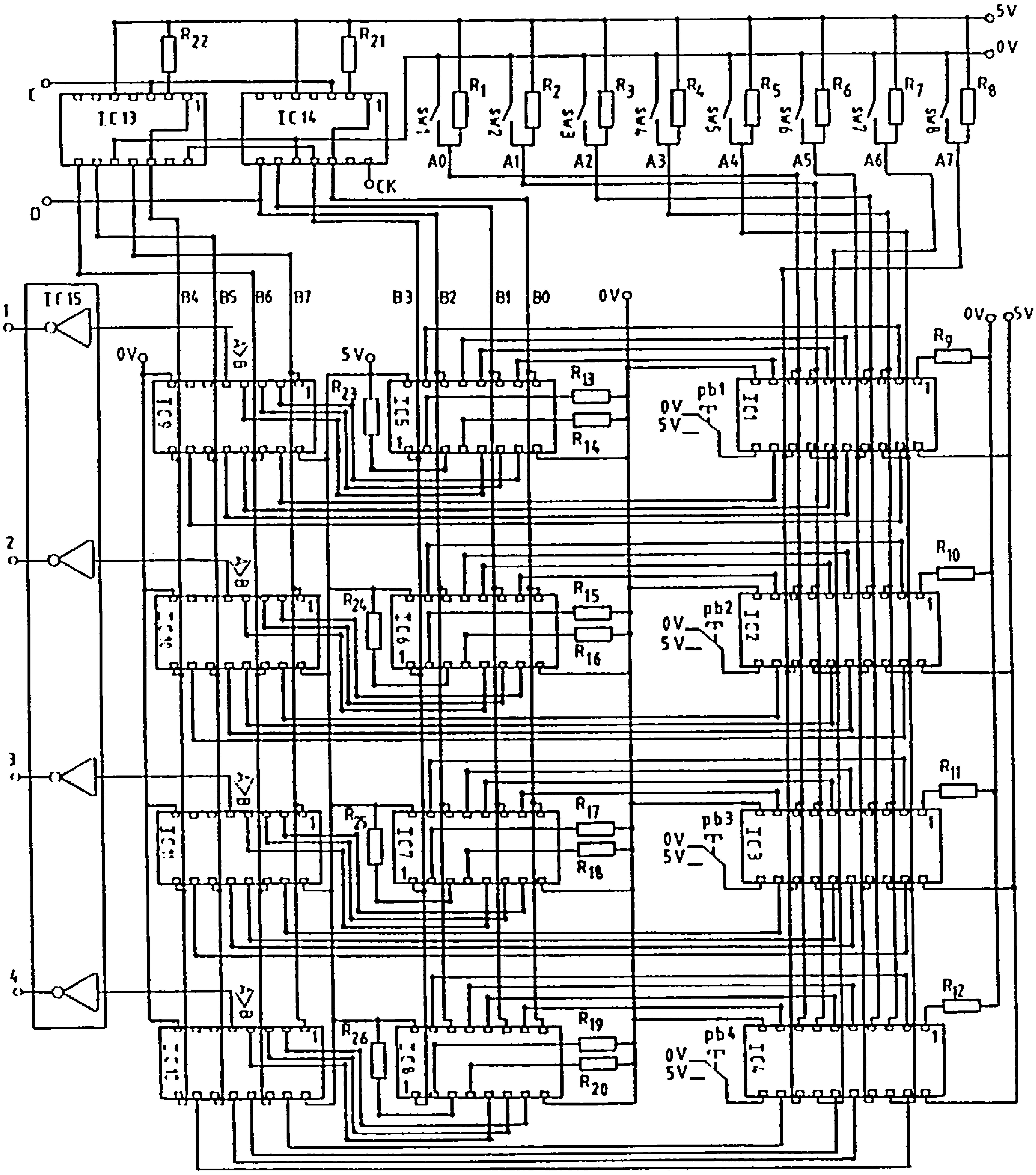

Figure3.9 Circuit diagram of digital control system.
(List of components given in Appendix A10)

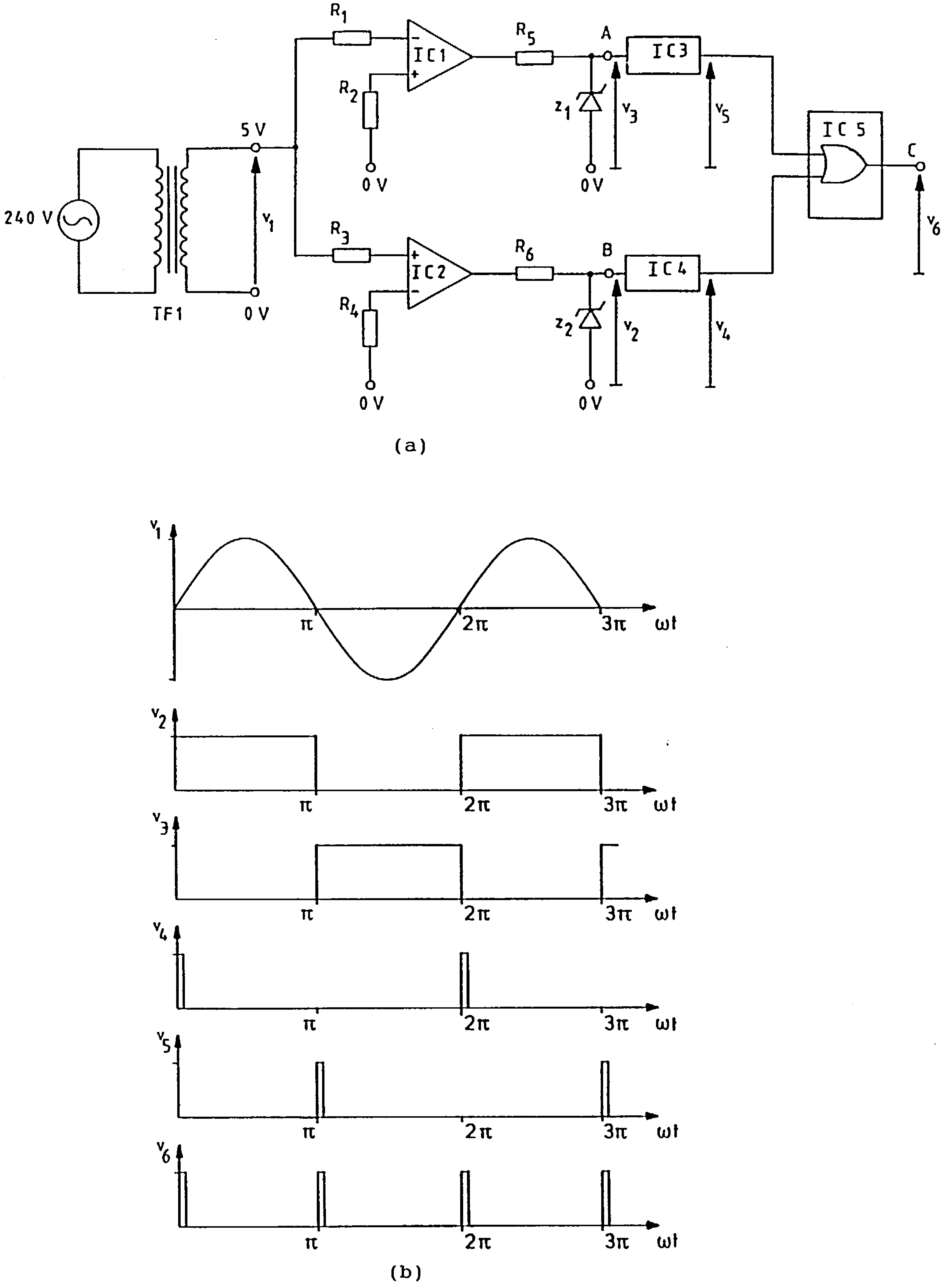

Figure3.10 Synchronization circuit diagram.
(a) Connection.
(b) Waveforms.
(List of components given in Appendix A10)

Figure3.11 Steering and pulse-train signal generator.
(a) Connection.
(b) Waveforms.

CHAPTER 4

Fully-controlled PWM Bridge Converter

This chapter presents the design principles for the fully-controlled PWM bridge converter described in Chapter 2. The circuit given in figure 4.1 shows that each GTO has a series diode for protection against reverse voltage and over-current protection is provided by the high-speed fuse FS1, the selection procedure of which is the same as that outlined in Appendix A4. The GTO thyristor and its series diode are mounted on the same heat sink and the design calculation to determine a suitable heat sink is given in Appendix A7. Each GTO has a parallel snubber circuit to limit the rate-of-rise of the off-state voltage. The design of the snubber is explained in Appendix A8.

The ratings of the power devices are discussed in section 4.1, and section 4.2 describes the isolated gate-drive circuit. The power supplies for the main control circuit and GTO gate-drive circuits are described in sections 4.3 and 4.4 respectively. Finally, generation of the firing pulses to turn-on and turn-off the GTOs in a PWM manner is discussed in section 4.5.

4.1 Device Rating

The selection of the semiconductor devices depends on both the magnitude of the supply voltage and the maximum anticipated load current. With a 240V supply and a 5A load current, the devices must be rated appropriately with a reasonable overload capability. The Mullard GTO (BTV 58-1000 R) and fast-recovery diode (BY 329-1000) were selected.

4.2 Gate Drive Requirements[24-26]

The gate turn-on mechanism of the GTO is similar to that of a conventional thyristor, in that a steep-fronted pulse of gate current is required to turn-on the device. However, since the regenerative loop gain of the GTO is smaller than that of a conventional thyristor, a relatively higher level of gate current is required for triggering the device and this must be maintained until the anode current exceeds the latching current level. Subsequently, for the remainder of the conduction period, the current is reduced to decrease the on-state voltage and hence the on-state losses. The GTO is turned off by extracting a current of between $\frac{1}{5}$ and $\frac{1}{3}$ of the anode current from the gate before expiry of the storage time, which can be as short as 500ns. The inductance of the gate circuit must clearly be kept as low as possible, since this determines the rate at which the reverse gate-current builds up.

4.2.1 Isolated Gate-drive Circuit

The gate-drive requirements mentioned in the previous section are satisfied by use of the isolated gate-drive circuit of figure 4.2 [26]. The control signal is isolated by the pulse transformer TF1 which is energized by switching on the transistor TR1. The secondary voltage is a differentiated version of the control signal and takes the form of a series of positive and negative voltage spikes. Resistors R_5 and R_4 form a voltage divider, biasing INV_a at -6V when no signal is applied to the transformer primary. Each positive spike of the differentiated voltage sets the output of INV_a at logic 0, which in turn sets the output of INV_b at logic 1 and latches the input of INV_a at logic 1. The output of INV_a is held at logic 0 and the output of the buffer stage INV_c to INV_f at logic 1, until a negative spike from the differentiated waveform resets the output of INV_a to logic 1, the output of INV_b to logic 0 and the buffer output to logic 0. The output of the buffer stage drives the Darlington transistor TR2. When TR2 is off, TR3 conducts and the GTO is turned on by a positive pulse of gate current with a magnitude determined by the network R_9, C_5 and R_{10}. When C_5 is fully charged, a reduced steady-state gate current flows through R_9 for the remainder of the on-period. The GTO is turned off when TR2 is turned on, and current is extracted via diode D_2 into the reservoir capacitor C_4 connected to the -12V supply. To ensure that the gate current is withdrawn rapidly, the inductance of the loop formed by the GTO gate-cathode junction, D_2, TR2 and C_4 must be kept as low as possible and certainly to less than 1μH.

4.3 Power Supply of the Main Control Circuit

The power supply for the main control circuit is shown in figure 4.3. The 240V supply is stepped-down by transformer TF1, which has a centre-tapped double 15V secondary winding. The output voltage is rectified and smoothed, to provide a ±21V unregulated supply. Voltage regulators VR1 and VR2 are connected respectively to the positive and negative rails, to provide ±12V regulated power supplies.

4.4 Multiple-output Gate-drive Power Supply

Since the cathodes of the GTOs of figure 4.1 are at different potentials, isolation of the gate-drive supply is required. This presents no problem for the upper two devices, which have common cathode connections and can share a single isolated power supply. The lower two devices however have independent cathodes, with each gate drive requiring an isolated supply.

The gate-drive power supply requirements are best achieved using the multiple-output switched-mode power supply shown in figure 4.4 [26]. The oscillator, IC1, switches transistor TR1 on and off at about 60kHz, and the 1:3 turns ratio of transformer TF1 provides a 126V peak-to-peak secondary voltage. Transformers TF2, TF3 and TF4 step this down to about 42V peak-to-peak, with TF2 and TF3 providing the power supplies for the two GTOs in the lower section of the bridge and TF4 the single supply for the two GTOs in the upper section.

When transistor TR1 conducts, diodes D_5 to D_8 also conduct, charging the capacitors connected to the positive supply of the gate drive circuit. Conversely, when TR1 is off diodes D_9 to D_{12} conduct and the stored energy in the transformer cores TF1 to TF4 charges the capacitors connected to the negative supply of the drive circuits. Zener diodes D_{13}, D_{14} and D_{15} limit the negative voltage rail to -12V, in accordance with the maximum allowable reverse voltage which can be applied to the GTO's gate-cathode junction.

4.5 The Main Control Circuit

The control circuit provides PWM signals at frequencies of 2 and 4kHz, using the phase-locked loop (PLL) frequency synthesizer of section 4.5.1. Generation of the triangular carrier waveform is described in Section 4.5.2 and that of the PWM signals in Section 4.5.3. The steering of control signals to appropriate thyristors of figure 4.1 is described in section 4.5.4 for both rectification and inversion operation of the PWM converter.

4.5.1 Phase-locked Loop Frequency Synthesizer

A frequency synthesizer is a frequency source whose output frequency is an integer multiple N of the input frequency as given by equation 4.1 [29]. Thus

$$f_o = Nf_i \qquad (4.1)$$

where f_i and f_o are the input and output frequencies respectively. Figure 4.5(a) shows a typical PLL frequency synthesizer with its associated waveforms shown in figure 4.5(b). The input voltage v_3 to IC2 is obtained by first stepping down the mains voltage, using transformer TF1. This voltage v_1 is then applied to the zero cross-over detector IC1, with the resultant square-wave v_2 chopped to 5.6V by the resistor R_3 and zener-diode D_1 combination to provide an appropriate signal v_3 to IC2. Further use of this waveform is made in the pulse-steering process explained in section

4.5.4.

The frequency of the carrier waveform v_4 is selected according to the value of N of equation 4.1, which is either 40 or 80 and is obtained by cascading counters IC3, IC4 and IC5 to give respectively output frequencies of either 2 or 4kHz. These frequencies are obtained by linking pin 3 of IC2 to terminals b or c respectively. The synthesizer output v_4 is buffered by IC6 and compared in IC7 with a 3.9V reference provided by the zener-diode voltage regulator, formed by resistor R_9 and diode D_2. The design of the PLL frequency synthesizer is outlined in Appendix A9.

4.5.2 Generation of The Triangular Carrier Waveform

The square-wave v_5 obtained in the previous section is applied to the integrator [30] of figure 4.6(a), which converts it to the triangular waveform v_2 whose amplitude depends on the carrier frequency. To fix the amplitude of this waveform and to provide a variable dc bias, the summing inverter of figure 4.6(a) is used. The amplitude of v_2 is fixed by trimming resistor R_3, and R_4 provides a variable dc bias. The resultant triangular carrier waveform v_3 is shown in figure 4.6(b).

4.5.3 Formation of The PWM Waveform

The secondary voltage v_1 of figure 4.5(a) is applied to the precision full-wave rectifier [31] of figure 4.7(a) to give a full-wave rectified modulating waveform whose amplitude is preset by using the trimming resistor R_9 of the non-inverting amplifier. The modulating waveform v_1, together with the triangular carrier waveform v_3 of figure 4.6(a), is applied to the comparator of figure 4.7(a) to obtain the PWM waveform v_2 [13]. The modulation index of the PWM waveform is changed by varying the amplitude of the modulating waveform [13] between zero and the preset value by means of the variable resistor R_7.

4.5.4 Pulse-steering Process

The PWM waveform v_2 of figure 4.7(a) together with the square-wave v_3 of figure 4.5(a) are applied respectively to ICs 1 and 2 of the pulse-steering circuit shown in figure 4.8(a). Voltage waveforms v_1 to v_7 obtained at different stages of this circuit are shown in figure 4.8(b). The control signals v_7, v_2, v_5 and v_3 are applied to the gates of GTOs T_1 to T_4 of figure 4.1 via the isolated gate-drive circuit of figure 4.2. The gate signals obtained from this circuit are shown in figure 4.8(c). The control signals derived from the pulse-steering circuit of figure 4.8(a) is used when the PWM converter operates in the rectification mode. However during inversion operation of the converter, the control signals are obtained by disconnecting point b of figure 4.8(a) and connecting it to point a. The resultant circuit diagram and its associated voltage waveforms is shown respectively in figures 4.9(a) and (b). The gate signals applied to GTOs T_1 to T_4 is shown in figure 4.9(c).

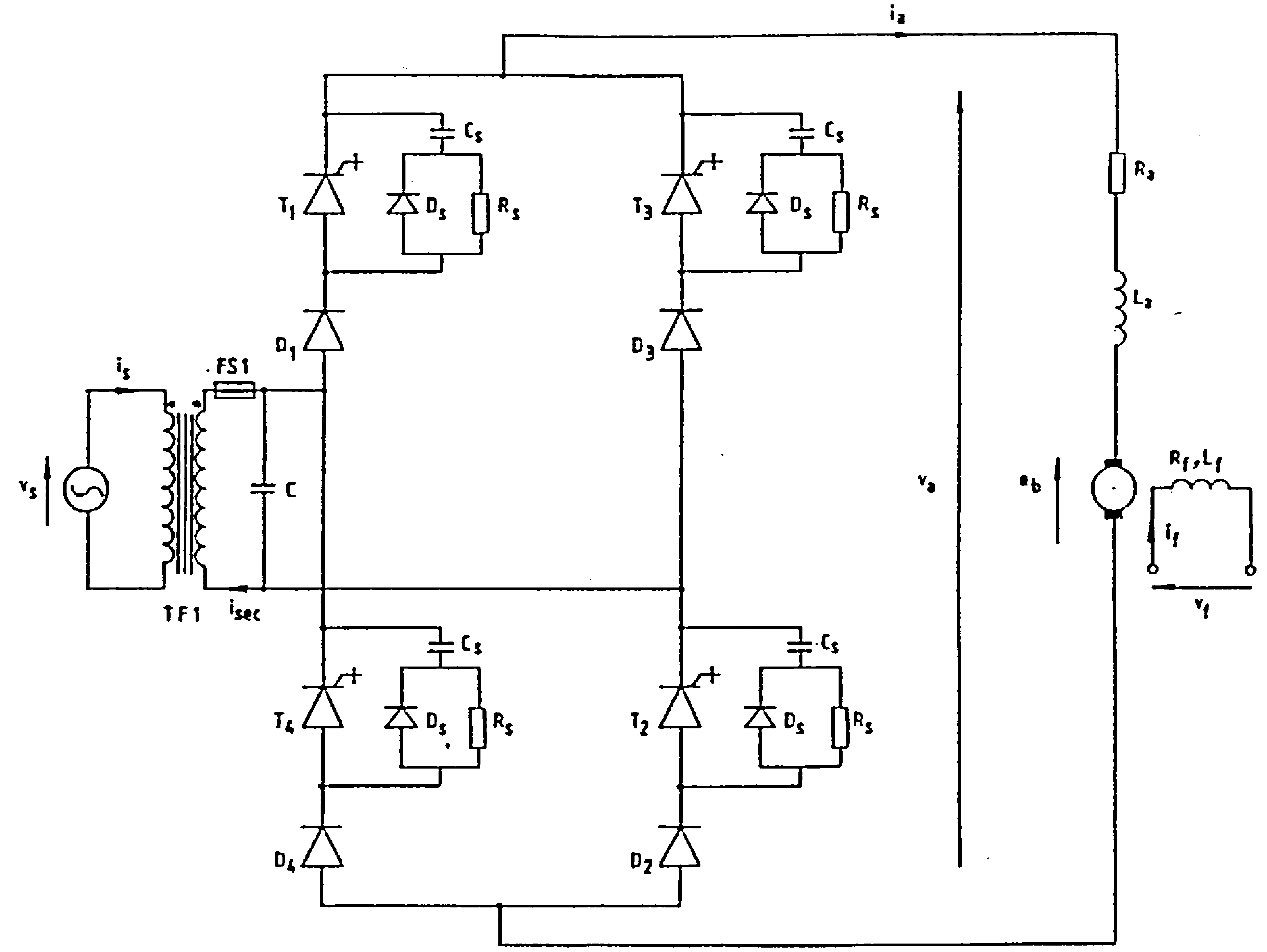

Figure4.1 Fully-controlled PWM bridge converter.

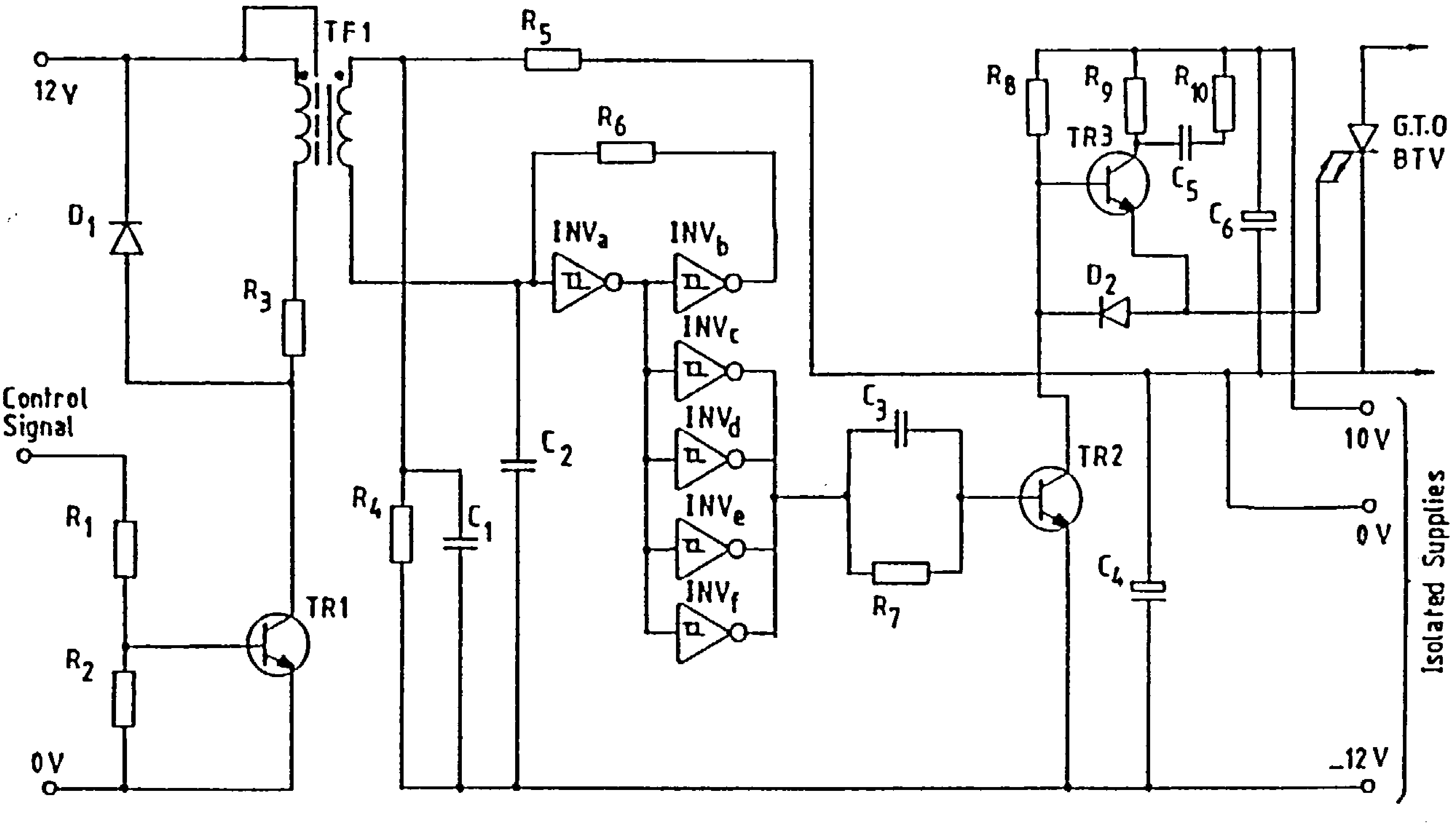

Figure4.2 Isolated gate-drive circuit.
(List of components given in Appendix A10)

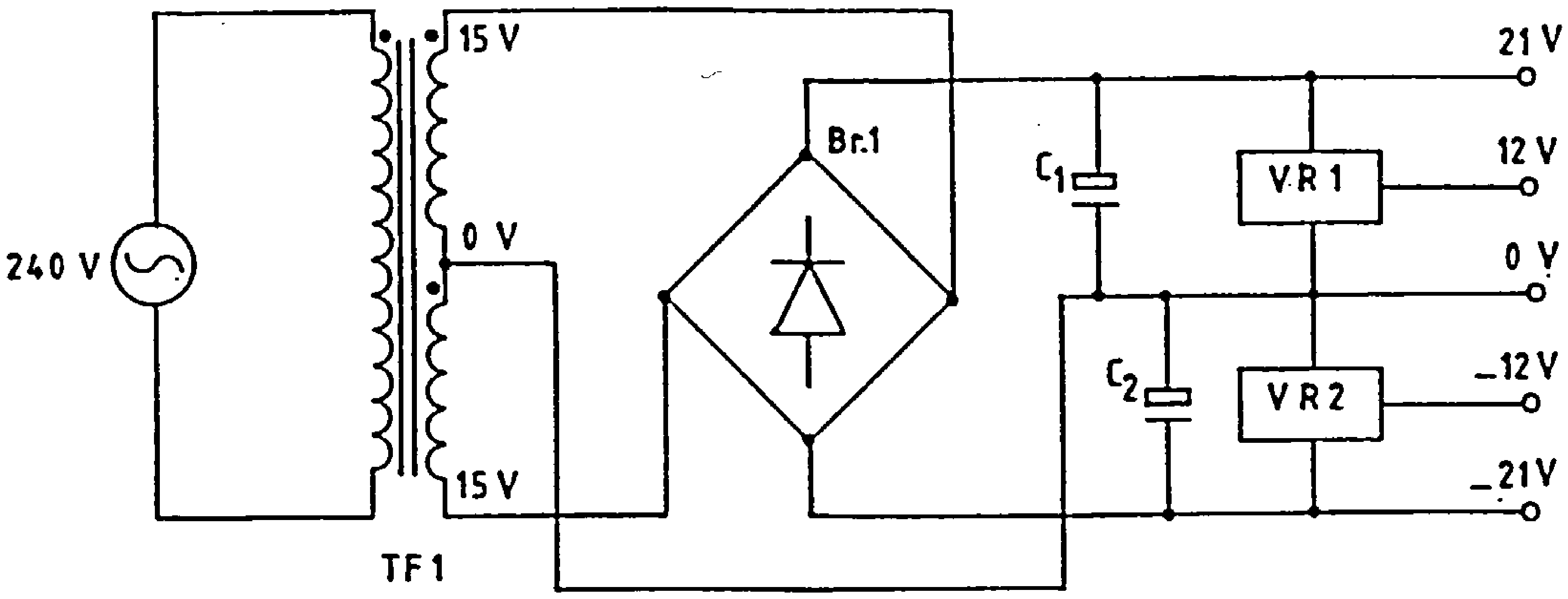

Figure4.3 Power supply for the main control circuit.

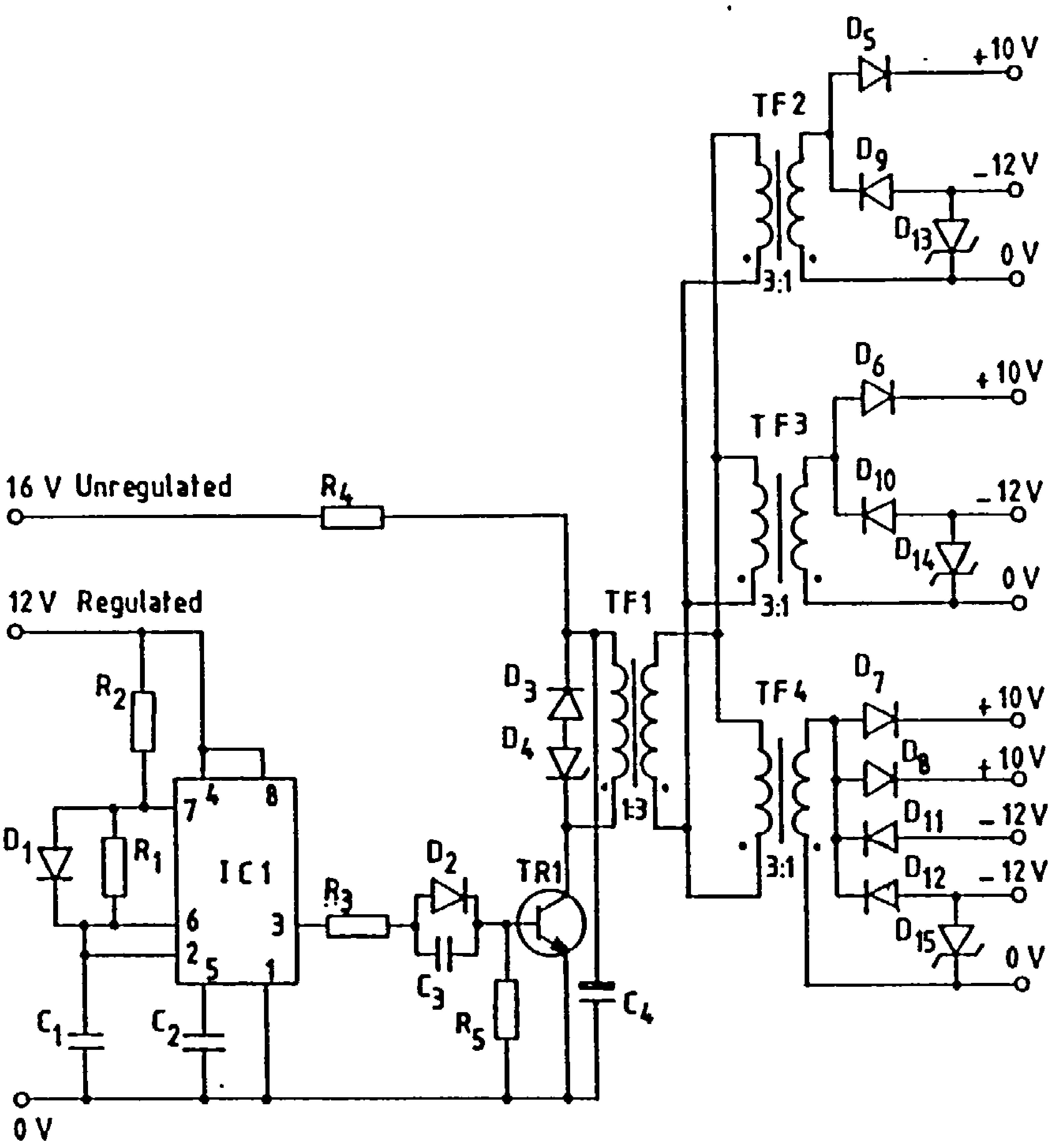

Figure4.4 Multiple-output switched-mode power supply.
(List of components given in Appendix A10)

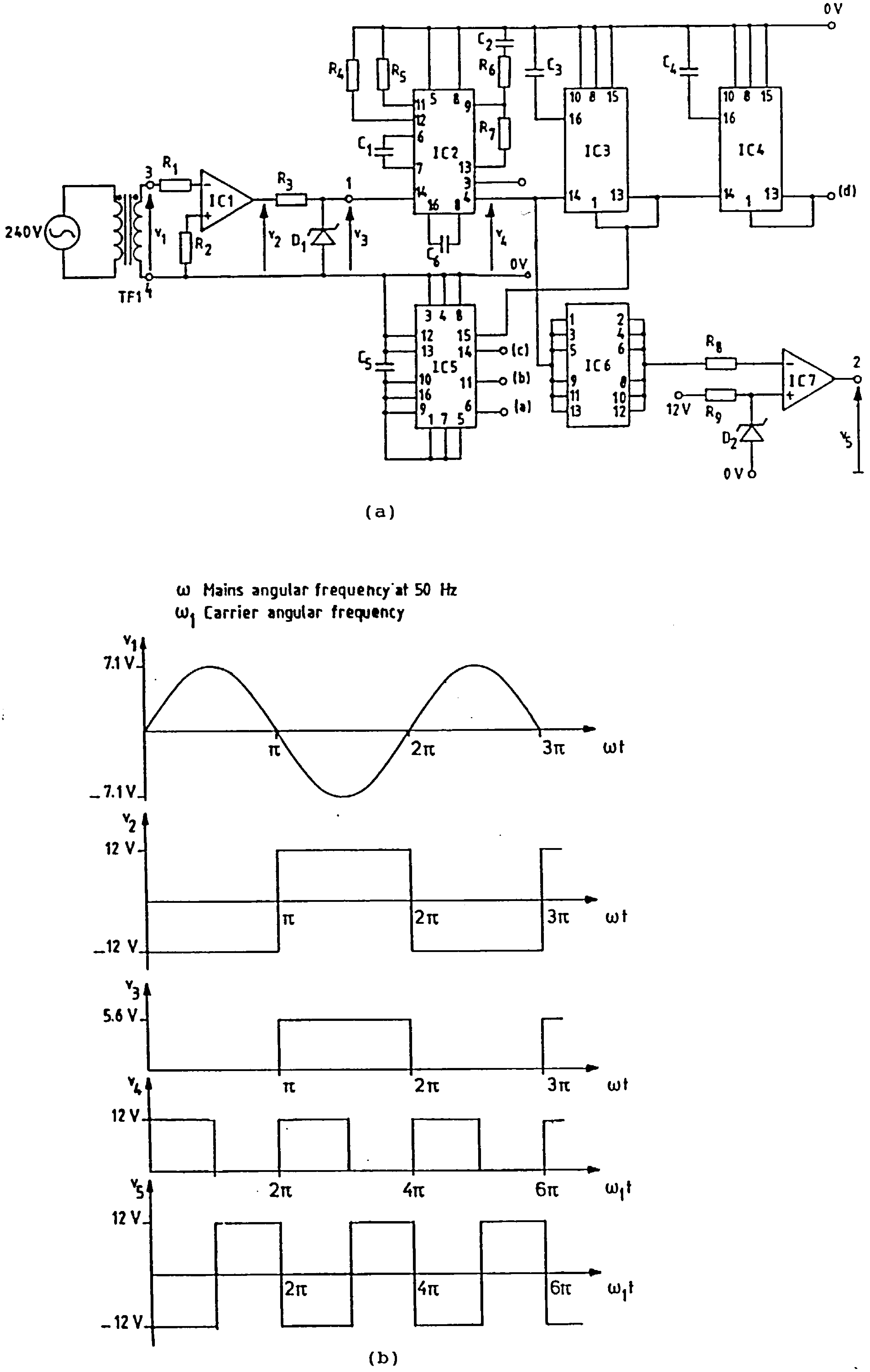

Figure4.5 Phase-locked loop frequency synthesizer.
(a) Connection.
(b) Waveforms.
(List of components given in Appendix A10)

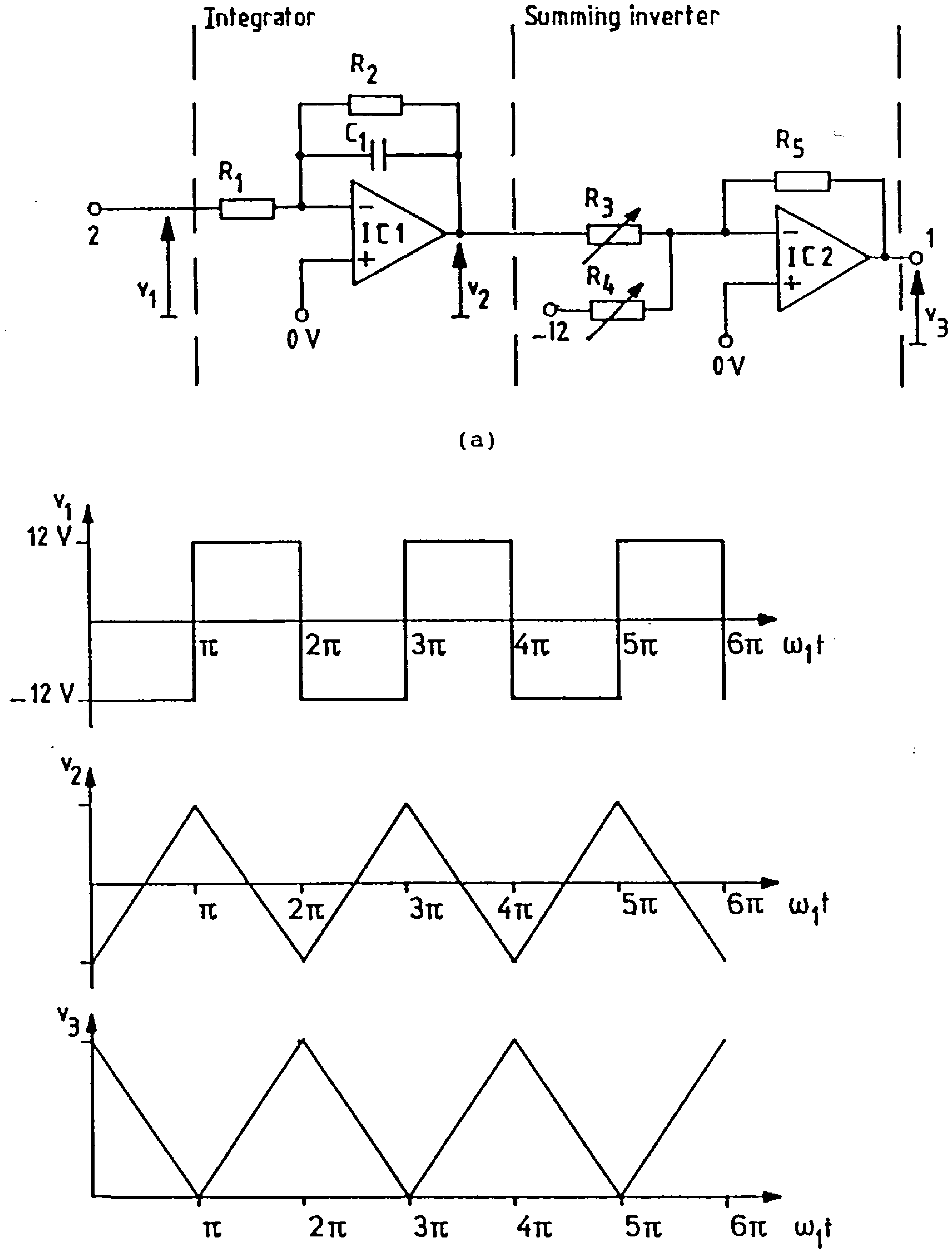

(a)

(b)

Figure4.6 Generation of triangular carrier waveform.
(a) Connection.
(b) Waveforms.
(List of components given in Appendix A10)

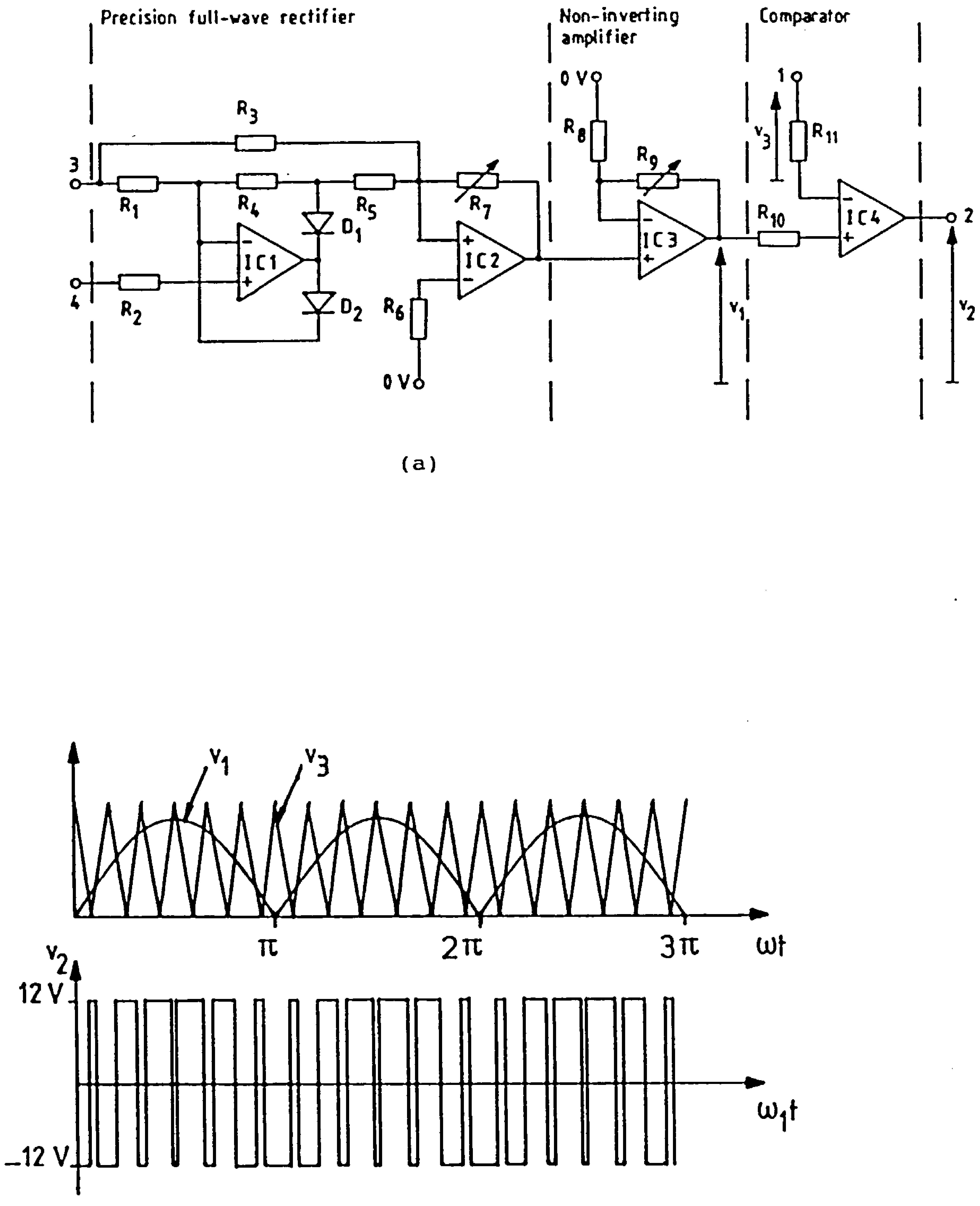

(a)

(b)

Figure4.7 Formation of PWM waveform.
(a) Connection.
(b) Waveforms.
(List of components given in Appendix A10)

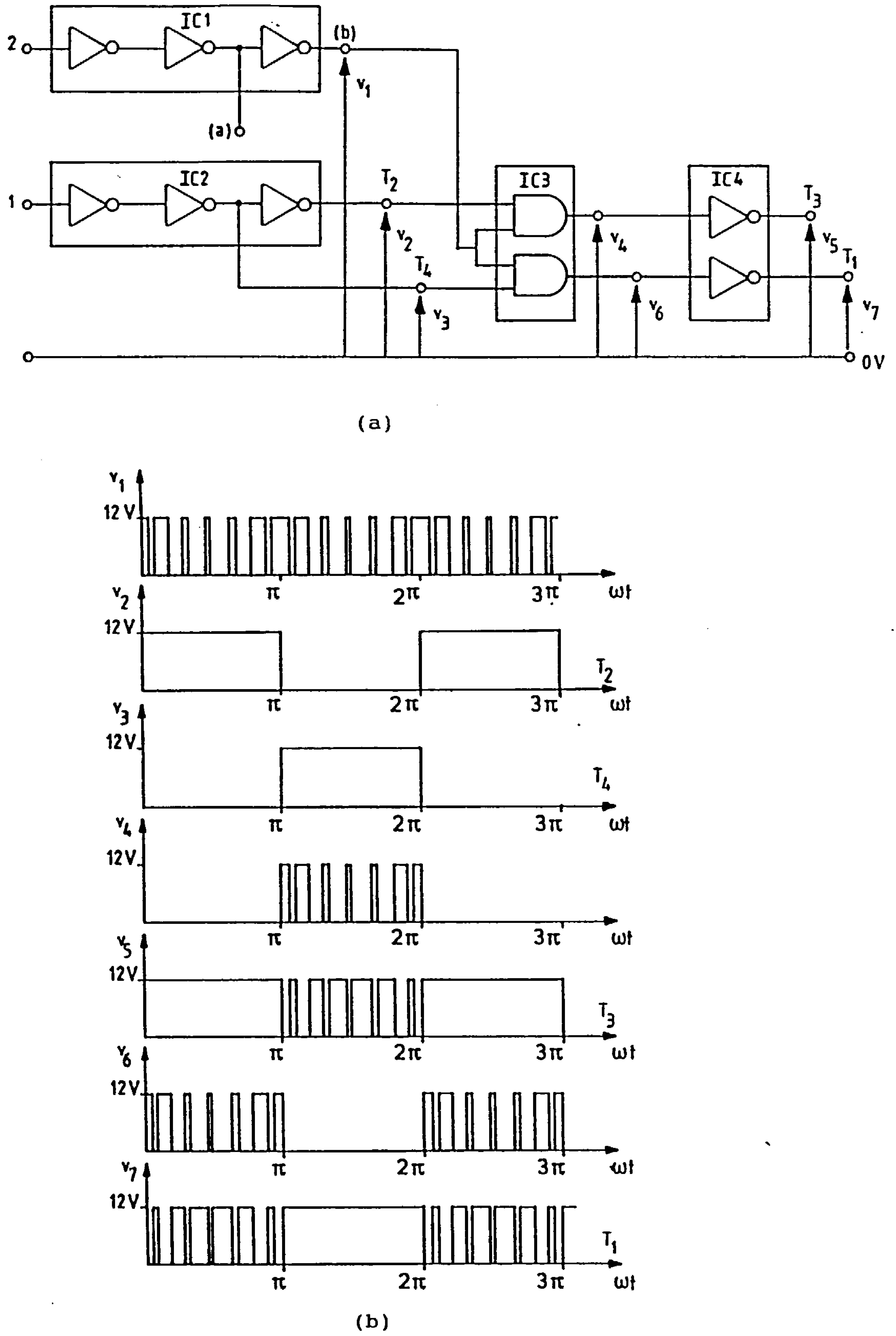

Figure4.8 Circuit diagram of pulse-steering process during rectification.
(a) Connection.
(b) Waveforms.
(list of components given in Appendix A10)

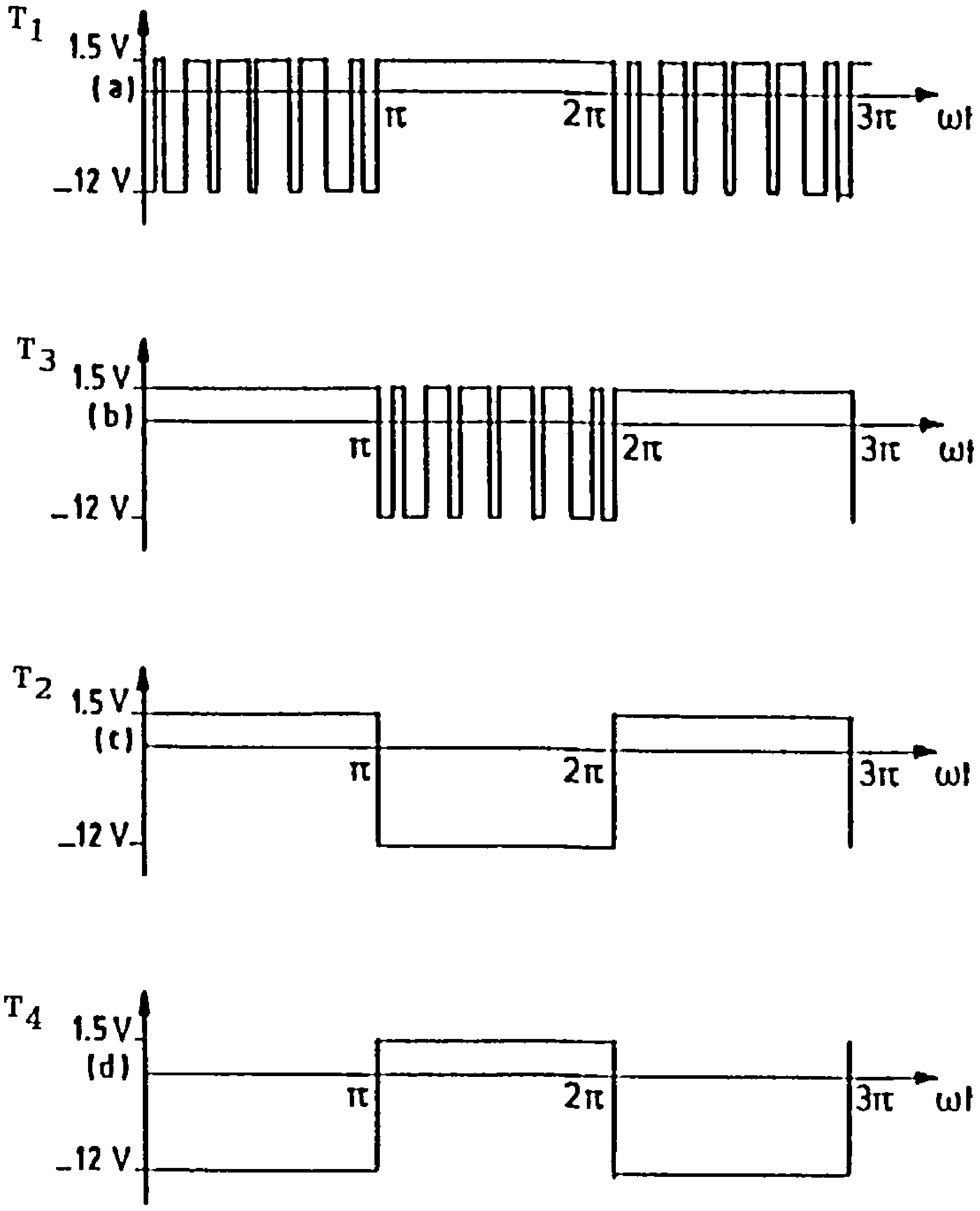

(c)

Figure4.8 Continued.
(c) Gate signals to GTO thyristors T_1 to T_4.

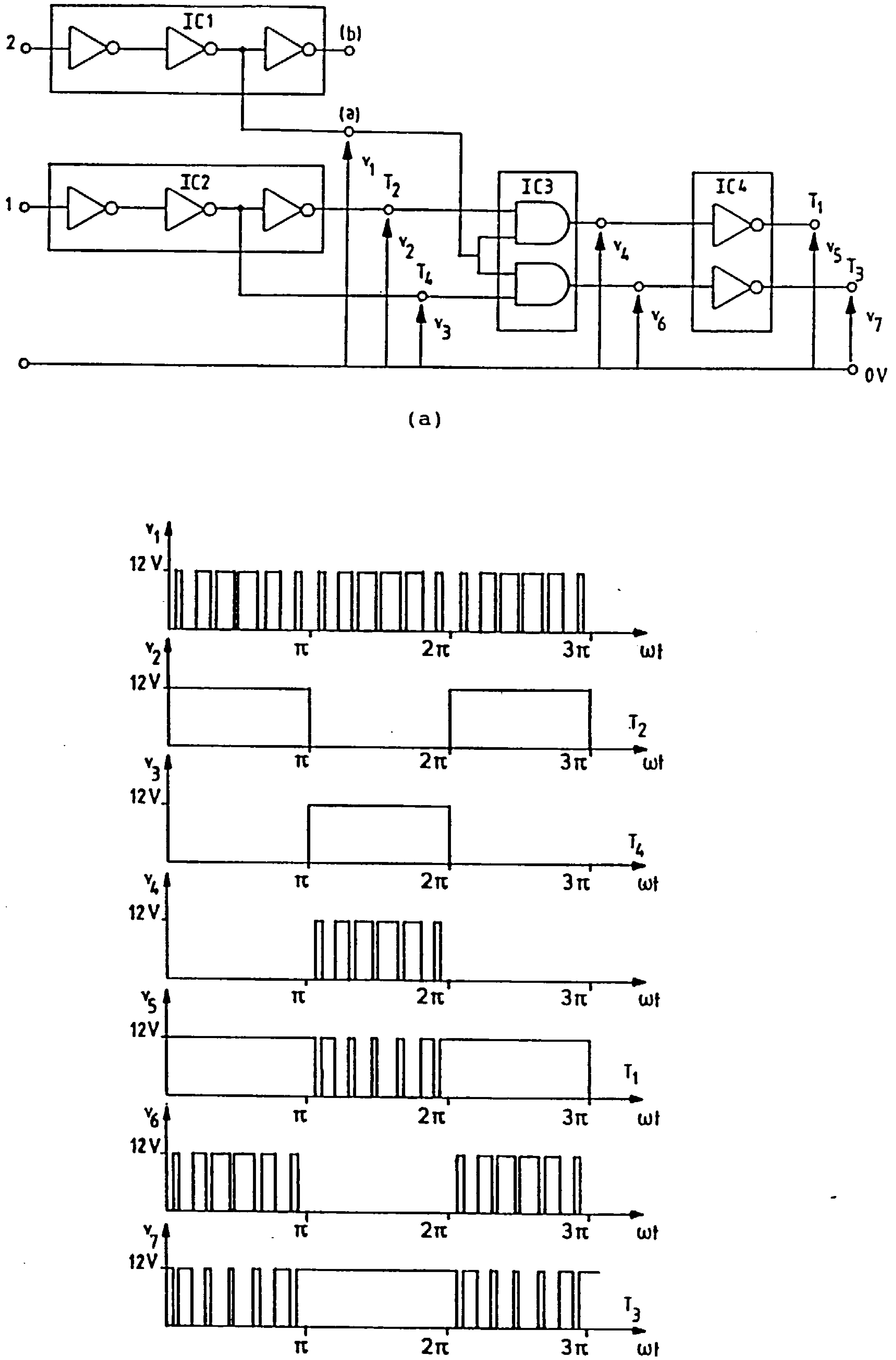

(a)

(b)

Figure4.9 Circuit diagram of pulse-steering process during inversion.
(a) Connection.
(b) Waveforms.
(List of components given in Appendix A10)

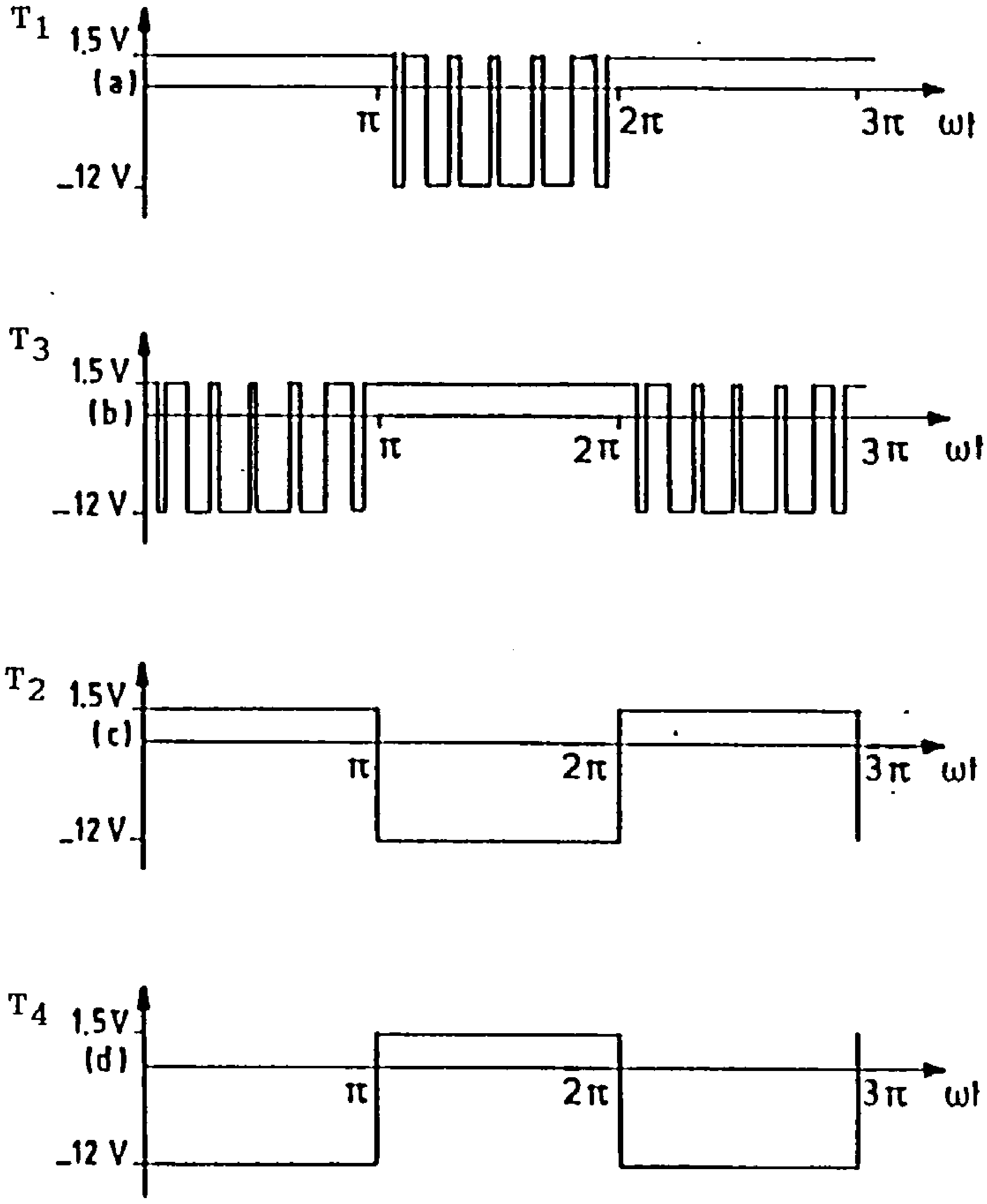

(c)

Figure4.9 Continued.
(c) Gate signals to GTO thyristors T_1 to T_4.

CHAPTER 5

Mathematical Models For Bridge Converters

Mathematical models for sequence controlled single- and double-bridge coverters are developed in sections 5.1 and 5.2 using tensor techniques [32-35]. This approach defines the circuit mesh currents as the system state variables, and generates automatically the relevant mesh differential equations as the thyristor conduction pattern changes. The equations are solved using a numerical integration method to obtain an update of the mesh currents, and the individual branch currents and voltages are then calculated from the mesh values. Assembly of the mesh differential equations requires the use of both branch and mesh reference frames, and the subsequent development of transformation matrices by which these two frames are related. The mathematical model for the PWM controlled single-bridge developed in section 5.3 uses a model-subroutine technique, which has individual subroutines holding the differential equations for each of the possible thyristor switching patterns [36,37]. Saturation and hysteresis effects in the transformer core are neglected and the thyristors are considered as ideal switches, with zero impedance and voltage drop when conducting and an infinite impedance when non-conducting. The circuit parameters used in the computer program are given in Appendix A11, together with the parameters of the power transformer that were obtained from no-load and short-circuit tests performed on the transformer used in the experimental model. Analytical models for different controllers are described in section 5.4 and computed results together with analytical ones for both single- and double-bridge converters are presented in section 5.5 with a comparison between different controllers being given in section 5.6.

5.1 Sequence Controlled Single-bridge

The branch reference frame for the converter of figure 5.1(a) may be represented by the disconnected system of figure 5.1(b). The branch-voltage matrix equation for this circuit is:

$$\begin{bmatrix} e_1+V_1 \\ V_2 \\ V_3 \\ V_4 \\ V_5 \\ V_6 \\ V_7 \\ V_8 \end{bmatrix} = \begin{bmatrix} R_1+L_1p & 0 & 0 & 0 & 0 & 0 & 0 & 0 \\ 0 & R_2+L_2p & L_{23}p & 0 & 0 & 0 & 0 & 0 \\ 0 & L_{32}p & R_3+L_3p & 0 & 0 & 0 & 0 & 0 \\ 0 & 0 & 0 & L_4p & 0 & 0 & 0 & 0 \\ 0 & 0 & 0 & 0 & L_5p & 0 & 0 & 0 \\ 0 & 0 & 0 & 0 & 0 & L_6p & 0 & 0 \\ 0 & 0 & 0 & 0 & 0 & 0 & L_7p & 0 \\ 0 & 0 & 0 & 0 & 0 & 0 & 0 & R_8+L_8p \end{bmatrix} \begin{bmatrix} i_1 \\ i_2 \\ i_3 \\ i_4 \\ i_5 \\ i_6 \\ i_7 \\ i_8 \end{bmatrix} \qquad (5.1)$$

Using Happ's tensor notation [38], equation 5.1 may be written in the abbreviated form

$$E_b + V_b = R_{bb}I^b + L_{bb}pI^b \qquad (5.2)$$

where V_b and I^b are respectively the branch voltage and current vectors and E_b is the vector of source voltages within the branches. R_{bb} and L_{bb} are respectively matrices formed by the resistance and inductance terms, and the operator $p = \frac{d}{dt}$.

The mesh reference frame is concerned with the mesh equations formed when conducting thyristors connect the transformer secondary to the load. The typical thyristor conduction pattern shown in figure 5.2 represents an overlap period, where thyristors T_1, T_2 and T_3 are conducting and commutation is taking place between T_1 and T_3, with T_3 turning on and T_1 turning off. The mesh voltage equation which defines this situation is

$$E_m + V_m = R_{mm}I^m + L_{mm}pI^m \qquad (5.3)$$

and the transformation tensor $C^b_{\cdot m}$ relating the branch to the mesh reference frame follows by inspection of figure 5.2 as

$$C^{b}_{\cdot m} = \begin{array}{c|ccc} \text{Branch} \diagdown \text{Mesh} & 1 & 2 & 3 \\ \hline 1 & 1 & 0 & 0 \\ 2 & 1 & 0 & 0 \\ 3 & 0 & -1 & 0 \\ 4 & 0 & 1 & 0 \\ 5 & 0 & 1 & 1 \\ 6 & 0 & 0 & 1 \\ 7 & 0 & 0 & 0 \\ 8 & 0 & 1 & 1 \end{array}$$

where 1 and -1 denote respectively whether the corresponding mesh and branch currents are in the same or the opposite senses and 0 that a mesh current is not flowing in the branch. Assuming power invariance between the two reference frames, [38], the following relationships apply:

$$I^{b} = C^{b}_{\cdot m} I^{m} \tag{5.4}$$

$$E_{m} = C_{\dot{m}}^{b} E_{b} \tag{5.5}$$

$$V_{m} = 0 \text{ (null vector: Kirchhoff's voltage law)} \tag{5.6}$$

$$R_{mm} = C_{\dot{m}}^{b} R_{bb} C^{b}_{\cdot m} \tag{5.7}$$

$$L_{mm} = C_{\dot{m}}^{b} L_{bb} C^{b}_{\cdot m} \tag{5.8}$$

where $C_{\dot{m}}^{b}$ is the transpose of $C^{b}_{\cdot m}$, R_{mm} and L_{mm} are the mesh resistance and inductance matrices, I^{m} and E_{m} are the mesh current and impressed voltage vectors.

Implementation of the model requires the automatic generation of the appropriate $C^{b}_{\cdot m}$ tensor as the thyristor conduction pattern varies. A technique by which this may be achieved is now described.

5.1.1 Assembly of $C^{b}_{\cdot m}$ [34]

The columns of $C^{b}_{\cdot m}$ are obtained from the master matrix given in figure 5.3(a), which defines the five meshes shown in figure 5.3(b). These meshes are sufficient for the study of all practical conditions experienced by the bridge network. Each column of the master matrix is loaded into $C^{b}_{\cdot m}$ when its respective thyristor-pair becomes both forward biased and triggered. It is retained in C^b_m until the corresponding mesh current attempts to become negative.

5.1.2 Thyristor Discontinuities

A thyristor commences conduction when the anode-cathode voltage v_t is positive and a positive pulse is applied to the gate. It ceases conduction when the anode current i_A is reduced below the holding level (approximately zero) These changes in conduction pattern are termed respectively turn-on and turn-off discontinuities. There are two types of turn-on discontinuity within an integration interval h, the first being where gate pulses are present and v_t changes from negative to positive and the second where v_t is already positive and a gate pulse is applied. These two conditions are illustrated respectively in figures 5.4(a) and (b). The times to the discontinuities t_{dv} and t_{fv} using linear interpolation [39,40] are

$$t_{dv} = - \frac{v_{t0}h}{v_{t1} - v_{t0}} \qquad (5.9)$$

$$t_{df} = \frac{(v_f - v_{t0})h}{v_{t1} - v_{t0}} \qquad (5.10)$$

where v_{t0} and v_{t1} are respectively the voltages at the start and end of the integration interval and v_{tf} that at the instant of firing. The turn-off discontinuity is shown in figure 5.5 and the time to the discontinuity t_{di} is

$$t_{di} = \frac{i_{A0}h}{i_{A0} - i_{A1}} \qquad (5.11)$$

where i_{A0} and i_{A1} are respectively the anode current at the start and end of the integration interval.

5.1.3 Computer Implementation

A computer program was written in Fortran 77 [41] to implement the model defined by the equations developed in this section. The mesh differential equation 5.3 is re-arranged as

$$pI^{m} = L_{mm}^{-1} [E_{m} + V_{m} - R_{mm}I^{m}] \qquad (5.12)$$

which is suitable for numerical integration.
Substituting equations 5.5 to 5.8 into 5.12 gives

$$pI^{m} = [C_{\dot{m}}^{\;b}L_{bb}C^{b}_{.m}]^{-1}[C_{\dot{m}}^{\;b}E_{b} - C_{\dot{m}}^{\;b}R_{bb}C^{b}_{.m}I^{m}] \qquad (5.13)$$

which may be integrated using a single step 4th-order Runge-Kutta method [40] to obtain the mesh current vector I^{m}. The branch currents and voltages defined by the branch reference frame are then calculated using equations 5.4 and 5.1 respectively. The process is repeated in accordance with the algorithm described by the flow chart of figure 5.6.

5.2 Sequence Controlled Double-bridge

The branch reference frame for the double-bridge circuit of figure 5.7(a) is shown in figure 5.7(b), with the corresponding branch-voltage matrix given in equation 5.14. In the typical thyristor conduction pattern of figure 5.8 thyristors T_1, T_2, $\dot{T}_1$ and $\dot{T}_2$ are conducting, and inspection of this figure yields the transformation tensor as:

$$C^{b}_{.m} = \begin{array}{r|cc|} \text{Branch} \backslash \text{Mesh} & 1 & 2 \\ \hline 1 & 1 & 0 \\ 2 & 1 & 0 \\ 3 & 0 & -1 \\ 4 & 0 & -1 \\ 5 & 0 & 1 \\ 6 & 0 & 1 \\ 7 & 0 & 0 \\ 8 & 0 & 0 \\ 9 & 0 & 1 \\ 10 & 0 & 1 \\ 11 & 0 & 0 \\ 12 & 0 & 0 \\ 13 & 0 & 1 \end{array}$$

$$\begin{bmatrix} e_1+V_1 \\ V_2 \\ V_3 \\ V_4 \\ V_5 \\ V_6 \\ V_7 \\ V_8 \\ V_9 \\ V_{10} \\ V_{11} \\ V_{12} \\ V_{13} \end{bmatrix} = \begin{bmatrix} R_1+L_1p & 0 & 0 & 0 & 0 & 0 & 0 & 0 & 0 & 0 & 0 & 0 & 0 \\ 0 & R_2+L_2p & L_{23}p & L_{24}p & 0 & 0 & 0 & 0 & 0 & 0 & 0 & 0 & 0 \\ 0 & L_{32}p & R_3+L_3p & L_{34}p & 0 & 0 & 0 & 0 & 0 & 0 & 0 & 0 & 0 \\ 0 & L_{42}p & L_{43}p & L_4p & 0 & 0 & 0 & 0 & 0 & 0 & 0 & 0 & 0 \\ 0 & 0 & 0 & 0 & L_5p & 0 & 0 & 0 & 0 & 0 & 0 & 0 & 0 \\ 0 & 0 & 0 & 0 & 0 & L_6p & 0 & 0 & 0 & 0 & 0 & 0 & 0 \\ 0 & 0 & 0 & 0 & 0 & 0 & L_7p & 0 & 0 & 0 & 0 & 0 & 0 \\ 0 & 0 & 0 & 0 & 0 & 0 & 0 & L_8p & 0 & 0 & 0 & 0 & 0 \\ 0 & 0 & 0 & 0 & 0 & 0 & 0 & 0 & L_9p & 0 & 0 & 0 & 0 \\ 0 & 0 & 0 & 0 & 0 & 0 & 0 & 0 & 0 & L_{10}p & 0 & 0 & 0 \\ 0 & 0 & 0 & 0 & 0 & 0 & 0 & 0 & 0 & 0 & L_{11}p & 0 & 0 \\ 0 & 0 & 0 & 0 & 0 & 0 & 0 & 0 & 0 & 0 & 0 & L_{12}P & 0 \\ 0 & 0 & 0 & 0 & 0 & 0 & 0 & 0 & 0 & 0 & 0 & 0 & R_{13}+L_{13}p \end{bmatrix} \begin{bmatrix} i_1 \\ i_2 \\ i_3 \\ i_4 \\ i_5 \\ i_6 \\ i_7 \\ i_8 \\ i_9 \\ i_{10} \\ i_{11} \\ i_{12} \\ i_{13} \end{bmatrix} \quad (5.14)$$

The technique by which this matrix is assembled automatically, in the event of a discontinuity, was explained in section 5.1.1 and requires the master matrix of figure 5.9(a) which defines the 11 meshes of figure 5.9 (b) to (d). The computer implementation is the same as that explained in section 5.1.3, except that the branch voltages are obtained by using equation 5.14.

5.3 Fully-controlled PWM Bridge Converter

An existing computer model for the PWM controlled single-bridge rectifier of figure 5.10(a) was used for theoretical simulations [42]. A model subroutine technique was used, in which individual subroutines are assigned to hold the differential equations for different modes of operation. The three modes of operation which define the normal conduction pattern of the GTOs are explained below:

In mode 1, the supply is connected to the load via T_1, T_2 when the supply voltage is positive and via T_3, T_4 when it is negative. With reference to figure 5.10(b), the corresponding differential equation is

$$pi_l = (L_s + L_l)^{-1}[E_s - (R_s + R_l)i_l] \qquad (5.15)$$

where E_s is the supply voltage and I_l the load current.

Mode 2 is concerned with the free-wheeling period where either T_3, T_2 or T_1, T_4 are conducting. This condition is shown in figure 5.10(c) with its differential equation being

$$pi_l = -[L_l]^{-1}R_li_l \qquad (5.16)$$

Mode 3 considers the commutation of load current from an outgoing to an incoming thyristor and is illustrated by figure 5.10(d), from which it follows that

$$pi_l = -L_s^{-1} (E_s - R_si_l) \qquad (5.17)$$

and $pi_2 = -L_1^{-1}(R_1 i_2)$ (5.18)

The gate signals to turn-on and turn-off the GTOs in a PWM manner are generated by comparing a full-wave rectified modulating waveform with a triangular carrier waveform, as shown in figure 5.11. The mean output voltage is controlled by varying the modulation index M, which in turn varies the width of the individual output pulses. The algorithm for the program, which was written in Fortan 77, is defined by the flow chart shown in figure 5.12.

5.4 Analytical Models

Analytical models were developed for sequence-controlled single and double-bridge converters and for a conventional-controlled single-bridge converter. The advantage of the analytical model over the digital one is that it allows the designer to assess which circuit parameters influence the converter characteristics, such as the input power factor, peak-to-peak load current ripple, harmonic content of the supply current and load voltage waveforms. The models were developed by performing a Fourier analysis on the supply current and load voltage waveforms, as described in Appendix A2. Mathematical expressions were then derived for the Fourier coefficients, and from these the r.m.s. value of the n-th harmonic and the corresponding phase displacement angle were calculated. One of the assumptions made in deriving these equations was that the load current is completely smooth i.e. there is an infinite load inductance on the dc side. This assumption suggests that the induced voltage generated by the load inductance, which in fact is equal to the voltage difference between the instantaneous and mean load voltage, is zero. However, with ac-to-dc converters this voltage difference always has to be generated across the load inductance which is also responsible for producing the load current ripple, and consequently the assumption of a smooth load current is not strictly justifiable with converter circuits. Although the load current ripple has no effect on the harmonic content of the load voltage waveform, it does however modify the amplitude of the harmonics in the supply current and their relative phase displacement angle and consequently the input power factor. It is therefore necessary to include the load current ripple in calculating the supply current harmonics. This objective is achieved by modulating the load current waveform by a square-wave switching function, which is co-phasal with the load current and has an amplitude of ±1 and a period of 2π. The resultant is the supply current waveform with the load current ripples superimposed on it. Hence, multiplying the Fourier series for the load current with that for the square-wave gives the Fourier series for the supply current and subsequently its harmonic content. This square-wave, or switching function, has a different shape for different controllers as shown in figure 5.13. Inspection of this figure indicates clearly that the shape of these switching functions are exactly the same as that of the supply current waveforms produced by the same controllers for a completely smooth load current as shown in Chapter 2. The Fourier coefficients a_n and b_n for these waveforms are given by equations A2.4 and A2.7 of Appendix A2 for an armature current I_a. However, substituting $I_a=1$ in the above equations give the Fourier coefficients for the switching function which has an amplitude of ±1. Multiplying this function and the load current waveform gives the supply current waveform as:

$$i_s = I_{s0} + \sum_{n=1}^{\infty} \sqrt{2} I_{ns} \sin(n\omega t + \phi_{ns}) \qquad n=1,3,5,\ldots \quad (5.19)$$

where i_s is the instantaneous value of the supply current,

I_{s0} is the mean value of the supply current (its value is zero, since the areas of the positive and negative half-cycles are equal)

I_{ns} is the r.m.s. value of the n-th harmonic, ϕ_{ns} is the relative displacement angle and $\omega=2\pi f$, where f is the frequency of the fundamental component.

The harmonic order $n=mp\pm1$ where m is an integer and the pulse-number $p=2$ for single-phase bridge converters.

Alternatively, equation 5.19 can be expressed in terms of the Fourier coefficients A_n and B_n as:

$$i_s = \sum_{n=1}^{\infty} [A_n \cos(n\omega t) + B_n \sin(n\omega t)] \qquad n=1,3,5,... \qquad (5.20)$$

Equating equations 5.19 and 5.20 yields the r.m.s. value of the nth-harmonic current I_{ns} as

$$I_{ns} = \sqrt{\frac{A_n^2 + B_n^2}{2}} \qquad n=1,3,5,... \qquad (5.21)$$

and its phase displacement angle ϕ_{ns} as

$$\phi_{ns} = \arctan \frac{A_n}{B_n} \qquad n=1,3,5,... \qquad (5.22)$$

Since the computed results were taken for a constant load current of 2A, the analytical results were calculated for the same conditions. The fundamental, 3rd and 5th harmonics of the supply current are the dominant components and consequently the harmonic analysis was determined only up to the 5th harmonic. Hence from equation 5.20,

$$i_s = A_1 \cos \omega t + B_1 \sin \omega t + A_3 \cos 3\omega t + B_3 \sin 3\omega t + A_5 \cos 5\omega t + B_5 \sin 5\omega t \qquad (5.23)$$

The expressions for calculating the coefficients A_1, A_3, A_5 and B_1, B_3, B_5 are developed by multiplying the Fourier series for the load current with that for the switching function. The series for the load current is:

$$i_l = I_0 + \sum_{n=1}^{\infty} [a_n \cos(n\omega t) + b_n \sin(n\omega t)] \qquad n=2,4,.. \qquad (5.24)$$

where i_l and I_0 are respectively the instantaneous and mean load currents.

Since the 2nd harmonic component is the dominant component of the load current waveform, its Fourier series may be approximated to by its mean value and the 2nd harmonic or,

$$i_1 = I_0 + a_2 \cos 2\omega t + b_2 \sin 2\omega t \tag{5.25}$$

where a_2 and b_2 are:

$$a_2 = \frac{\sqrt{2}V_2}{Z_2} \sin(\phi_2 - \theta_2) \tag{5.26}$$

$$b_2 = \frac{\sqrt{2}V_2}{Z_2} \cos(\phi_2 - \theta_2) \tag{5.27}$$

in which Z_2 is the 2nd harmonic load impedance and θ_2 is the phase angle between the 2nd harmonic components of the load current and load voltage. V_2 is the r.m.s. value of the 2nd harmonic component of the load voltage and ϕ_2 is its phase displacement angle. Z_2, θ_2, V_2 and ϕ_2 are given by the equations,

$$Z_2 = \sqrt{R_1^2 + (2\omega L_1)^2} \tag{5.28}$$

$$\theta_2 = \arctan \frac{2\omega L_1}{R_1} \tag{5.29}$$

$$V_2 = \pm\sqrt{\frac{a_{2v}^2 + b_{2v}^2}{2}} \tag{5.30}$$

$$\phi_2 = \arctan \frac{a_{2v}}{b_{2v}} \tag{5.31}$$

where a_{2v} and b_{2v} are the Fourier coefficients for the 2nd harmonic component of the load voltage waveform.

The Fourier series for the switching function `s´ is:

$$s = \sum_{n=1}^{\infty} [a_n \cos(n\omega t) + b_n \sin(n\omega t)] \quad n=1,3,5,7,.. \tag{5.32}$$

In order to obtain all the components for calculating the 5th harmonic component of the supply current waveform, the Fourier series of the switching function must include terms up to the 7th harmonic which from equation 5.32 is:

$$s = a_1 \cos \omega t + b_1 \sin \omega t + a_3 \cos 3\omega t + b_3 \sin 3\omega t + a_5 \cos 5\omega t + b_5 \sin 5\omega t + a_7 \cos 7\omega t + b_7 \sin 7\omega t \tag{5.33}$$

Multiplying equation 5.25 with 5.33 and equating the resulting equation with equation 5.23, gives the Fourier coefficients for the supply current waveform as:

$$A_1 = I_0 a_1 + \frac{a_1 a_2}{2} + \frac{a_2 a_3}{2} + \frac{b_1 b_2}{2} + \frac{b_2 b_3}{2} \qquad (5.34)$$

$$B_1 = I_0 b_1 - \frac{a_2 b_1}{2} + \frac{a_2 b_3}{2} + \frac{a_1 b_2}{2} - \frac{b_2 a_3}{2} \qquad (5.35)$$

$$A_3 = I_0 a_3 + \frac{a_1 a_2}{2} - \frac{b_1 b_2}{2} + \frac{a_2 a_5}{2} + \frac{b_2 b_5}{2} \qquad (5.36)$$

$$B_3 = I_0 b_3 + \frac{a_2 b_1}{2} + \frac{a_1 b_2}{2} + \frac{a_2 b_5}{2} - \frac{b_2 a_5}{2} \qquad (5.37)$$

$$A_5 = I_0 a_5 + \frac{a_2 a_3}{2} - \frac{b_2 b_3}{2} + \frac{a_2 a_7}{2} + \frac{b_2 b_7}{2} \qquad (5.38)$$

$$B_5 = I_0 b_5 + \frac{a_2 b_3}{2} + \frac{b_2 a_3}{2} + \frac{a_2 b_7}{2} - \frac{b_2 a_7}{2} \qquad (5.39)$$

The above analysis of the supply current waveform does not include the exciting current of the transformer, which was included in the computer model. As mentioned earlier, hysteresis and eddy current effects in the transformer core are neglected and consequently the exciting current is the same as the magnetising current, which is 0.2A r.m.s. and lags the supply voltage by 90^o (this value was obtained from the no-load test on the power transformer used in the experimental work). The instantaneous value of the magnetizing current i_m is,

$$i_m = \sqrt{2} \times 0.2 \sin(\omega t - 90^o) \qquad (5.40)$$

From equation 5.20, the supply current including only the fundamental component, is

$$i_{1s} = A_1 \cos \omega t + B_1 \sin \omega t \qquad (5.41)$$

adding equation 5.40 to 5.41 gives,

$$i_{1sm} = (A_1 - 0.28)\sin \omega t + B_1 \cos \omega t \qquad (5.42)$$

or,

$$i_{1sm} = \sqrt{2}\, I_{1sm} \sin(\omega t + \phi_{1sm}) \qquad (5.43)$$

where i_{1sm} and I_{1sm} are respectively the instantaneous and r.m.s. values of the fundamental component of the resulting supply current and are given by,

$$I_{1sm} = \sqrt{\frac{(A_1-0.28)^2 + B_1}{2}} \tag{5.44}$$

$$\phi_{1sm} = \arctan \frac{A_1-0.28}{B_1} \tag{5.45}$$

The Fourier coefficients for the switching function and the load voltage waveform for different controllers are given below.

5.4.1 Conventional Controlled Single-bridge

The Fourier coefficients for the load voltage waveform of figure 5.16(c) are given by equations A2.57 and A2.58 of Appendix A2. The coefficients for the 2nd harmonic component a_{2v} and b_{2v} are obtained by substituting n=2 in equations A2.57 to A2.60, which gives:

$$a_{2v} = \frac{2V_m}{\pi} \left(\frac{1}{3} \cos 3\alpha - \cos \alpha\right)$$
$$b_{2v} = \frac{2V_m}{\pi} \left(\frac{1}{3} \sin 3\alpha - \sin \alpha\right)$$

where α is the firing delay angle and V_m is the peak supply voltage.

The Fourier coefficients for the supply current waveform is given by equations A2.4 and A2.7 of Appendix A2. Substituting $\alpha_{v1}=\alpha_{f1}=\alpha_{v2}=\alpha_{f2}=\alpha$ and $I_a=1$ in the above equations gives the Fourier coefficients of the switching function as,

$$a_n = -\frac{4}{n\pi} \sin n\alpha \qquad n=1,3,5,7$$
$$b_n = \frac{4}{n\pi} \cos n\alpha \qquad n=1,3,5,7$$

5.4.2 Sequence Controlled Single-bridge

Substituting n=2 in equations A2.51 to A2.56 of Appendix A2, gives the Fourier coefficients a_{2v} and b_{2v} (for the waveform of figure 5.19(c)) as:

$$a_{2v} = \frac{V_m}{\pi}\left(\frac{1}{3}\cos 3\alpha_f - \cos\alpha_f + \frac{1}{3}\cos 3\alpha_v - \cos\alpha_v\right)$$
$$b_{2v} = \frac{V_m}{\pi}\left(\frac{1}{3}\sin 3\alpha_f - \sin\alpha_f + \frac{1}{3}\sin 3\alpha_v - \sin\alpha_v\right)$$

and substituting $\alpha_{v1}=\alpha_{v2}=\alpha_v$, $\alpha_{f1}=\alpha_{f2}=\alpha_f$ and $I_a=1$ in equations A2.4 and A2.7 of Appendix A2 gives the Fourier coefficients of the switching function as:

$$a_n = -\frac{2}{n\pi}(\sin\alpha_v + \sin\alpha_f) \qquad n=1,3,5,7$$
$$b_n = \frac{2}{n\pi}(\cos\alpha_v + \cos\alpha_f) \qquad n=1,3,5,7$$

where α_v and α_f are the firing delay angles.

5.4.3 Sequence Controlled Double-bridge

Substituting n=2 in equations A2.41 to A2.50 of Appendix A2 gives a_{2v} and b_{2v} (for the waveform of figure 5.21(c)) as:

$$a_{2v} = \frac{V_m}{\pi}\left[\frac{1}{3}\cos A\cos B - \cos C\cos D + \frac{1}{3}\cos E\cos F - \cos G\cos H\right]$$

and

$$b_{2v} = \frac{V_m}{\pi}\left[\frac{1}{3}\sin A\cos B - \sin C\cos D + \frac{1}{3}\sin E\cos F - \sin G\cos H\right]$$

in which

$$A = \frac{3(\alpha_{f2}+\alpha_{v2})}{2}$$
$$B = \frac{3(\alpha_{f2}-\alpha_{v2})}{2}$$
$$C = \frac{(\alpha_{f2}+\alpha_{v2})}{2}$$
$$D = \frac{(\alpha_{f2}-\alpha_{v2})}{2}$$
$$E = \frac{3(\alpha_{v1}+\alpha_{f1})}{2}$$
$$F = \frac{3(\alpha_{v1}-\alpha_{f1})}{2}$$

$$G = \frac{(\alpha_{v1}+\alpha_{f1})}{2}$$

$$H = \frac{(\alpha_{v1}-\alpha_{f1})}{2}$$

and substituting $I_a=1$ in equations A2.4 and A2.7 of Appendix A2 gives the Fourier coefficients for the switching function as:

$$a_n = -\frac{1}{n\pi}(\sin n\alpha_{v2} + \sin n\alpha_{f2} + \sin n\alpha_{v1} + \sin n\alpha_{f2})$$

$$b_n = \frac{1}{n\pi}(\cos n\alpha_{v2} + \cos n\alpha_{f2} + \cos n\alpha_{v1} + \cos n\alpha_{f2})$$

where n=1,3,5,7 and α_{v1}, α_{f1}, α_{v2}, α_{f2} are the firing delay angles.

5.5 Computed Results

The double- and single-bridge converters of figures 5.14 and 5.15 were connected to a passive load of 0.3H inductance L_l in series with a variable resistor R_l. The supply voltage to these converters was 240V, 50Hz and the load current I_l was maintained constant at 2A by changing the load resistance R_l. The results presented include circuit waveforms and the r.m.s. values of their harmonic spectra for different controllers, together with theoretical results obtained from the analytical models. The results for inversion were obtained by connecting a 200V dc voltage in series with the load.

5.5.1 Conventional Controlled Single-bridge

Results for this section were obtained by making the sequence controlled firing delay angles equal, so that $\alpha_v=\alpha_f=\alpha$. The voltage and current waveforms, together with the r.m.s. values of their harmonic spectra at firing delay angles of $\alpha=45^o$ and 135^o in the rectification and inversion modes are presented in figures 5.16 and 5.17. The load voltage of figures 5.16(c) and 5.17(c) contain even harmonics, with their magnitudes decreasing with the increasing harmonic order, as shown in figures 5.16(d) and 5.17(d), which also indicate that the 2nd harmonic is the predominant component. These voltage harmonics produce load current harmonics of the same frequency as those in figures 5.16(f) and 5.17(f). The magnitudes of the current harmonics are equal as is evident by comparing figure 5.16(f) to 5.17(f), and the corresponding peak-to-peak current ripples of figures 5.16(e) and 5.17(e) are consequently the same (2.1A). Since the shapes of the supply current waveforms of figure 5.16(a) and 5.17(a) are the same, the magnitudes of their corresponding harmonics are also the same, as is confirmed by comparing figure 5.16(b) with 5.17(b).

5.5.2 Sequence Controlled Single-bridge

Circuit waveforms with firing delay angles $\alpha_f=10^o$, $\alpha_v=90^o$ are shown in figure 5.18. The two commutation notches in figure 5.18(c) located at α_f and α_v, are also evident in figure 5.18(a), but with a reduced magnitude due to the transformer impedance. The load voltage of figure 5.18(i) and the transformer secondary current of figure 5.18(d) are zero during the free-wheeling period $(\alpha_v-\alpha_f)$, and only magnetising current circulates in the primary side, as is clear in figure 5.18(b). The load current of figure 5.18(j) is continuous, with a peak-to-peak ripple of 1.7A.

Voltage and current waveforms, together with their harmonic spectra, for firing delay angles of $\alpha_f=10^o$, $\alpha_v=60^o$ and $\alpha_f=90^o$, $\alpha_v=160^o$ are shown in figures 5.19 and 5.20, for the rectification and inversion modes respectively. The rate of rise and fall of the load current ripple of figure 5.19(e) is expressed by the following equation,

$$\frac{di_l}{dt} = \frac{v_l-V_l}{L_l} \qquad t_1<t>t_2 \;\&\; t_2<t>t_3 \qquad (5.46)$$

where v_l and V_l are respectively the instantaneous and mean load voltage,

t_1 is the firing delay time for α_v,

t_2 is the time in which $v_l=V_l$,

t_3 is the firing delay time for α_f.

As shown in figure 5.19(c), between $t_1<t>t_2$, v_l is greater than its mean voltage V_l and consequently the load current rises at a rate given by equation 5.46. However, between $t_2<t>t_3$, v_l is smaller than V_l which results in a fall in the load current ripple at a rate given again by equation 5.46. During free-wheeling $t_3<t>t_4$, the instantaneous load voltage v_l is zero and the load current of figure 5.19(c) falls at a constant rate given by,

$$\frac{di_l}{dt} = -\frac{V_l}{L_l} \qquad t_3<t>t_4 \qquad (5.47)$$

where $t_4 = \frac{1}{2f} + t_1$

The computed results for inversion were obtained by connecting a 200V dc voltage source V_{dc} in series with the load as shown in figure 5.15(a). The rate of rise and fall of the load current ripple of figure 5.20(e) is also expressed by equations 5.46 and 5.47, where the mean load voltage in this case is,

$$V_l = I_l R_l - V_{dc} \qquad (5.48)$$

The shape of the supply current waveform of figure 5.19(a) is different to that of figure 5.20(a), and consequently their corresponding harmonic magnitudes are different, as shown in figures 5.19(b) and 5.20(b). Since the shape of the load voltage of figures 5.19(c) and 5.20(c) varies with the firing delay angle, so also does the magnitude of their harmonics, as shown in figures 5.19(d) and 5.20(d), which again indicate that the 2nd harmonic predominates.

5.5.3 Sequence Controlled Double-bridge

Chapter 2 described the four zones of operation of the sequence controlled double-bridge converter. Voltage and current waveforms, together with their harmonic spectra in each zone of operation, are presented in figures 5.21 to 5.24. With a

2:1:1 turns ratio for transformer TF1 of figure 5.14, the instantaneous load voltage is one-half of the supply voltage, and the supply current is one-half of the load current when either bridge 1 or bridge 2 is free-wheeling. When neither free-wheels, the instantaneous load voltage equals the supply voltage and the supply current equals the load current. The above conditions are shown in figure 5.21(a) and (c), and 5.24(a) and (c). When both bridges free-wheel the load voltage is zero, and the supply current is simply the magnetising current, as shown in figures 5.22(a) and (c), and 5.23(a) and (c). The rate of rise and fall of the load current ripple of figure 5.24(e) is expressed by the following equations,

$$\frac{di_1}{dt} = \frac{v_1 - V_1}{L_1} \qquad t_1<t>t_2 \ \& \ t_2<t>t_3 \qquad (5.49)$$

$$\frac{di_1}{dt} = \frac{v_1 - 2V_1}{2L_1} \qquad t_3<t>t_4 \ \& \ t_4<t>t_5 \qquad (5.50)$$

There is a significant difference between the rate of rise and fall of the load current ripple between $t_1<t>t_3$ and $t_3<t>t_5$, this is because in the latter case the instantaneous load voltage is halved as is indicated in equation 5.50.

5.4.4 Fully Controlled PWM Bridge Converter

Figure 5.25 shows voltage and current waveforms and their harmonic spectra, for a switching frequency f_c=4kHz and a modulation index M=0.9, and figure 5.26 shows the same results when M=0.5. The supply current waveform of 5.29(a) and 5.30(a) contain odd harmonics and also high-order harmonics located at the side-bands of the switching frequency. These are not however evident in figures 5.25(b) and 5.26(b), since they lie outside the range of the harmonic analyser. The load voltage of figure 5.25(c) and 5.26(c) also contains high-order harmonics at multiples of the switching frequency and their side-bands, but these again are not shown. Load current harmonics associated with these high order voltage harmonics are negligible due to the reactance of the load, and the harmonic copper losses are consequently negligible. Nevertheless, these harmonics need to be filtered to eliminate supply voltage distortion. The high frequency distortion evident on the load current waveforms of figure 5.25(e) and 5.26(e) arises since the current decays when free-wheeling and rises when the load is connected to the supply.

5.6 Comparison Between Different Controllers

The fundamental component of current produced by the sequence controlled double-bridge is larger than that with PWM control, as is evident by comparing figures 5.21(b) and 5.25(b). The discrepancy is partly due to the supply current waveform of figure 5.25(a) being chopped in a PWM manner which results in a reduction in low-order harmonics at the expense of producing high-order harmonics located at the side-bands of the switching frequency and multiples of it. Another reason for the discrepancy is that the magnetising current produced by the power transformer was included in the models for the sequence and conventional controlled bridges but not in the PWM controller. The transformer is considered to be linear, so that the magnetising current is sinusoidal and of fundamental frequency. Comparing the load voltage spectrum of figure 5.21(d) with that of figure 5.25(d) shows that the 2nd harmonic is the predominant component and was measured to be 96V and 110V respectively. Since the load conditions in which the above results were taken are the same, consequently the peak-to-peak load current ripple produced by the sequence-controlled double-bridge converter should be better than that produced by the PWM controller and was measured to be 1.2A and 1.5A respectively. However comparing the PWM results of figures 5.25(d) and (e) with those of figures 5.19(d) and (e), which is for a sequence-controlled single-bridge, shows that the second harmonic and peak-to-peak load current ripple are improved by 20% and 33% respectively, when PWM control is used. However the disadvantage with the PWM bridge converter is that the output voltage produced is chopped, as shown in figures 5.25(c) and 5.26(c), resulting in a reduction in the mean output voltage and the power output to below that produced by conventional or sequence controllers for a given input voltage and load current.

The analytical load voltage and current harmonics produced by conventional and sequence-controlled single-bridge converters and by a sequence-controlled double-bridge converter are the same as that produced by the computer models. However, there is some discrepancy between the computed and analytical results for the supply current harmonics. This is due to the mathematical expressions for the switching function and load current waveforms possibly not being sufficiently accurate. Only the mean and 2nd harmonic terms were considered in the load current waveform and only terms up to 7th harmonic in the switching function waveform. If more accurate results were required, more terms should be considered in both waveforms.

The overall results obtained from the analytical models agree very closely with those obtained from the computer model, and it can even be concluded that the computer model can be replaced by the analytical models in predicting the performance of the converter circuits. The most important advantage of using the analytical models is that they allow the designer to assess which circuit parameters influence the converter characteristics, such as the input power factor, peak-to-peak load current ripple, harmonic content of the supply current and load voltage waveforms.

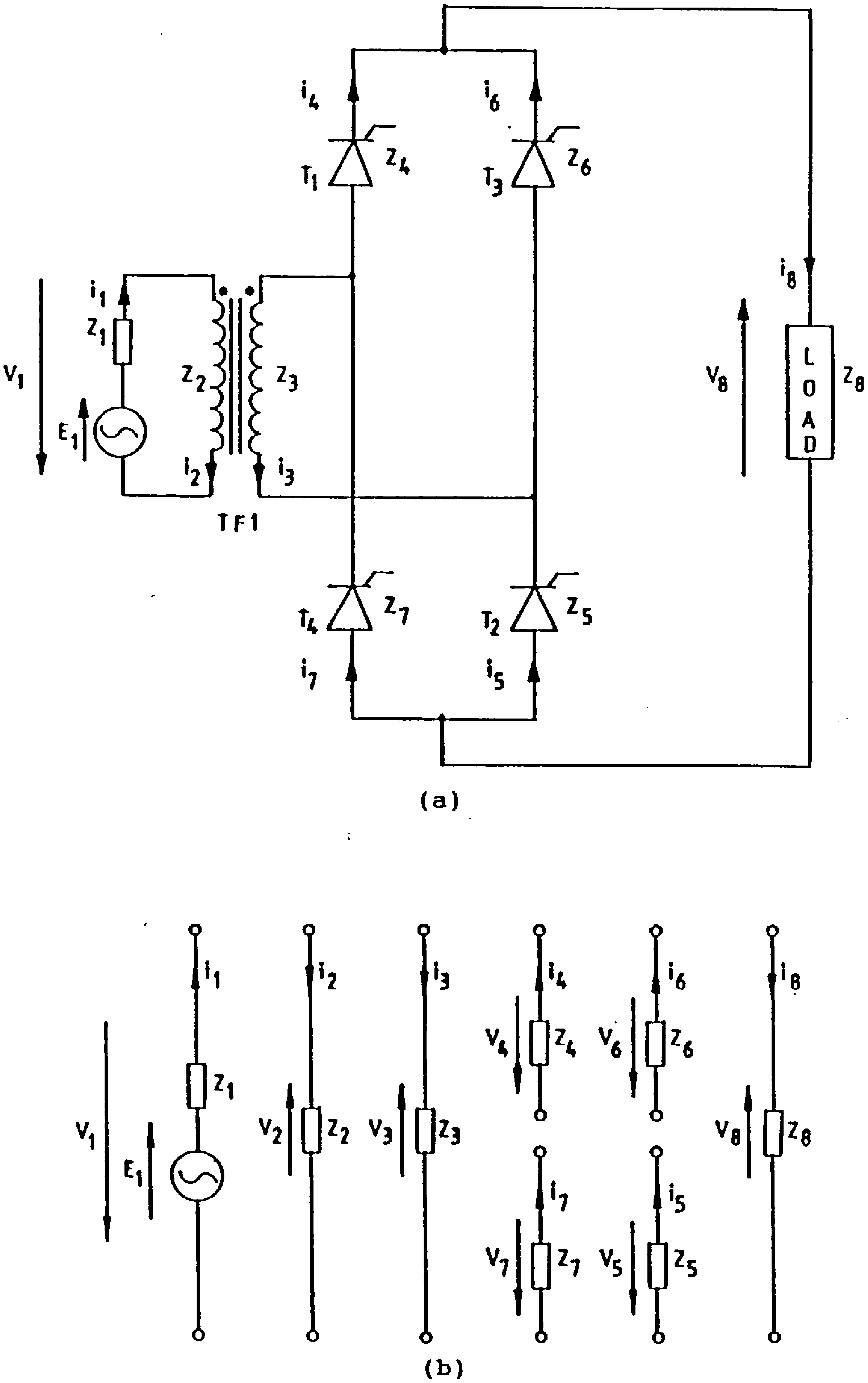

Figure5.1 Fully-controlled single-bridge converter.
(a) Connection.
(b) Branch reference frame.

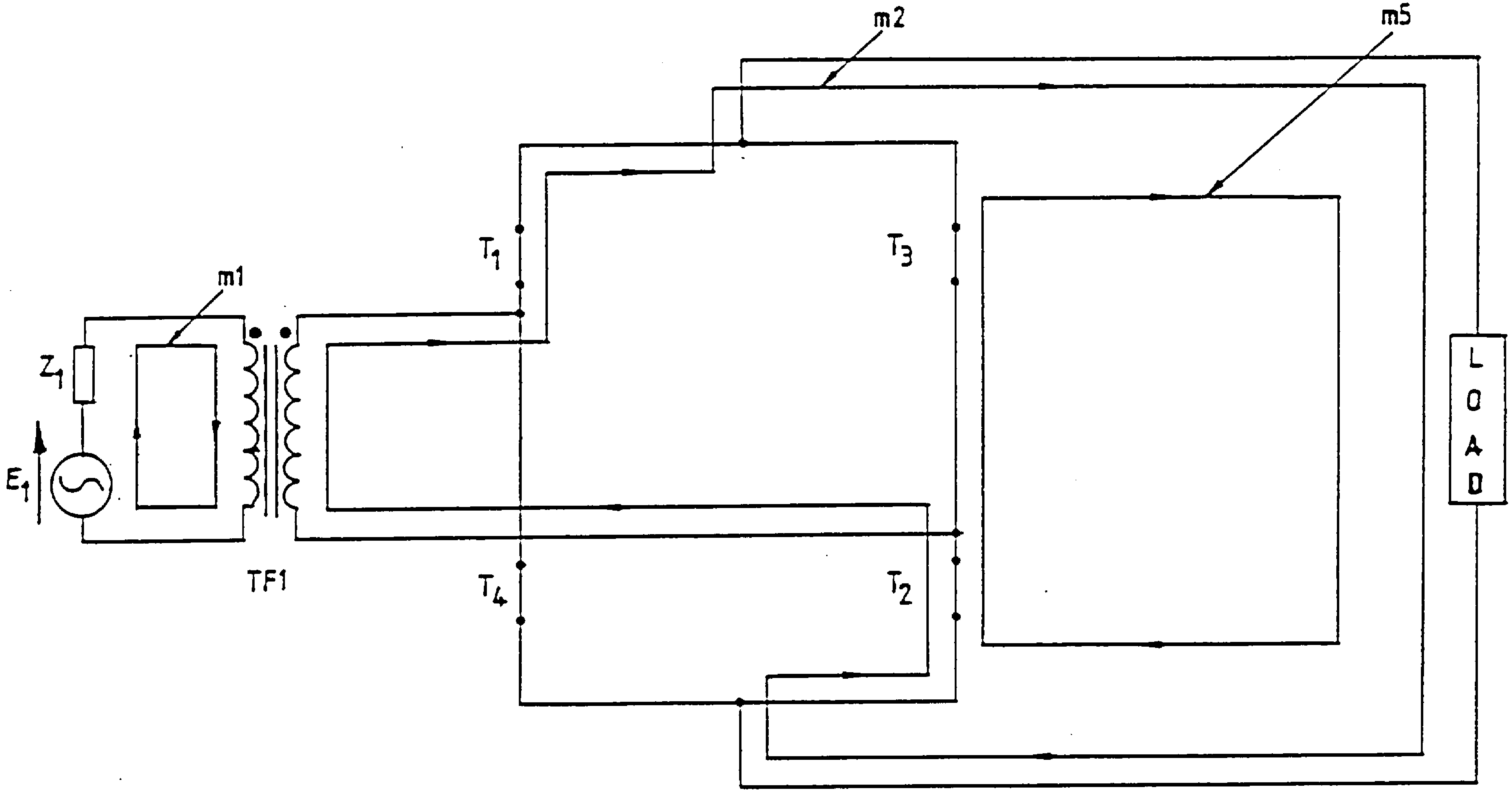

Figure5.2 Typical conduction pattern for overlap condition for sequence-controlled single-bridge converter.

	Mesh				
	1	2	3	4	5
Branch 1	1	0	0	0	0
2	1	0	0	0	0
3	0	-1	1	0	0
4	0	1	0	1	0
5	0	1	0	0	1
6	0	0	1	0	1
7	0	0	1	1	0
8	0	1	1	1	1

(a)

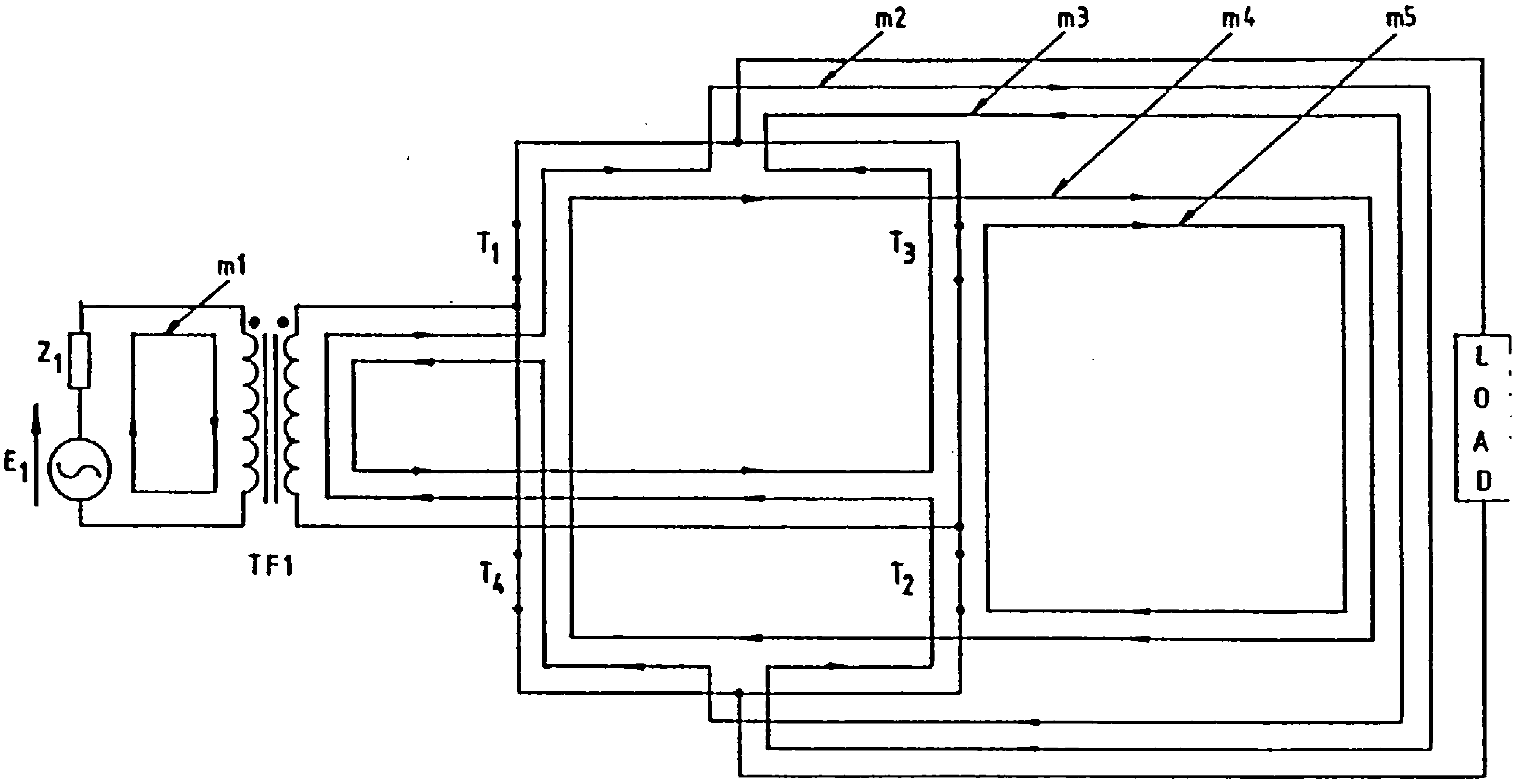

(b)

Figure5.3(a) Master matrix to obtain $C^{b}_{\cdot m}$ for single-bridge converter.
(b) All possible mesh currents to produce sequence control.

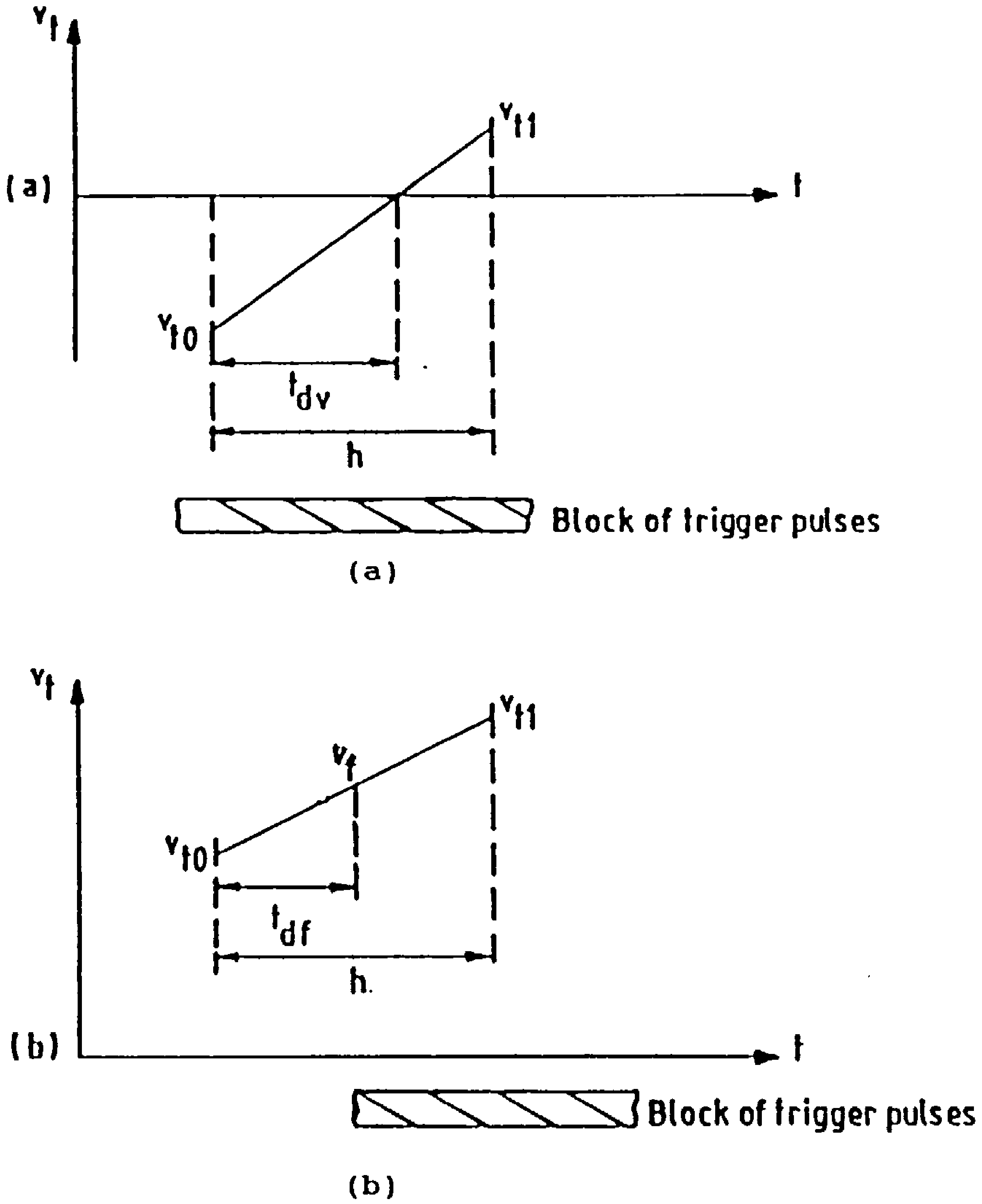

Figure5.4 Turn-on discontinuity.
(a) Gate pulses are present and thyristor voltage changes from negative to positive within the step-length h.
(b) Thyristor voltage is already positive and gate pulses are applied within the step-length h.

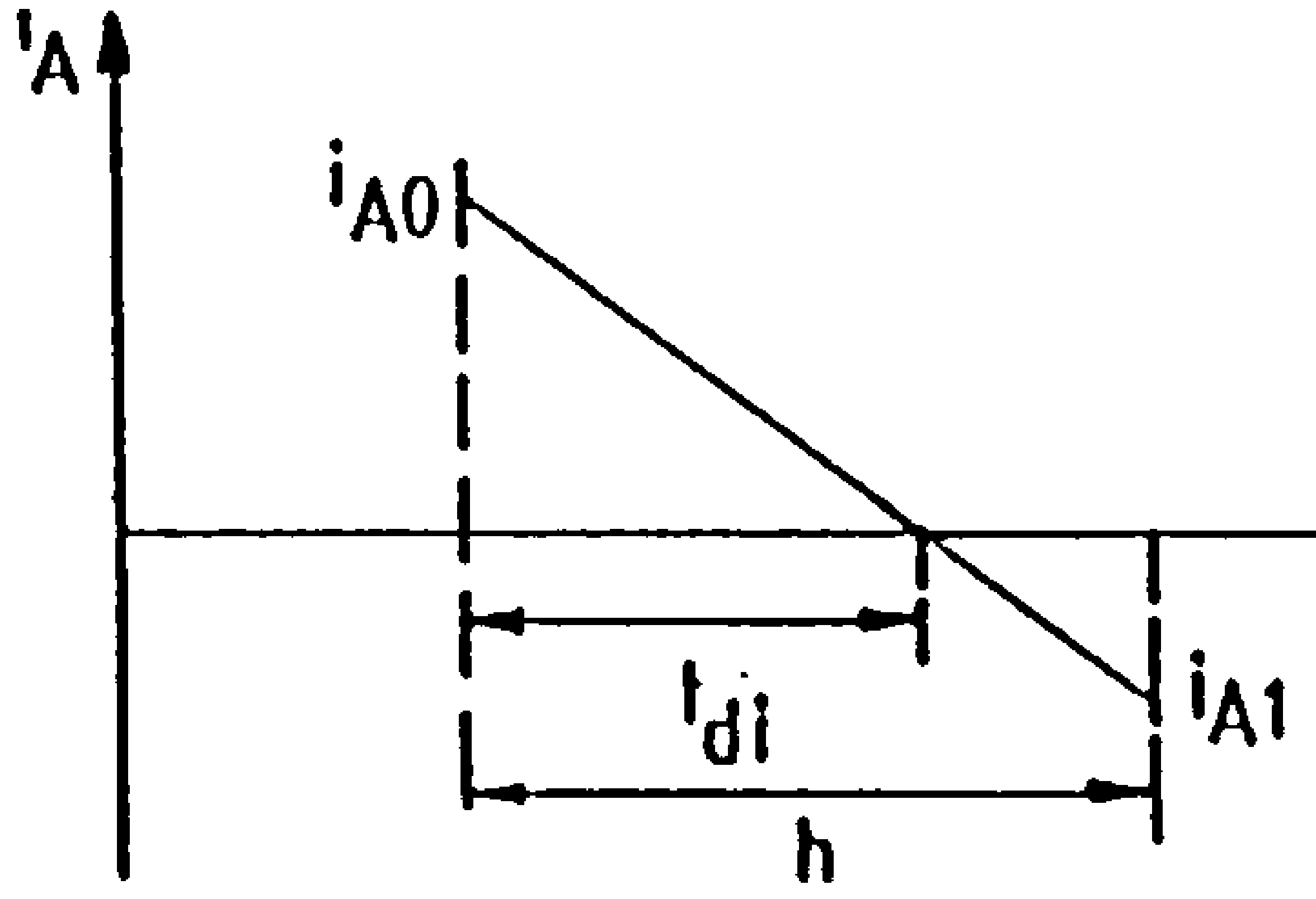

Figure5.5 Turn-off discontinuity.

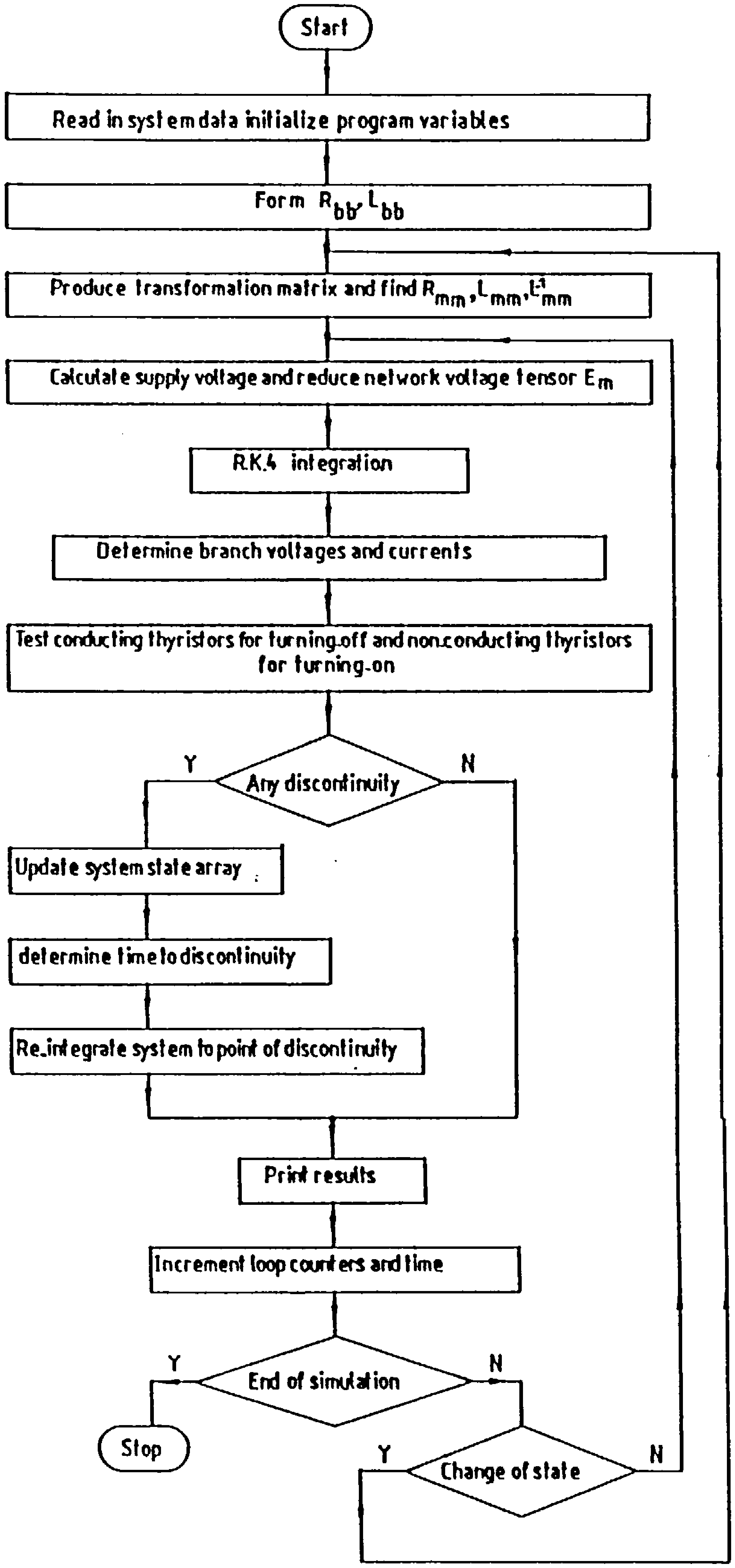

Figure5.6 Flow chart for sequence-controlled single and double-bridge converters.

(a)

(b)

Figure5.7 Fully-controlled series connected double-bridge converter.
(a) Connection.
(b) Branch reference frame.

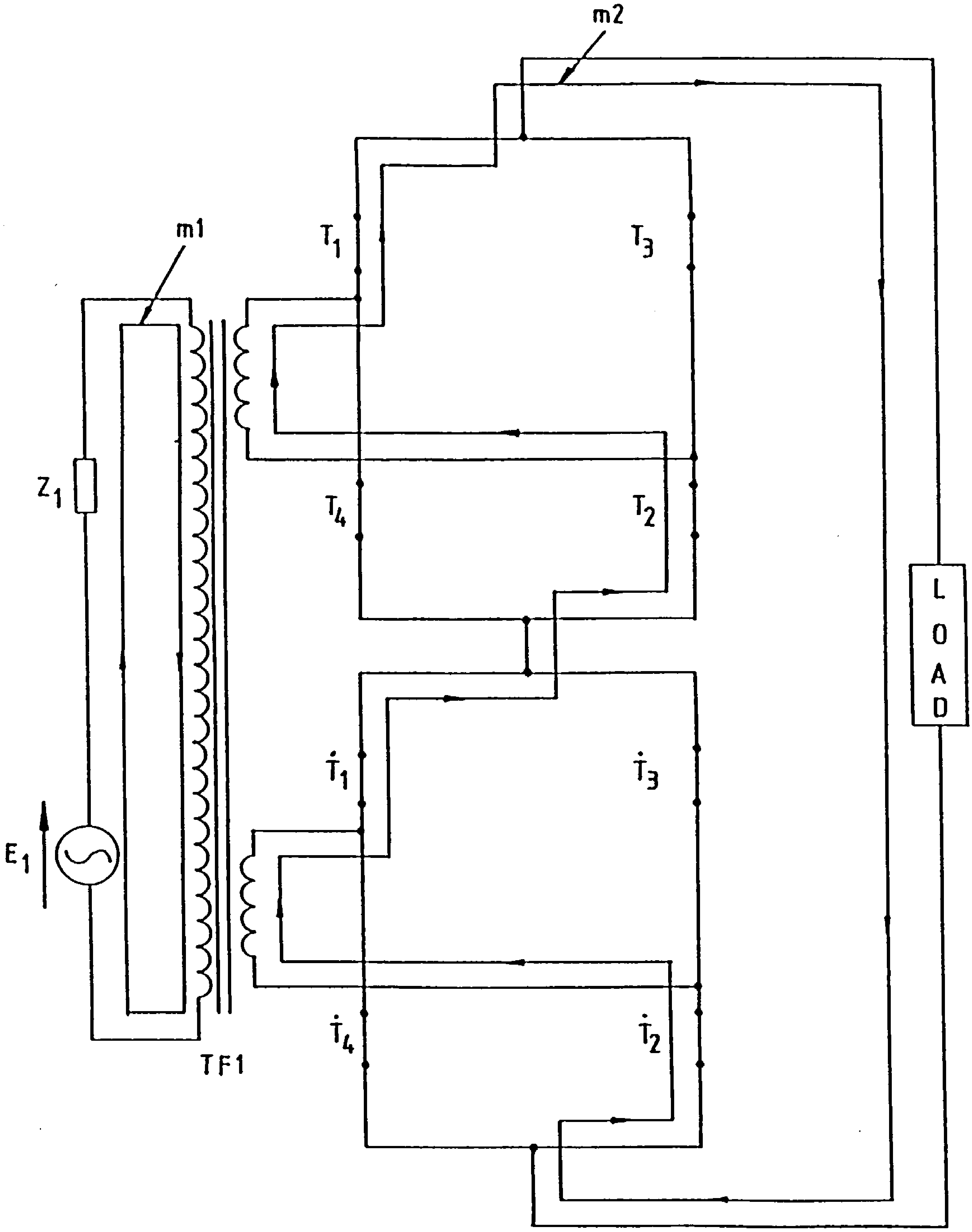

Figure5.8 Typical conduction pattern for double-bridge converter.

	Mesh										
	1	2	3	4	5	6	7	8	9	10	11
Branch 1	1	0	0	0	0	0	0	0	0	0	0
2	1	0	0	0	0	0	0	0	0	0	0
3	0	-1	1	0	0	0	0	-1	1	1	-1
4	0	-1	1	0	0	-1	1	0	0	0	0
5	0	1	0	0	1	0	1	1	0	0	1
6	0	1	0	1	0	1	0	1	0	0	1
7	0	0	1	1	0	1	0	0	1	1	0
8	0	0	1	0	1	0	1	0	1	1	0
9	0	1	0	0	1	1	0	1	0	1	0
10	0	1	0	1	0	1	0	0	1	0	1
11	0	0	1	1	0	0	1	0	1	0	1
12	0	0	1	0	1	0	1	1	0	1	0
13	0	1	1	1	1	1	1	1	1	1	1

(a)

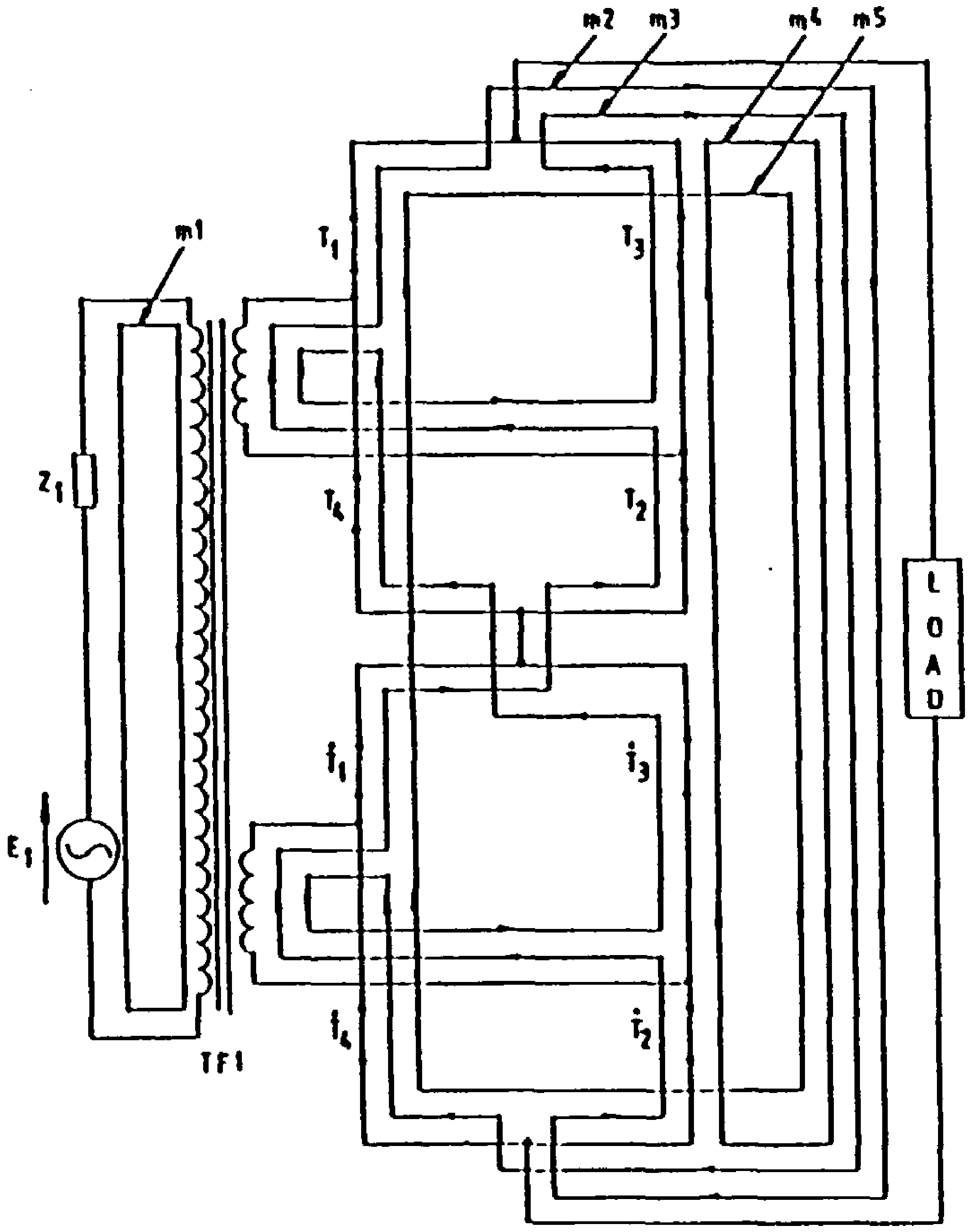

(b)

Figure5.9(a) Master matrix to obtain $C^{b}_{.m}$ for double-bridge converter.
(b)to(d) All possible mesh currents to produce sequence control.

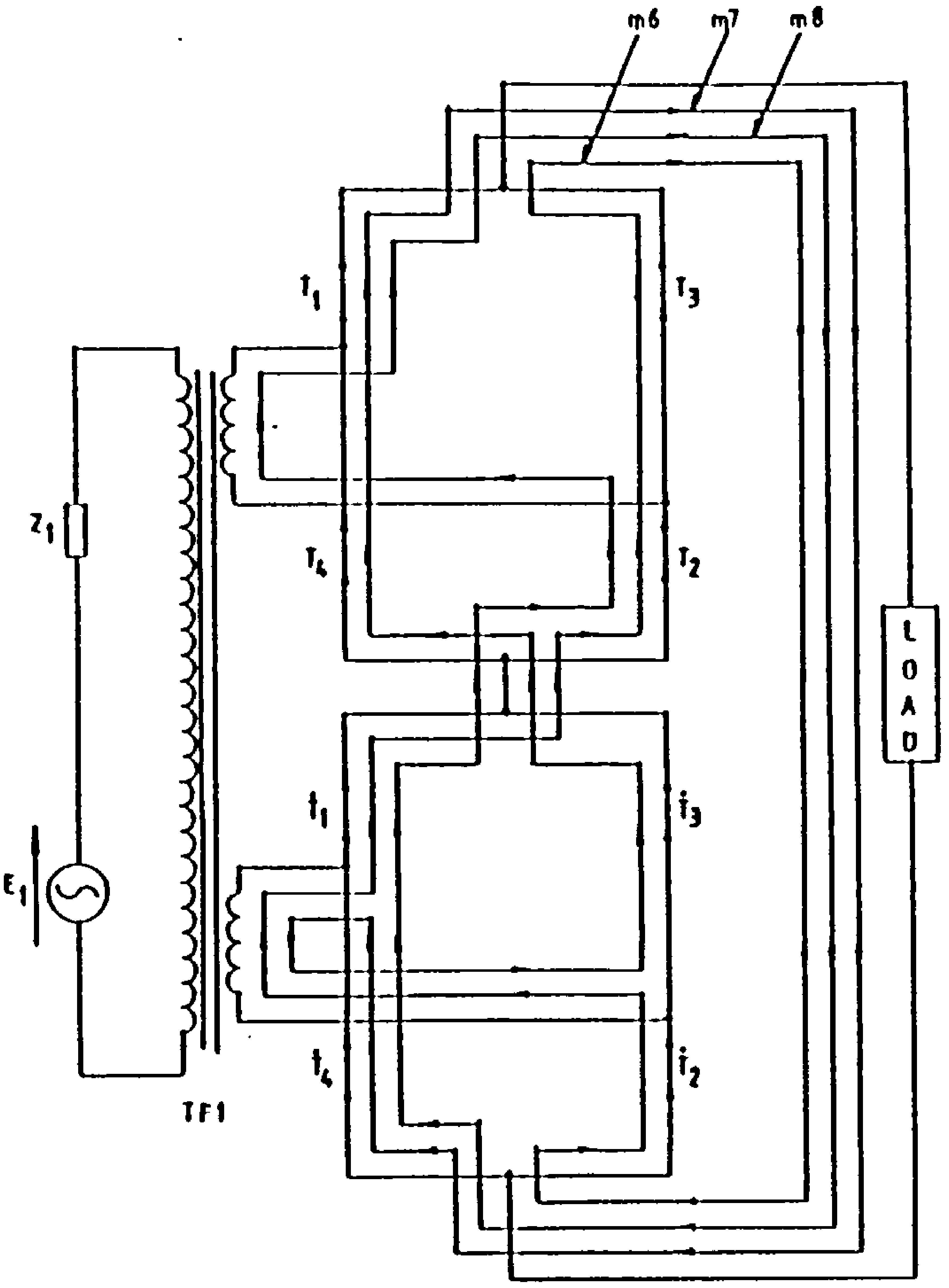

(c)

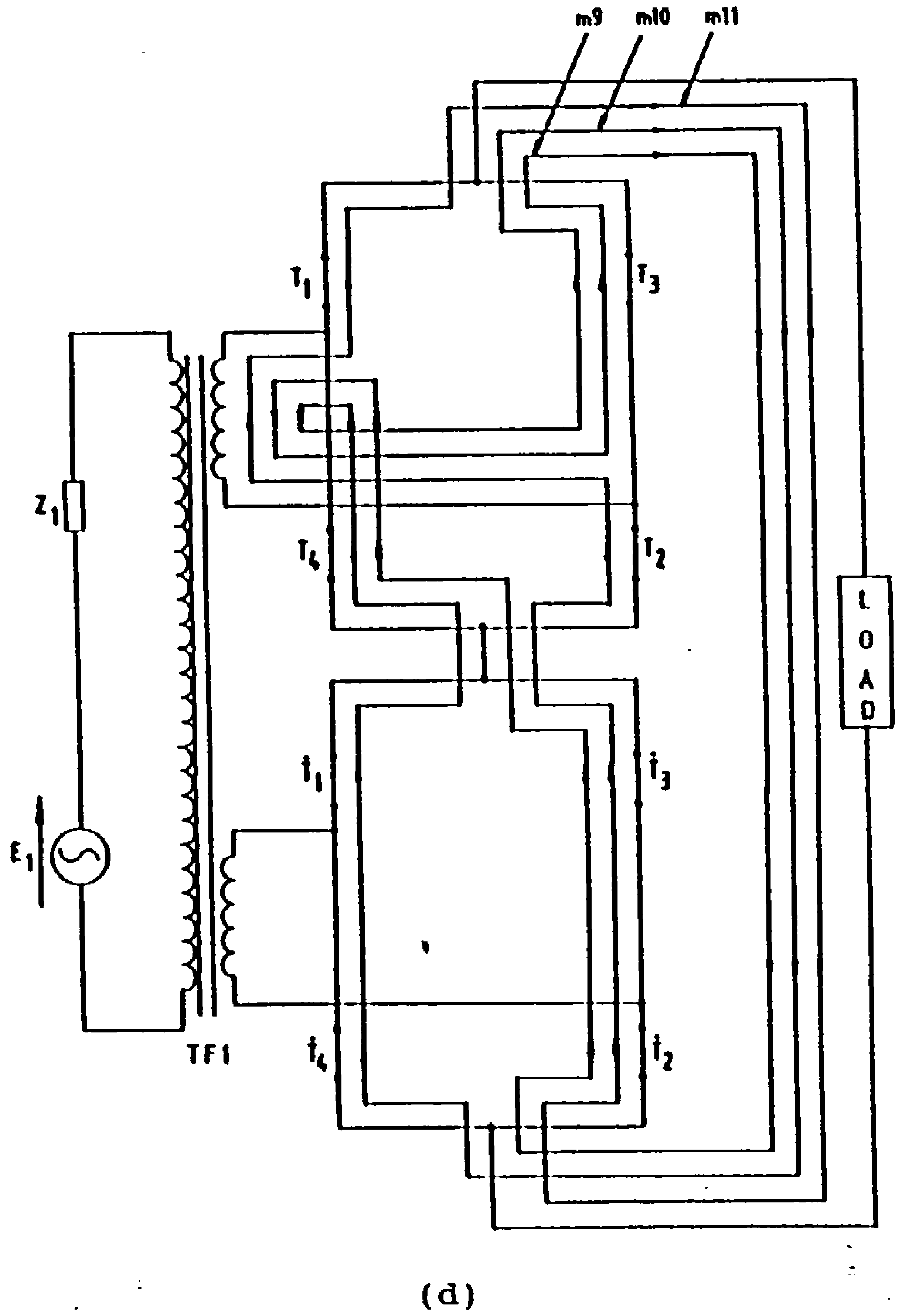

(d)

Figure5.9 Continued.

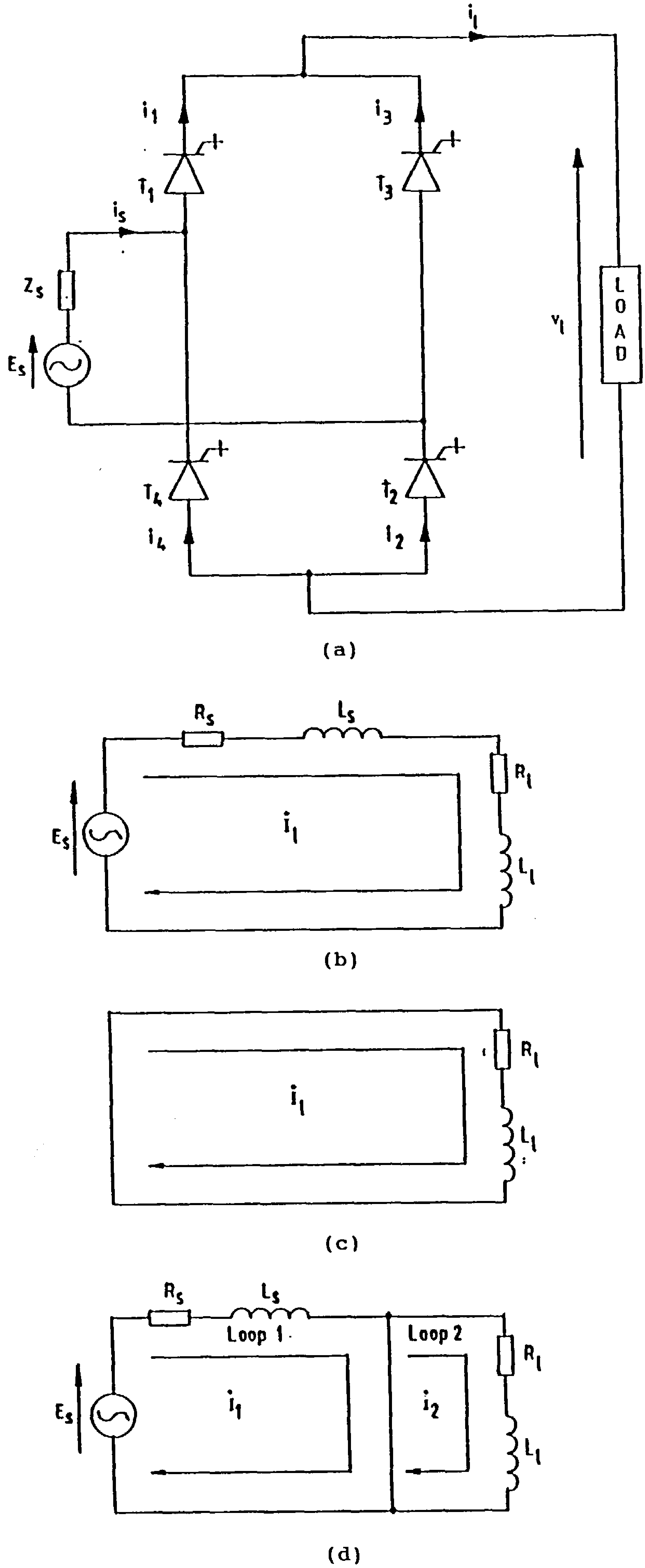

Figure5.10 Fully-controlled PWM converter.
(a) Connection.
(b)to(d) Three operating modes.

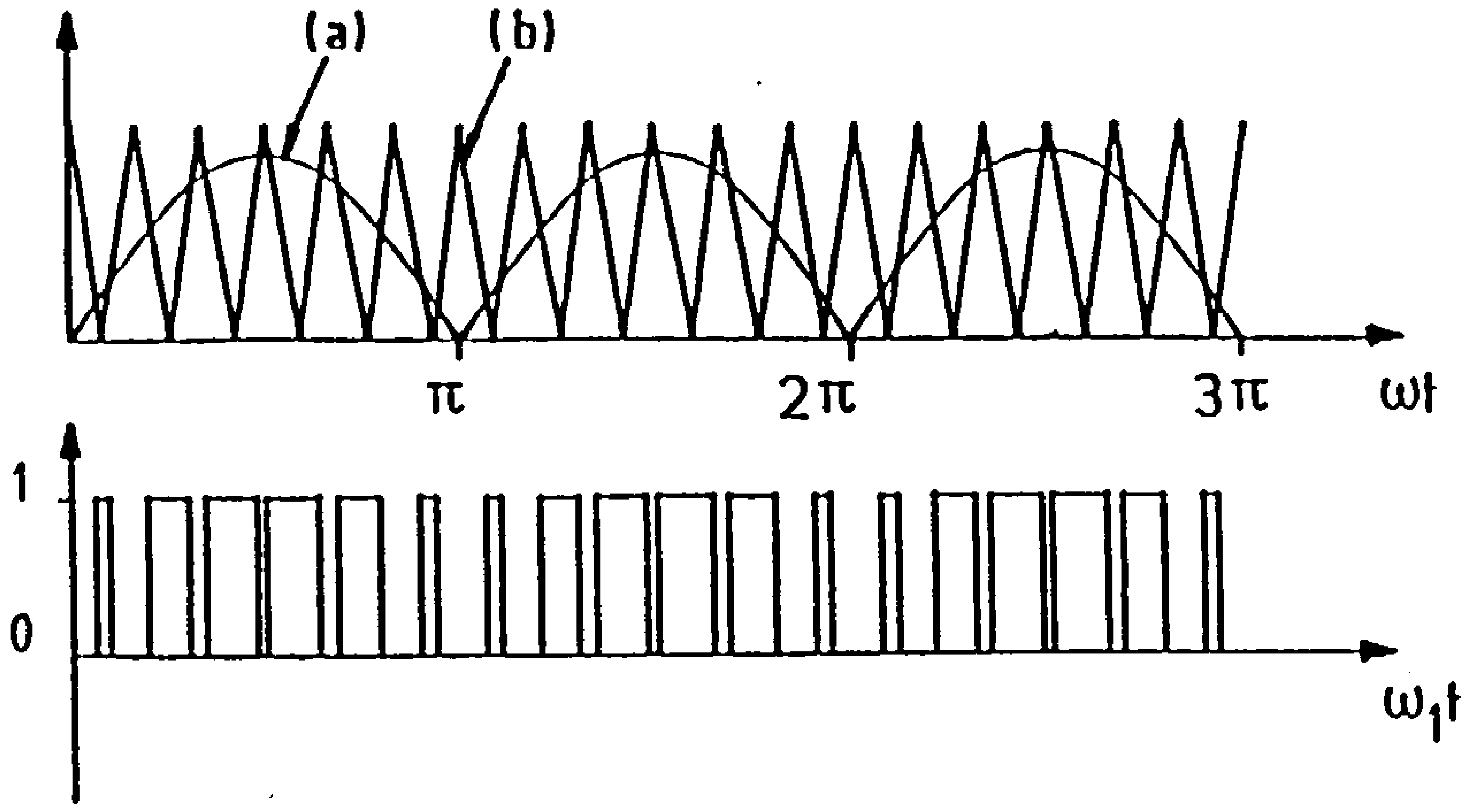

(c)

Figure5.11 Formation of PWM signal.
(a) Full-wave rectified modulating waveform.
(b) Triangular carrier waveform.
(c) PWM gate signal.

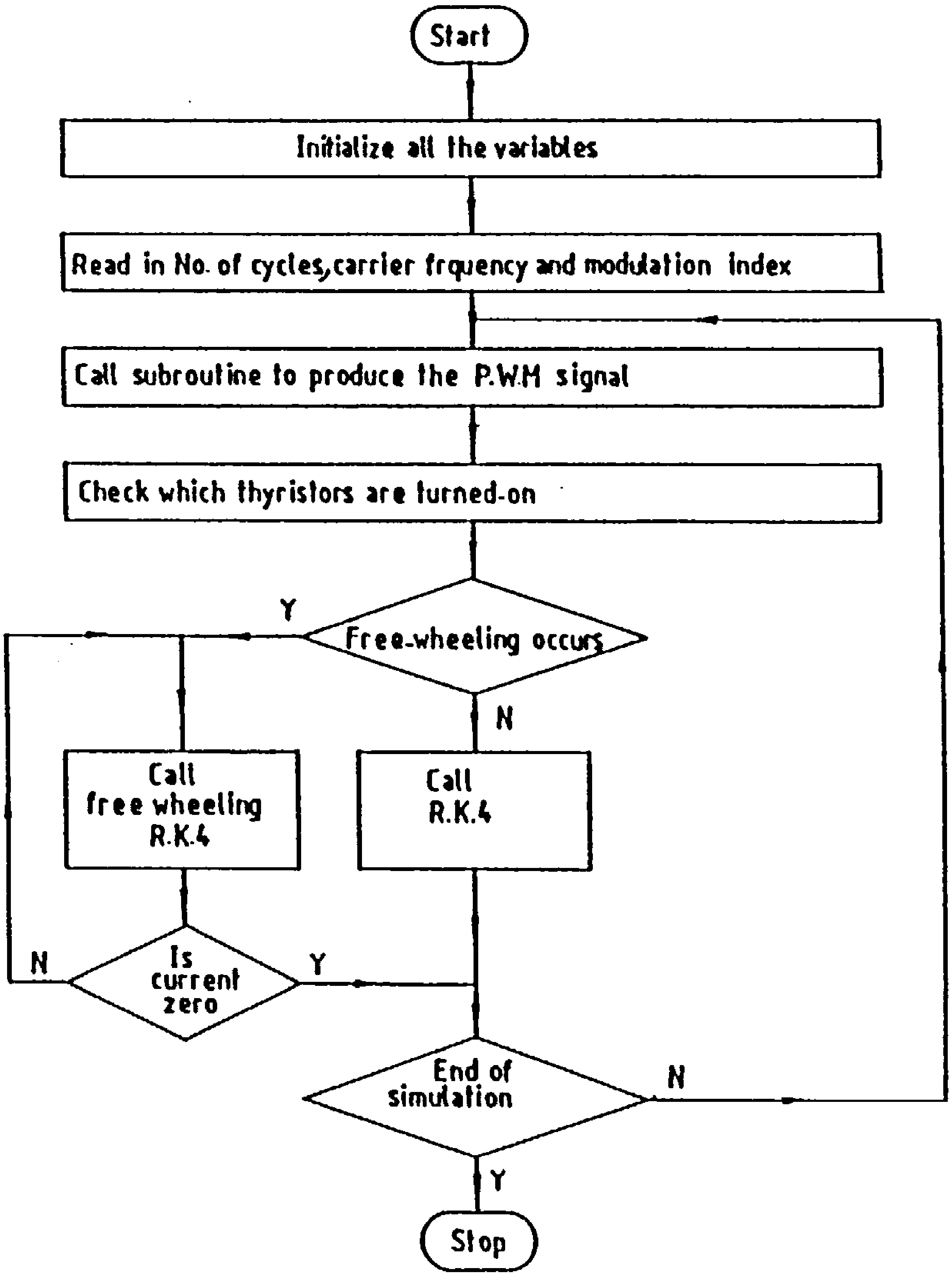

Figure5.12 Flow chart for PWM converter.

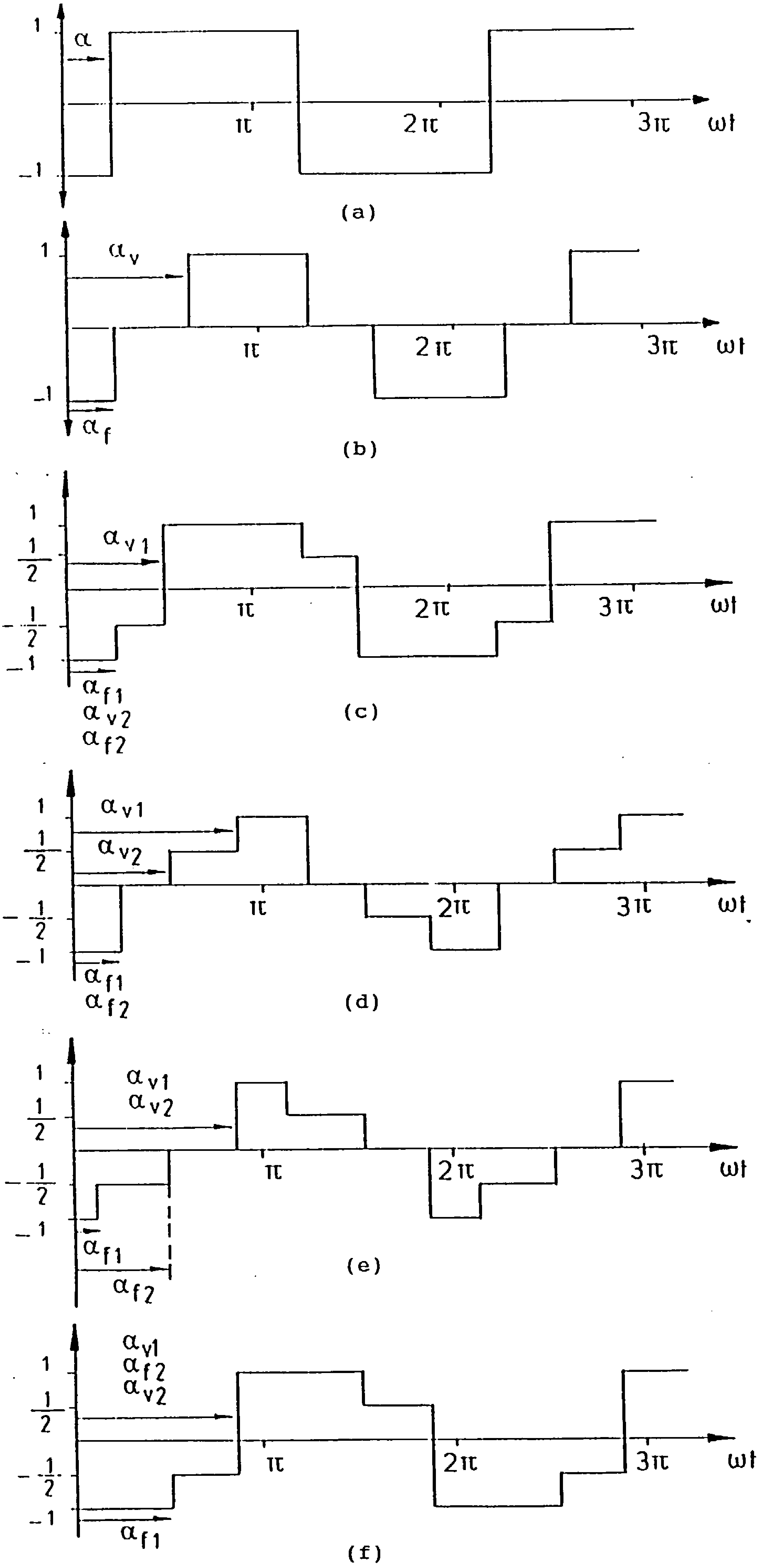

Figure5.13 Switching functions for different controllers.
(a) Conventional controlled single-bridge converter.
(b) Sequence-controlled single-bridge converter.
(c)to(f) Sequence-controlled double-bridge converter in zones 1 to 4 respectively.

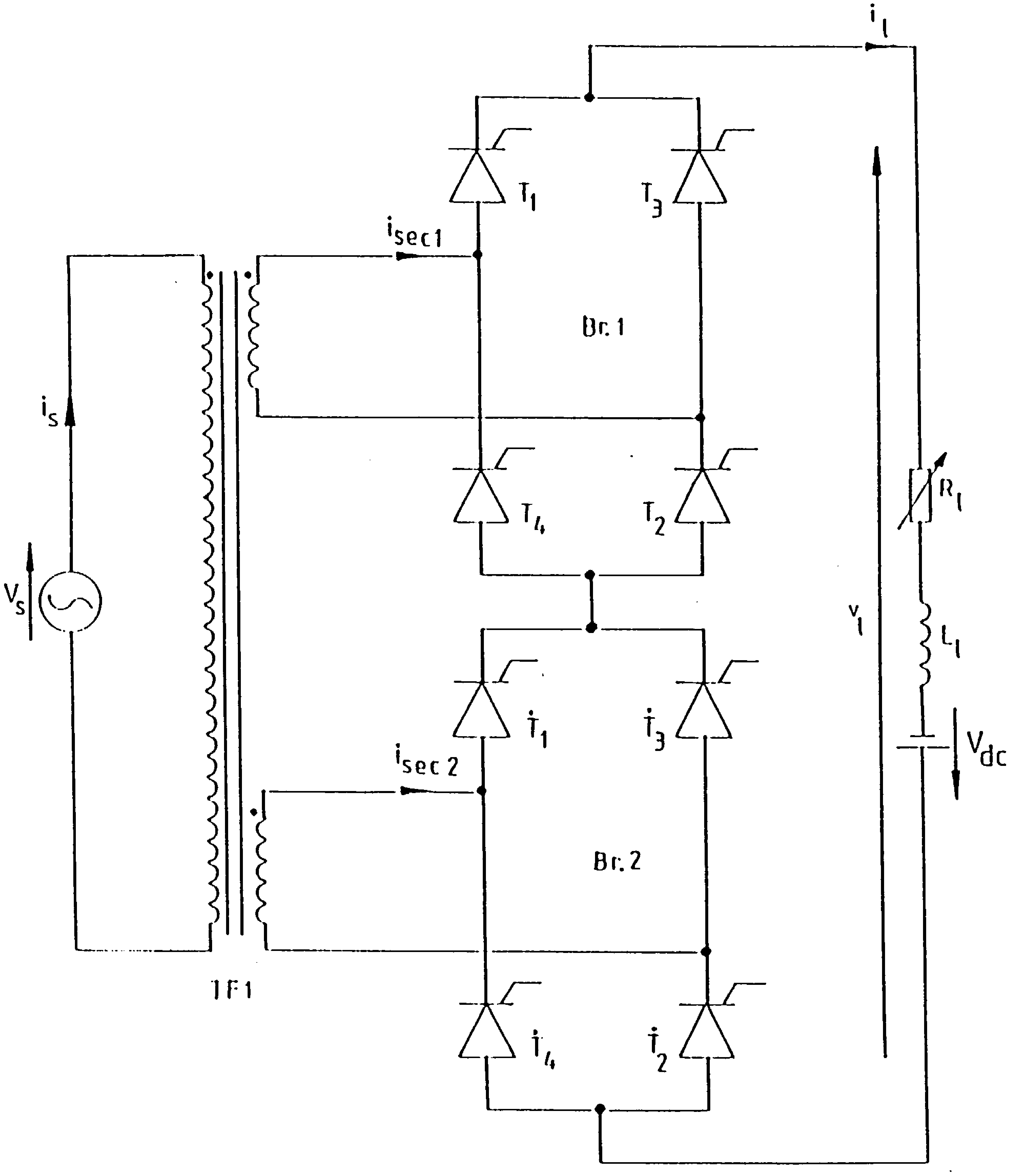

Figure5.14 Fully-controlled series connected double-bridge converter.

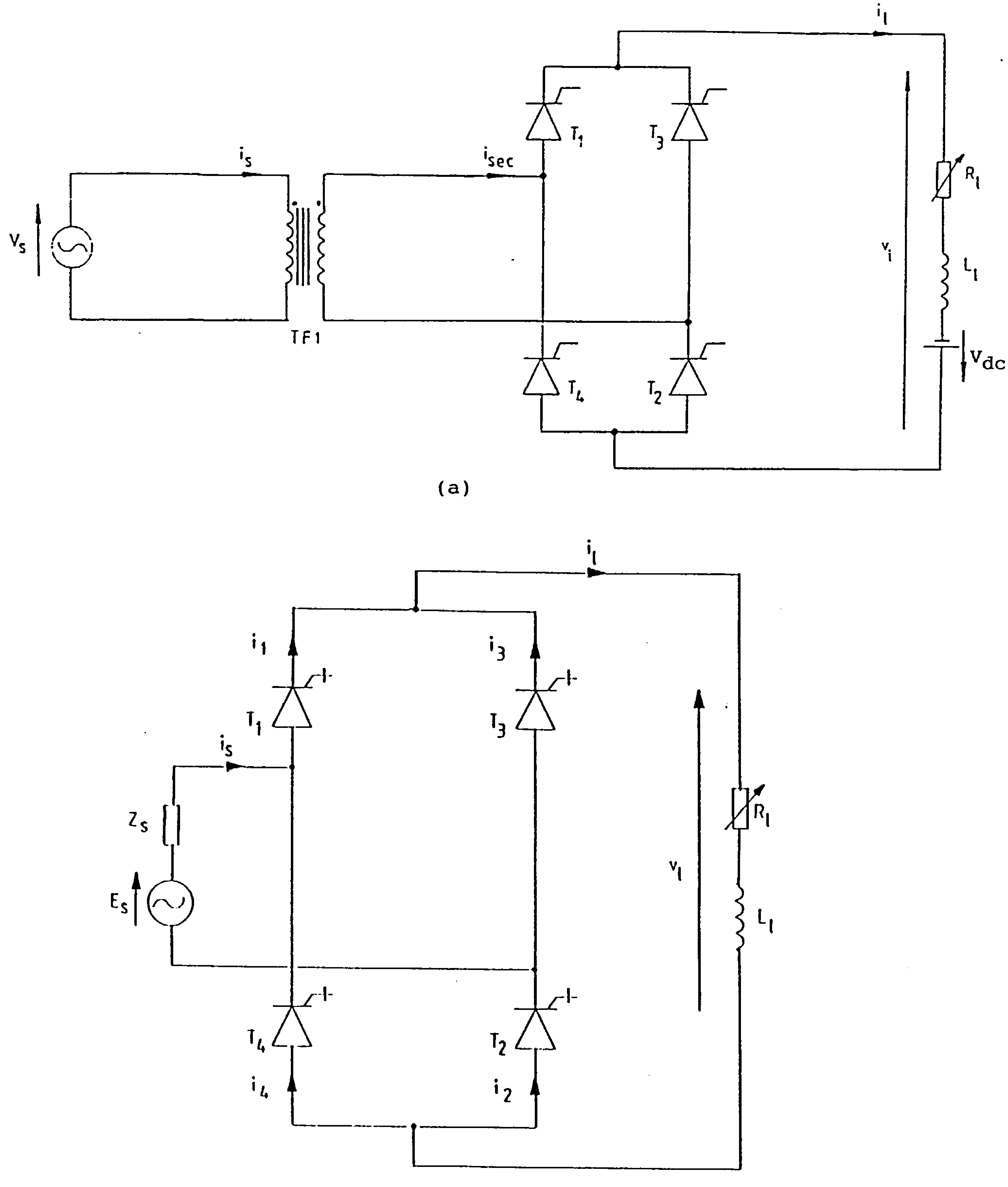

(a)

(b)

Figure5.15 Circuit connection for bridge converters.
(a) Fully-controlled converter.
(b) Fully-controlled PWM converter.

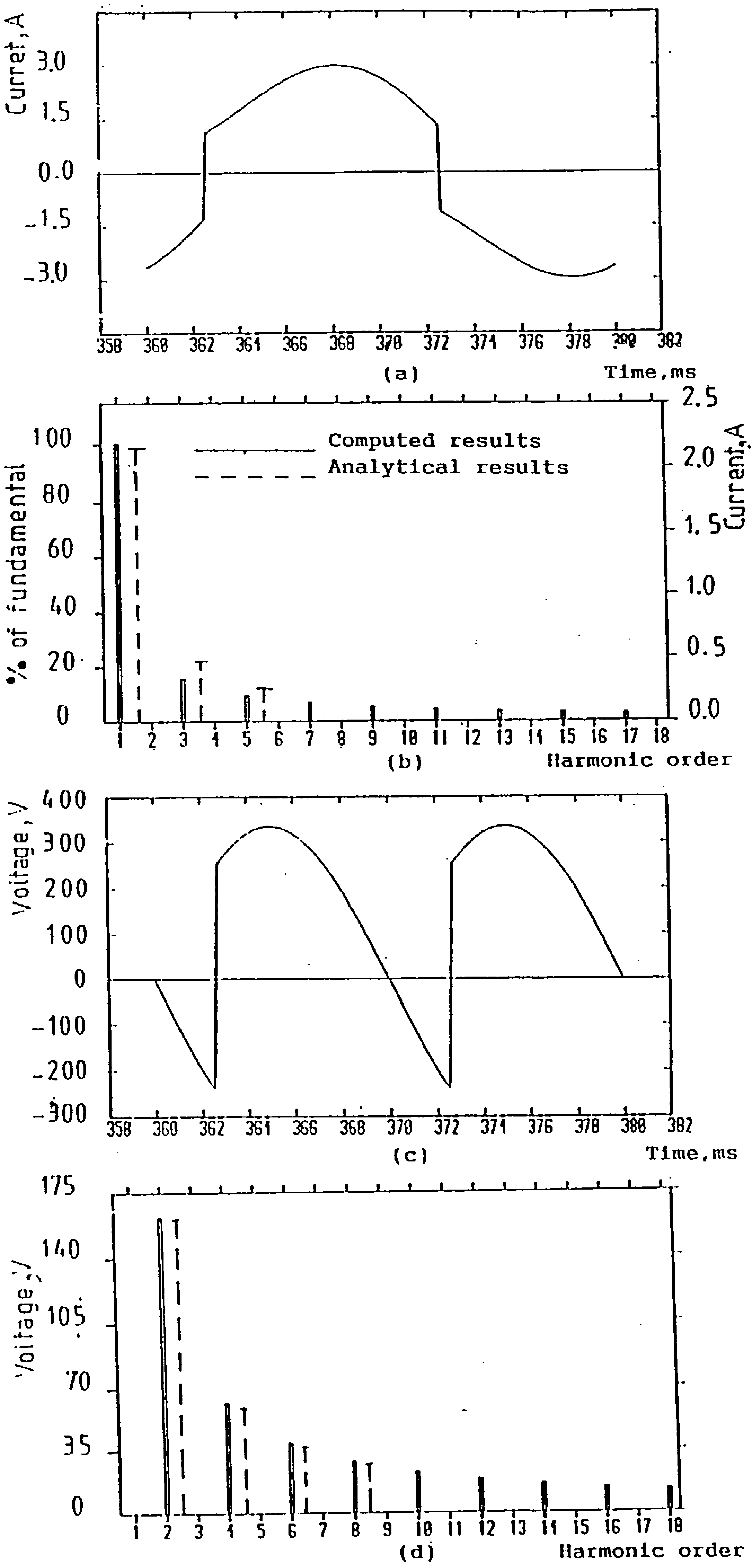

Figure5.16 Computed results for conventional controlled single-bridge converter.
(a),(b) Supply current and harmonic spectrum.
(c),(d) Load voltage and harmonic spectrum.

($\alpha=45^{o}, R_1=76\Omega, L_1=0.3H, V_1=152V$)

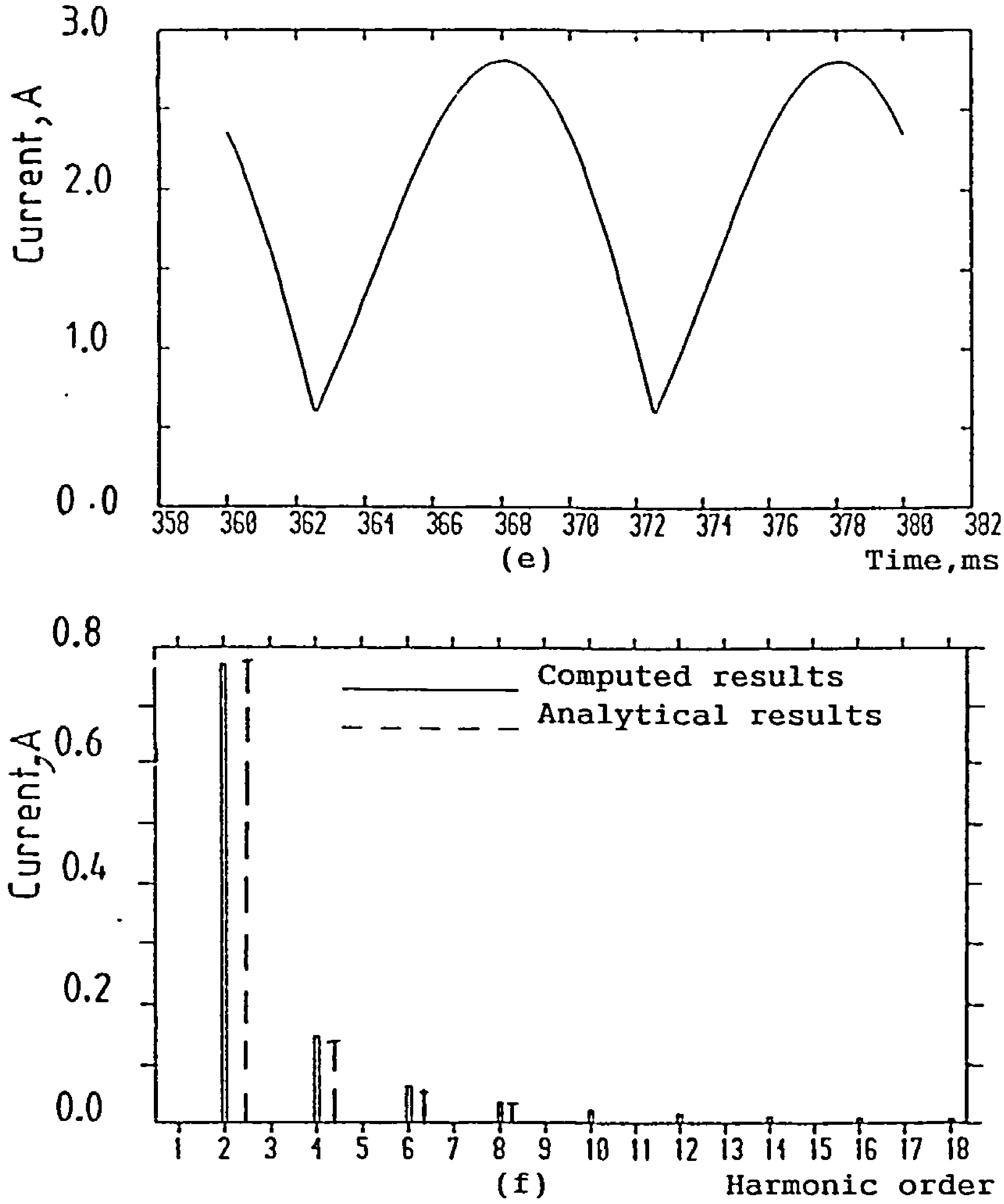

Figure5.16 Continued.
(e),(f) Load current and harmonic spectrum.

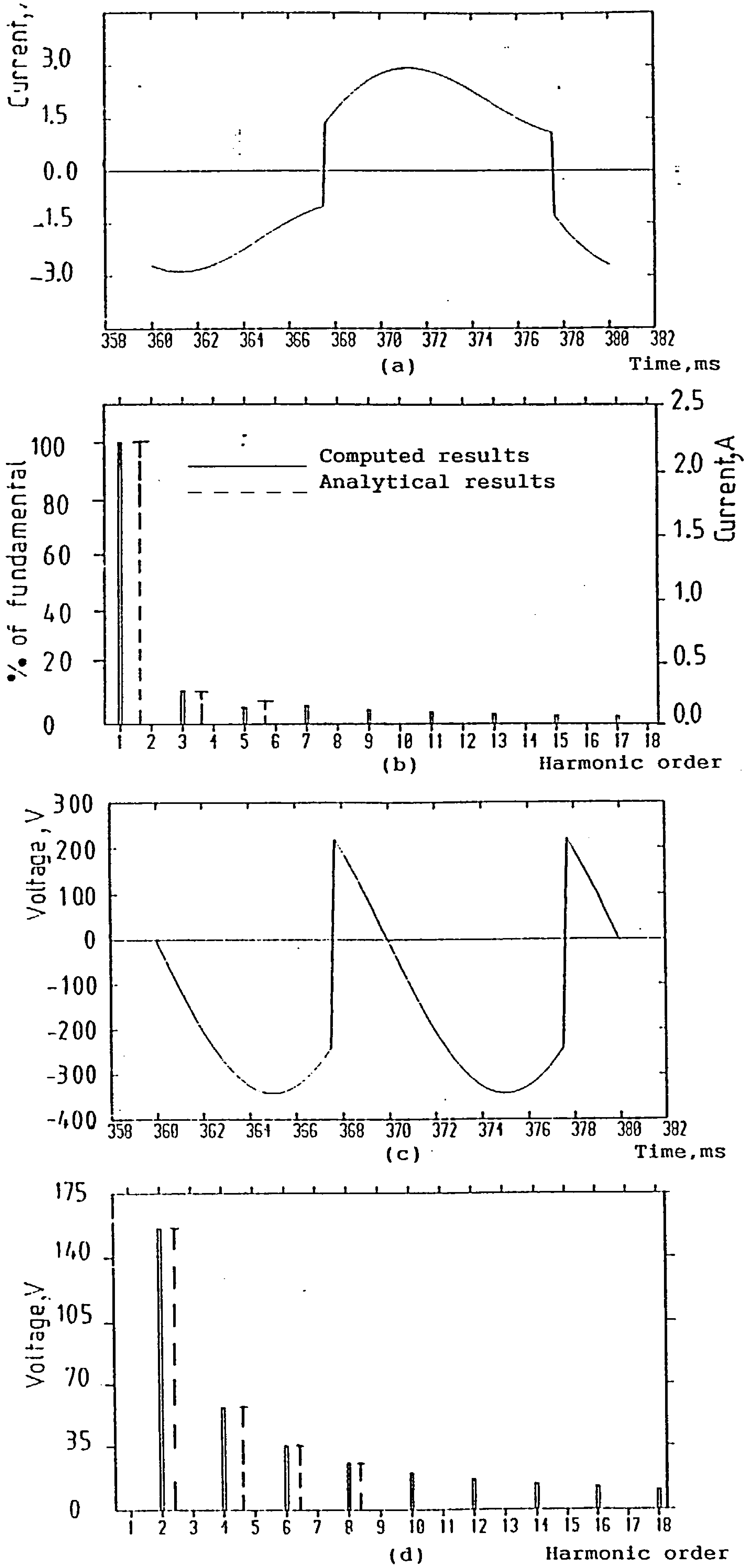

Figure5.17 Computed results for conventional controlled single-bridge converter.

(a),(b) Supply current and harmonic spectrum.

(c),(d) Load voltage and harmonic spectrum.

(α=135^{o},R_1=24Ω,L_1=0.3H,V_1=-150V,V_{dc}=200V)

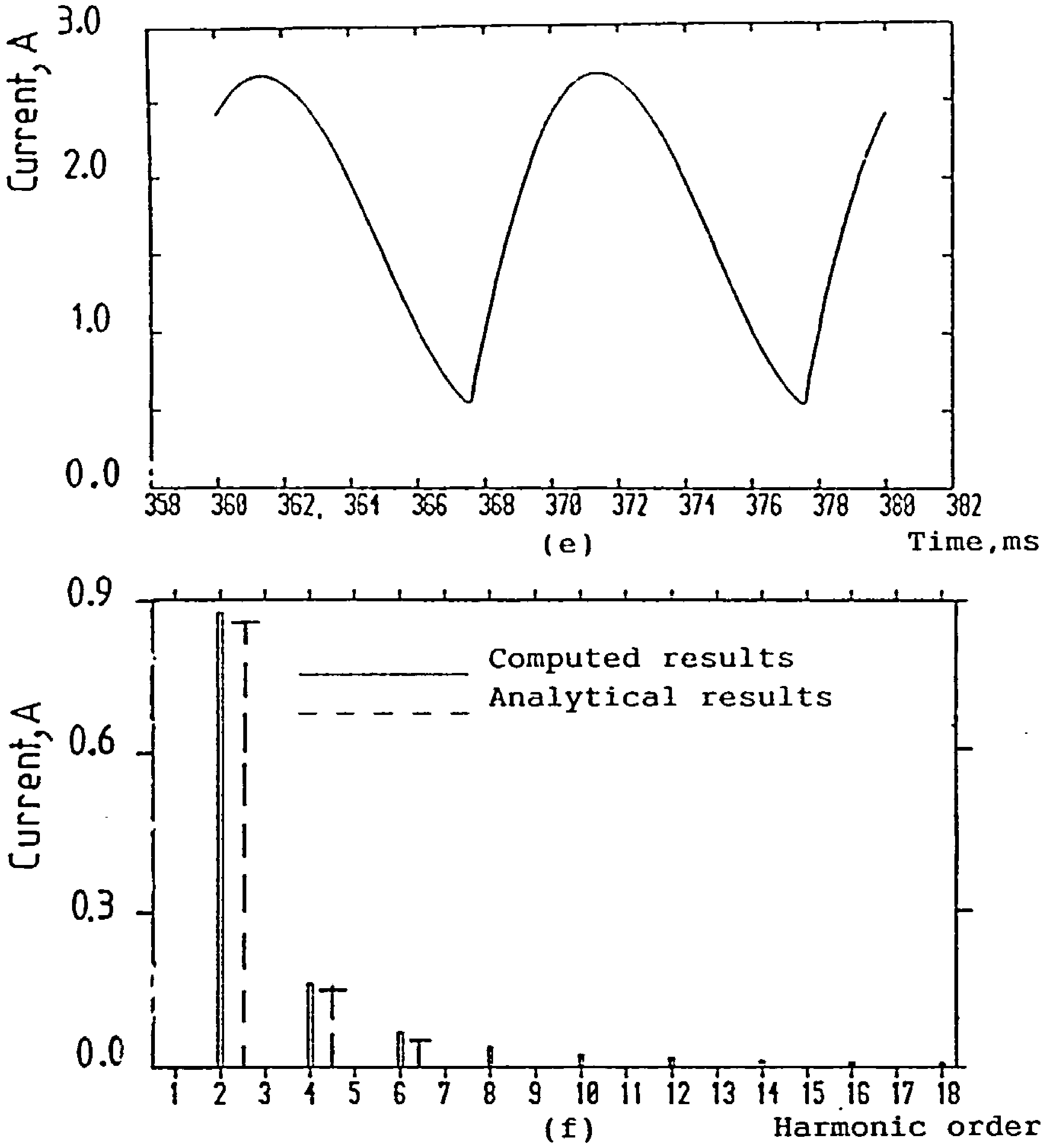

Figure5.17 Continued.
(e),(f) Load current and harmonic spectrum.

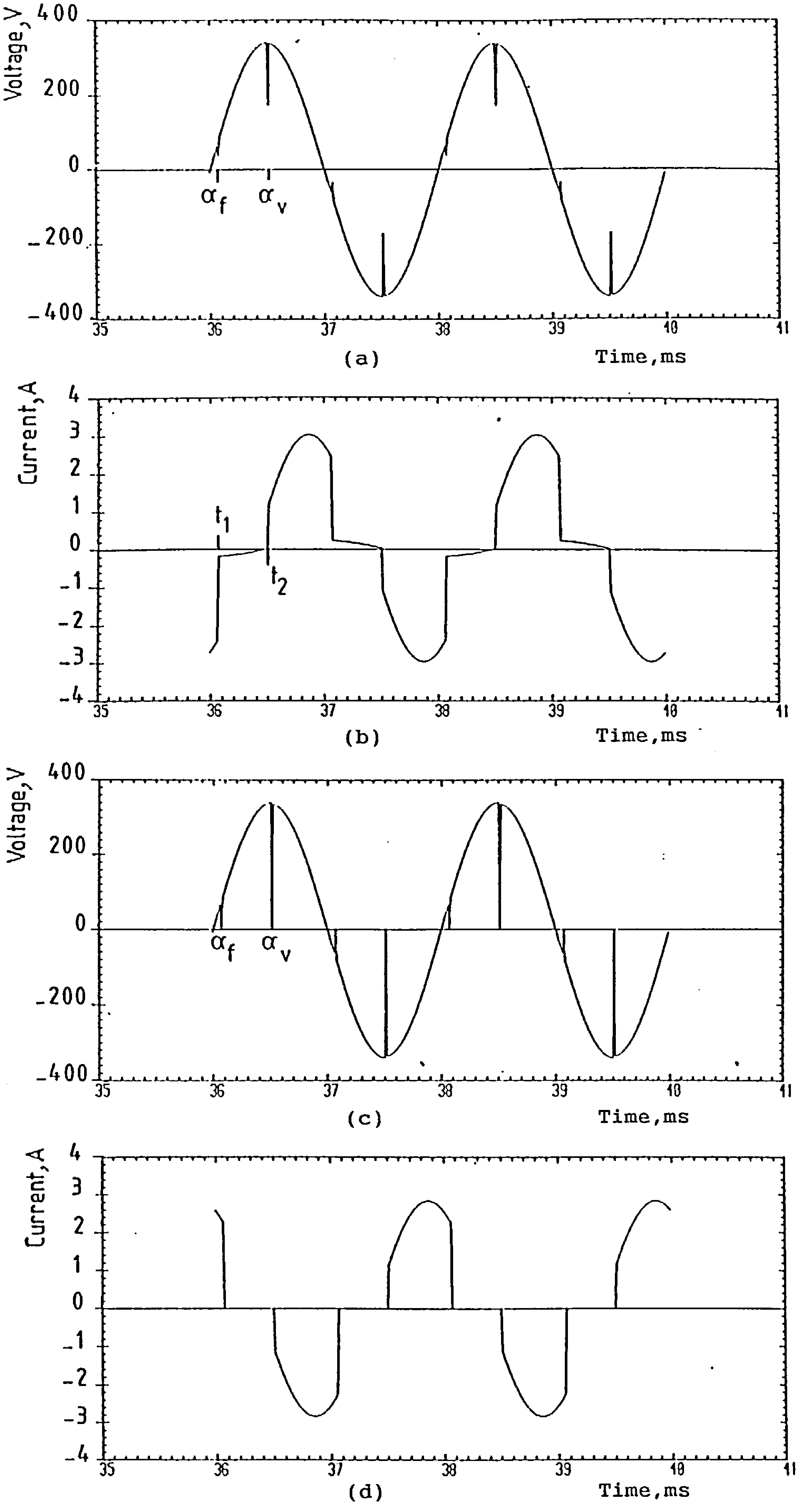

Figure5.18 Waveforms for sequence-controlled single-bridge converter.
(a),(b) Supply voltage and current.
(c),(d) Transformer secondary voltage and current.
($\alpha_f=10^o, \alpha_v=90^o, R_1=52\Omega, L_1=0.3H, V_1=104V$)

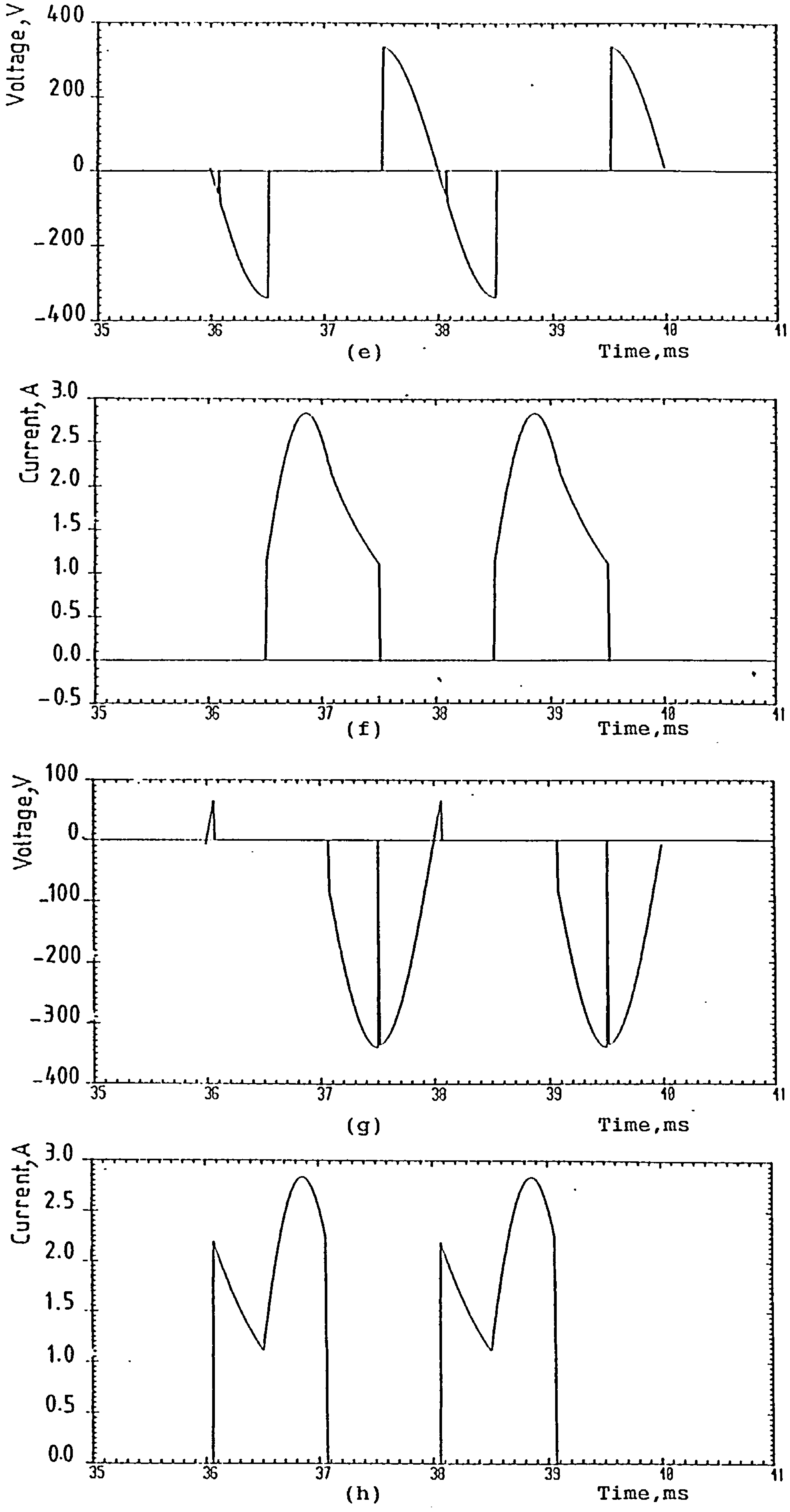

Figure5.18 Continued.

(e),(f) Voltage across and current through thyristor T_1.

(g),(h) Voltage across and current through thyristor T_2.

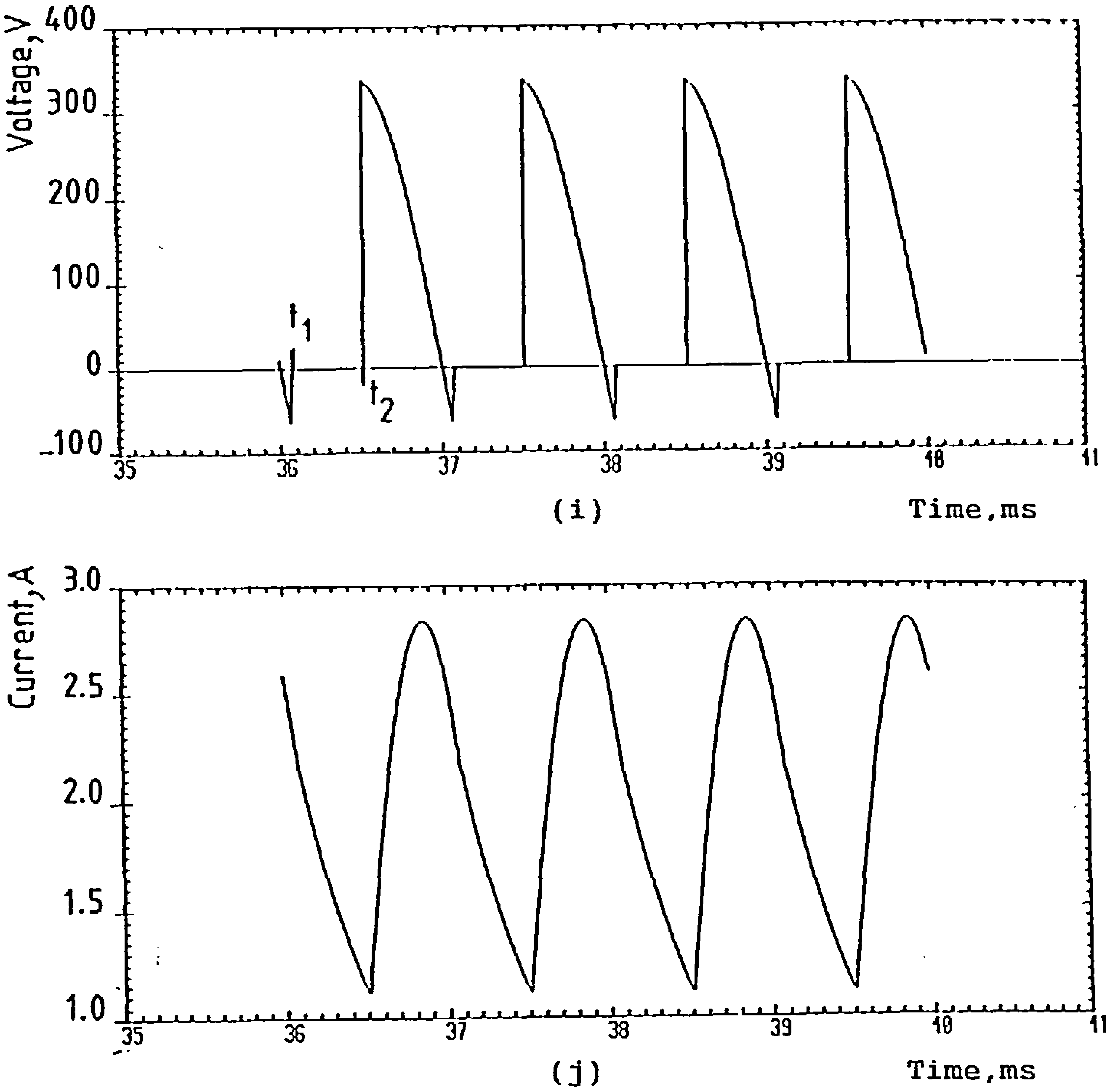

Figure5.18 Continued.
(i),(j) Load voltage and current.

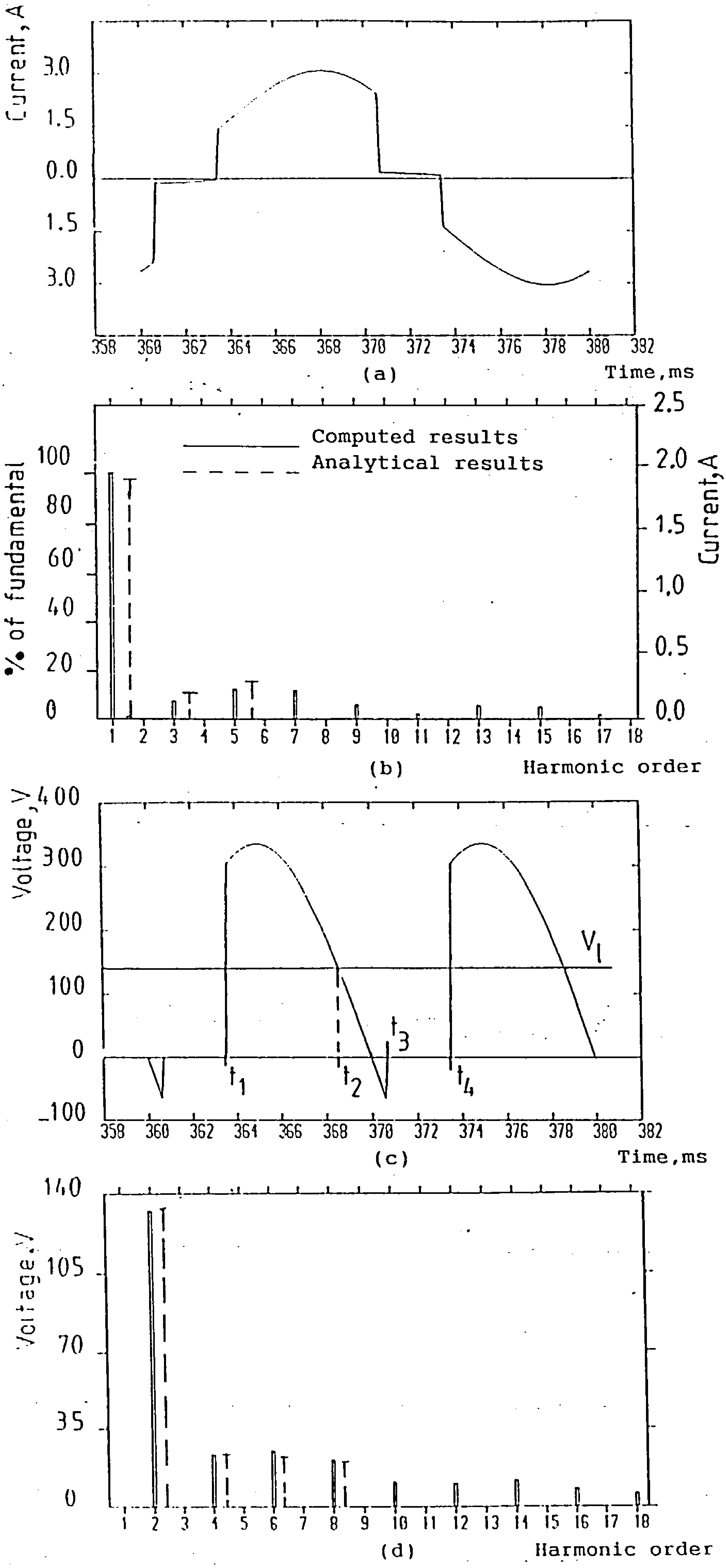

Figure5.19 Computed results for sequence-controlled single-bridge converter.
(a),(b) Supply current and harmonic spectrum.
(c),(d) Load voltage and harmonic spectrum.
($\alpha_f=10^o, \alpha_v=60^o, R_l=80\Omega, L_l=0.3H, V_l=160V$)

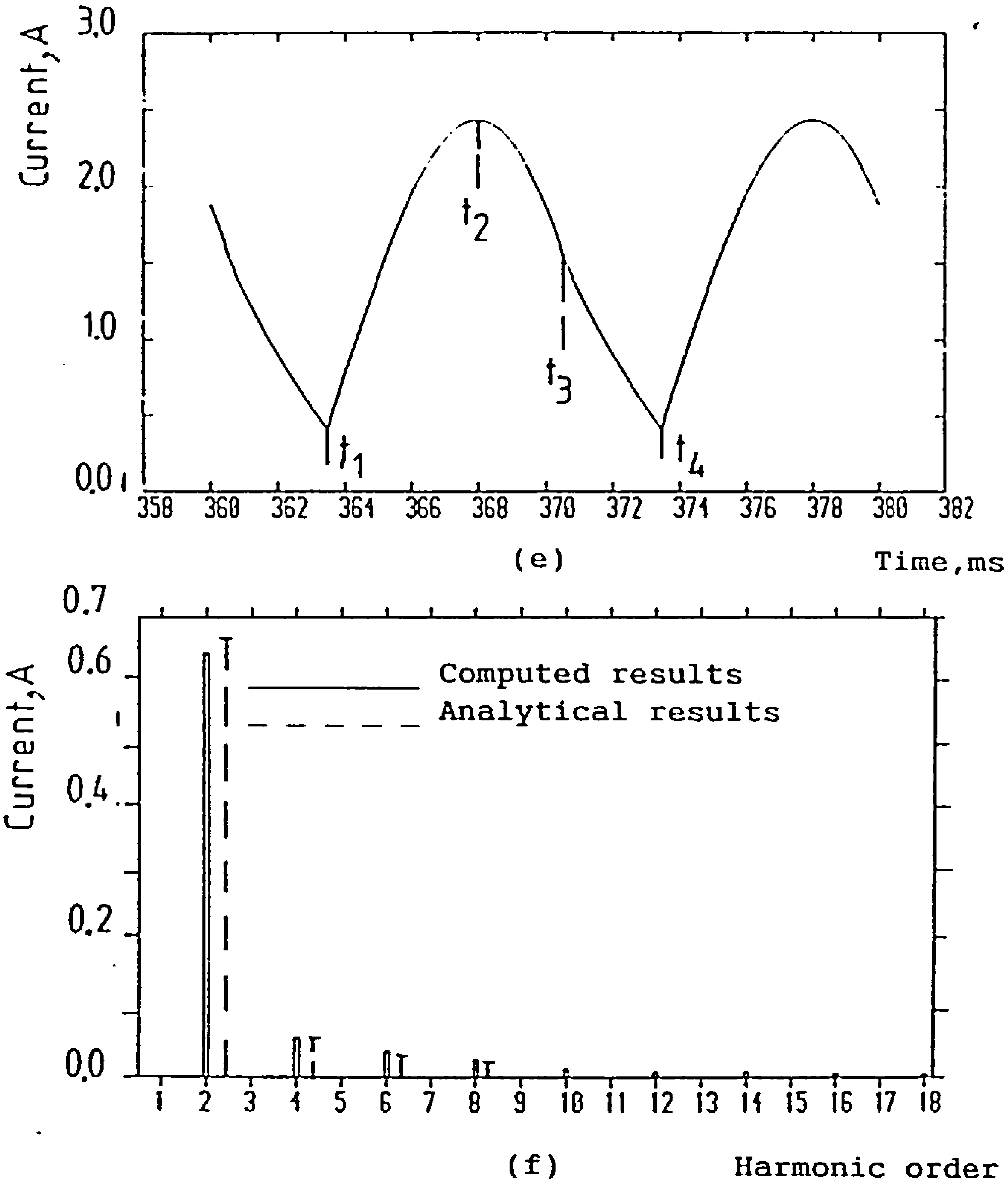

Figure5.19 Continued.
(e),(f) Load current and harmonic spectrum.

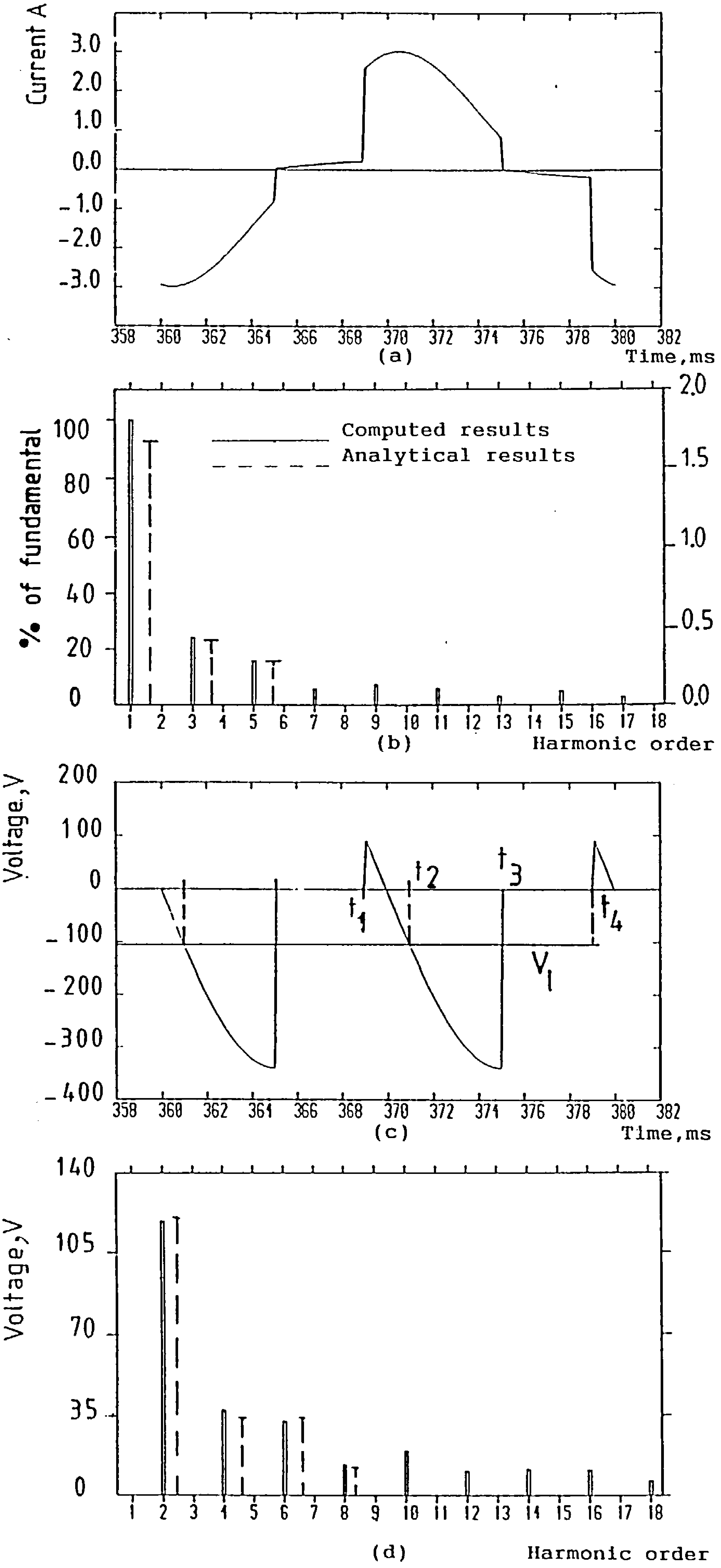

Figure5.20 Computed results for sequence-controlled single-bridge converter.
(a),(b) Supply current and harmonic spectrum.
(c),(d) Load voltage and harmonic spectrum.
($\alpha_f=90^\circ, \alpha_v=160^\circ, R_1=50\Omega, L_1=0.3H, V_1=-101V, V_{dc}=200V$)

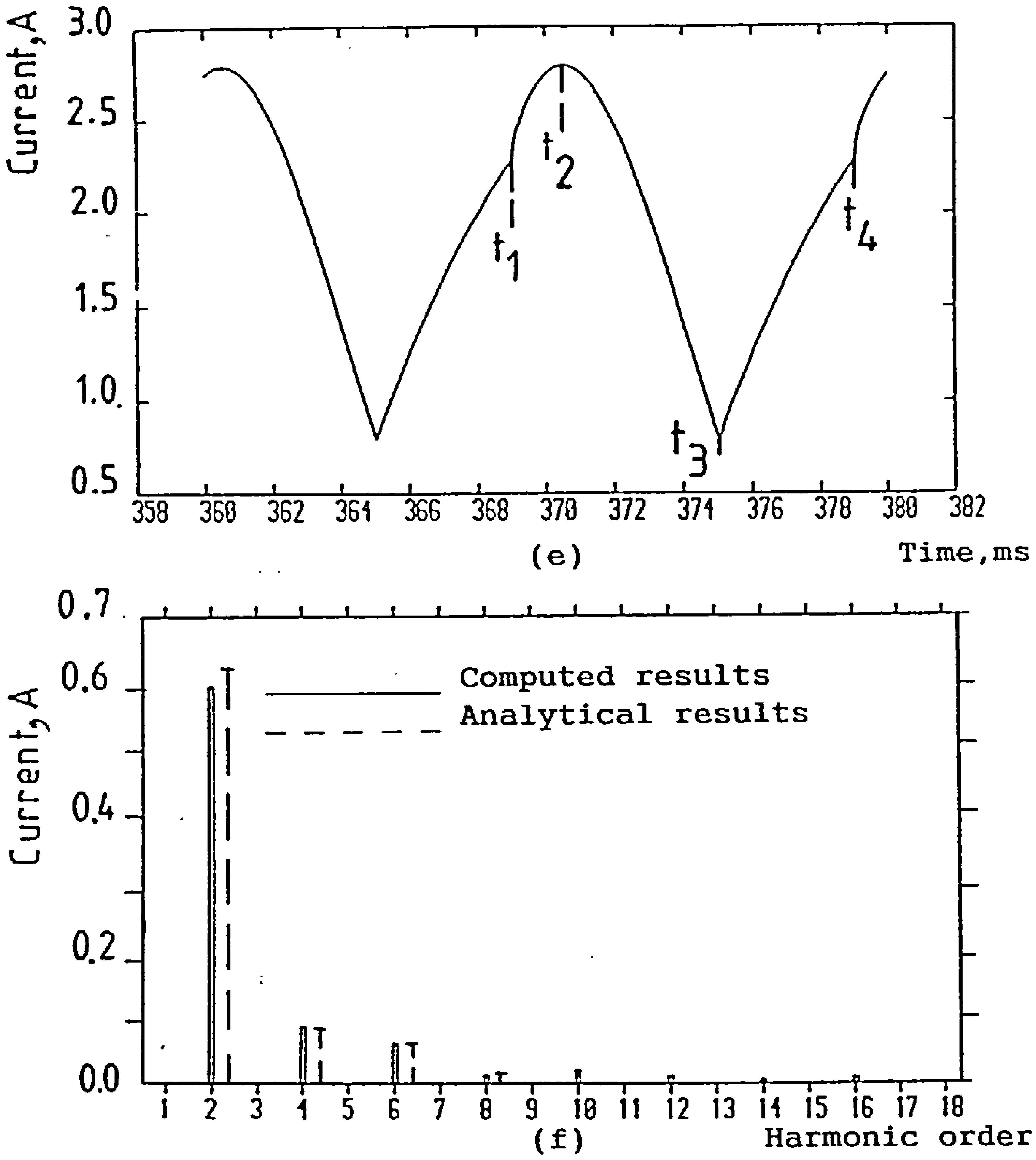

Figure5.20 Continued.
(e),(f) Load current and harmonic spectrum

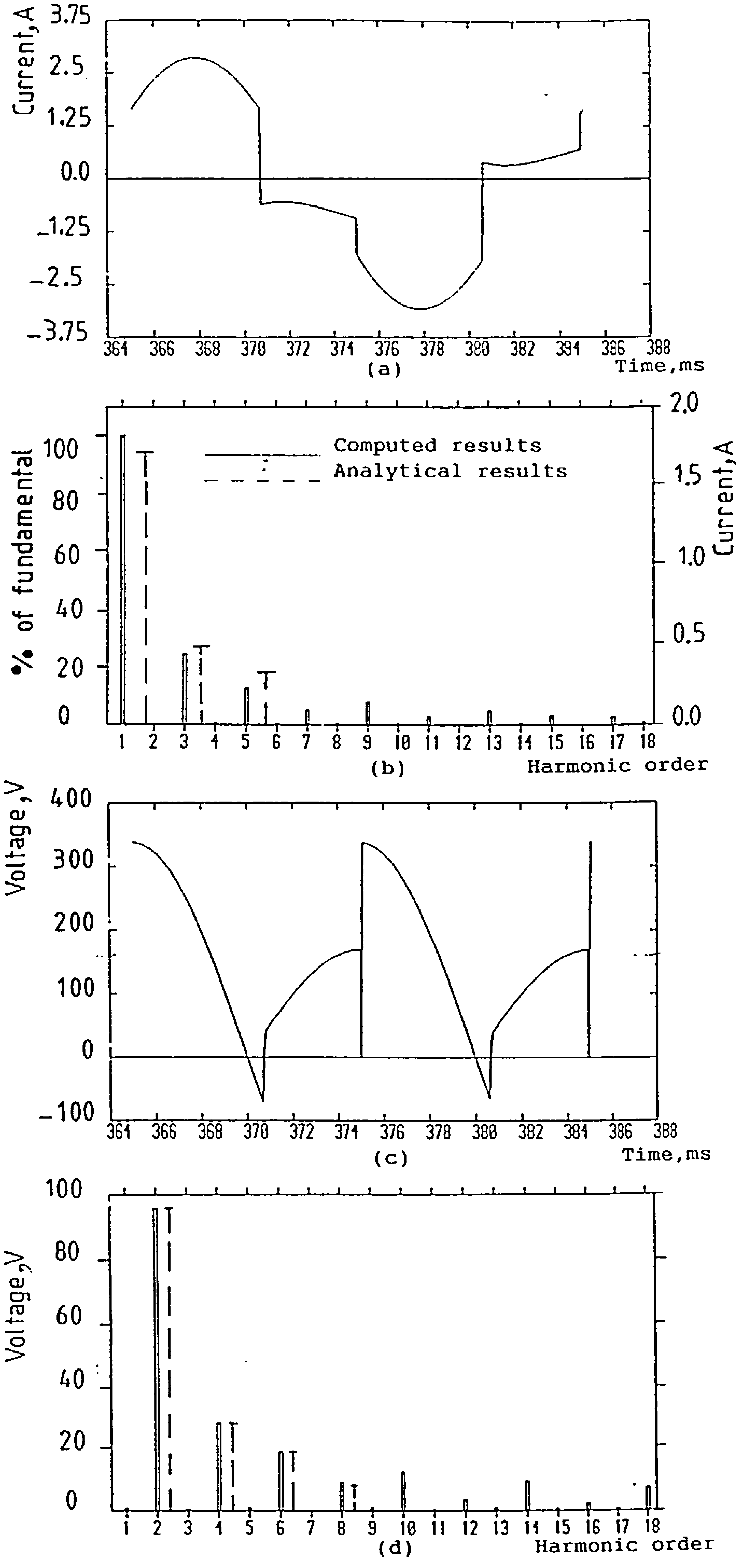

Figure5.21 Computed results for sequence-controlled double-bridge converter.
(a),(b) Supply current and harmonic spectrum.
(c),(d) Load voltage and harmonic spectrum.
($\alpha_{f1}=\alpha_{f2}=\alpha_{v2}=10^o,\alpha_{v1}=90^o,R_1=79\Omega,L_1=0.3H,V_1=158V$)

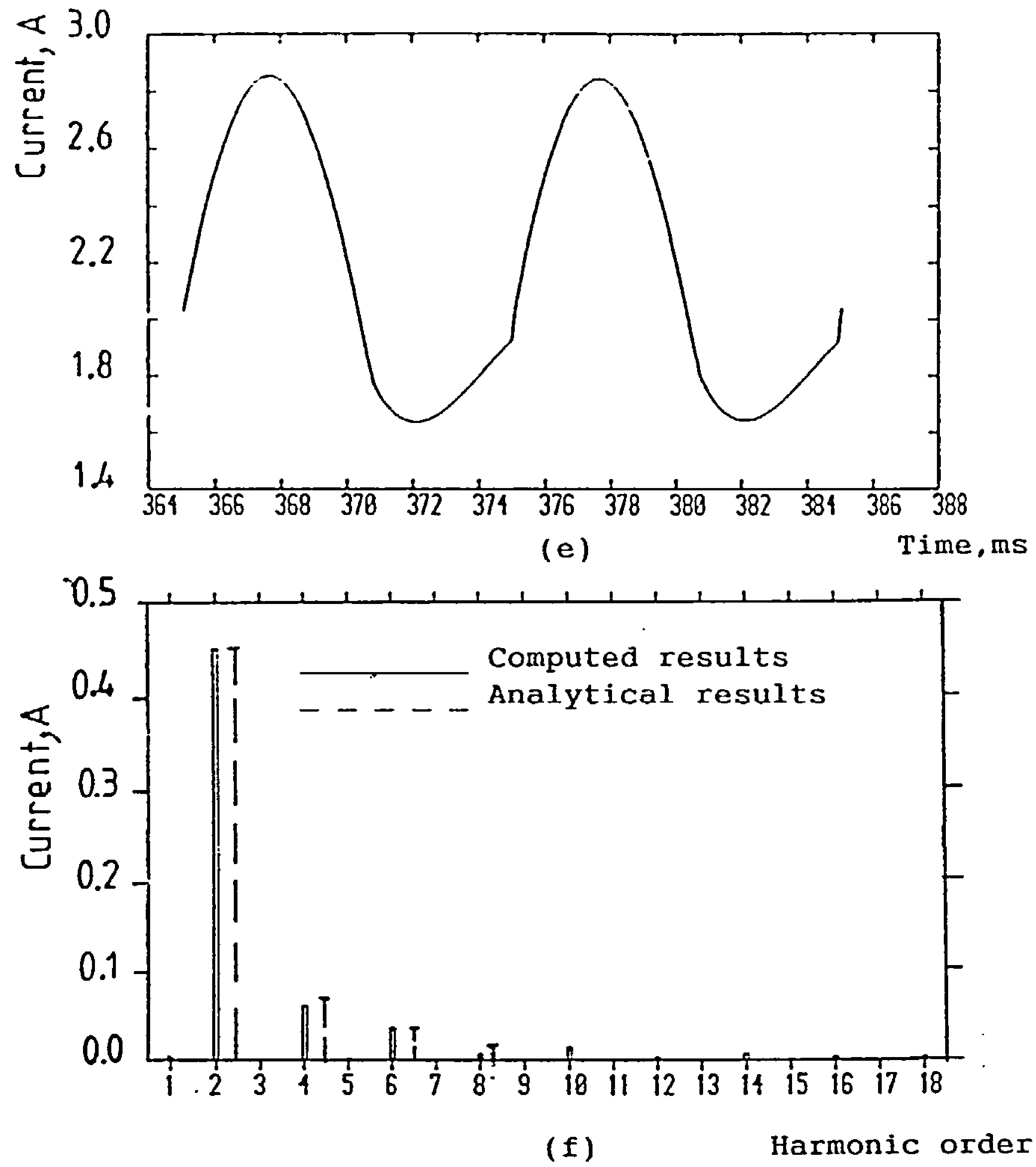

Figure5.21 Continued.
(e),(f) Load current and harmonic order.

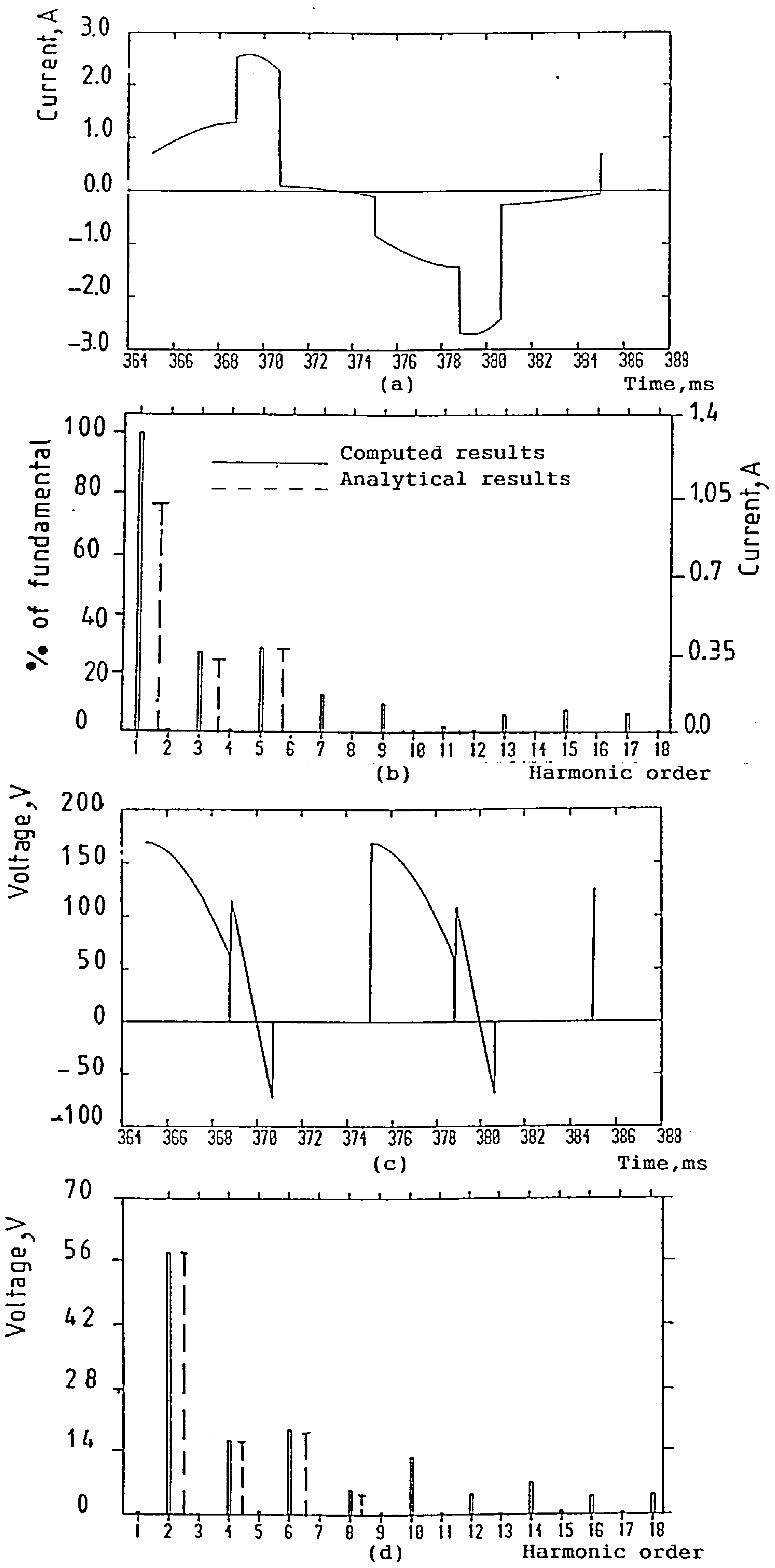

Figure5.22 Computed results for sequence-controlled double-bridge converter.
(a),(b) Supply current and harmonic spectrum.
(c),(d) Load voltage and harmonic spectrum.
($\alpha_{f1}=\alpha_{f2}=10^{o}, \alpha_{v1}=160^{o}, \alpha_{v2}=90^{o}, R_1=28\Omega, L_1=0.3H, V_1=55V$)

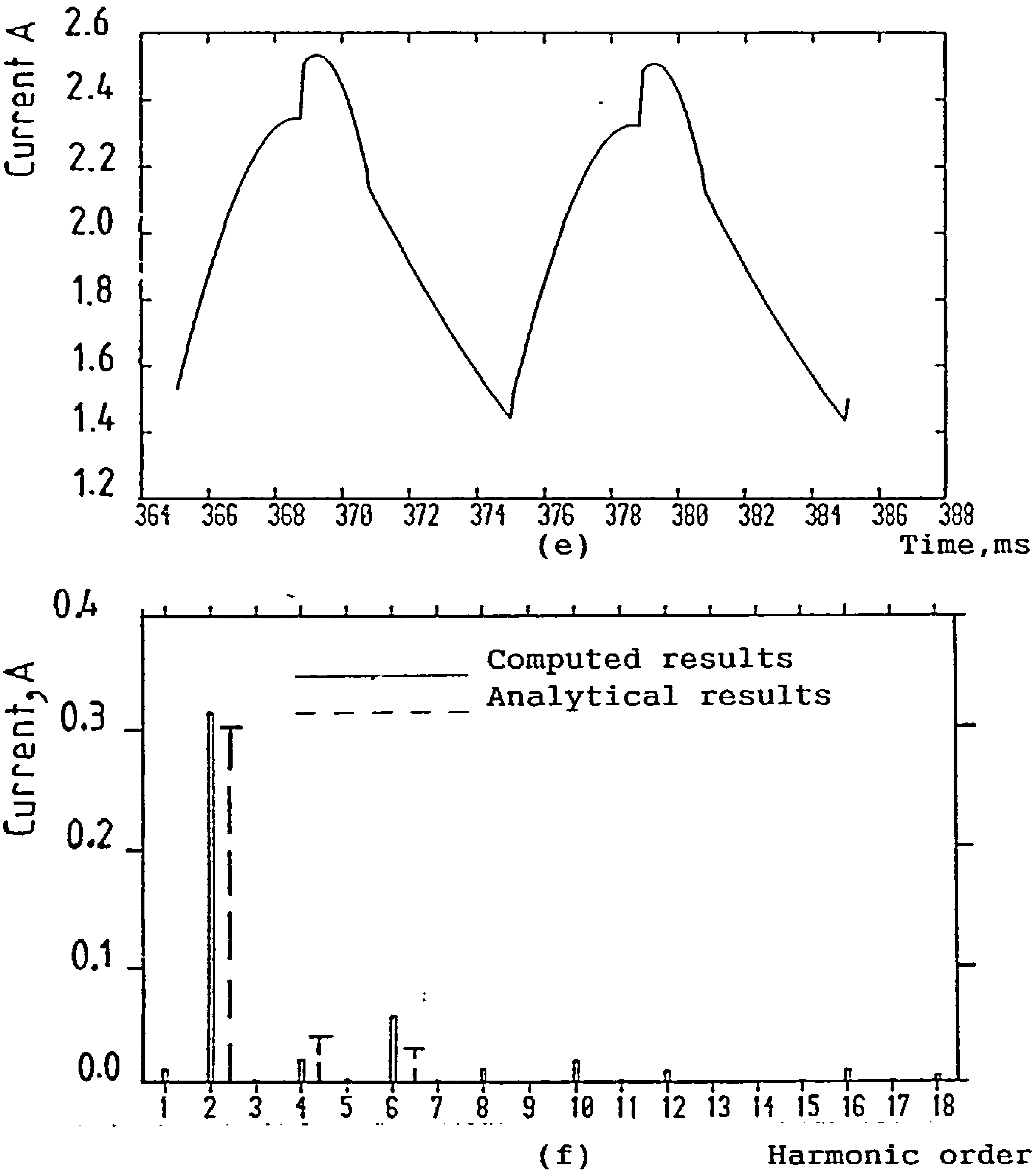

Figure5.22 Continued.
(e),(f) Load current and harmonic spectrum.

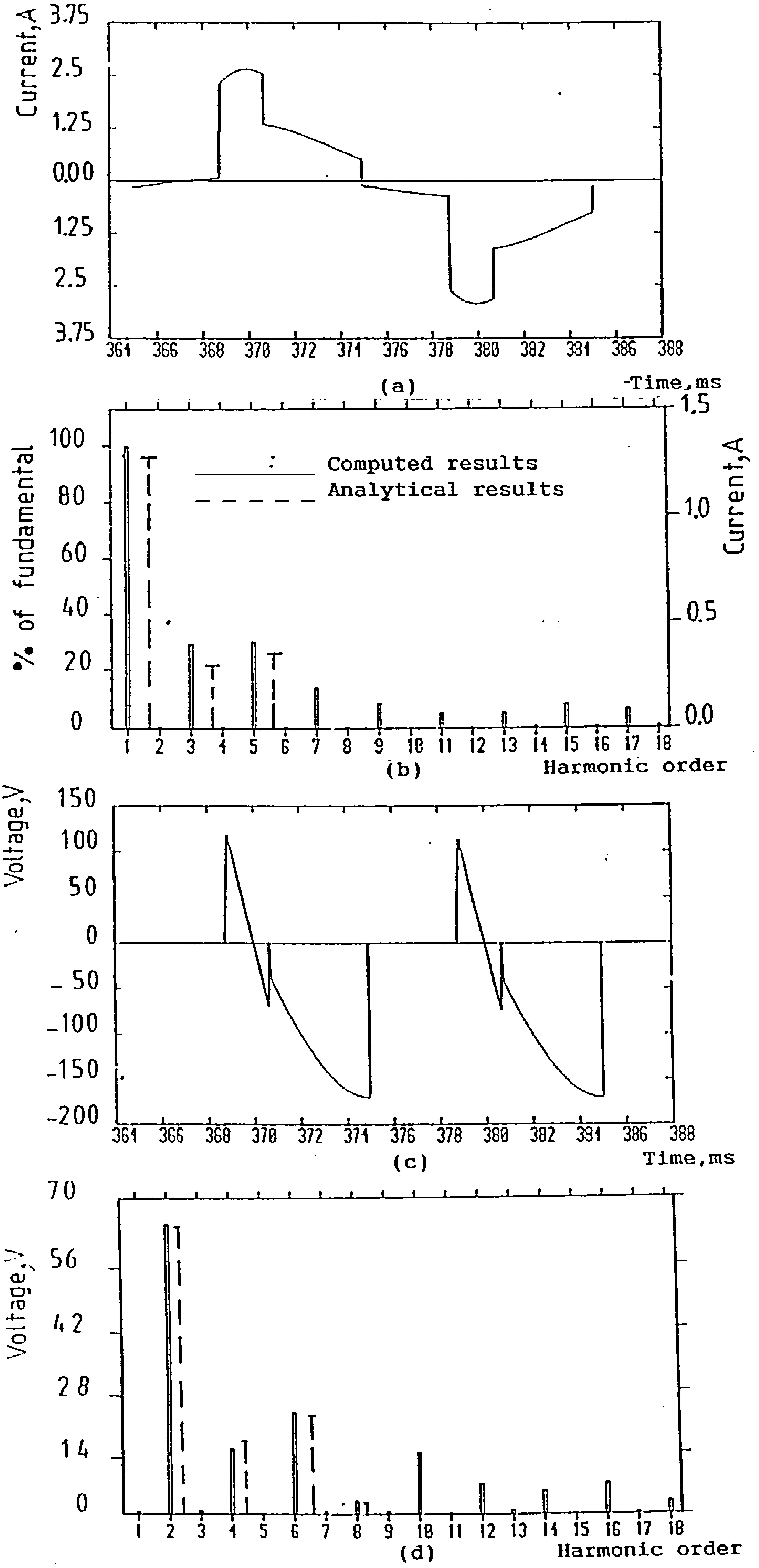

Figure5.23 Computed results for sequence-controlled double-bridge converter.
(a),(b) Supply current and harmonic spectrum.
(c),(d) Load voltage and harmonic spectrum.

($\alpha_{f1}=10^o, \alpha_{f2}=90^o, \alpha_{v1}=\alpha_{v2}=160^o, R_1=76\Omega, L_1=0.3H, V_1=-48V, V_{dc}=200V$)

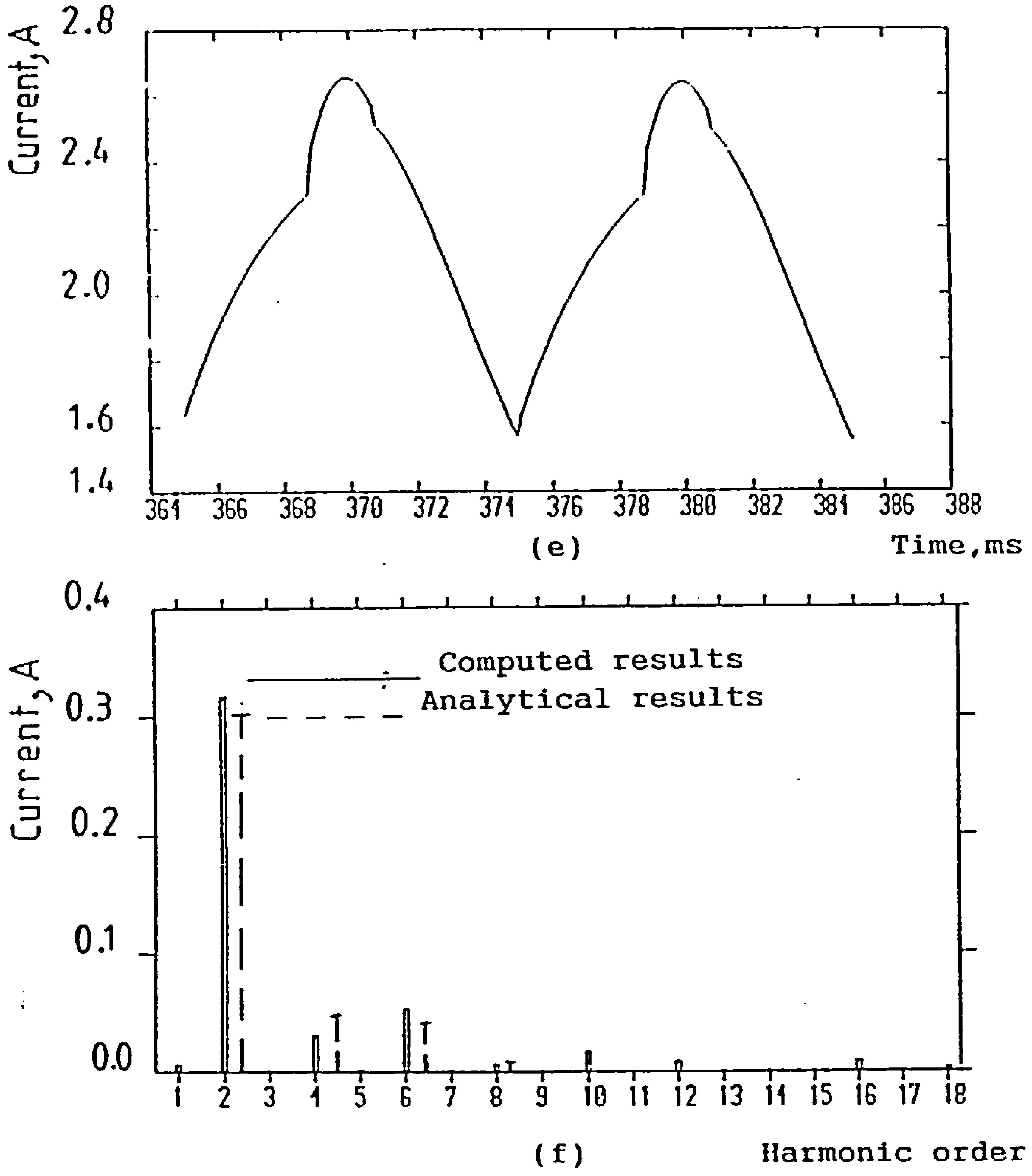

Figure5.23 Continued.
(e),(f) Load current and harmonic spectrum.

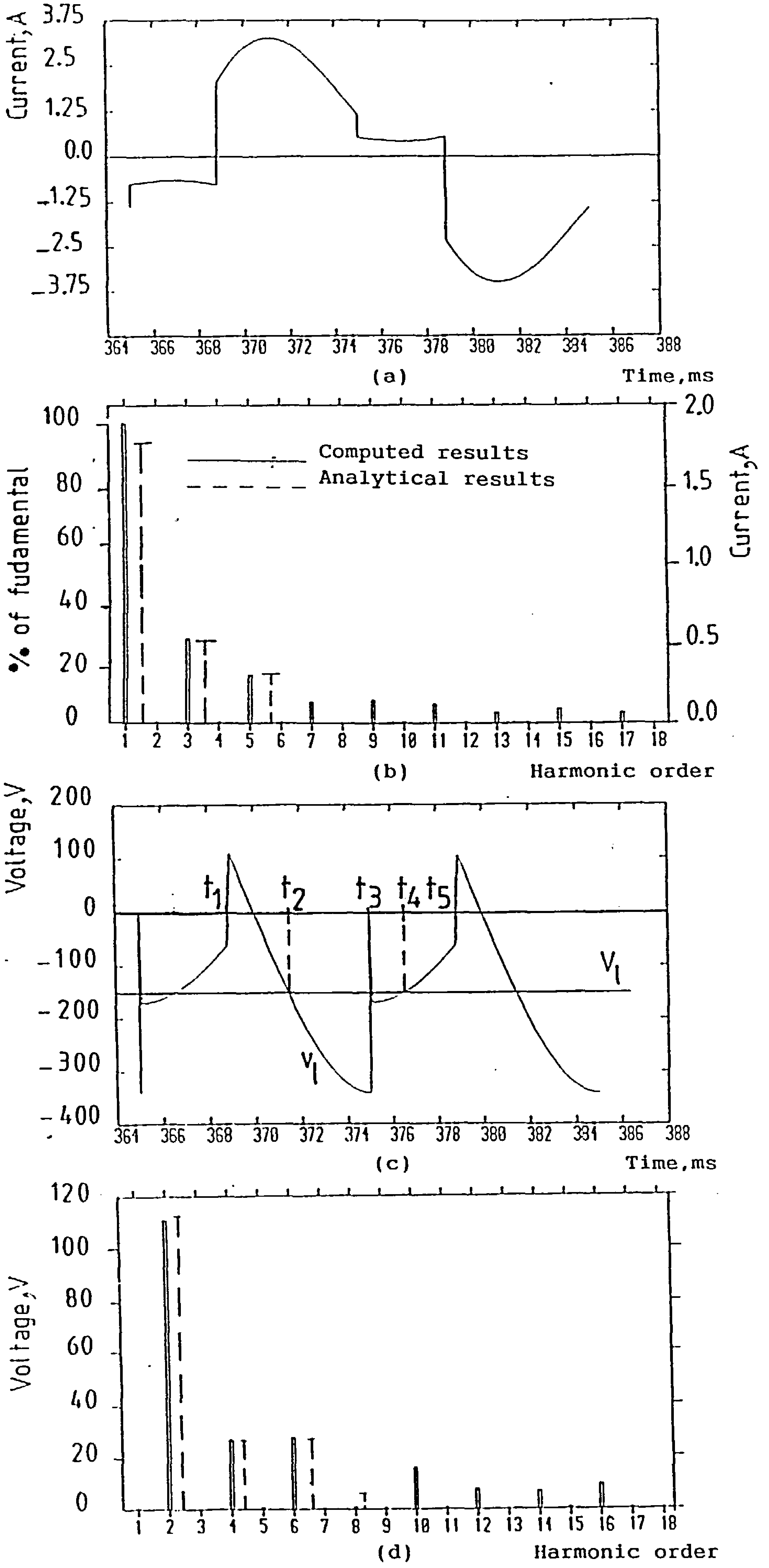

Figure5.24 Computed results for sequence-controlled double-bridge converter.

(a),(b) Supply current and harmonic spectrum.

(c),(d) Load voltage and harmonic spectrum.

($\alpha_{f1}=90^o, \alpha_{v1}=\alpha_{v2}=\alpha_{f2}=160^o, R_1=24\Omega, L_1=0.3H, V_1=-152V, V_{dc}=200V$)

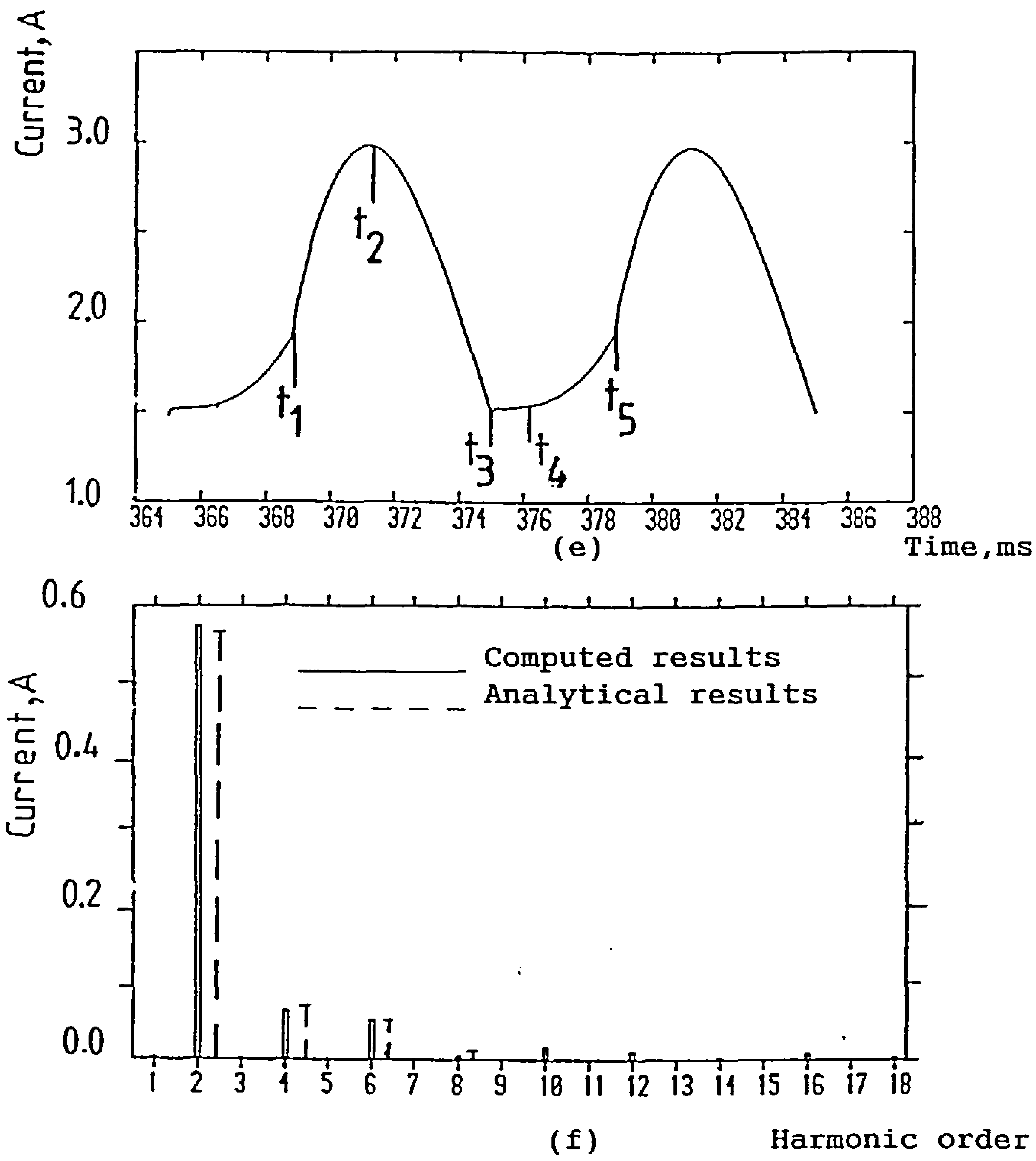

(e)

(f)

Figure5.24 Continued.
(e),(f) Load current and harmonic spectrum.

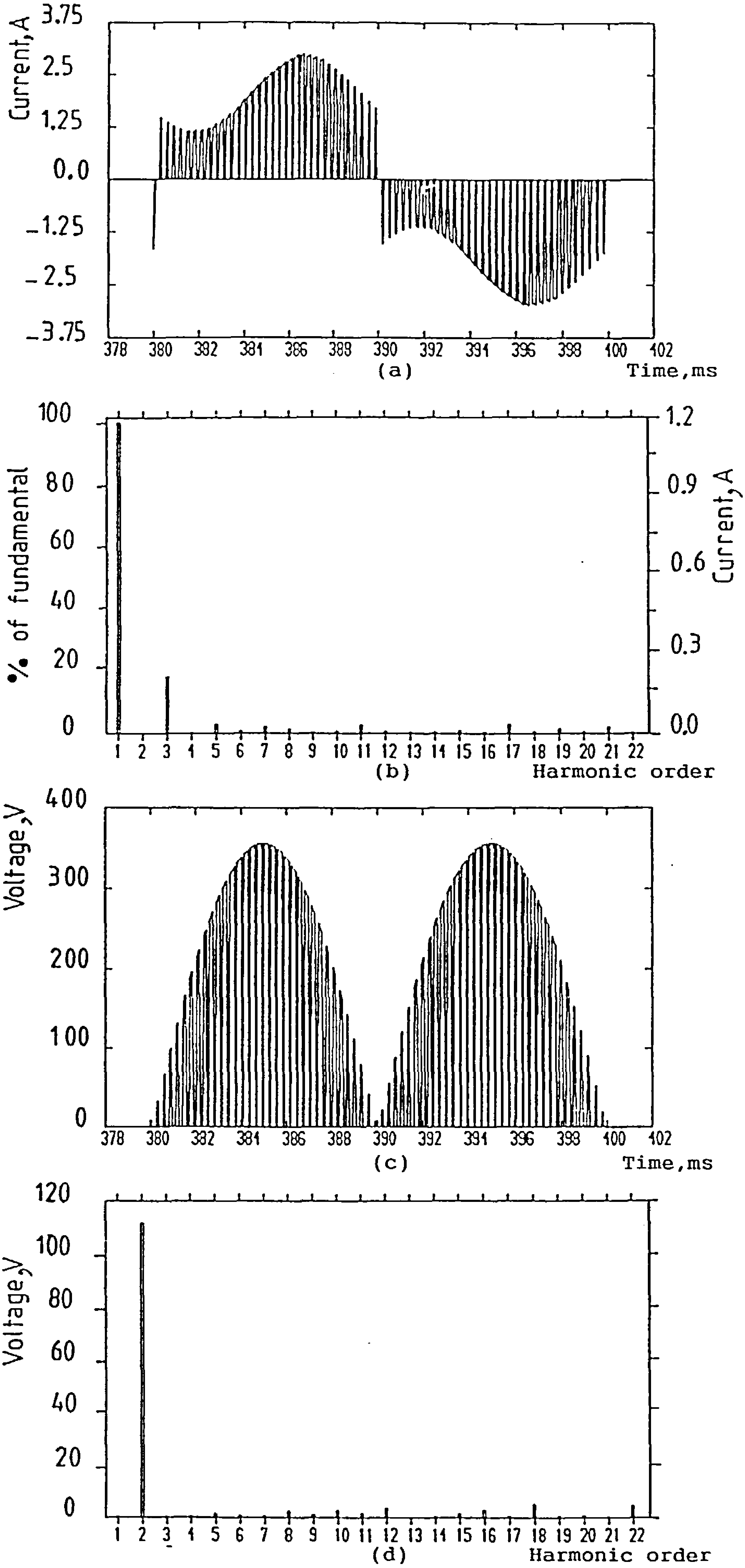

Figure5.25 Computed results for fully-controlled PWM bridge converter.
(a),(b) Supply current and harmonic spectrum.
(c),(d) Load voltage and harmonic spectrum.
($M=0.9, f_c=4kHz, R_l=77\Omega, L_l=0.3H, V_l=144V$)

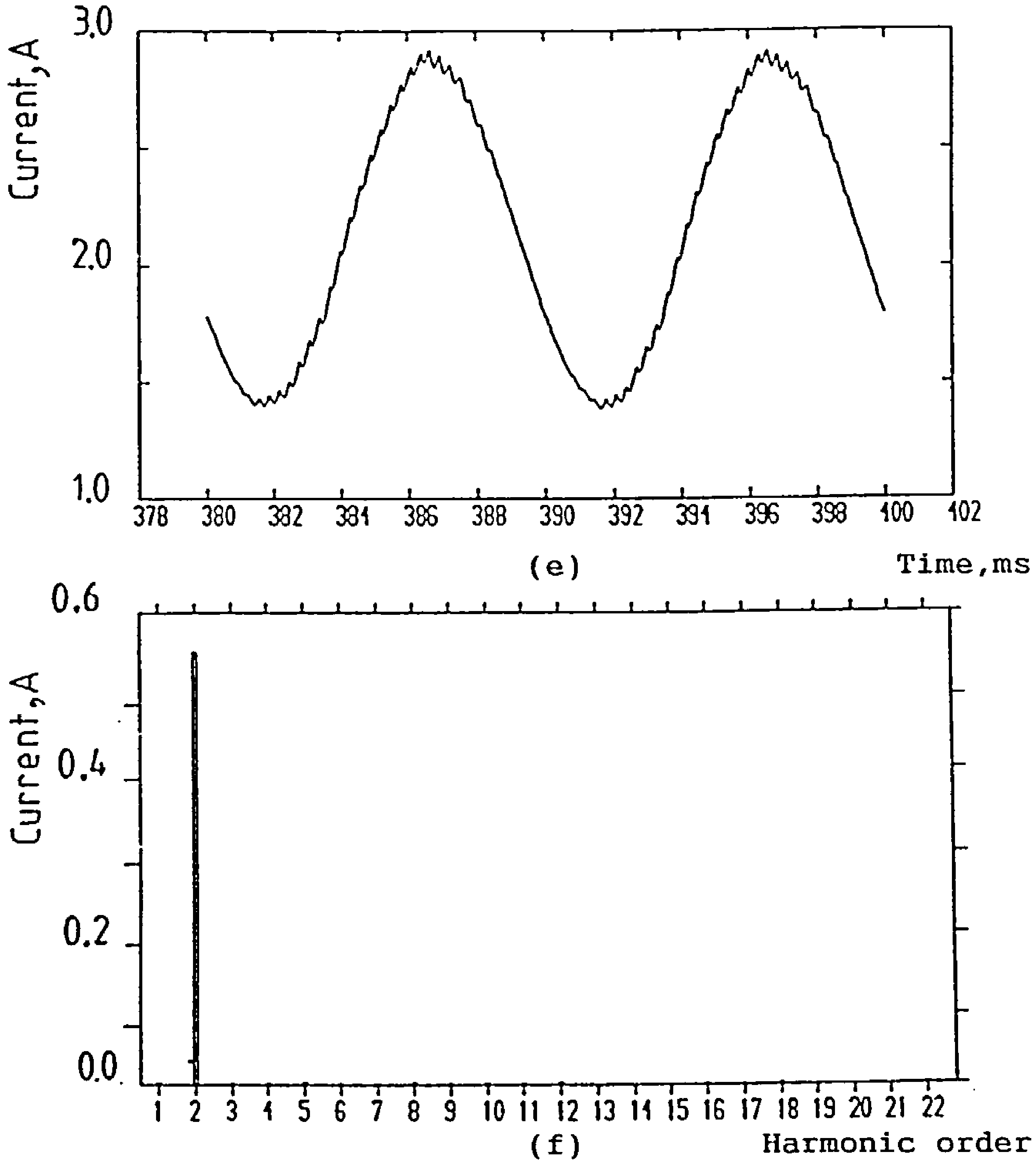

Figure5.25 Continued.
(e),(f) Load current and harmonic spectrum.

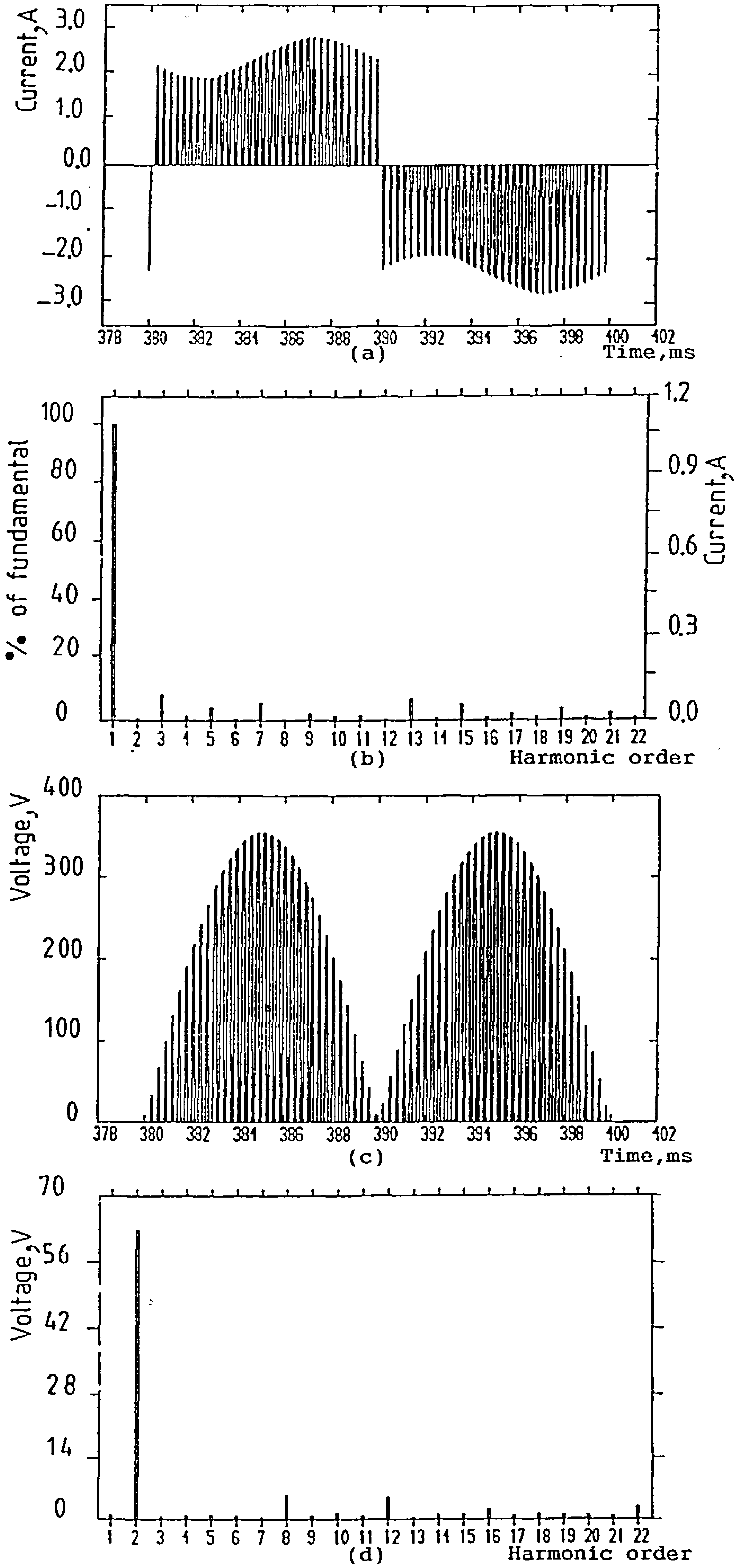

Figure5.26 Computed results for fully-controlled PWM bridge converter.
(a),(b) Supply current and harmonic spectrum.
(c),(d) Load voltage and harmonic spectrum.
($M=0.5, f_c=4kHz, R_l=47\Omega, L_l=0.3H, V_l=94V$)

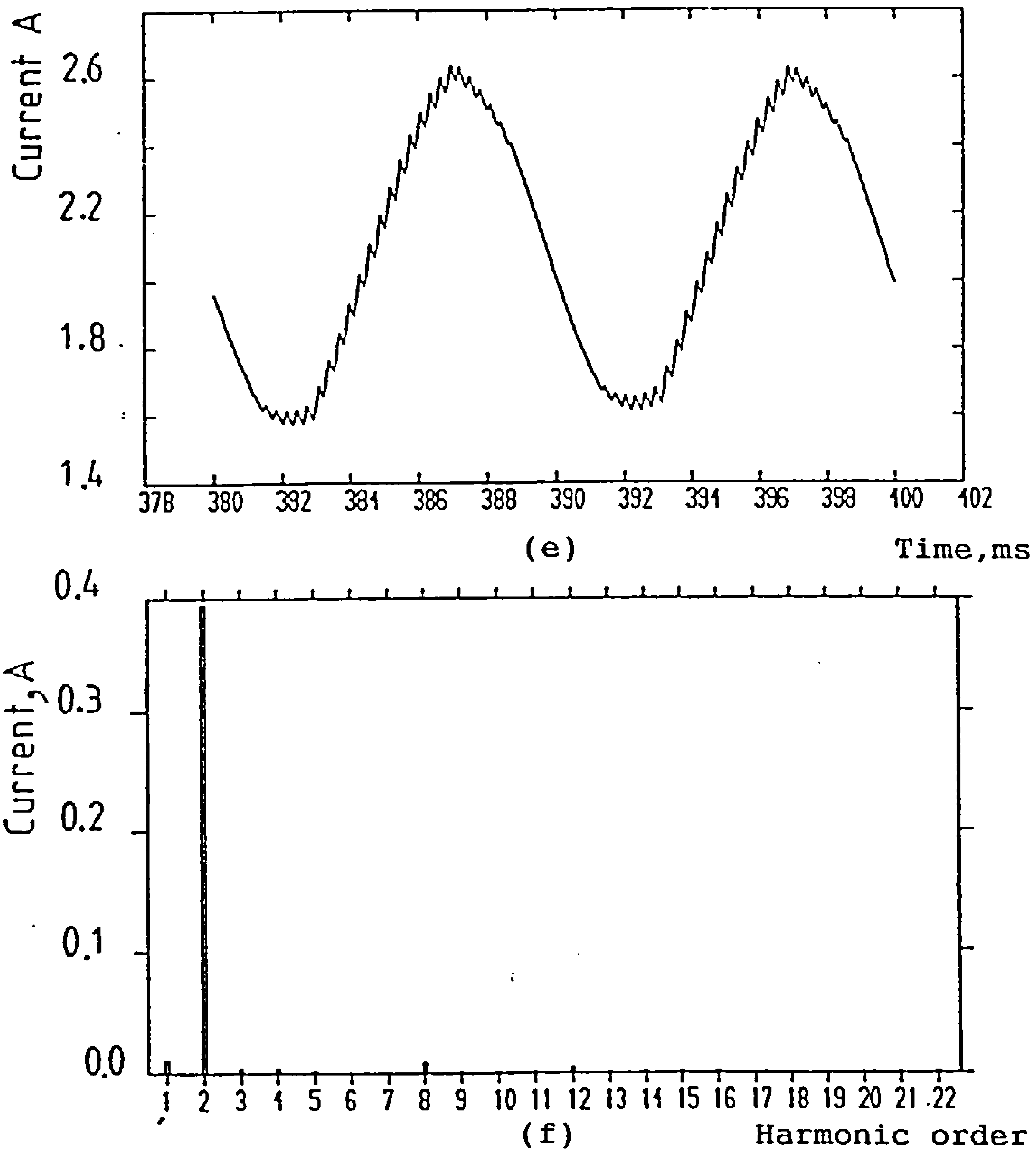

Figure5.26 Continued.
(e),(f) Load current and harmonic spectrum.

CHAPTER 6

Experimental Results For Various Converters

Experimental results relating to phase and PWM controllers are presented in sections 6.1 and 6.2. A single-bridge converter, operating under both conventional and sequence control, and a double-bridge under sequence control are considered for the phase controller and a single bridge for the PWM controller. Results are presented for both rectification and inversion modes, with a comparison between different controllers being made in section 6.3.

6.1 Phase Controllers

Circuit diagrams for the experimental single and double-bridge converters are shown respectively in figures 6.1 and 6.2, where W_1 to W_4 represent wattmeters. The supply was 240V, 50Hz and the load comprised a 0.3H inductor L_1 in series with a variable resistor R_1, and a variable dc voltage source V_{dc}, obtained from a motor-generator set. The load current I_1 was maintained constant at 2A for a wide range of different firing delay angles, by changing R_1 and V_{dc}. Power measurements were taken for different controllers and, from these, the experimental input power factor and efficiency were calculated from:

$$P.F = \frac{W_1}{V_s I_s} \qquad (6.1)$$

where V_s and I_s are the r.m.s. supply voltage and current respectively and

$$\eta = \frac{\text{Output Power}}{\text{Input Power}} \times 100 \qquad (6.2)$$

The experimental power factor calculated from equation 6.1

includes the transformer no-load current, a large part of which is due to the iron losses which are 34W at 240V as measured from the no-load test. It is therefore important to include these effects in the analytical model and this is achieved by adding the excitation current of the transformer to the analytical supply current developed in chapter 5. Neglecting the harmonics of the excitation current, the r.m.s. value of the fundamental component was measured from the no-load test as 0.2A, with a lagging phase angle of 45°, which gives:

$$i_{1e}=0.2\times\sqrt{2}\sin(\omega t - 45^{o}) \qquad (6.3)$$

where i_{1e} is the instantaneous value of the fundamental component of the excitation current.

The equation for the fundamental component of the supply current i_1 is:

$$i_1 = A_1 \cos \omega t + B_1 \sin \omega t \qquad (6.4)$$

where A_1 and B_1 are the Fourier coefficients as defined by equations 5.34 and 5.35 of chapter 5.

Adding equation 6.3 to 6.4 gives:

$$i_{1s} = (A_1-0.2)\cos \omega t + (B_1+0.2) \sin \omega t \qquad (6.5)$$

which is equivalent to

$$i_{1s} = \sqrt{2}\, I_{1s} \sin(\omega t+\phi_{1s}) \qquad (6.6)$$

where I_{1s} is the r.m.s. value of the fundamental component plus the excitation current and ϕ_{1s} is its phase displacement angle given by the following equations:

$$I_{1s} = \sqrt{\frac{(A_1-0.2)^2 + (B_1+0.2)^2}{2}} \qquad (6.7)$$

$$\phi_{1s} = \arctan \frac{A_1 - 0.2}{B_1 + 0.2} \tag{6.8}$$

The analytical power factors were calculated on the assumption that the supply voltage is sinusoidal and no power is associated with the harmonic supply current, hence the input power W_1 is,

$$W_1 = V_s I_{1s} \cos \phi_{1s} \tag{6.9}$$

substituting equation 6.9 into 6.1 gives,

$$P.F = \frac{I_{1s}}{I_s} \cos \phi_{1s} \tag{6.10}$$

in which $\frac{I_{1s}}{I_s}$ is defined as the input distortion factor and $\cos\phi_1$ as the input displacement factor.

Since fundamental, 3rd and 5th harmonic components of the supply current were considered in the analytical model, the r.m.s. value of the supply current I_s is

$$I_s = \sqrt{I_{1s}^2 + I_3^2 + I_5^2} \tag{6.11}$$

where I_3 and I_5 are the r.m.s. values of the 3rd and 5th components of the supply current.

The analytical power factors were calculated using equation 6.10 together with equations 6.7, 6.8 and 6.11. The analytical and experimental power factors are then plotted against output voltage for different controllers as shown later in this chapter.

Other results presented in this chapter are the experimental circuit waveforms and their harmonic spectra, together with analytical predictions based on the model developed in Appendix A2 and chapter 5.

6.1.1 Conventional Controlled Single-bridge

The rectifier of figure 6.1 was operated conventionally, by making the firing delay angles α_v and α_f equal ($\alpha_v=\alpha_f=\alpha$(say)). Voltage and current waveforms together with their harmonic spectra, for delay angles of 10^o,90^o and 160^o, are presented in figures 6.3, 6.4 and 6.5. The commutation notches evident in the transformer secondary voltage of figure 6.3(a) are located at the delay angles α_f and α_v. The separation of the notches indicates a slight imbalance between the two delay angles, which accounts for the zero intervals on the transformer secondary current and load voltage of figure 6.3(a) and (c). The load voltage of figures 6.3(c), 6.4(c) and 6.5(c) contains a dc component plus even harmonics whose magnitudes decrease with increasing harmonic order as shown in figures 6.3(d), 6.4(d) and 6.5(d), which also indicate that the 2nd harmonic is predominant. Comparison of figures 6.3(d), 6.4(d) and 6.5(d) indicates that the load voltage harmonics are a maximum at $\alpha=90^o$, which is also confirmed by the graphs of figure 2.11 of Chapter 2. These voltage harmonics produce load current harmonics of the same frequency as those in figures 6.3(e), 6.4(e) and 6.5(e). Addition of the harmonics determines the peak-to-peak load current ripple and since the load current harmonics of figure 6.4(e) are a maximum, so too is the corresponding load current ripple of figure 6.4(c). Power measurements for different firing delay angles are shown in table 6.1 and from these readings experimental input power factors are calculated using equation 6.1. The analytical power factors on the assumption that the supply voltage is sinusoidal are calculated using equation 6.3 for different firing delay angles. The analytical and experimental variation of power factor with load voltage is shown in figure 6.6 which also indicates that there is a slight discrepancy between the two when the converter operates in the inversion mode. From the results of table 6.1, it is evident that the predominant losses occur in the transformer.

Firing Angle α^{o}	V_1 V	I_s r.m.s. A	W_1 W	W_2 W	W_3 W	Power Factor	Effic. η %	Trans. Loss W	Bridge Loss W	E_b V
RECTIFICATION										
10	212	2.50	541	500	480	0.90	89	41	20	2
36	176	2.45	460	420	410	- 0.78	89	40	10	24
54	132	2.45	376	340	320	0.64	85	36	20	67
72	70	2.52	278	240	220	0.46	79	38	20	132
90	8	2.51	157	120	100	0.26	64	37	20	192
INVERSION										
108	-62	2.47	2.0	-40	-50	0.004	4	38	10	228
126	-128	2.45	-170	-200	-220	-0.29	77	30	20	228
144	-178	2.37	-312	-350	-362	-0.54	86	38	12	228
160	-208	2.27	-382	-420	-440	-0.70	87	38	20	225

Table 6.1 Power measurements for conventional controlled single-bridge.

6.1.2 Sequence Controlled Single-bridge

Voltage and current waveforms, together with their harmonic spectra for different operating conditions, are shown in figures 6.7, 6.8 and 6.9 for both rectification and inversion. The waveform of the transformer secondary current in figure 6.7(a) is explained by consideration of the firing pattern of the thyristors. Thus, when thyristors T_1, T_2 or T_3, T_4 commence conduction at a firing delay angle α_v, the load is connected to the supply and $i_{sec}=i_1$ in the positive half cycle and $i_{sec}=-i_1$ in the negative half-cycle of the transformer secondary voltage. When T_1, T_4 or T_3, T_2 conduct at α_f, the converter is free-wheeling and $i_{sec}=0$. The load voltage harmonics of figure 6.7(c) and 6.9(c) are the same, as verified by comparing figures 6.7(d) and 6.9(d); consequently the peak-to-peak load current ripples of figure 6.7(c) and 6.9(c) should also be the same if the load conditions were the same. However, the peak-to-peak load current ripple of figure 6.7(c) was measured as 1.3A and that of figure 6.9(c) as 1.6A. The difference of 0.3A between these two results is due to a change in load resistance which was varied from 100Ω to 58Ω and consequently a reduction in the harmonic load impedance and an increase in the load current ripple. The mean load voltage of figure 6.7(c) is zero, as is evident from the voltage spectrum of figure 6.7(d) where the dc component, which represents the mean voltage, is zero. The amplitude of the voltage harmonics and consequently their corresponding load current harmonics are negligible, as shown in figure 6.7(e). Consequently, there will be no ac ripple superimposed on the load current, as confirmed by figure 6.7(c).

The analytical and practical variations of the commutation angle with firing delay angle α_v, for a constant 2A load current are given in figure 6.10. The discrepancy between the two results is due to the voltage-drop across the thyristors reducing the commutation voltage and thereby increasing the commutation angle. Power measurements for different firing delay angles given in table 6.2 indicate that the predominant losses again occur in the transformer. The experimental and

RECTIFICATION										
Firing Angle $\alpha_v{}^o$	V_1 V	I_s r.m.s. A	W_1 W	W_2 W	W_3 W	Power Factor	Effic. η %	Trans. Loss W	Bridge Loss W	E_b V
10	212	2.50	541	500	480	0.90	89	41	20	2
36	196	2.33	480	440	420	0.85	87	40	20	2
54	172	2.32	441	410	380	0.79	86	31	30	27
72	140	2.23	371	340	320	0.69	86	31	20	58
90	108	2.11	298	260	240	0.58	80	38	20	90
108	74	1.95	222	180	160	0.47	72	42	20	124
126	44	1.68	141	100	80	0.35	57	41	20	156
144	20	1.40	81	40	30	0.24	37	41	10	180
160	4	1.09	44	10	0.0	0.16	0.0	34	10	197
$\alpha_f{}^o$	INVERSION									
36	-20	1.31	0.6	-30	-40	0.00	1.5	30	10	202
54	-43	1.49	-42	-75	-90	-0.11	46	33	15	224
72	-76	1.71	-100	-135	-150	-0.24	67	35	15	224
90	-112	1.91	-166	-200	-220	-0.36	75	34	20	224
108	-145	2.08	-237	-280	-290	-0.47	82	33	10	224
126	-176	2.19	-310	-345	-370	-0.59	84	35	25	224
144	-200	2.21	-366	-410	-425	-0.69	86	44	15	224

Table 6.2 Power measurements for sequence controlled single-bridge.

analytical variation of power factor with load voltage is shown in figure 6.11 which clearly indicates that they are the same.

6.1.3 Sequence Controlled Double-bridge

Figures 6.12, 6.13 and 6.14 show voltage and current waveforms, together with their harmonic spectra, for three different conditions in the rectification mode, and figures 6.15, 6.16 and 6.17 show the same results in the inversion mode. With a 2:1:1 turns ratio for the transformer TF1 of figure 6.2, the instantaneous load voltage of figure 6.12(e) is one-half the supply voltage and the supply current of figure 6.12(a) is one-half the load current, when either bridge A or B is free-wheeling. If neither free-wheels, the instantaneous load voltage equals the supply voltage and the supply current equals the load current, which is also shown in figures 6.12(e) and (a). During the time when both bridges free-wheel the load voltage is zero, and the supply current is the excitation current of the power transformer, as shown respectively in figures 6.14(e) and (a). The load current of figure 6.12(e) rises between times t_1 and t_3 where the instantaneous load voltage v_l is greater than its mean value V_l. However, this current rises at a slower rate between times t_1 and t_2 where v_l is equal to one-half the supply voltage and at a faster rate between t_2 and t_3 where v_l is equal to supply voltage. Between times t_3 and t_5 load current decays, since v_l is smaller than its mean value V_l, again at two different rates as is clearly shown in figure 6.12(e). During inversion, the load current of figure 6.15(e) decays between times t_1 and t_3 where v_l exceeds its mean value V_l and rises between times t_3 and t_5 where v_l is smaller than V_l. The load voltage harmonics of figures 6.13(e) and 6.14(e) in the rectification mode is the same as that of figures 6.16(e) and 6.17(e) in the inversion mode, as is confirmed by comparing figures 6.13(f) and 6.14(f) with that of figures 6.16(f) and 6.17(f). Since the load conditions are the same, the peak-to-peak load current ripple of figures 6.13(e) and 6.14(e) is the same as that of figures 6.16(e) and 6.17(e) as was measured to be 0.7A and 0.9A respectively. The load voltage harmonic of figure 6.12(e) is also the same as that of figure 6.15(e). However, since load conditions are different, their corresponding load current ripple would be different as was measured to be 1.0A and 1.2A respectively. The supply current harmonics of figures 6.13(a) and 6.14(a) are the same as those of figures 6.16(a) and 6.17(a). This is because their corresponding peak-to-peak load current ripples are the same as explained earlier. The 3rd harmonic of the supply current of figure 6.12(a) was measured as 0.5A and that of figure 6.15(a) was 0.6A. This discrepancy is due to their corresponding load current ripples which are different. power measurements at different firing delay angles for a constant 2A load current are presented in table 6.3 for both rectification and inversion modes. It is clear that the predominant losses again occur in the transformer. The experimental and analytical variation of power factor with load voltage is shown in figure 6.18 and indicates that there is some variation in power factor when the converter operates in the inversion mode. The power factor improves about mid-range of the load voltage in both rectification and inversion modes. This is because within these ranges the input distortion and displacement factors are improved and consequently the input power factor, which is the product of these two factors, is also improved.

6.2 PWM Control

The PWM controlled single-bridge converter was connected to an passive load, as shown in figure 6.19. The supply was 240V, 50Hz and the load comprised a 0.3H inductor in series with a 100Ω variable resistor. The load current was maintained constant at 2A for a wide range of output voltage and results in the inversion mode were obtained by connecting a dc source V_{dc} in series with the load. The converter was then connected to a separately excited dc machine as shown in figure 6.20, with the inductance of 0.15H connected in series with the armature to keep the load current continuous. The load current was maintained at the 1.5A full-load current of the machine for a wide range of output voltage. Power measurements were taken

RECTIFICATION										
Firing Angle α_{v1}°	V_1 V	I_s r.m.s. A	W_1 W	W_2 W	W_3 W	W_4 W	Power Factor	Effic. η %	Trans. Loss W	Bridge Loss W
10	212	2.48	534	248	248	480	0.89	90	38	16
36	203	2.36	510	237	245	472	0.90	92	38	10
54	194	2.31	472	208	232	430	0.85	91	32	10
72	176	2.26	432	176	228	390	0.8	90	28	14
90	162	2.19	393	140	224	350	0.75	89	29	14
108	142	2.03	350	96	224	310	0.72	88	30	10
126	128	1.85	310	56	224	270	0.70	87	30	10
144	116	1.68	288	24	232	240	0.71	83	32	16
160	106	1.50	268	7.2	232	220	0.74	82	29	19
α_{f1}°										
36	98	1.49	254	4	216	200	0.71	79	35	20
54	88	1.47	229	4	192	180	0.65	78	34	16
72	72	1.47	171	4	136	120	0.48	70	32	20
90	56	1.41	161	4	120	110	0.48	68	38	14
108	40	1.35	120	4	80	70	0.37	58	37	14
126	23	1.25	85	4	48	40	0.28	47	34	12

Table 6.3 Power measurements for sequence controlled double-bridge.

INVERSION										
Firing Angle α_{f2}^{o}	V_1 V	I_s r.m.s. A	W_1 W	W_2 W	W_3 W	W_4 W	Power Factor	Effic. η %	Trans. Loss W	Bridge Loss W
36	-5	1.3	34	-16	4	-10	0.11	30	46	10
54	-18	1.35	10	-40	4	-20	0.03	50	46	22
72	-24	1.41	-19	-68	4	-60	-0.05	32	35	12
90	-50	1.48	-50	-100	4	-100	-0.14	50	46	4
108	-68	1.51	-85	-136	4	-140	-0.23	61	47	8
126	-84	1.50	-118	-164	4	-170	-0.32	69	42	10
144	-96	1.52	-148	-192	4	-200	-0.40	74	40	12
α_{v2}^{o}										
36	-110	1.73	-179	-200	-16	-230	-0.43	78	37	14
54	-124	1.89	-203	-192	-48	-260	-0.44	78	37	20
72	-140	2.00	-232	-192	-80	-280	-0.48	83	40	8
90	-158	2.17	-273	-192	-120	-320	-0.52	85	39	8
108	-174	2.21	-300	-192	-144	-350	-0.56	86	36	16
126	-188	2.23	-330	-196	-168	-380	-0.61	87	34	16
144	-202	2.27	-367	-208	-200	-420	-0.67	87	41	12

Table 6.3 Continued.

for different output voltages and the input power factor and efficiency were calculated from equations 6.1 and 6.4.

6.2.1 PWM Bridge Converter Connected to a Passive Load

Voltage and current waveforms for the converter of figure 6.19, both with and without the capacitor C, are shown in figure 6.21, at a switching frequency of 2kHz. The ringing evident in the transformer secondary and load voltage waveforms of figure 6.21(b) and (c) is caused by the transformer interwinding capacitance, however the effect is not evident in the supply voltage waveform of 6.21(a) due to the transformer impedance. The ringing is completely eliminated in figures 6.21(a) to (c), by connecting a capacitor across the transformer secondary terminals. Problems were encountered with the gate signals of figure 6.22(a) when the load current was increased above 1A. This is explained by considering the period when T_1 is turning off and T_3 on. Should T_1 turn off faster than T_3 turns on, a large induced voltage due to the load inductance will appear across T_3, and can cause damage. An alternative drive strategy developed to overcome this problem is illustrated by figure 6.22(b), and its operation is explained in Chapter 2.

Voltage and current waveforms and their harmonic spectra for a switching frequency of 4kHz at high and low modulation indices are presented in figures 6.23 and 6.24 respectively. Figures 6.25 and 6.26 show the same results when the converter operates in the inversion mode. The high frequency distortion evident in the transformer secondary voltage of figure 6.23(c) and the load current of figure 6.23(f) is due to charging and discharging of the capacitor. However, due to the transformer impedance, the distortion is not present in the supply voltage as shown in figure 6.23(a). During the time when the load voltage of figure 6.23(f) is free-wheeling, the capacitor charges and when the load is connected to the supply, it discharges. This change in current is clearly seen in the transformer secondary current of figure 6.23(c). The load voltage of figure 6.23(f) and the converter current of figure

6.23(d) are chopped in a PWM manner. The current contains low order harmonics, together with others located at the side-bands of the switching frequency and its multiples, as shown in figure 6.23(e). However, these higher order harmonics are filtered by the capacitor so that only low order harmonics remain, as seen in figure 6.23(b). The load voltage of figure 6.23(f) contains low order harmonics and high order harmonics at the switching frequency and its side-bands, and multiples of them as seen in figure 6.23(g) which also indicates that the second harmonic is predominant. The high-order voltage harmonics produce negligible current harmonics as seen in figure 6.23(h), due to the load impedance. The change of transformer secondary current of figure 6.24(c), which corresponds to charging and discharging of the capacitor, is more pronounced than that of figure 6.23(c). This is because at Low Modulation Index, LMI, the load voltage is reduced and to keep the load current constant at 2A the load resistance must be reduced. Consequently the capacitor has to charge and discharge at a higher rate. The capacitor also acts to provide power factor correction, which in this case has over-corrected the input power factor and caused the supply current to lead the supply voltage, as is evident by inspection of the supply voltage and current waveforms. The supply current leads the voltage by an angle which is greater at LMI than at High Modulation Index, HMI, as is evident by comparing figures 6.24(a) and 6.23(a). This increase with reducing load voltage causes the displacement factor to reduce and as a result the supply power factor decreases. This is evident from table 6.4, which presents power measurements for a constant 2A load current at a switching frequency of 4kHz, for different output voltage levels in both the rectification and inversion modes. The power measurements of table 6.5 are taken both with and without the capacitor connected and at a constant 0.8A load current. It is clear that, by including the capacitor in the converter circuit, both the supply power factor and efficiency are improved, since elimination of harmonics improves the input distortion factor (hence improving the supply power factor) and reduces the losses. The load voltage harmonics of figure 6.23(f) in the rectification mode is the same as that of

RECTIFICATION								
V_1 V	I_s r.m.s. A	W_1 W	W_2 W	W_3 W	Power Factor	Effic. η %	Trans. Loss W	Bridge Loss W
158	1.96	461	420	400	0.98	86	41	20
150	1.89	440	410	390	0.97	89	30	20
140	1.74	404	380	350	0.96	89	24	30
130	1.60	373	350	320	0.97	86	23	30
120	1.49	345	320	300	0.96	87	25	20
110	1.38	323	300	270	0.97	84	23	30
100	1.26	290	260	240	0.96	83	30	20
90	1.15	265	240	220	0.96	83	15	20
80	1.04	236	210	190	0.94	80	26	20
70	0.93	212	180	160	0.94	75	32	20
60	0.84	187	160	140	0.92	75	27	20
50	0.75	162	130	110	0.90	68	32	20
40	0.66	137	110	90	0.86	66	27	20
30	0.60	115	90	70	0.80	61	25	20
20	0.55	96	60	40	0.72	42	36	20
10	0.49	73	40	20	0.62	27	33	20

Table 6.4 Power measurements for PWM controlled single-bridge at switching frequency of 4kHz.

INVERSION								
V_1 V	I_s r.m.s. A	W_1 W	W_2 W	W_3 W	Power Factor	Effic. η %	Trans. Loss W	Bridge Loss W
-140	0.78	-170	-196	-226	-0.91	75	26	30
-130	0.71	-155	-184	-209	-0.91	74	29	25
-120	0.67	-143	-172	-202	-0.89	71	29	30
-110	0.63	-130	-161	-181	-0.86	72	31	20
-100	0.60	-117	-149	-164	-0.81	71	33	15
-90	0.56	-101	-134	-144	-0.75	70	33	10
-80	0.52	-85	-117	-127	-0.68	67	32	10
-70	0.49	-69	-103	-118	-0.59	59	34	15
-60	0.47	-60	-89	-109	-0.53	55	29	20
-50	0.44	-38	-71	-91	-0.36	42	33	20
-40	0.43	-22	-52	-72	-0.21	30	30	20
-30	0.43	-4	-28	-48	-0.04	9	24	20

Table 6.4 Continued.

	WITHOUT CAPACITOR C.					WITH CAPACITOR C.				
V_1 v	I_s r.m.s A	W_1 W	W_3 W	Power Factor	Effic. η %	I_s r.m.s A	W_1 W	W_3 W	Power Factor	Effic. η %
60	0.89	89	56	0.84	63	0.78	76	60	0.98	79
50	0.81	76	40	0.80	53	0.66	64	48	0.99	75
40	0.77	68	32	0.75	47	0.55	54	38	0.99	70
30	0.68	57	22	0.71	39	0.44	43	30	0.98	70
20	0.57	44	14	0.65	32	0.33	32	18	0.98	56

Table 6.5 Power measurements for PWM controlled single-bridge at switching fresquency of 5kHz.

figure 6.25(f) in the inversion mode, as is verified by comparing figure 6.23(g) with that of figure 6.25(g). However their corresponding peak-to-peak load current ripples are different and was measured as 1.2A and 1.3A respectively. This discrepancy is due to the fact that the load condition for figure 6.23 is different to that of figure 6.25. The load voltage harmonics of figure 6.24(f) in the rectification mode are the same as those of figure 6.26(f) in the inversion mode and since the load conditions are the same, their corresponding peak-to-peak load current ripple were also the same and this was measured as 0.7A.

Circuit waveforms and their harmonic spectra at 2kHz switching frequency for both high and low modulation indices for 2A load current are shown respectively in figures 6.27 and 6.28. The low order supply current and load voltage harmonics produced at the switching frequency of 2kHz is almost the same as that produced at the switching frequency of 4kHz as is verified by comparing figures 6.27 and 6.28 with figures 6.23 and 6.24. However, operating the PWM converter at the switching frequency of 4kHz has the advantage that the cost and size of the filter elements to eliminate the high order current and voltage harmonics, which are located at the switching frequency and its side-band, are reduced compared to that at switching frequency of 2kHz. A disadvantage of operating at 4kHz is the increased switching losses.

6.2.2 PWM Bridge Converter Connected to a dc Machine

The converter was connected to a separately-excited dc machine as shown in figure 6.20. Figure 6.29 shows voltage and current waveforms together with their harmonic spectra for HMI at a switching frequency of 4 kHz under no load condition. The constant dc voltage level in the armature voltage waveform of figure 6.29(f) is the back emf of the machine, appearing due to the discontinuity of the armature current. Figures 6.30 and 6.31 show experimental results for high and low modulation indices at a switching frequency of 4 kHz and 1.5A full-load current. Table 6.6 gives measurements of power, efficiency,

RECTIFICATION									
V_a V	I_s r.m.s. A	W_1 W	W_2 W	W_3 W	Power Factor	Effic. η %	Trans. Loss W	Bridge Loss W	Speed r.p.m
156	1.29	306	276	250	0.98	82	36	26	1000
140	1.20	279	249	224	0.97	80	30	25	850
130	1.13	258	230	208	0.95	80	28	22	770
120	1.07	245	214	192	0.95	78	31	22	700
110	1.02	227	198	178	0.92	78	29	20	600
100	0.95	213	182	162	0.93	76	31	20	530
90	0.90	195	165	144	0.90	74	30	21	450
80	0.84	180	150	128	0.89	71	30	22	370
70	0.78	164	134	114	0.88	69	30	20	280
60	0.70	147	117	94	0.87	64	30	23	150

Table 6.6 Power measurements for PWM controlled single-bridge connected to a dc machine at a switching frequency of 4kHz.

speed and supply power factor at different output voltage levels at switching frequency of 4 kHz, and the predominant losses are again in the transformer.

6.3 Comparison Between Different Controllers

Load voltage harmonics for different controllers presented in this chapter clearly indicate that they contain a dc component plus even harmonics whose magnitudes decrease with increasing harmonic order and the 2nd harmonic is predominant. Load voltage harmonics produced by the sequence-controlled double-bridge converter is 44% of that produced with sequence-controlled single-bridge converter when the load voltage is 106V and 50% when the load voltage is -106V as is clearly indicated in figures 6.13(f) and 6.7(d) in the rectification mode and figures 6.16(f) and 6.9(d) in the inversion mode. This tremendous improvement in the load voltage harmonics results in a corresponding improvement in the peak-to-peak load current ripple, as confirmed by comparing figures 6.13(e) and 6.16(e) with figures 6.7(c) and 6.9(c). This improvement in load current ripple by using a double-bridge converter makes it possible to achieve substantial savings in the cost of output smoothing inductance. The load voltage harmonics produced by the PWM bridge converter are slightly improved compared to those of the sequence-controlled double-bridge converter as is verified by comparing figures 6.23(g), 6.24(g), 6.25(g) and 6.26(g) with figures 6.12(f), 6.14(f), 6.15(f) and 6.17(f). This slight improvement in the low-order load voltage harmonics of the PWM bridge converter is at the expense of producing high-order harmonics at multiples of the switching frequency and their side-bands as shown in figures 6.23(g), 6.24(g), 6.25(g) and 6.26(g). Load current harmonics associated with these high-order voltage harmonics are negligible due to the reactance of the load. Nevertheless, these voltage harmonics need to be filtered to eliminate supply voltage distortion. The peak-to-peak load current ripple of figures 6.23(f), 6.24(f), 6.25(f) and 6.26(f) is almost the same as that produced by figures 6.12(e), 6.14(e), 6.15(e) and 6.17(e) which is for sequence-controlled double-bridge converter. The 3rd and 5th harmonic currents drawn from supply lines using the sequence-controlled double-bridge converter are slightly improved to that of sequence-controlled single-bridge converter as shown by comparing figures 6.13(b) and 6.16(b) with figures 6.7(b) and 6.9(b). However the comparison of the above figures clearly indicate that there is a substantial improvement in the fundamental component by using the sequence-controlled double-bridge converter. Comparison of figures 6.23(b) to 6.26(b) with figures 6.12 (b), 6.14(b), 6.15(b) and 6.17(b) for a sequence-controlled double-bridge converter show a reduction in these harmonics by using PWM bridge converter. This reduction in low-order supply current harmonics is at the expense of producing high-order harmonics as is shown in converter current spectra of figures 6.23(e) to 6.26(e). However these high-order current components can easily be filtered.

Figure 6.31 shows the experimental variation of power factor with load voltage for different controllers in both the rectification and inversion modes. The supply was 240V, 50Hz and the load current was maintained at 2A for the static load and 1.5A for dc machine load. The power factor produced by the PWM controller is far superior to that produced by the other controllers, as is clearly shown in figure 6.32. This improvement in power factor would give a substantial savings in the cost of power factor correction. The variation of efficiency with load voltage for the different controllers obtained from tables 6.1 to 6.6 in the rectification and inversion modes is shown in figure 6.33. Losses considered in the efficiency calculation consist of those in both the transformer (iron and copper) and the bridge (snubber loss, on-state loss, gate drive loss and switching losses). The switching losses are particularly significant with the PWM controller, whereas the harmonic iron and copper losses in the transformer will be less than that for sequence and conventional controllers. Figure 6.32 shows that in the rectification mode, the PWM controller produces a higher efficiency, whereas in the inversion mode, the sequence controlled double-bridge is better.

The disadvantages in using a PWM bridge converter compared to a phase-controller are an increase in the switching losses and the fact that GTO thyristors require a more complicated drive circuit compared to that required by conventional thyristors. Another disadvantage with PWM control is that the output voltage produced is chopped, resulting in a reduction in the mean output voltage and hence a reduction in the power output to below that produced by conventional and sequence controllers for a given input voltage and load current.

Experimental and analytical variations of power factor with output voltage for conventional and sequence controllers are shown in figures 6.6, 6.11 and 6.18 which clearly indicate that there is a slight discrepancy between the two results which occurs when the converter operates in the inversion mode. This discrepancy can be due to the fact that the experimental power factor calculated from equation 6.1 includes the copper losses and the harmonic losses of the transformer; whereas in the analytical model these were not considered. Other analytical results for the phase-controllers presented in this chapter are the supply current harmonics together with load voltage and current harmonics. The comparison between these two indicate clearly that they are in close agreement. It may therefore be concluded that the analytical model may be used in predicting the performance of converters at different voltage and current levels to that considered in this thesis.

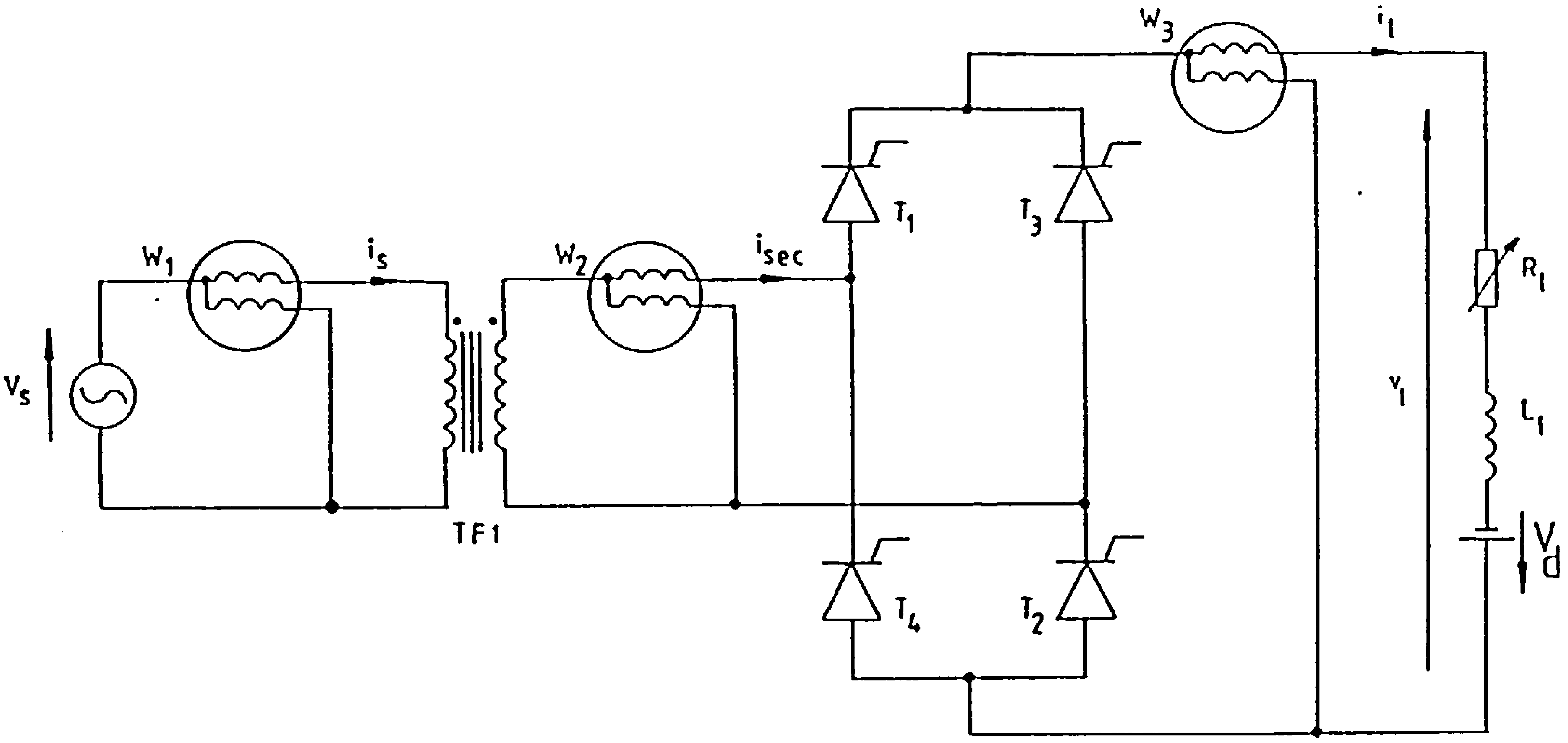

Figure6.1 Fully-controlled single-bridge converter.

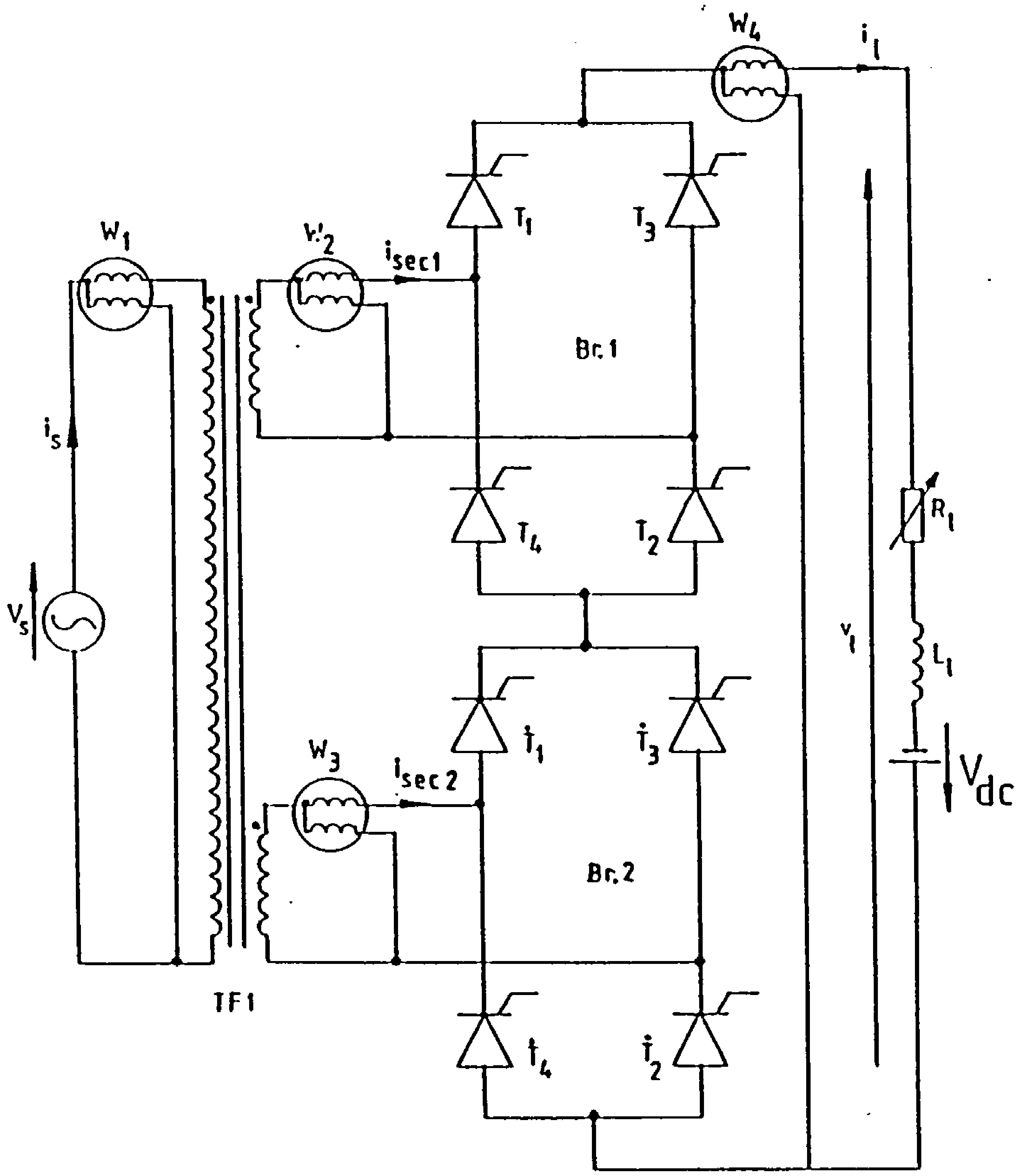

Figure6.2 Fully-controlled series connected double-bridge converter.

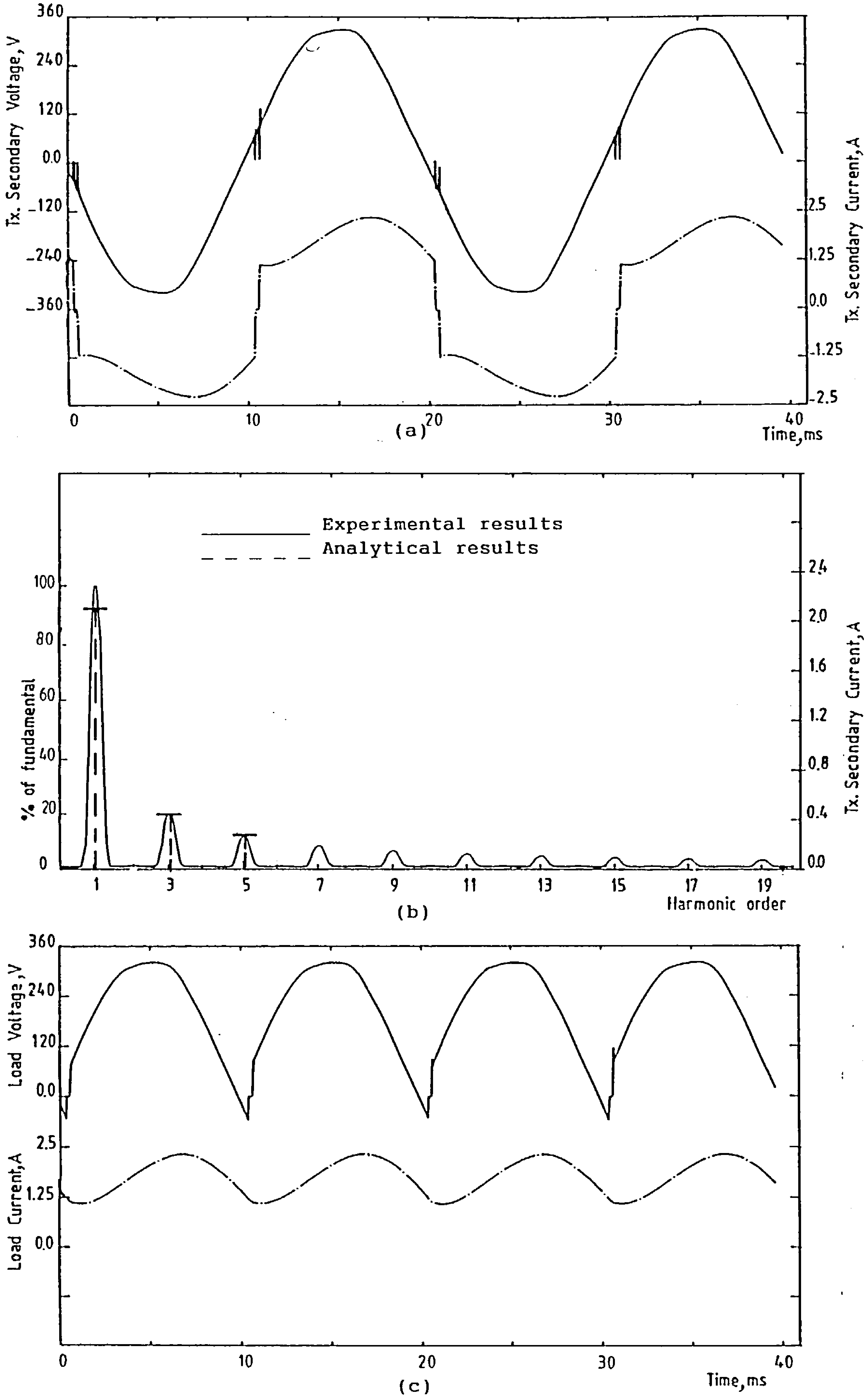

Figure6.3 Experimental results for conventional controlled single-bridge converter.

(a) Transformer secondary voltage and current.
(b) Transformer secondary current spectrum.
(c) Load voltage and current.

($\alpha=10^{o}, R_1=100\Omega, L_1=0.3H, V_1=212V, V_{dc}=2V$)

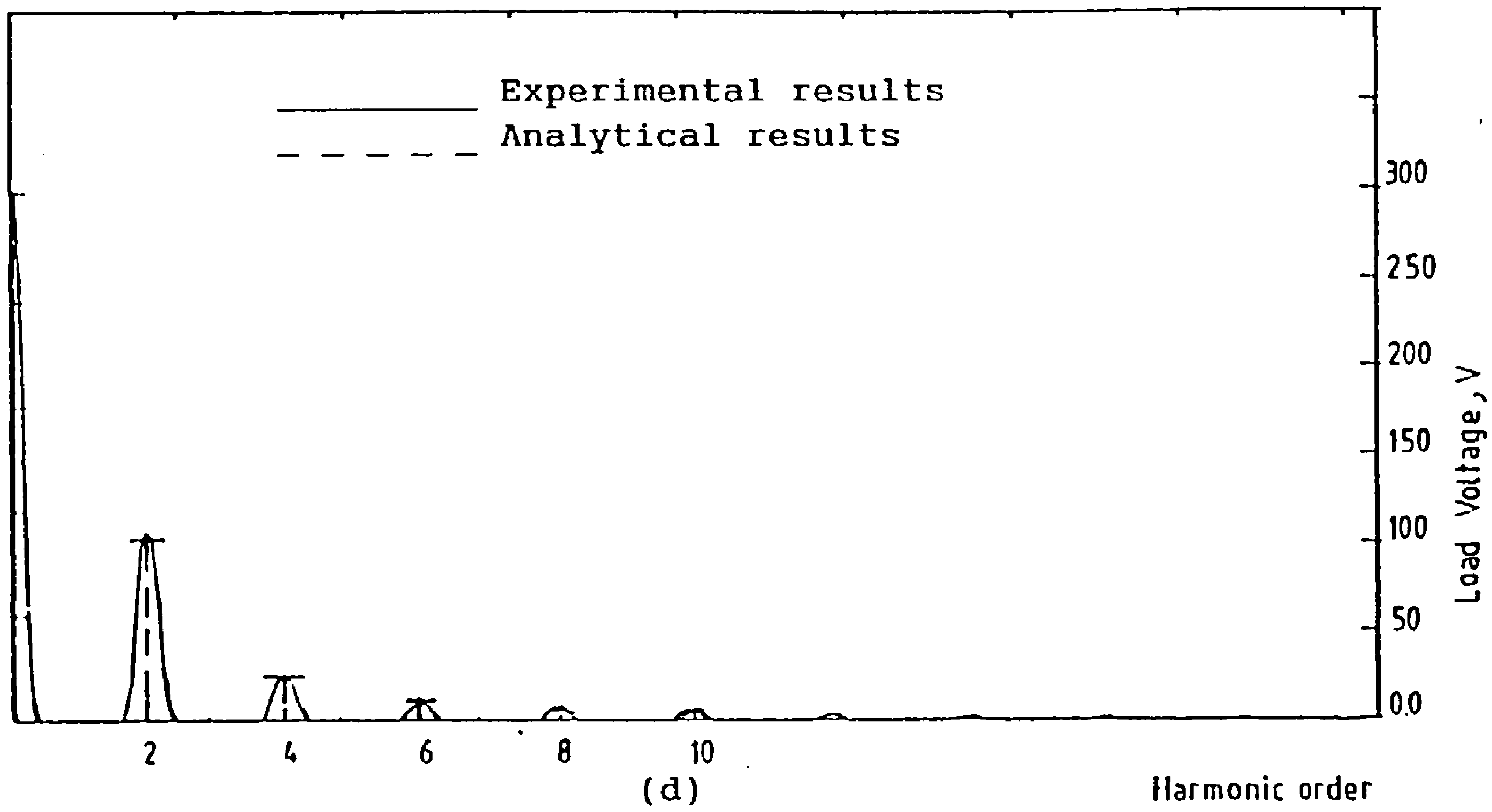

(d)

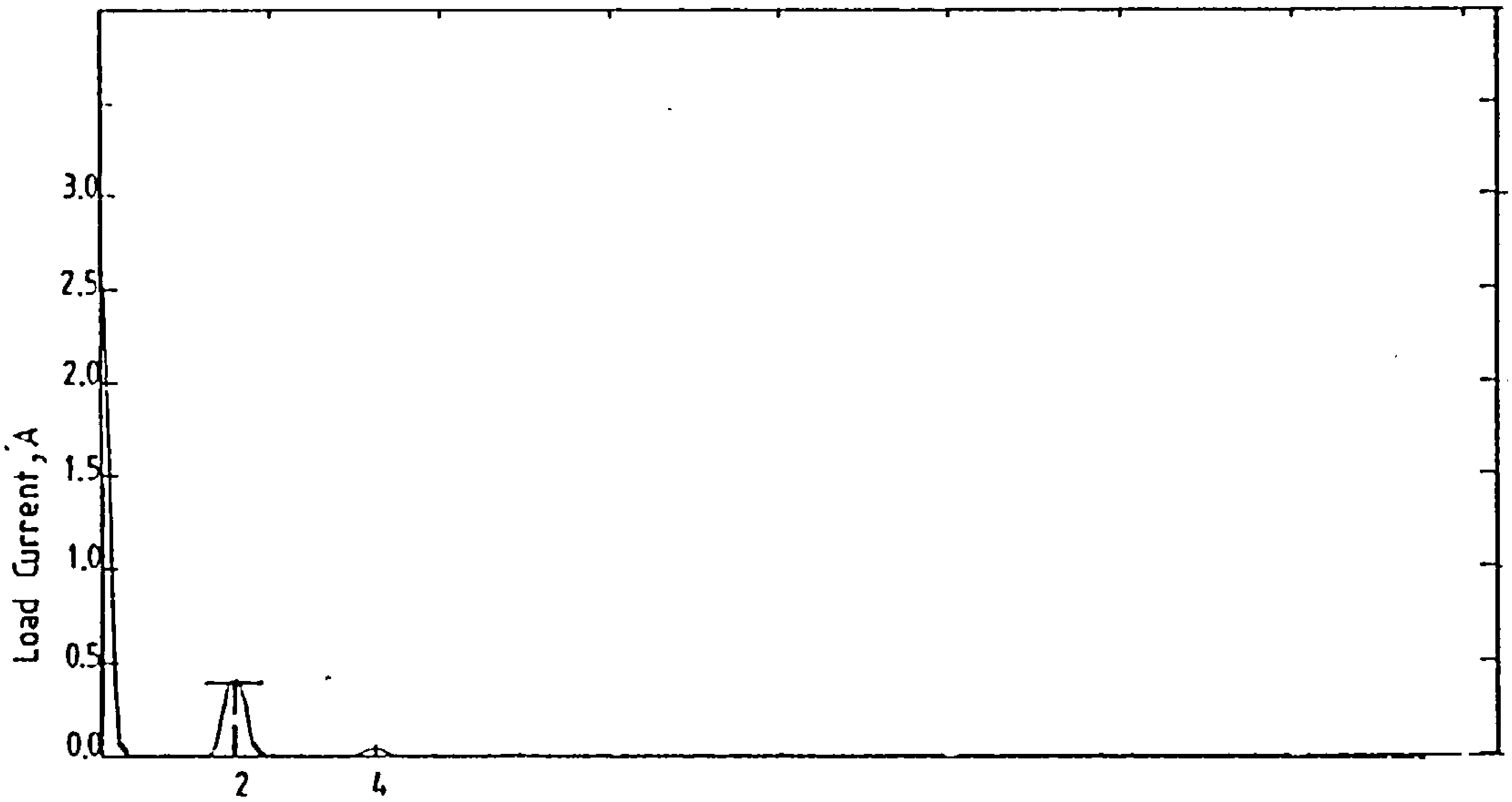

(e)

Figure6.3 Continued.
(d) Load voltage spectrum.
(e) Load current spectrum.

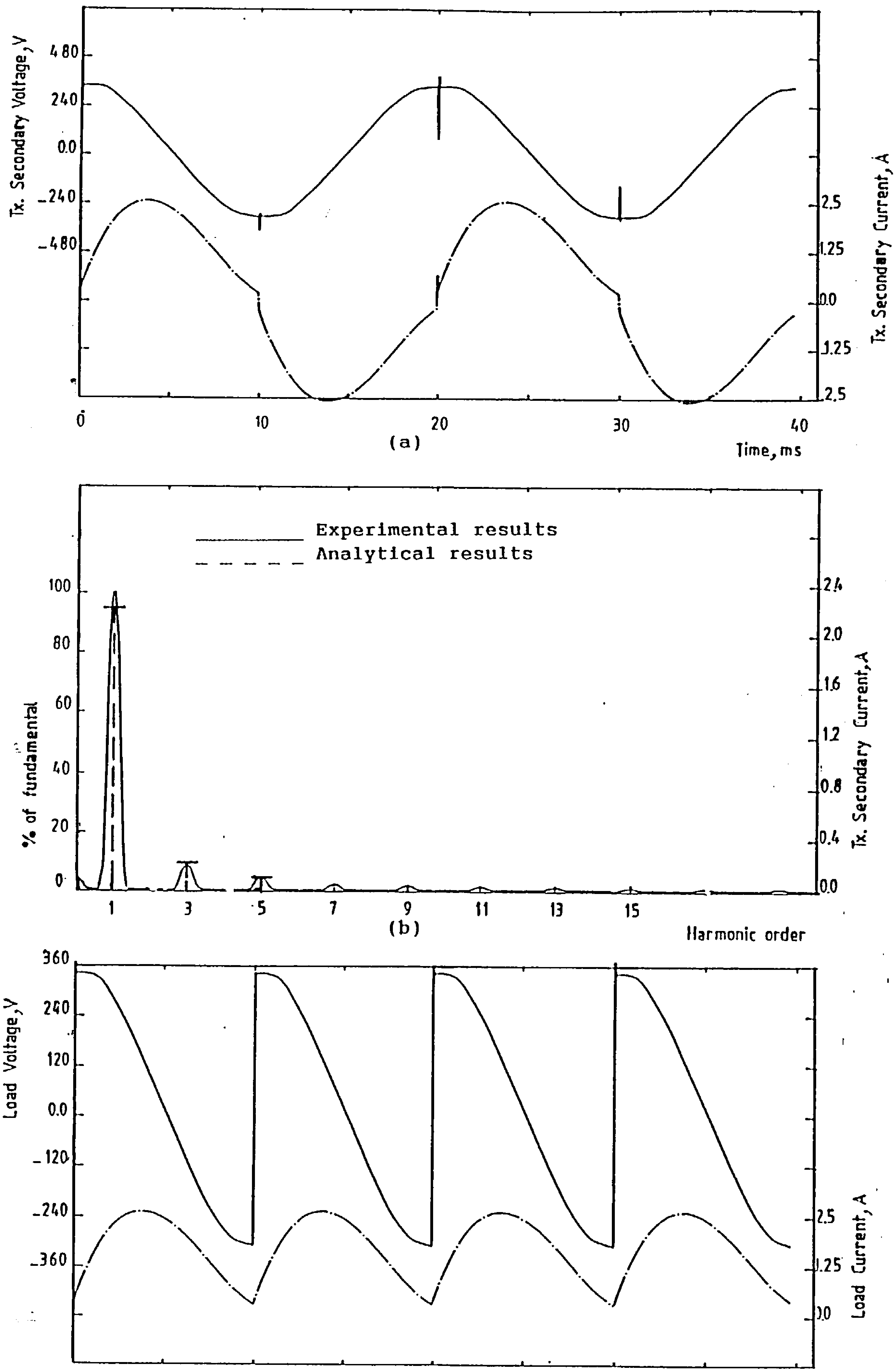

Figure6.4 Experimental results for conventional controlled single-bridge converter.
(a) Transformer secondary voltage and current.
(b) Transformer secondary current spectrum.
(c) Load voltage and current.
($\alpha=90^{\circ}, R_1=100\Omega, L_1=0.3H, V_1=0V, V_{dc}=200V$)

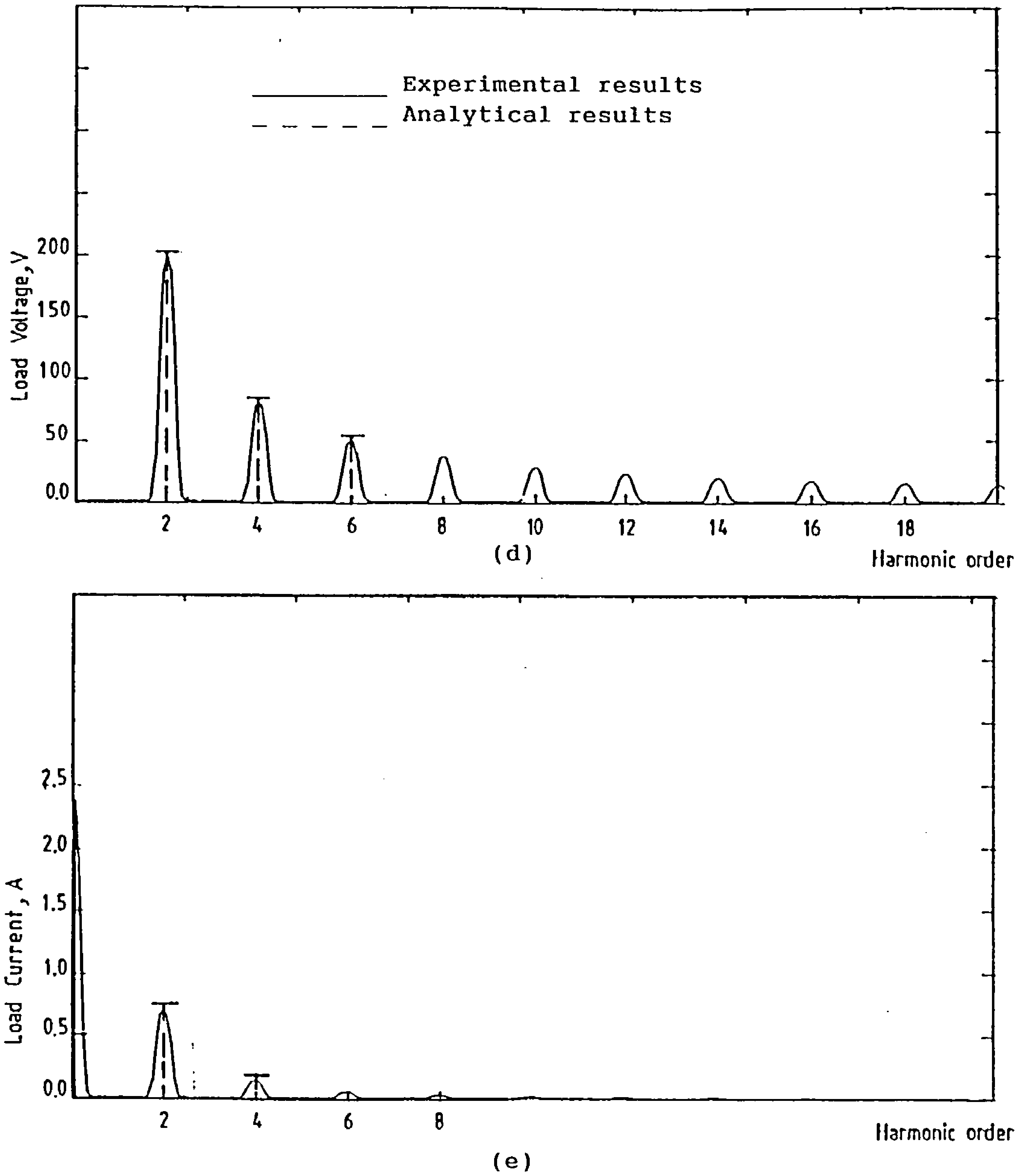

Figure6.4 Continued.
(d) Load voltage spectrum.
(e) Load current spectrum.

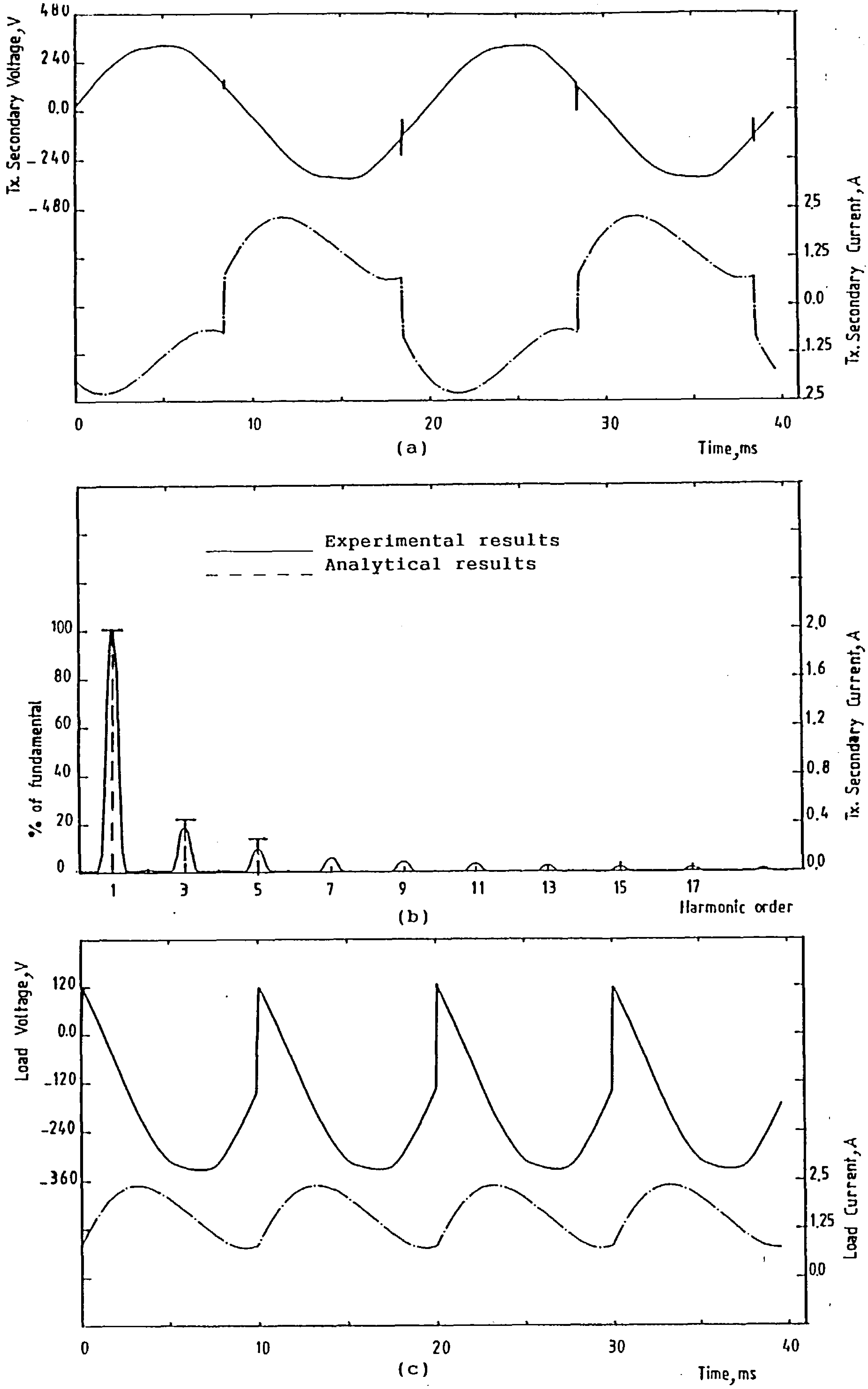

Figure6.5 Experimental results for conventional controlled single-bridge converter.

(a) Transformer secondary voltage and current.

(b) Transformer secondary current spectrum.

(c) Load voltage and current.

($\alpha=160^{\circ}, R_1=11\Omega, L_1=0.3H, V_1=-203V, V_{dc}=225V$)

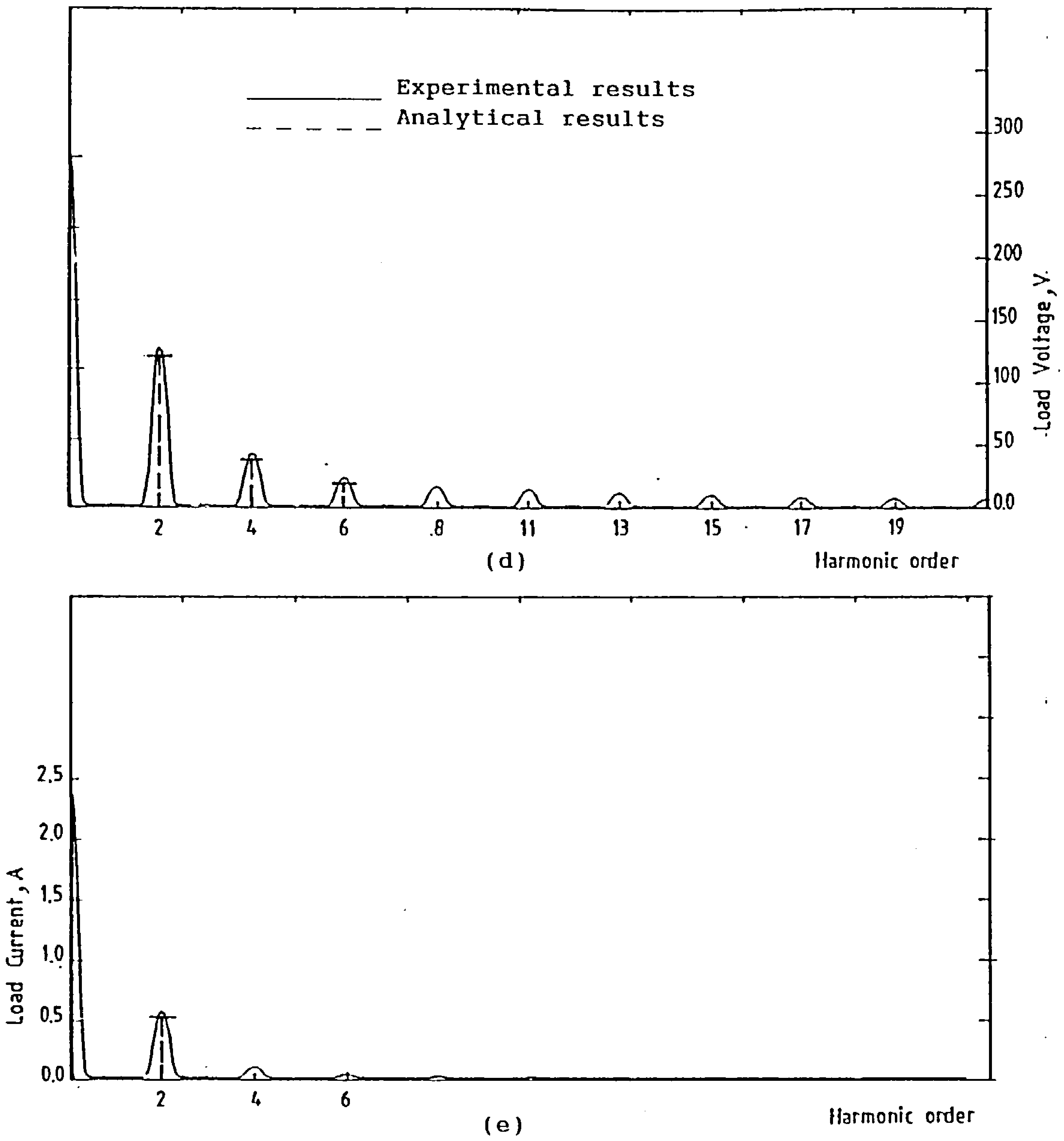

Figure6.5 Continued.
(d) Load voltage spectrum.
(e) Load current spectrum.

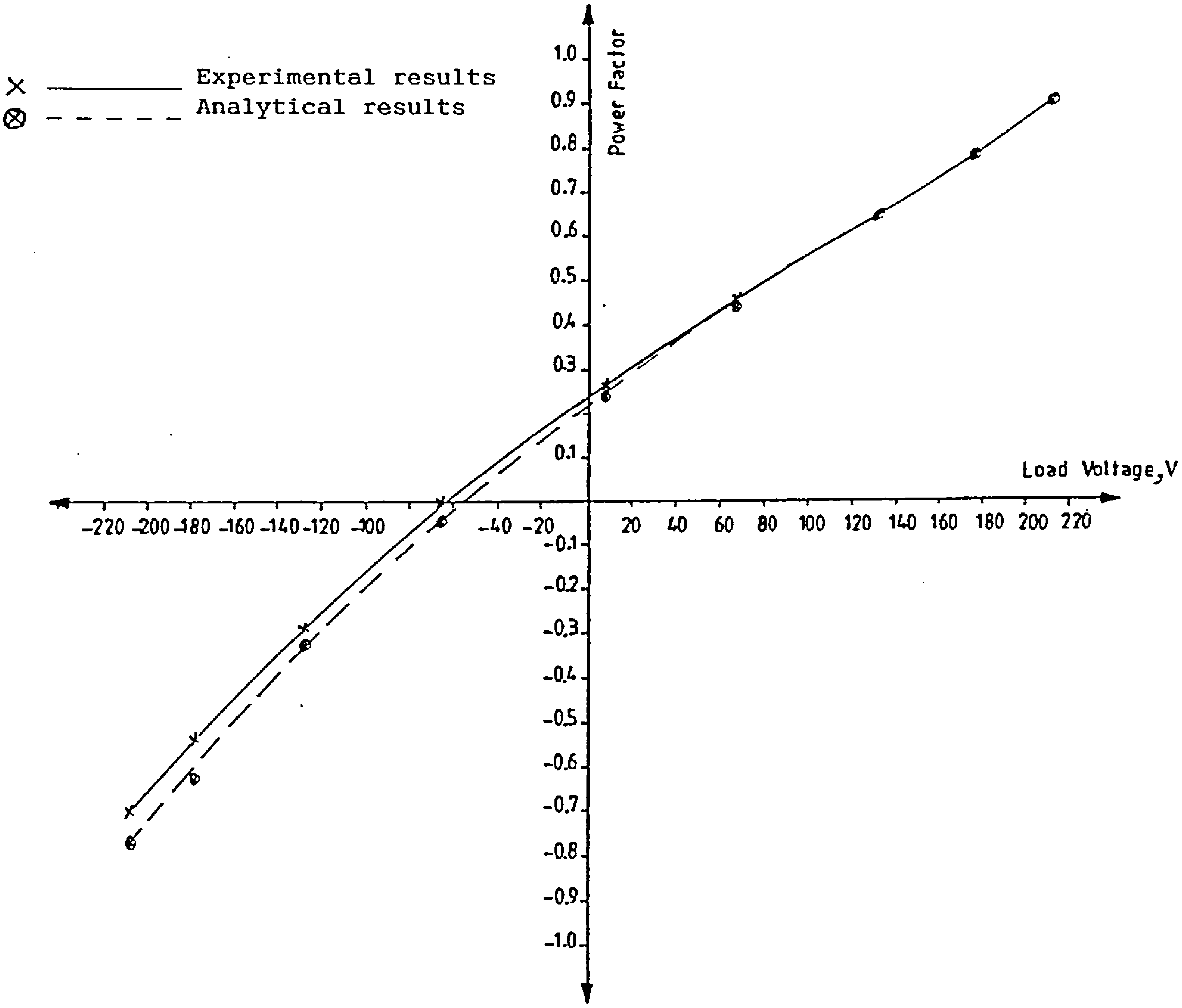

Figure6.6 Experimental and analytical variation of power factor with load voltage for conventional controlled single-bridge.

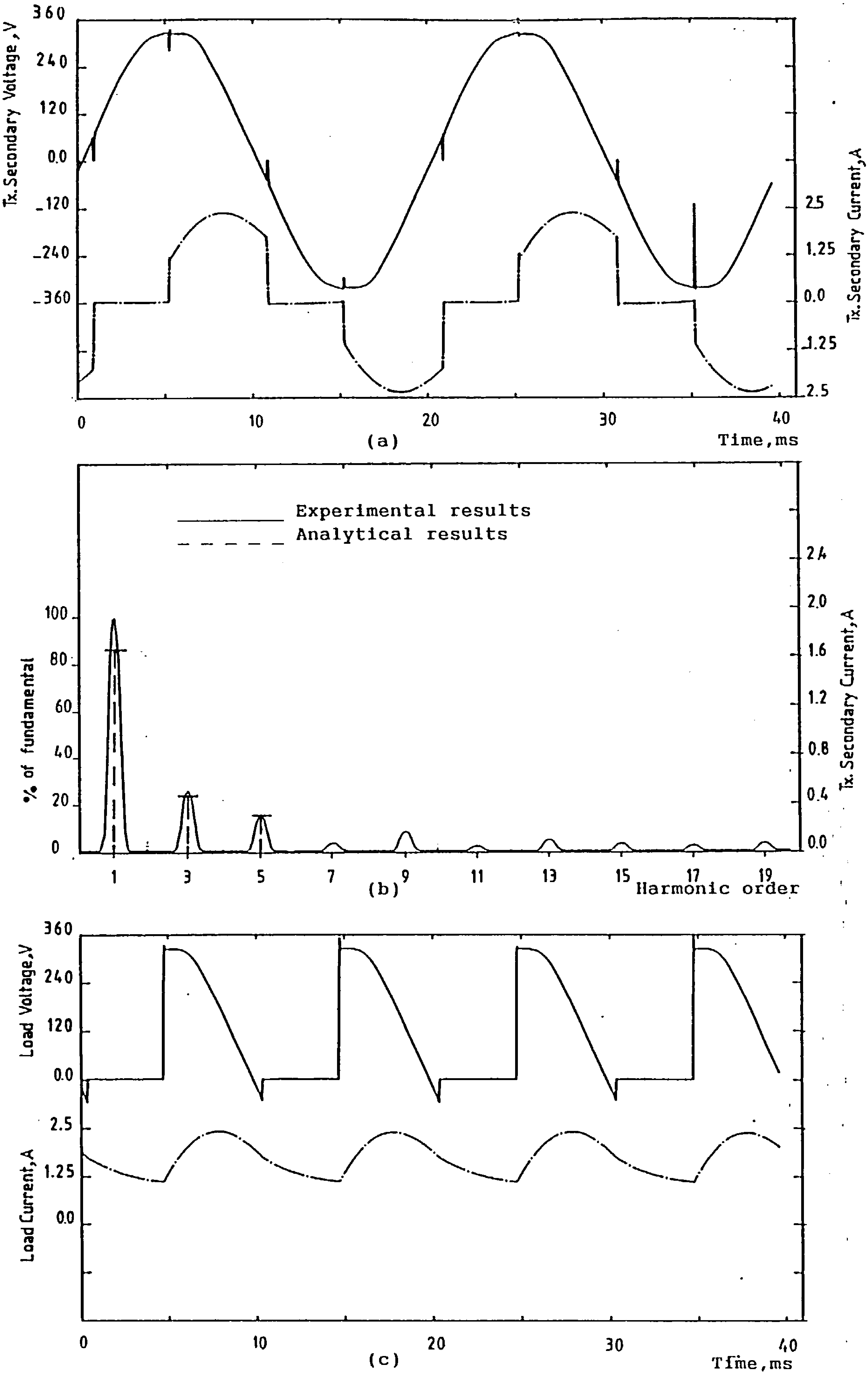

Figure6.7 Experimental results for sequence-controlled single-bridge converter.

(a) Transformer secondary voltage and current.

(b) Transformer secondary current spectrum.

(c) Load voltage and current.

($\alpha_f=10^o, \alpha_v=90^o, R_1=100\Omega, L_1=0.3H, V_1=106V, V_{dc}=94V$)

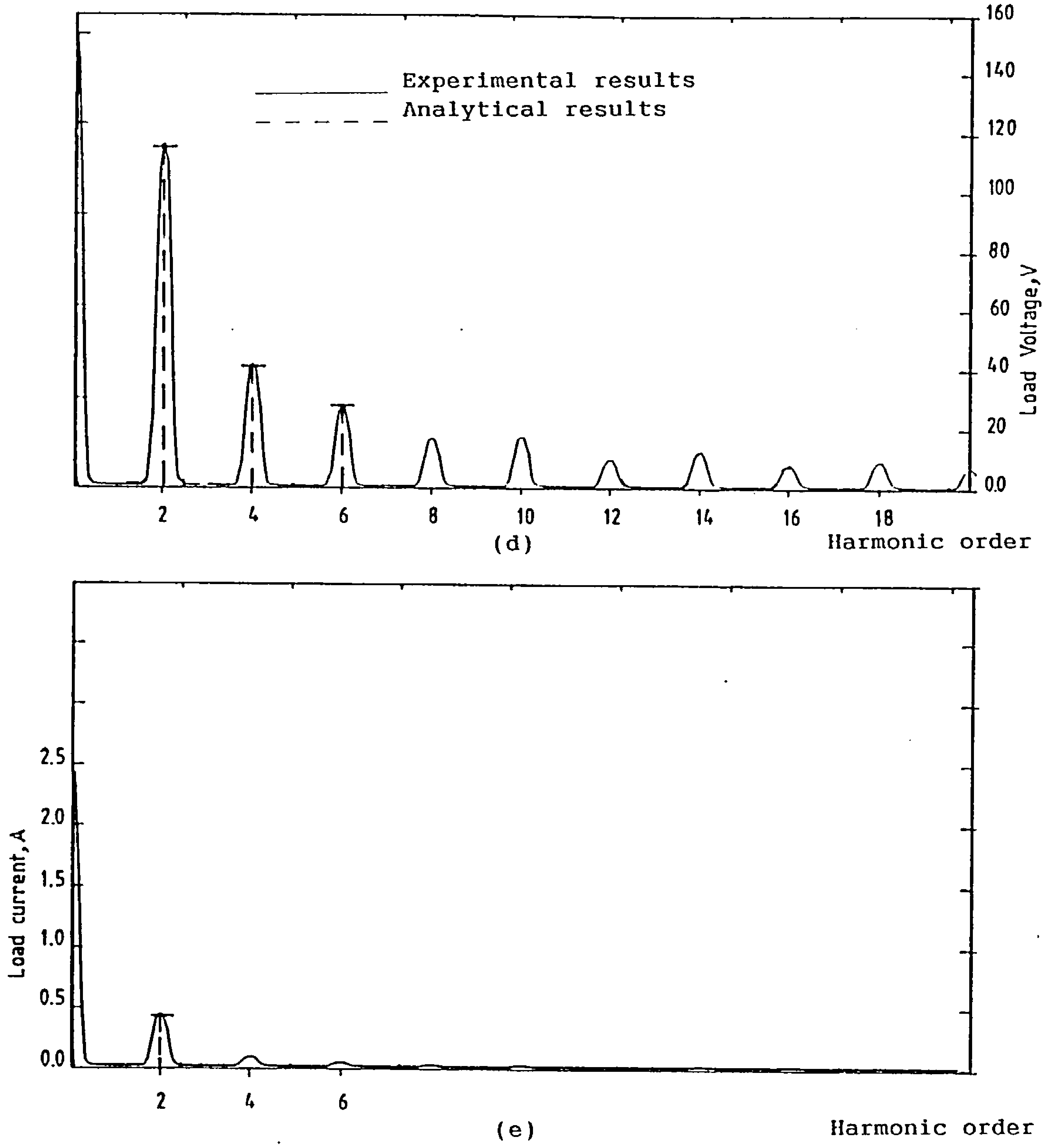

figure6.7 Continued.
(d) Load voltage spectrum.
(e) Load current spectrum.

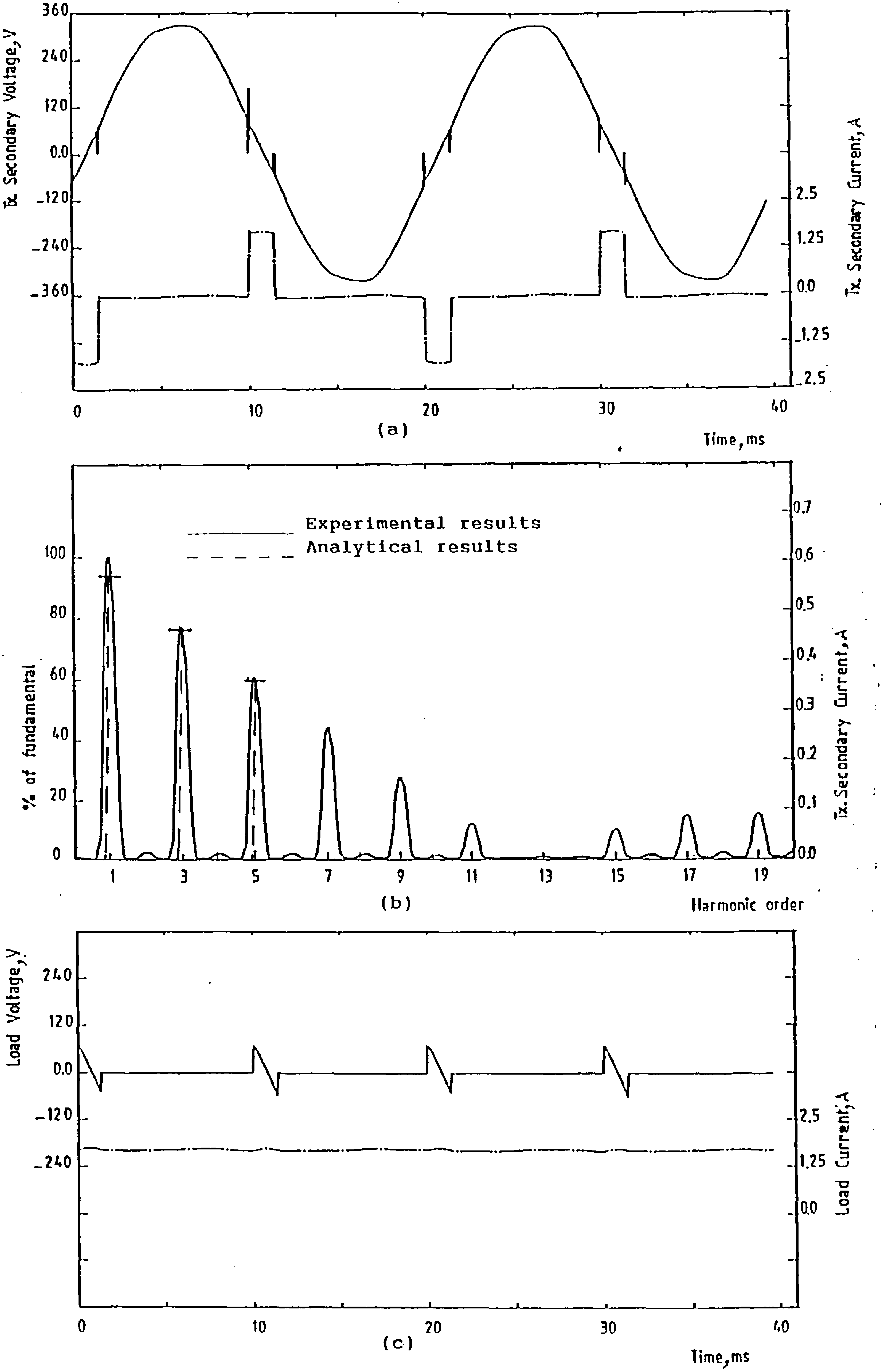

Figure6.8 Experimental results for sequence-controlled single-bridge converter.

(a) Transformer secondary voltage and current.

(b) Transformer secondary current spectrum.

(c) Load voltage and current.

($\alpha_f=10^\circ, \alpha_v=170^\circ, R_1=100\Omega, L_1=0.3H, V_1=0V, V_{dc}=200V$)

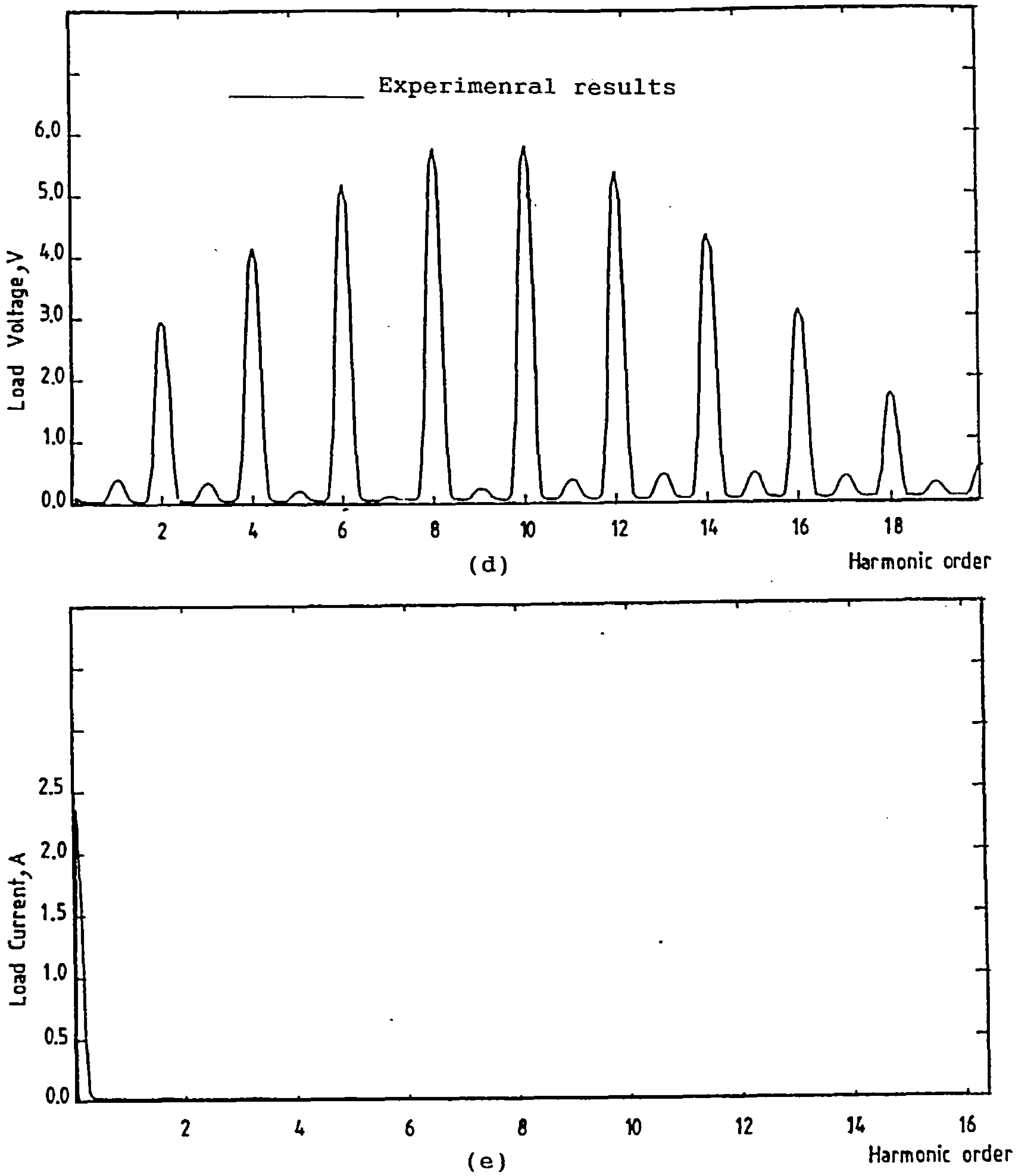

Figure6.8 Continued.
(d) Load voltage spectrum.
(e) Load current spectrum.

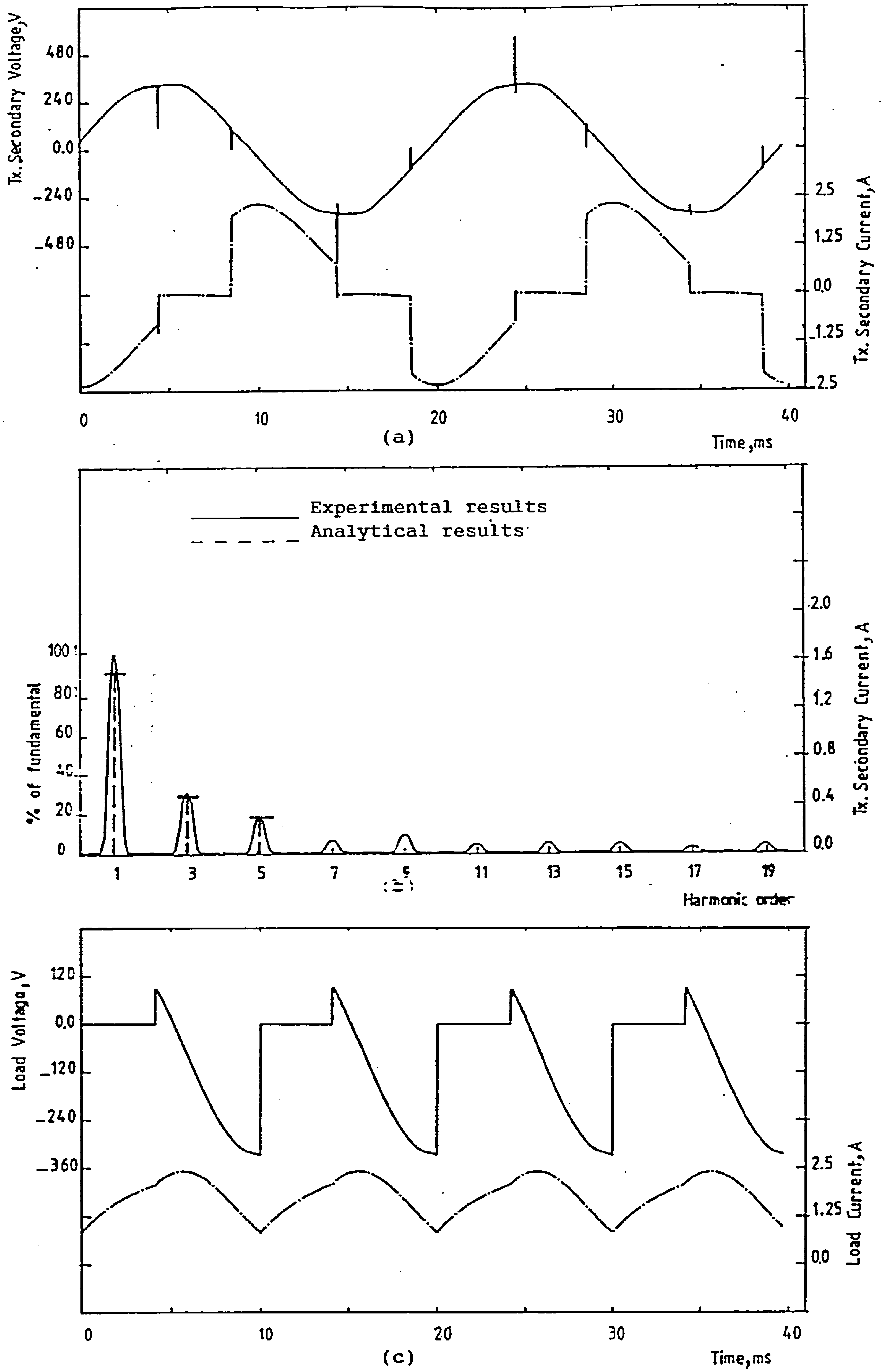

Figure6.9 Experimental results for sequence-controlled single-bridge converter.
(a) Transformer secondary voltage and current.
(b) Transformer secondary current spectrum.
(c) Load voltage and current.

($\alpha_f=90^o, \alpha_v=170^o, R_l=58\Omega, L_l=0.3H, V_l=-106V, V_{dc}=222V$)

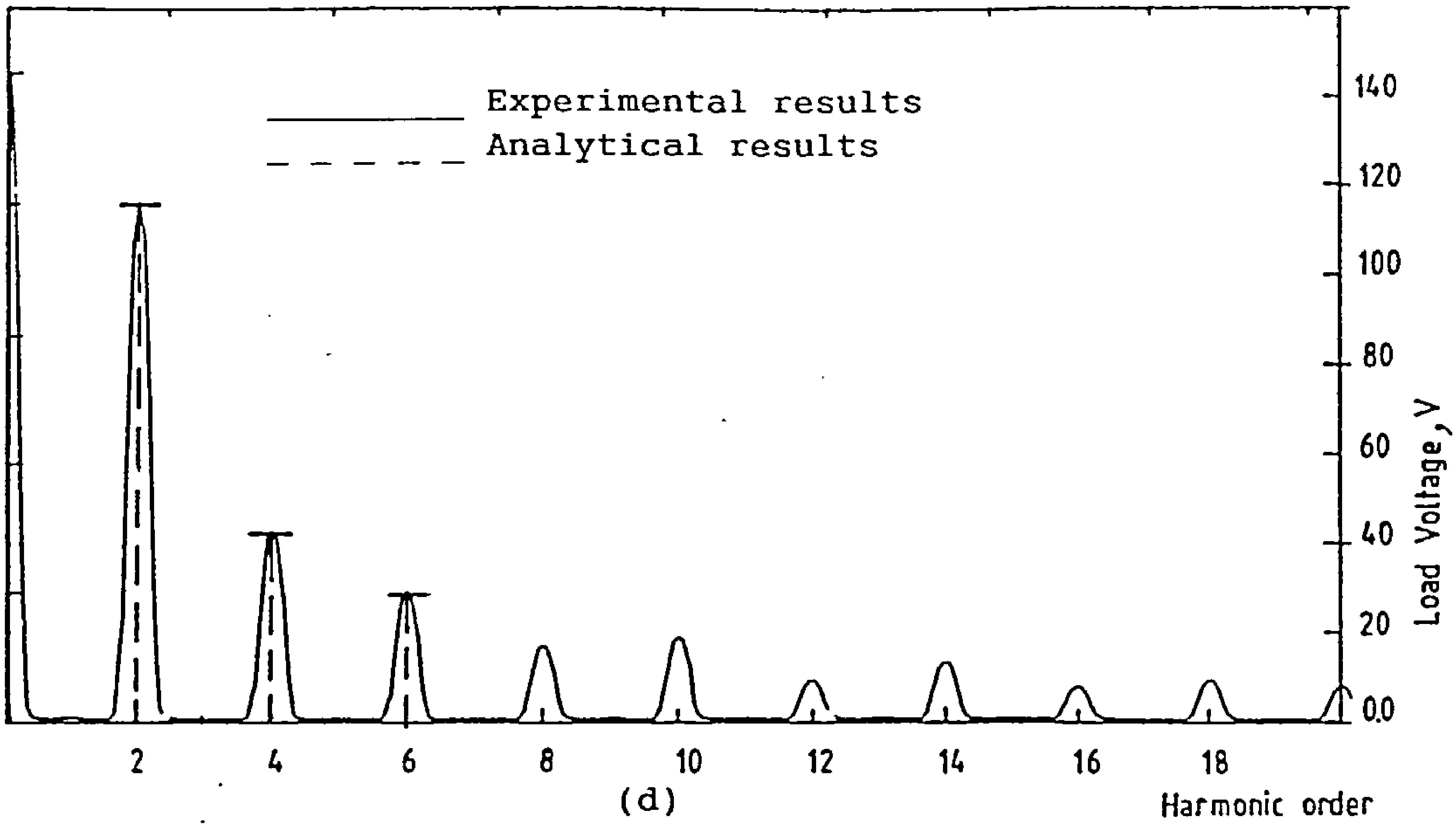

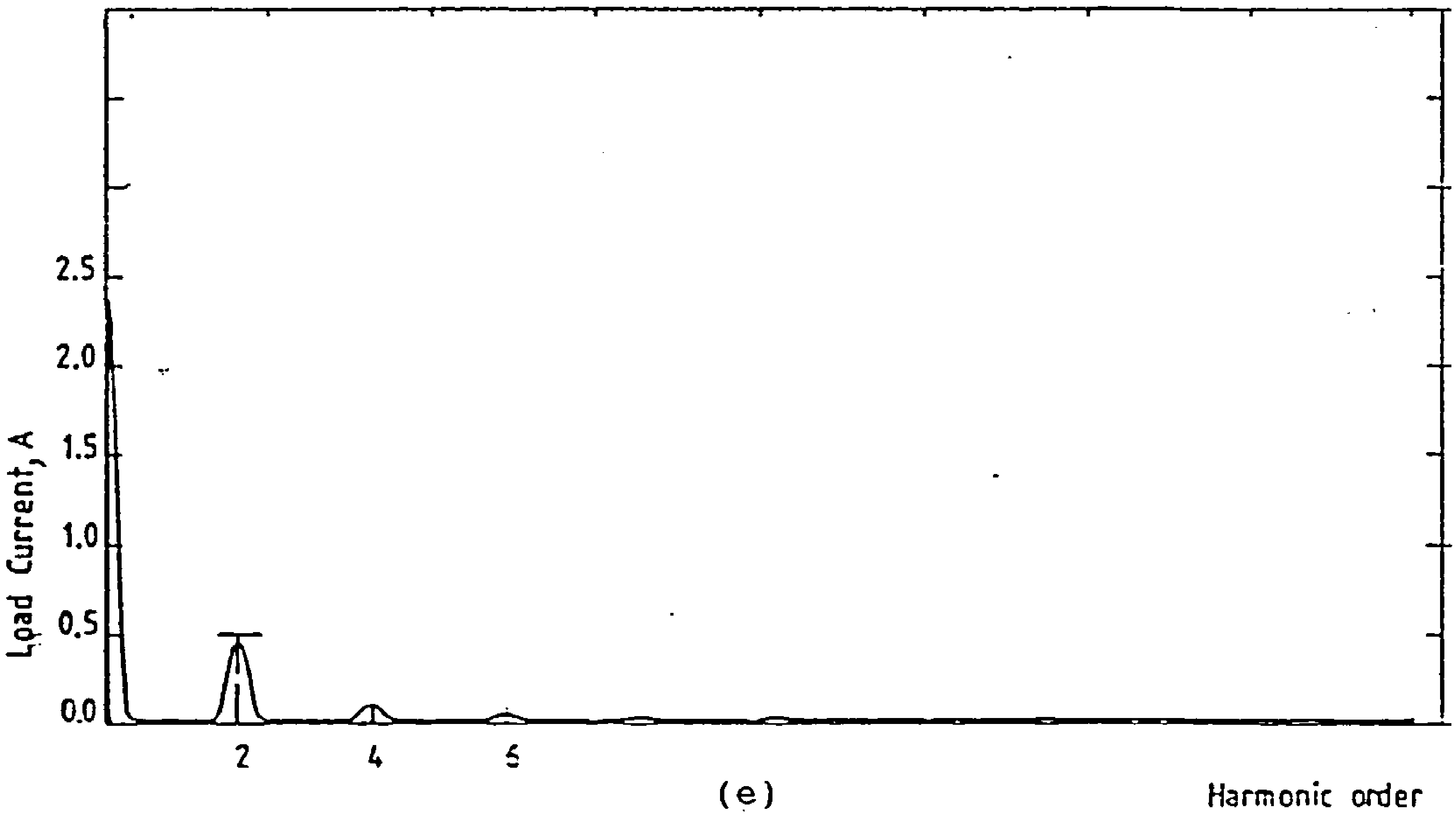

Figure6.9 Continued.
(d) Load voltage spectrum.
(e) Load current spectrum.

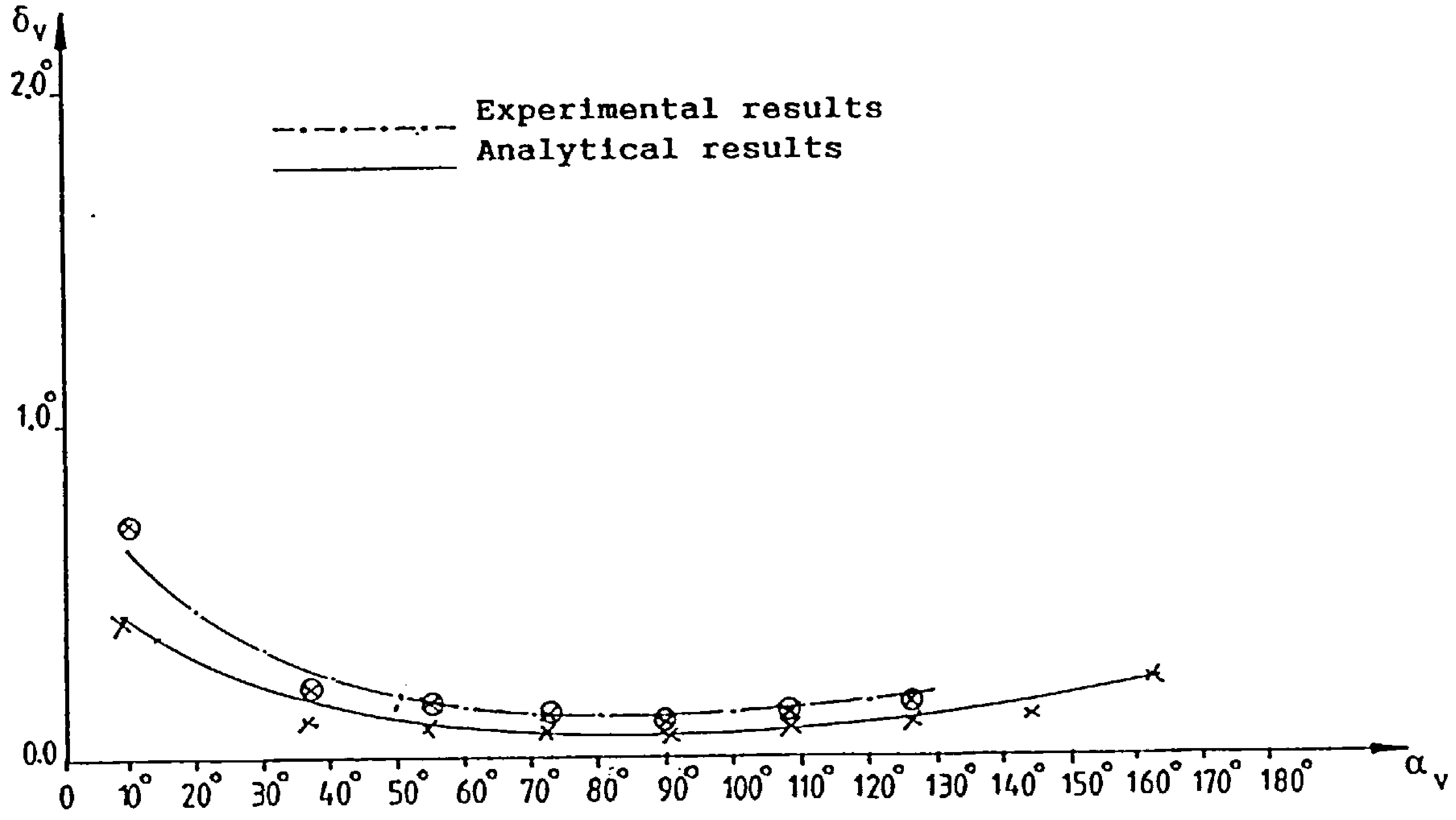

Figure6.10 Variation of commutation angle with firing delay angle for sequence-controlled single-bridge.

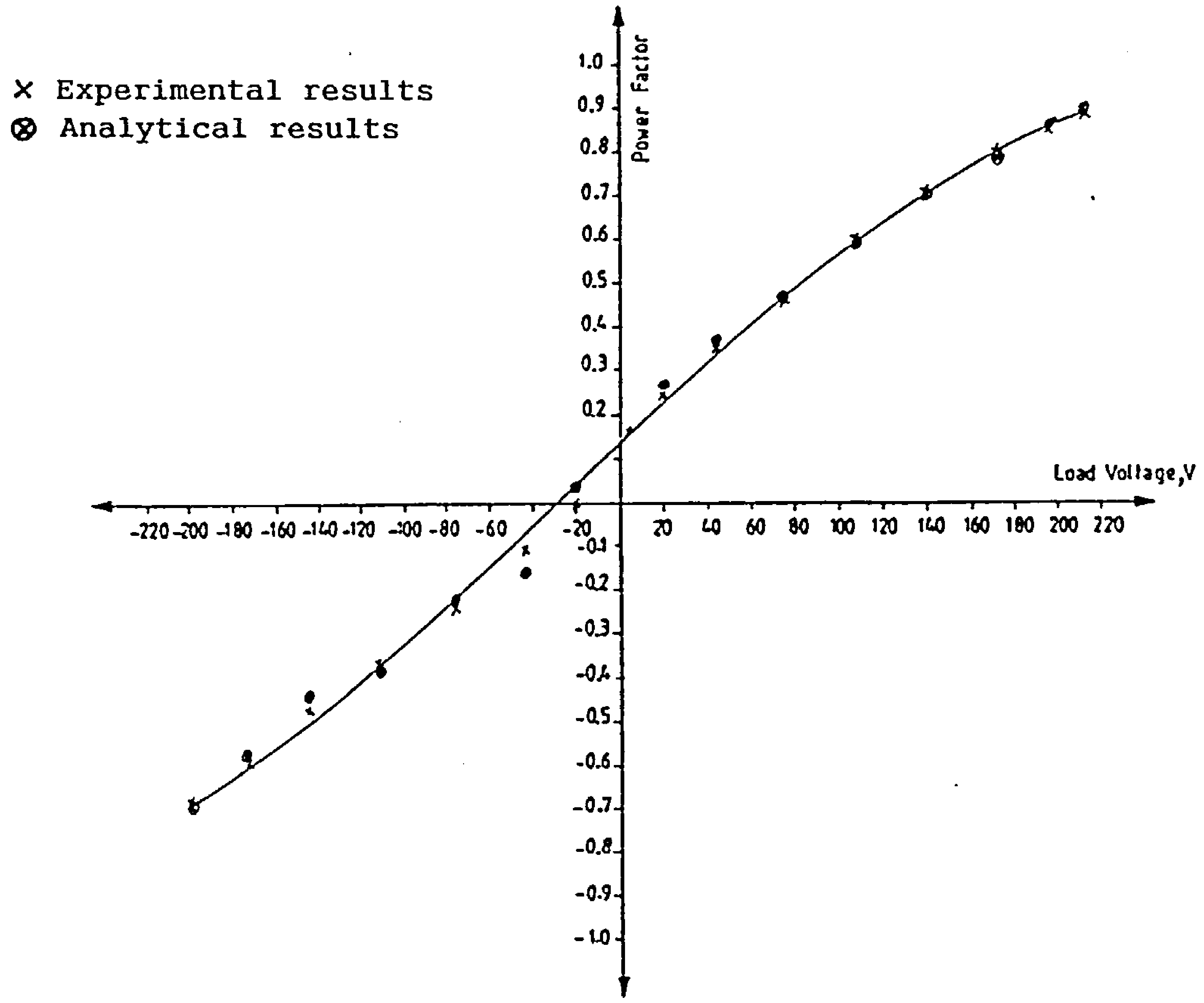

Figure6.11 Experimental and analytical variation of power factor with load voltage for sequence-controlled single-bridge.

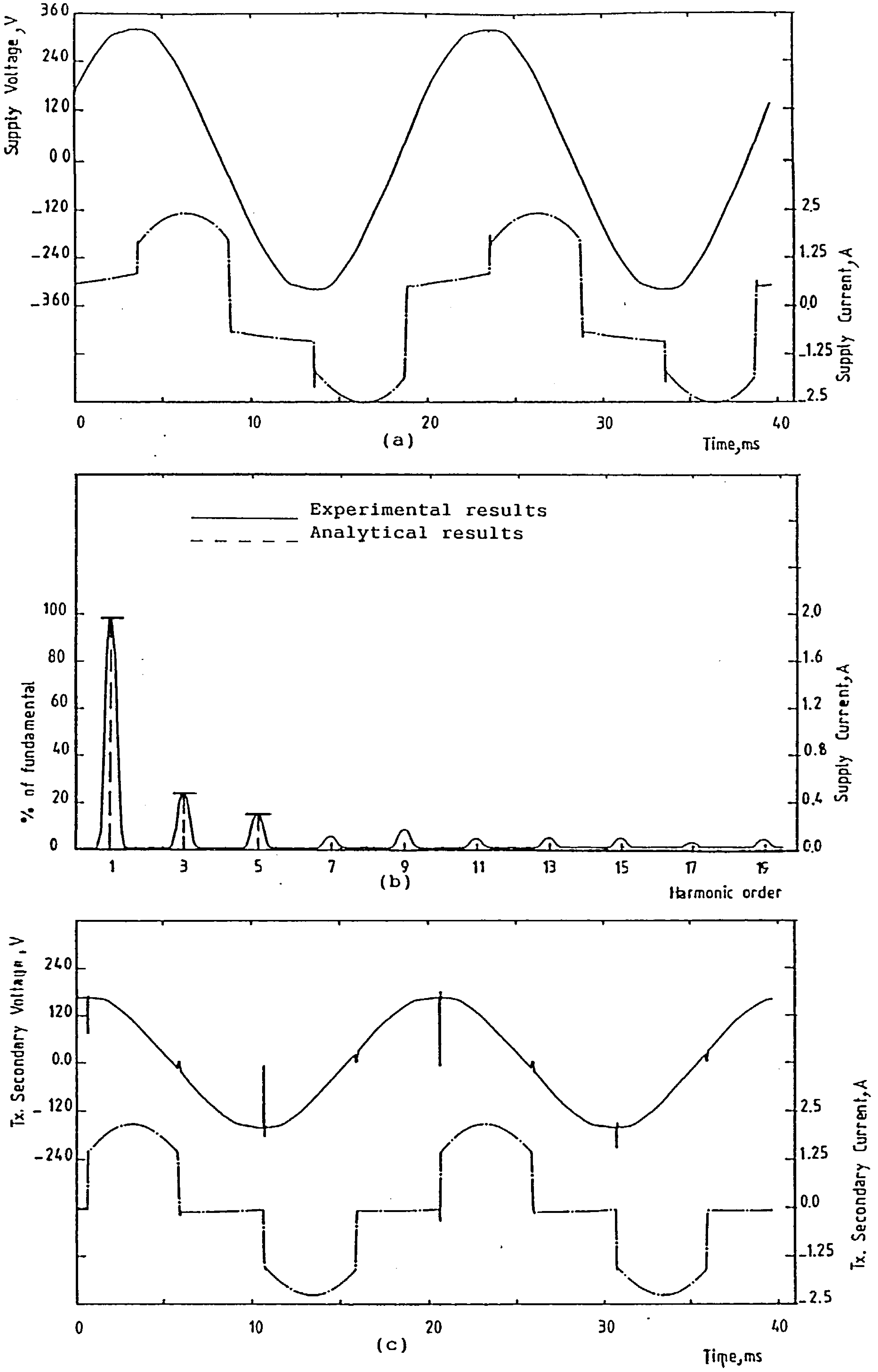

Figure6.12 Experimental results for sequence-controlled double-bridge converter.
(a) Supply voltage and current.
(b) Supplt current spectrum.
(c) Transformer secondary voltage and current of Br.1.
($\alpha_{f1}=\alpha_{f2}=\alpha_{v2}=10^{\circ}, \alpha_{v1}=90^{\circ}, R_1=80\Omega, L_1=0.3H, V_1=159V$)

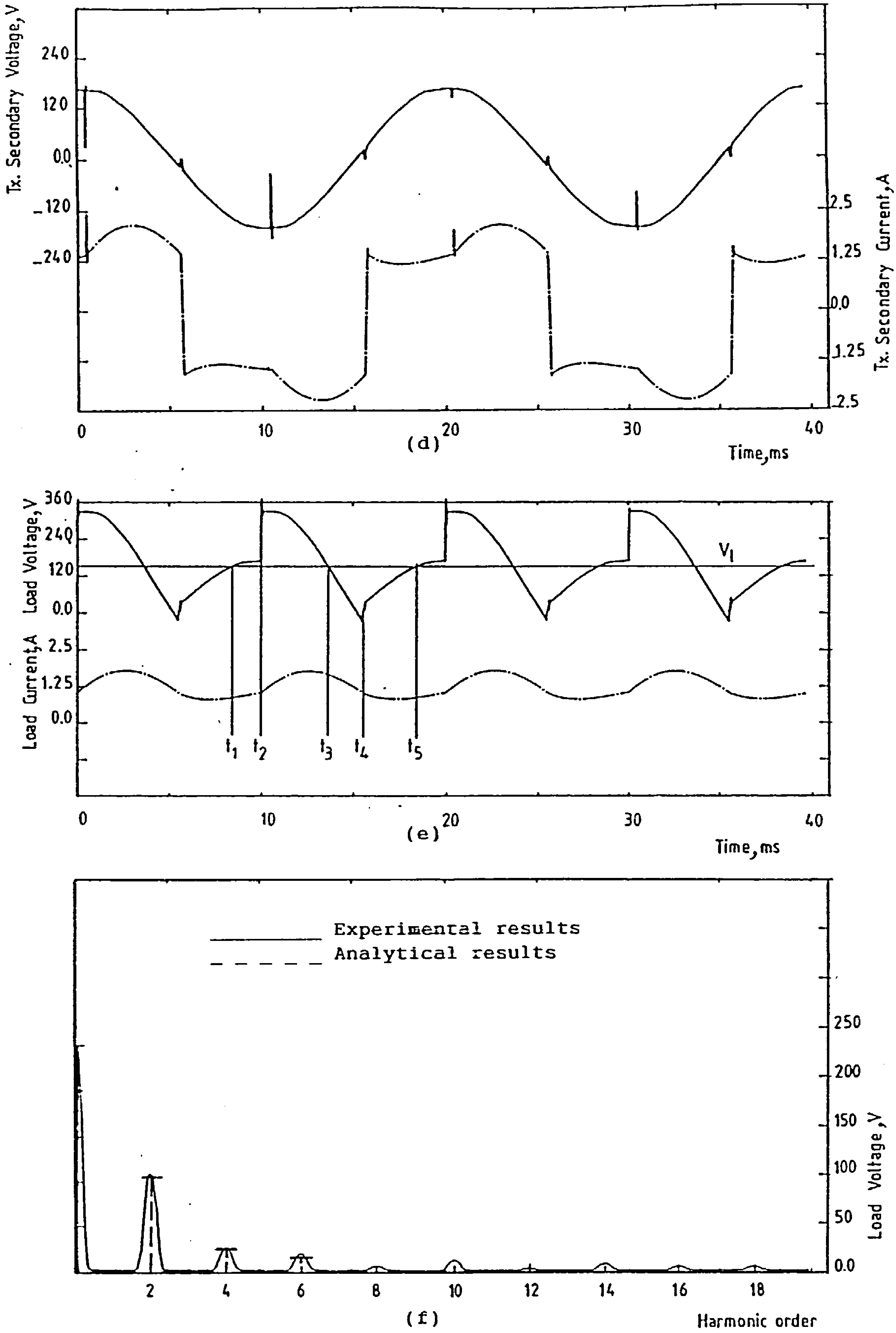

Figure6.12 Continued.
(d) Transformer secondary voltage and current of Br.2.
(e) Load voltage and current.
(f) Load voltage spectrum.

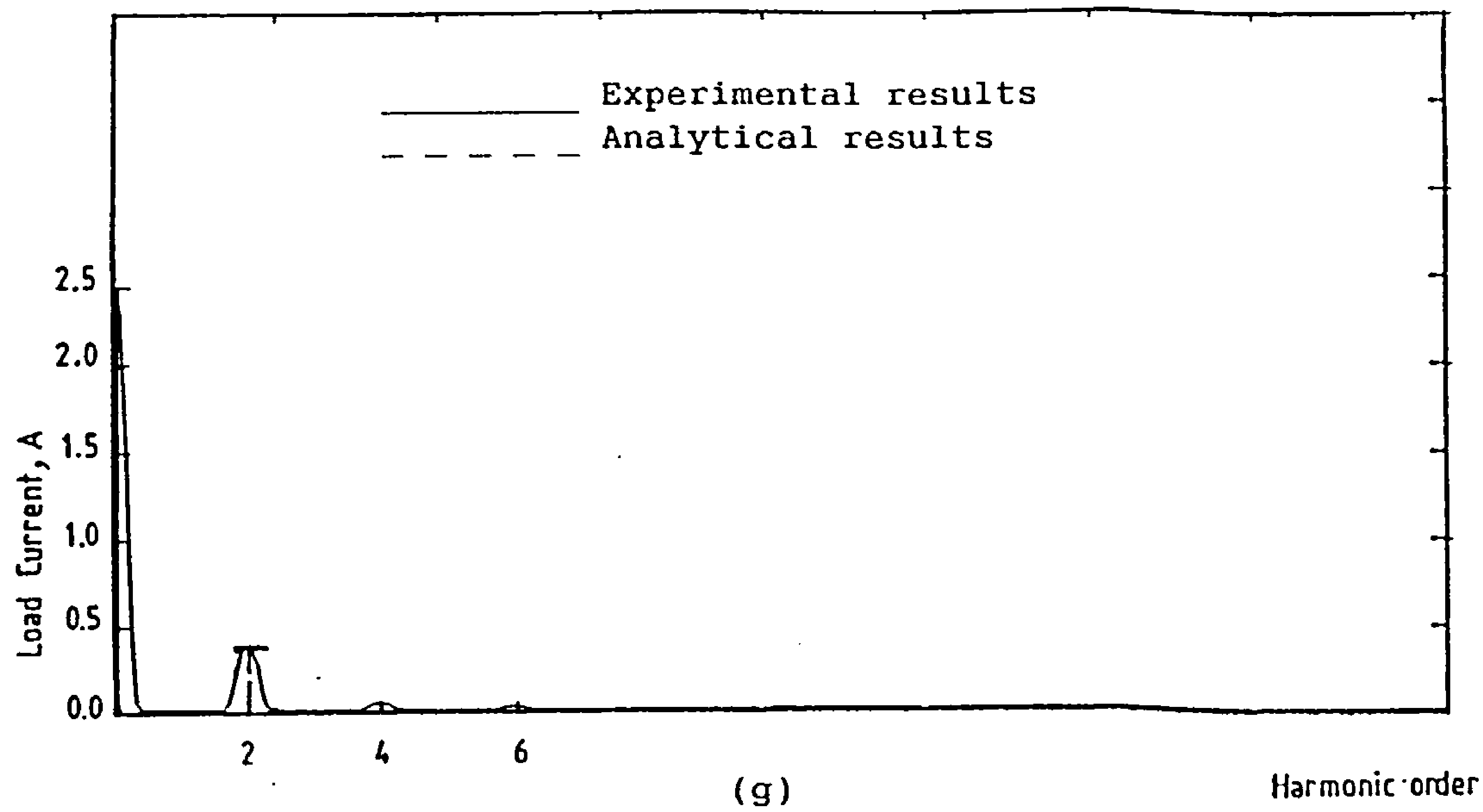

Figure6.12 Continued.
(g) Load current spectrum.

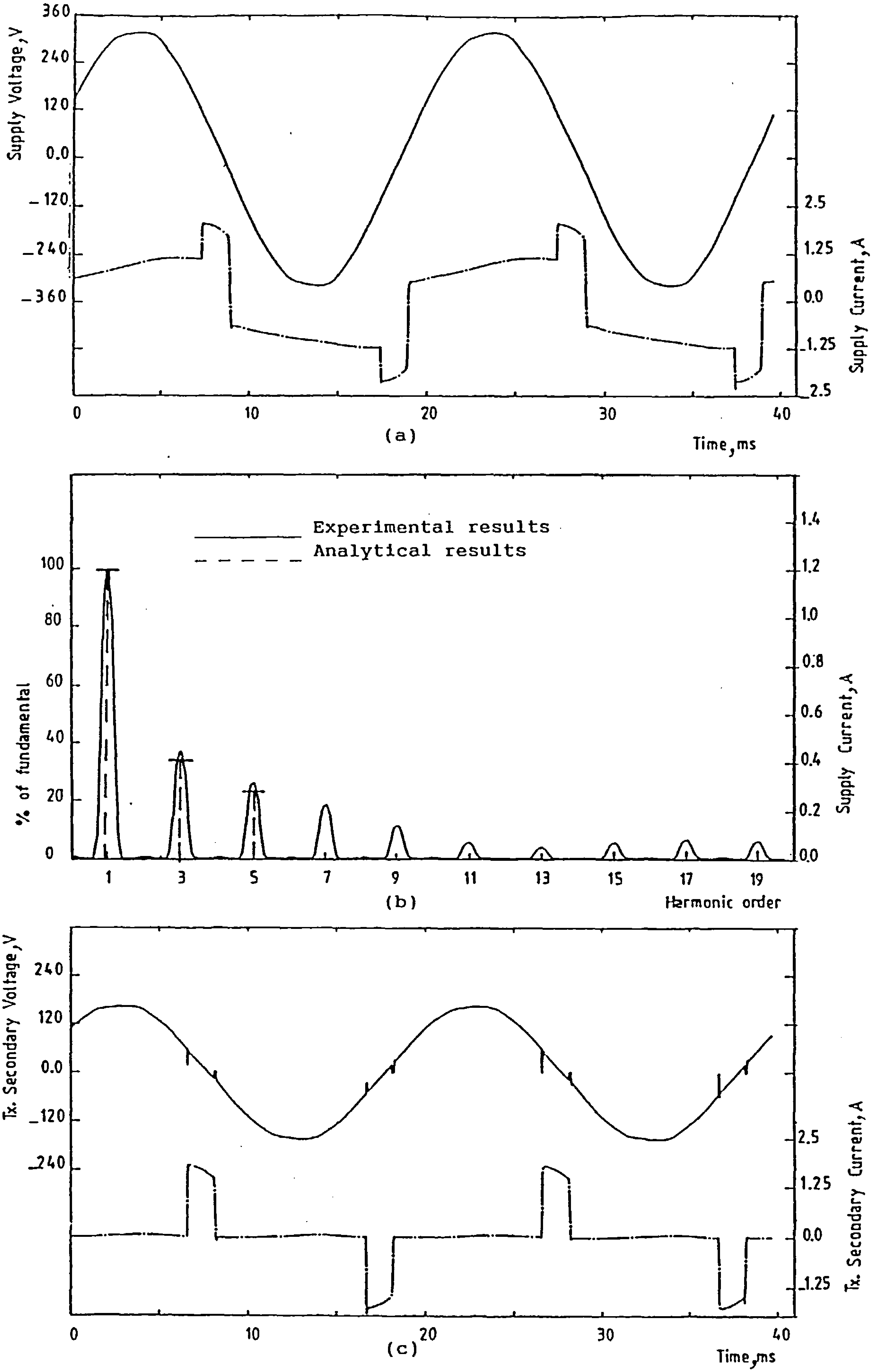

Figure6.13 Experimental results for sequence-controlled double-bridge converter.

(a) Supply voltage and current.

(b) Supply current spectrum.

(c) Transformer secondary voltage and current of Br.1.

($\alpha_{f1}=\alpha_{f2}=\alpha_{v2}=10^{o}, \alpha_{v1}=160^{o}, R_1=54\Omega, L_1=0.3H, V_1=108V$)

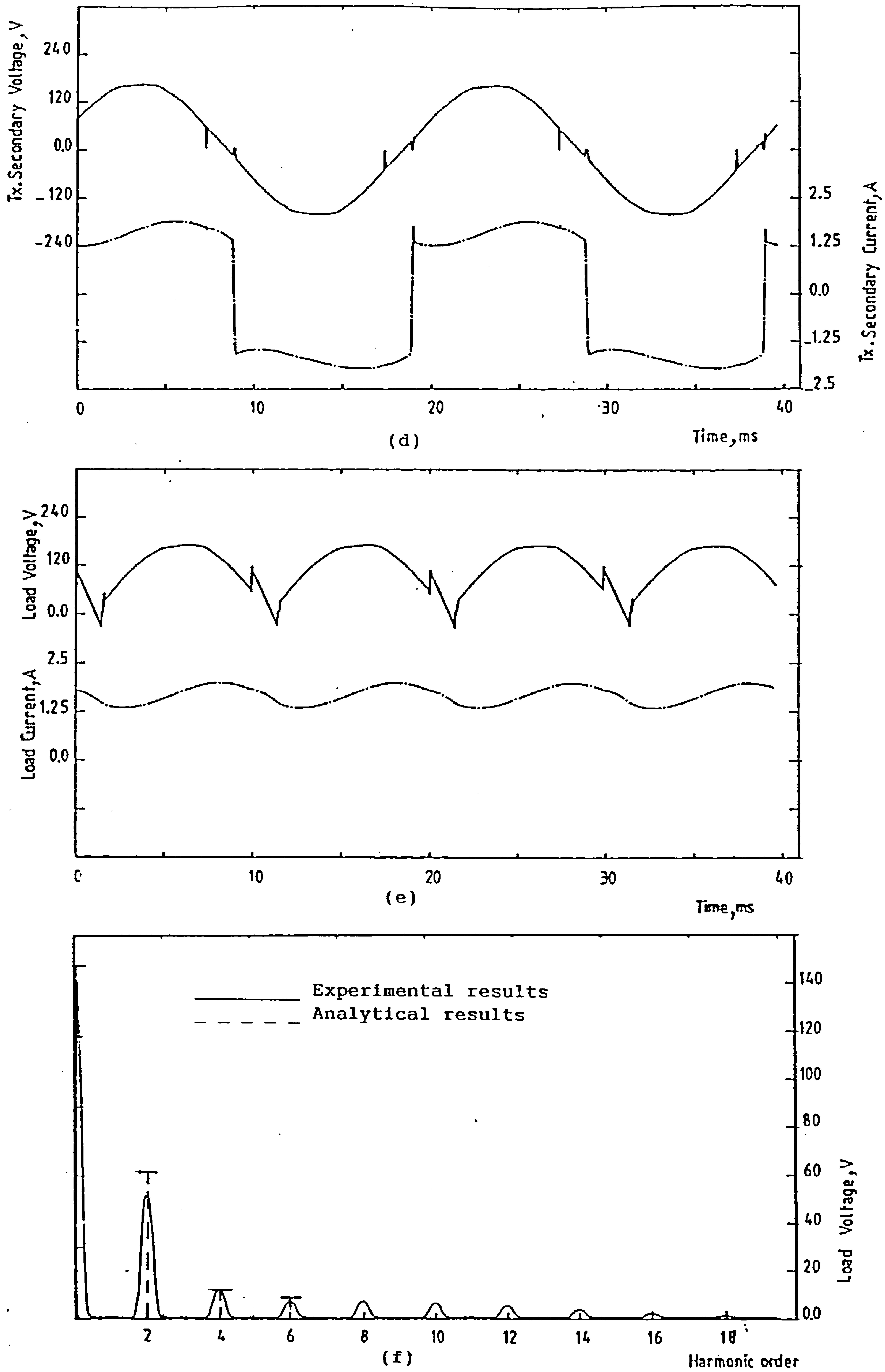

Figure6.13 Continued.
(d) Transformer secondary voltage and current of Br.2.
(e) Load voltage and current.
(f) Load voltage spectrum.

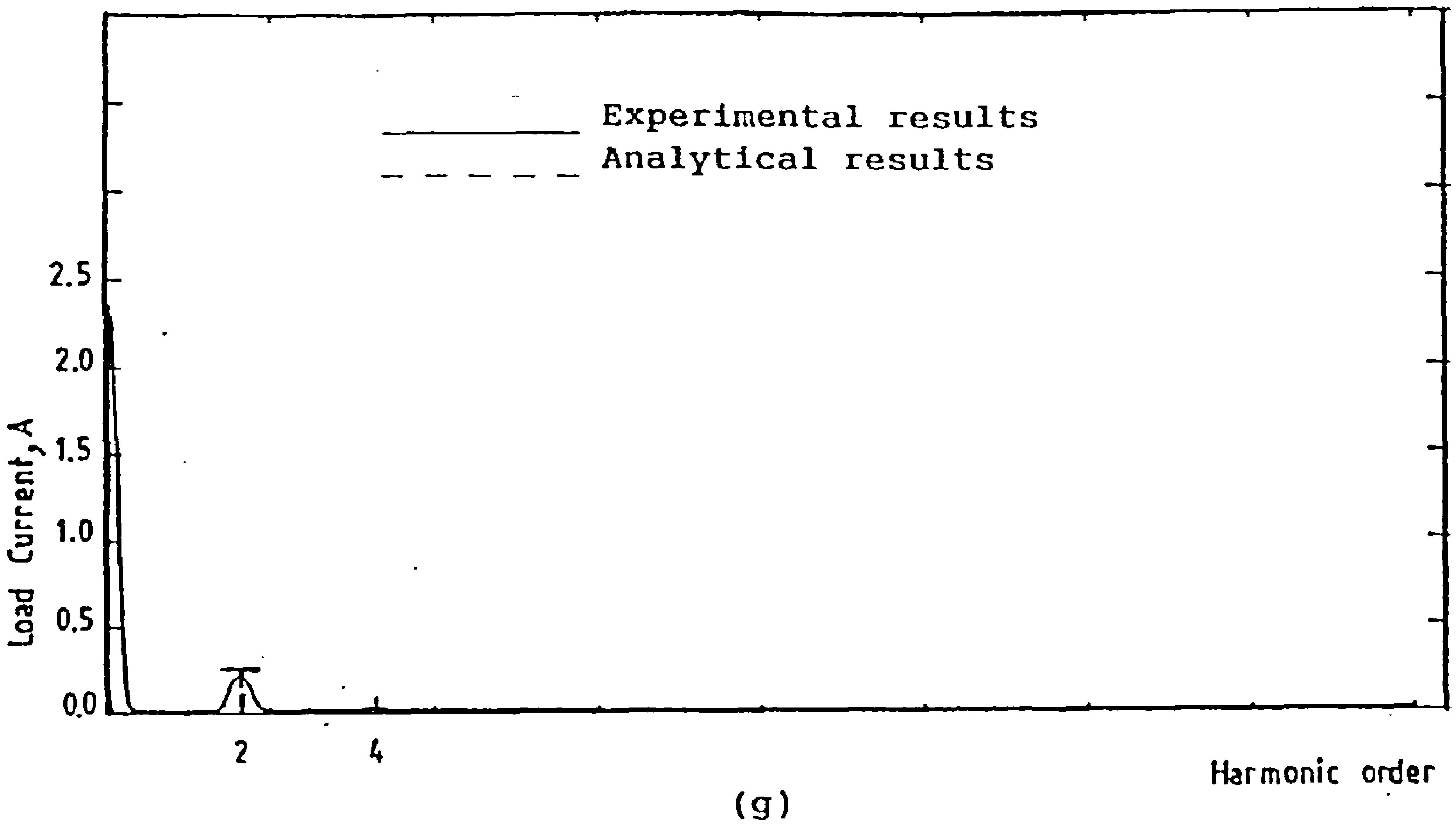

(g)

Figure6.13 Continued.
(g) Load current spectrum.

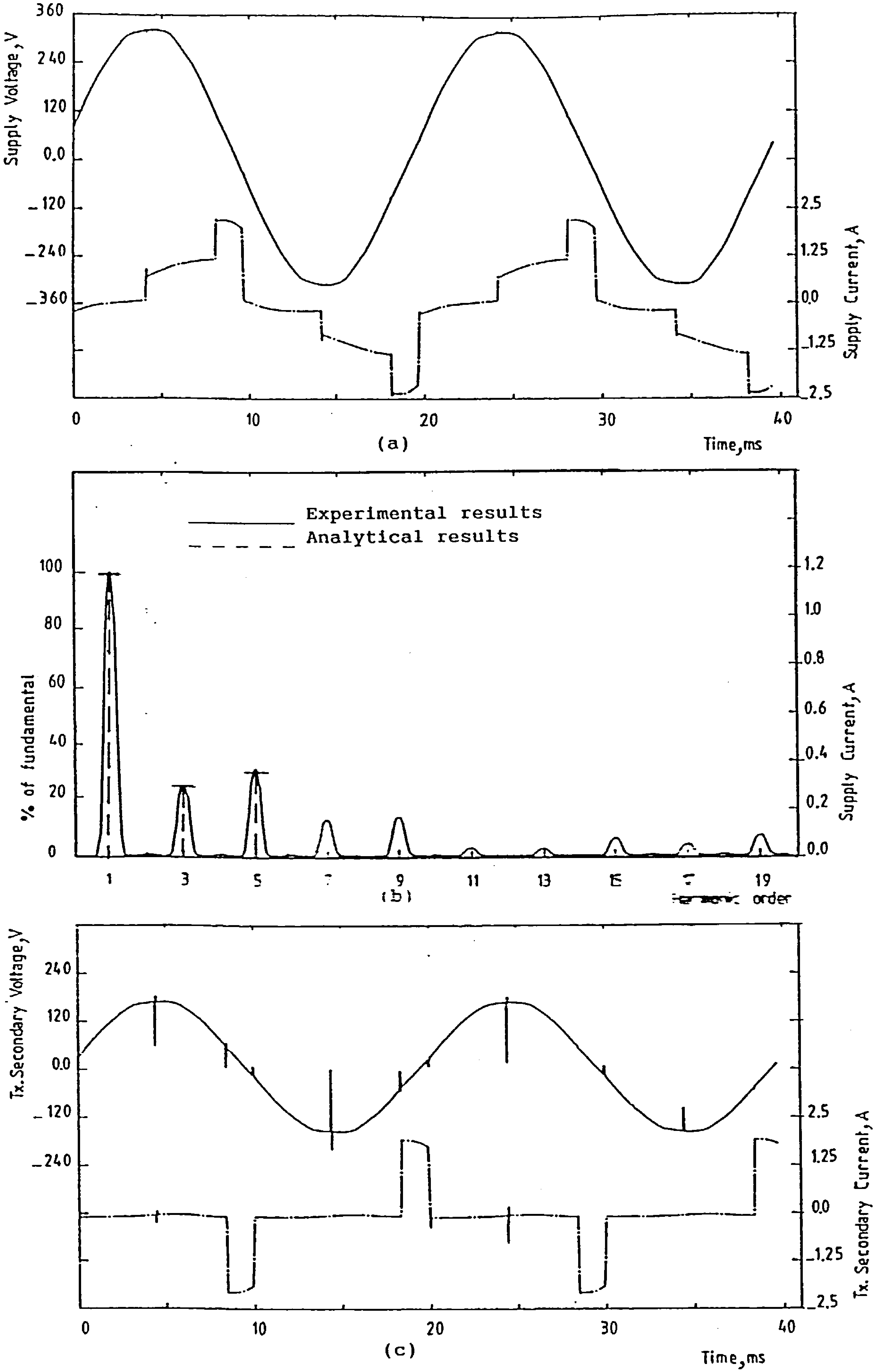

Figure6.14 Experimental results for sequence-controlled double-bridge converter.

(a) Supply voltage and current.

(b) Supply current spectrum.

(c) Transformer secondary voltage and current of Br.1.

($\alpha_{f1}=\alpha_{f2}=10^{\circ}, \alpha_{v1}=160^{\circ}, \alpha_{v2}=90^{\circ}, R_1=27\Omega, L_1=0.3H, V_1=55V$)

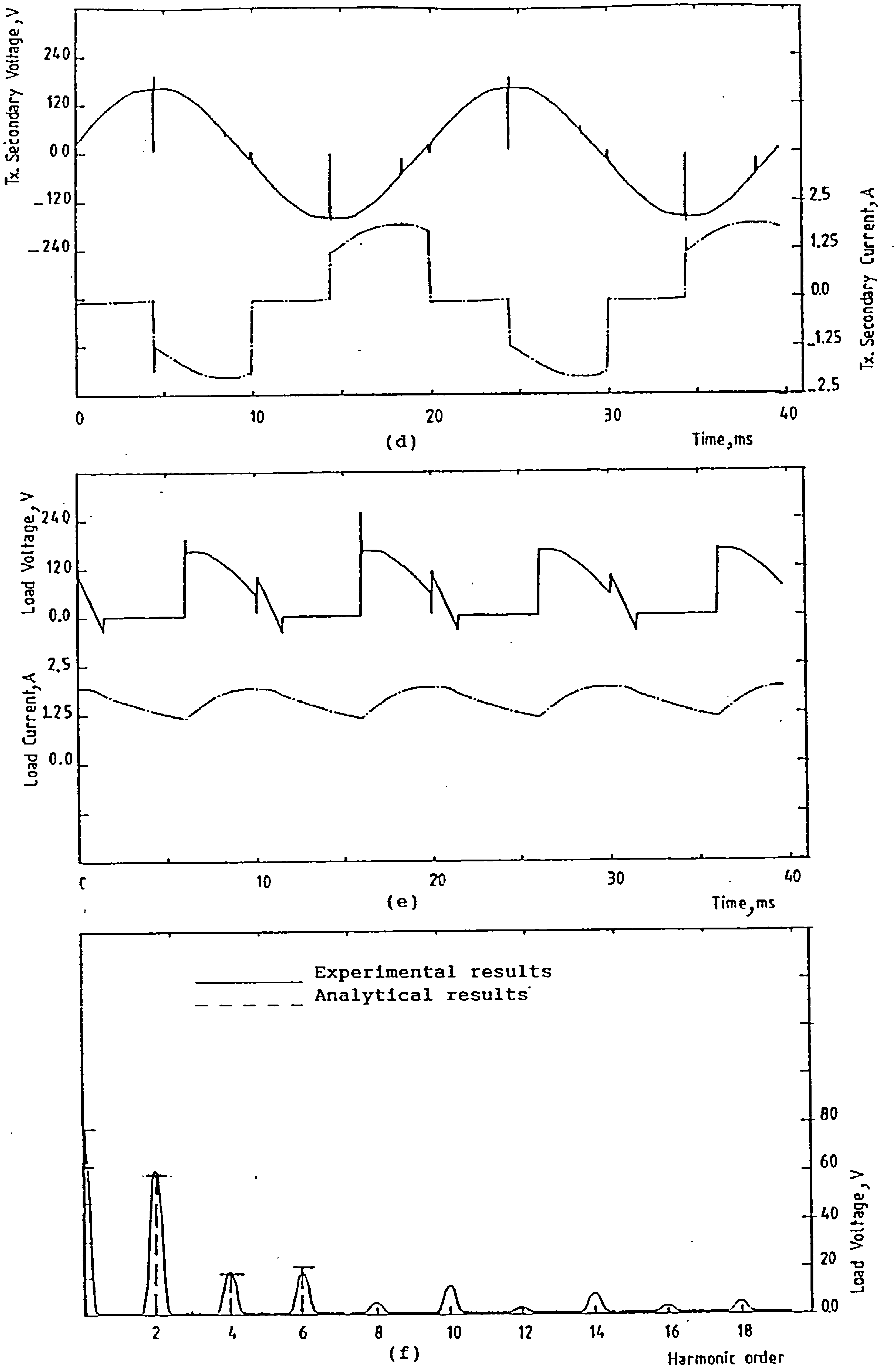

Figure6.14 Continued.
(d) Transformer secondary voltage and current of Br.2.
(e) Load voltage and current.
(f) Load voltage spectrum.

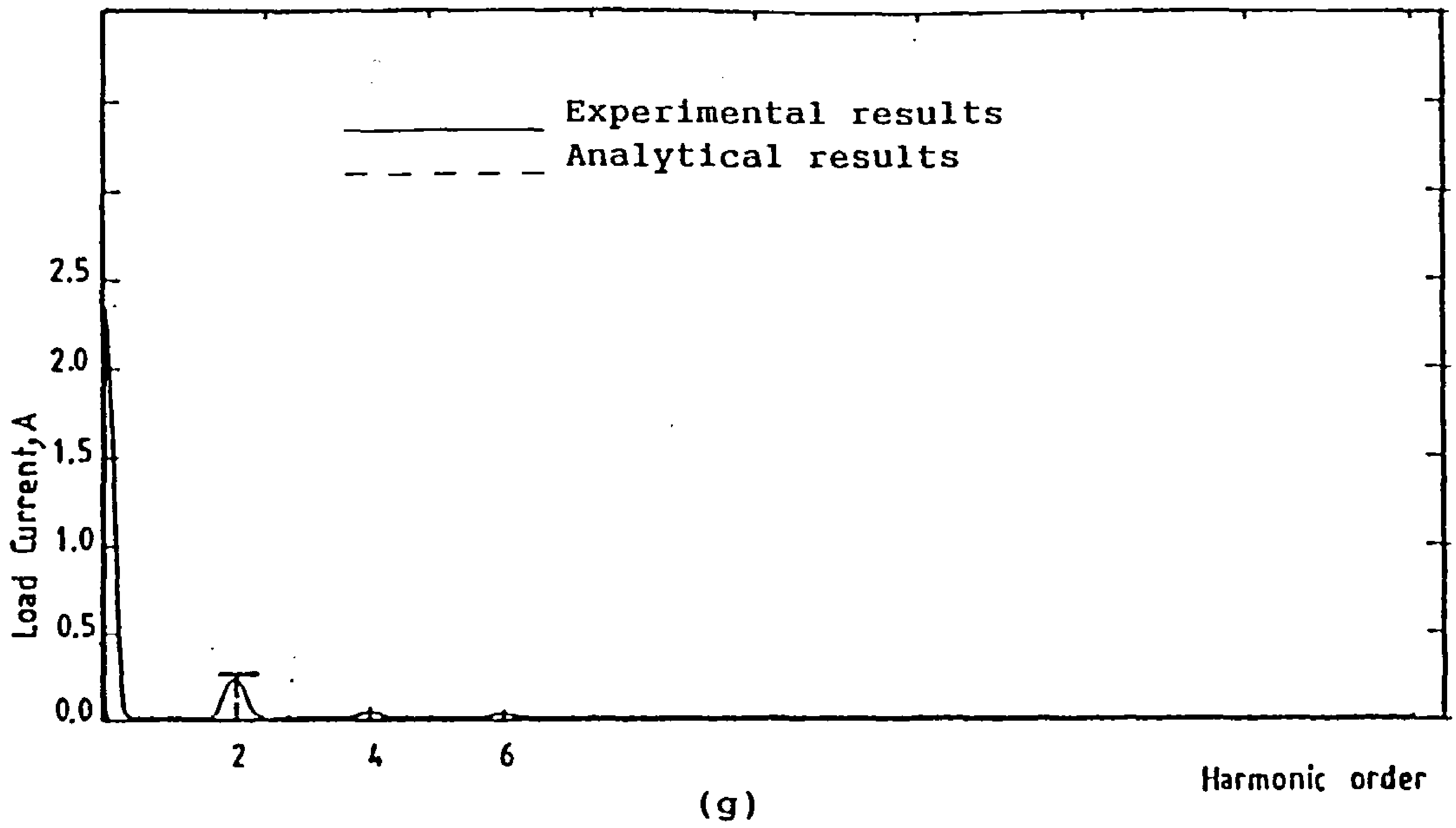

Figure6.14 Continued.
(g) Load current spectrum.

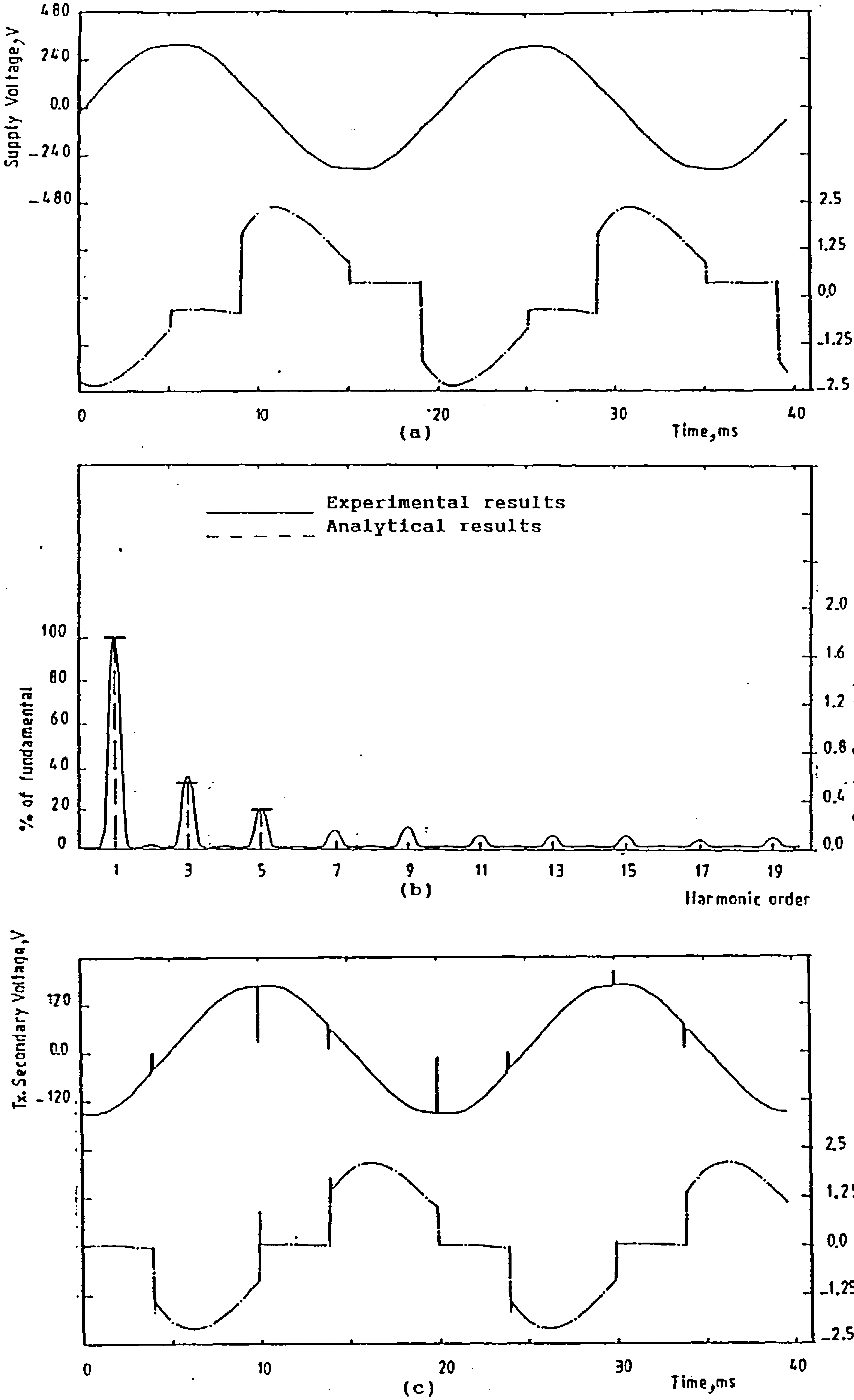

Figure6.15 Experimental results for sequence-controlled double-bridge converter.

(a) Supply voltage and current.

(b) Supply current spectrum.

(c) Transformer secondary voltage and current of Br.1.

($\alpha_{f1}=90^{\circ}, \alpha_{v1}=\alpha_{f2}=\alpha_{v2}=160^{\circ}, R_1=34\Omega, L_1=0.3H, V_1=-152V, V_{dc}=220V$)

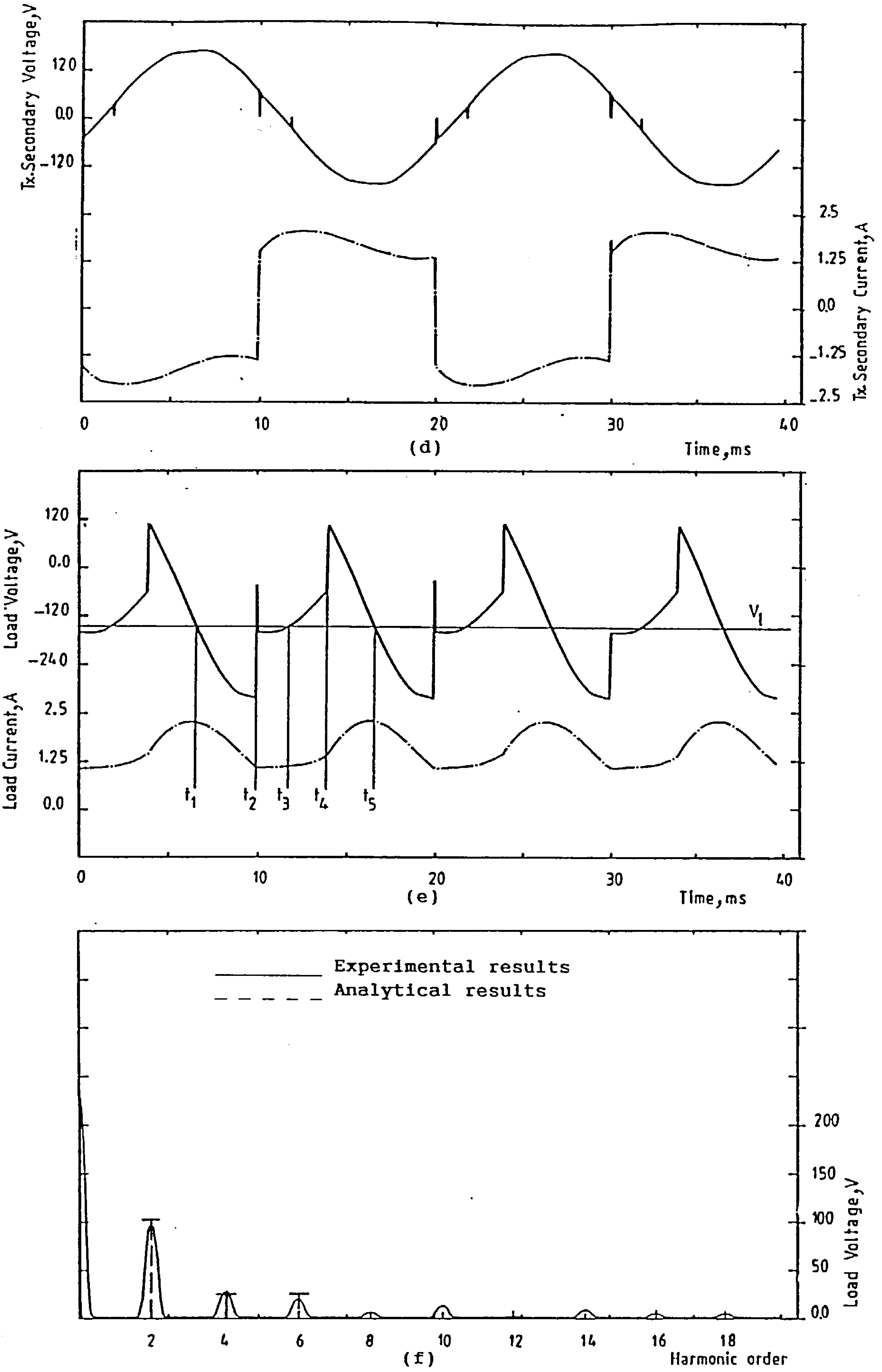

Figure6.15 Continued.
(d) Transformer secondary voltage and current of Br.2.
(e) Load voltage and current.
(f) Load voltage spectrum.

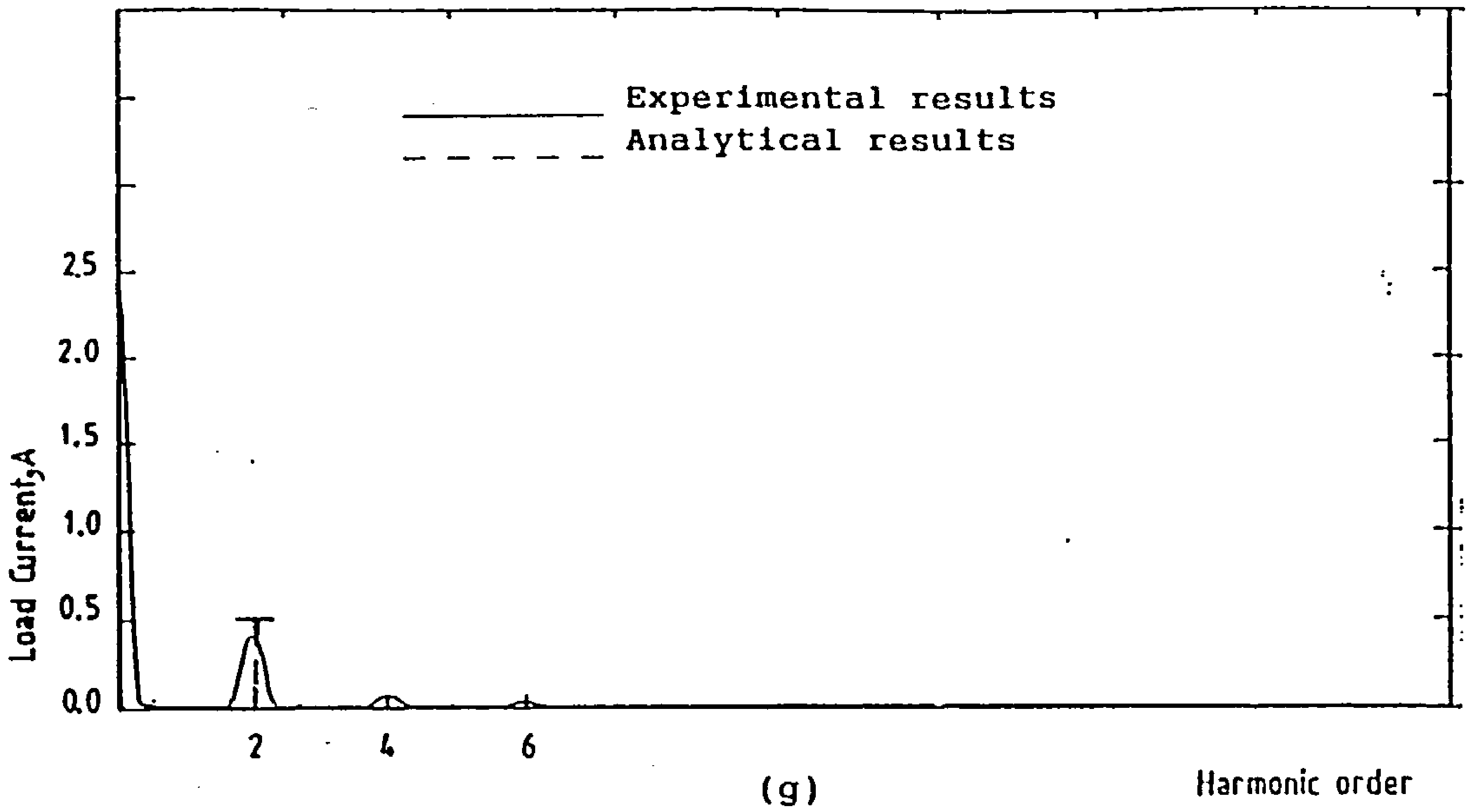

Figure6.15 Continued.
(g) Load current spectrum.

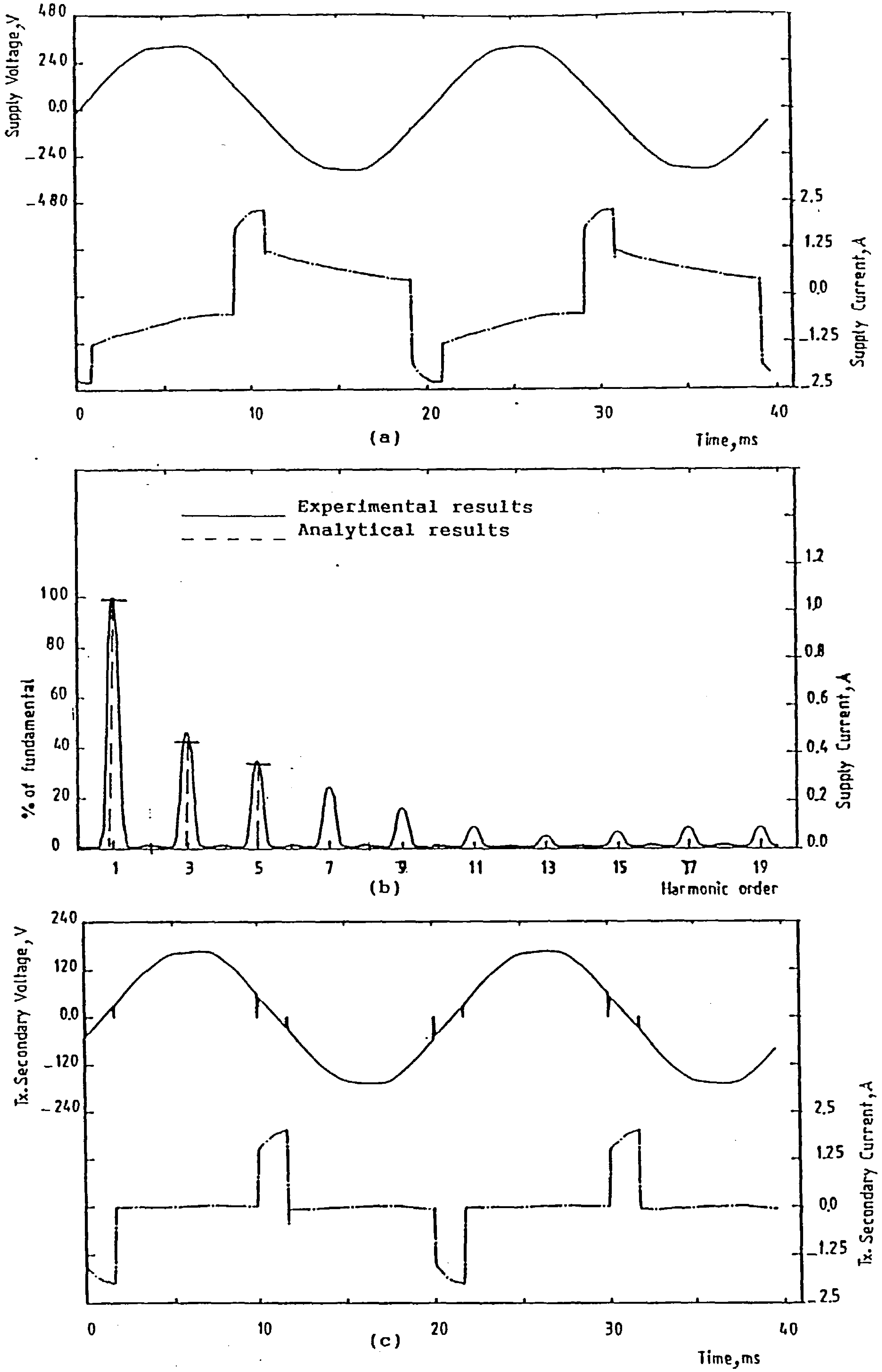

Figure6.16 Experimental results for sequence-controlled double-bridge converter.
(a) Supply voltage and current.
(b) Supply current spectrum.
(c) Transformer secondary voltage and current of Br.1.
($\alpha_{f1}=10^o, \alpha_{v1}=\alpha_{f2}=\alpha_{v2}=160^o, R_1=54\Omega, L_1=0.3H, V_1 \doteq -99V, V_{dc}=207V$)

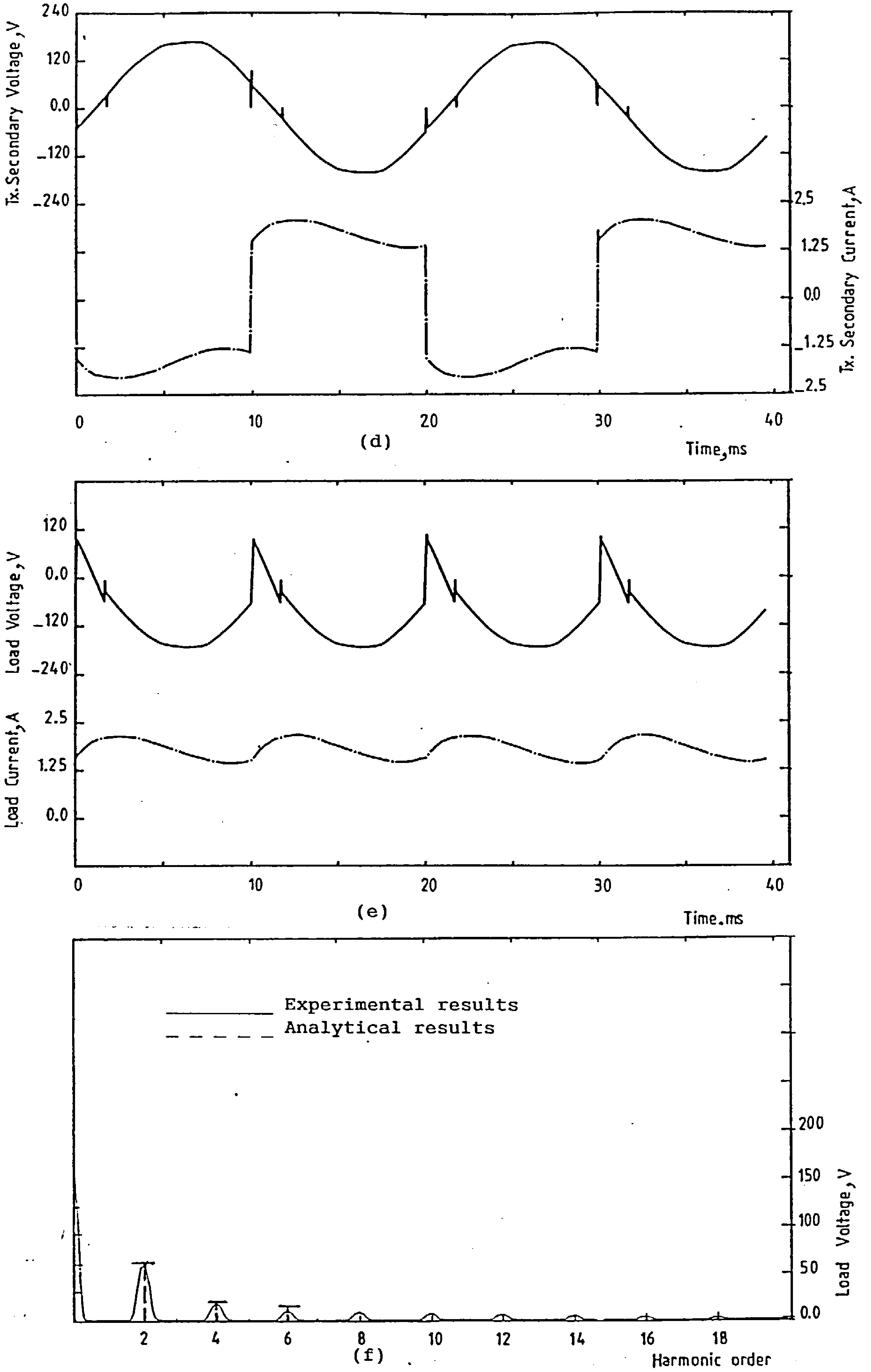

Figure6.16 Continued.
(d) Transformer secondary voltage and current of Br.2.
(e) Load voltage and current.
(f) Load voltage spectrum.

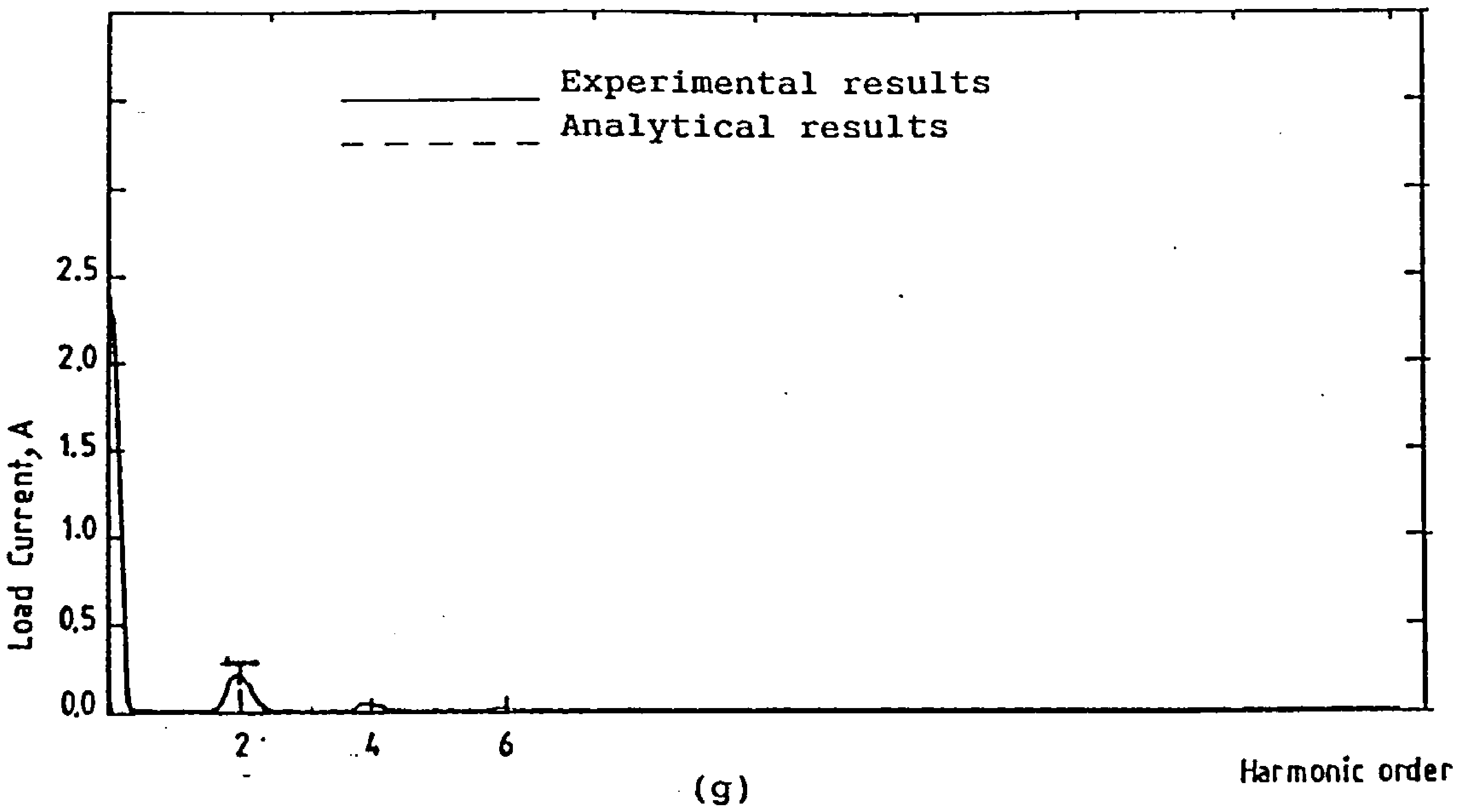

Figure6.16 Continued.
(g) Load current spectrum.

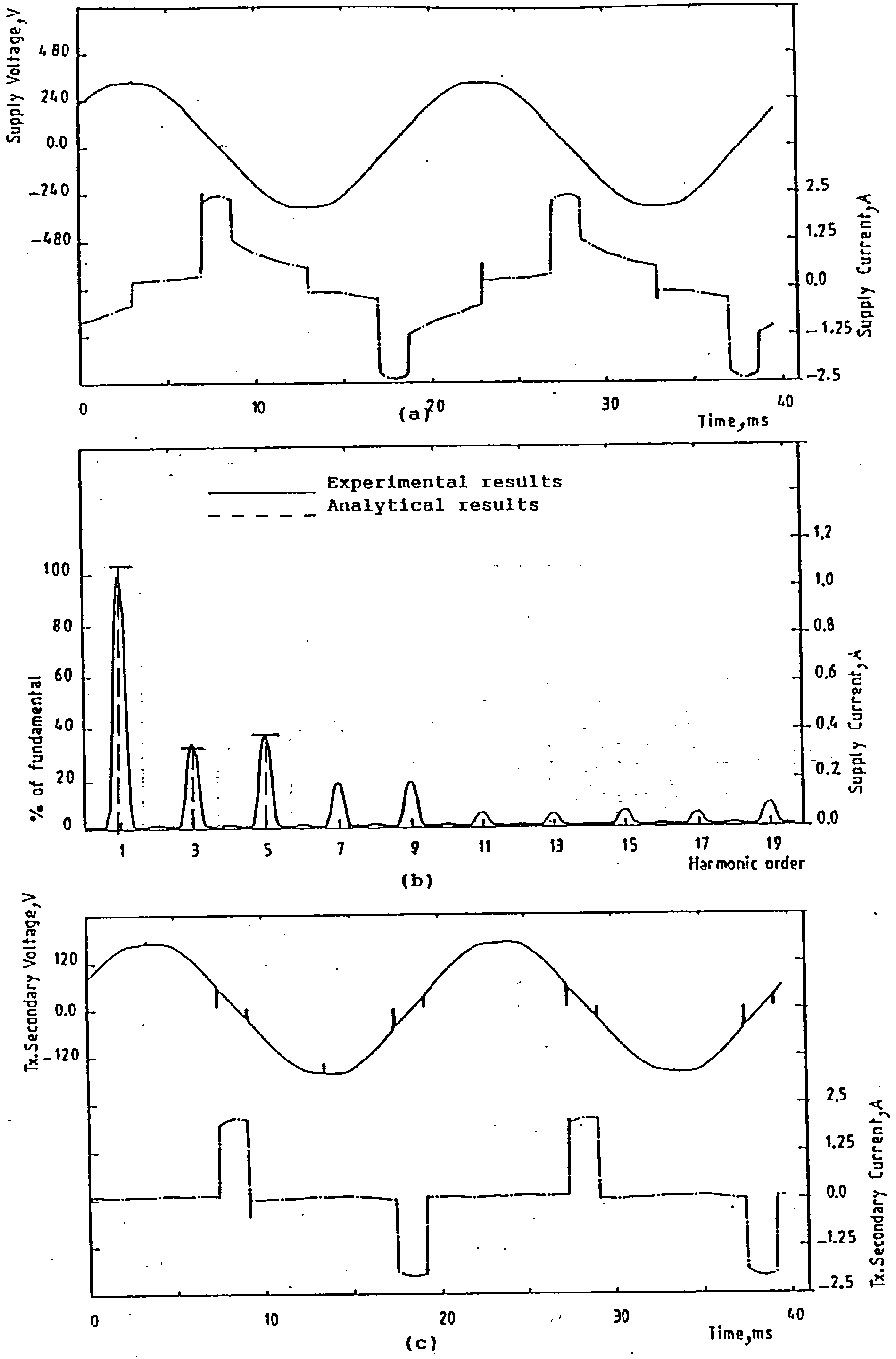

Figure6.17 Experimental results for sequence-controlled double-bridge converter.
(a) Supply voltage and current.
(b) Supply current spectrum.
(c) Transformer secondary voltage and current of Br.1.

$(\alpha_{f1}=10^{o}, \alpha_{v1}=\alpha_{v2}=160^{o}, \alpha_{f2}=90^{o}, R_1=27\Omega, L_1=0.3H, V_1=-48V, V_{dc}=102V)$

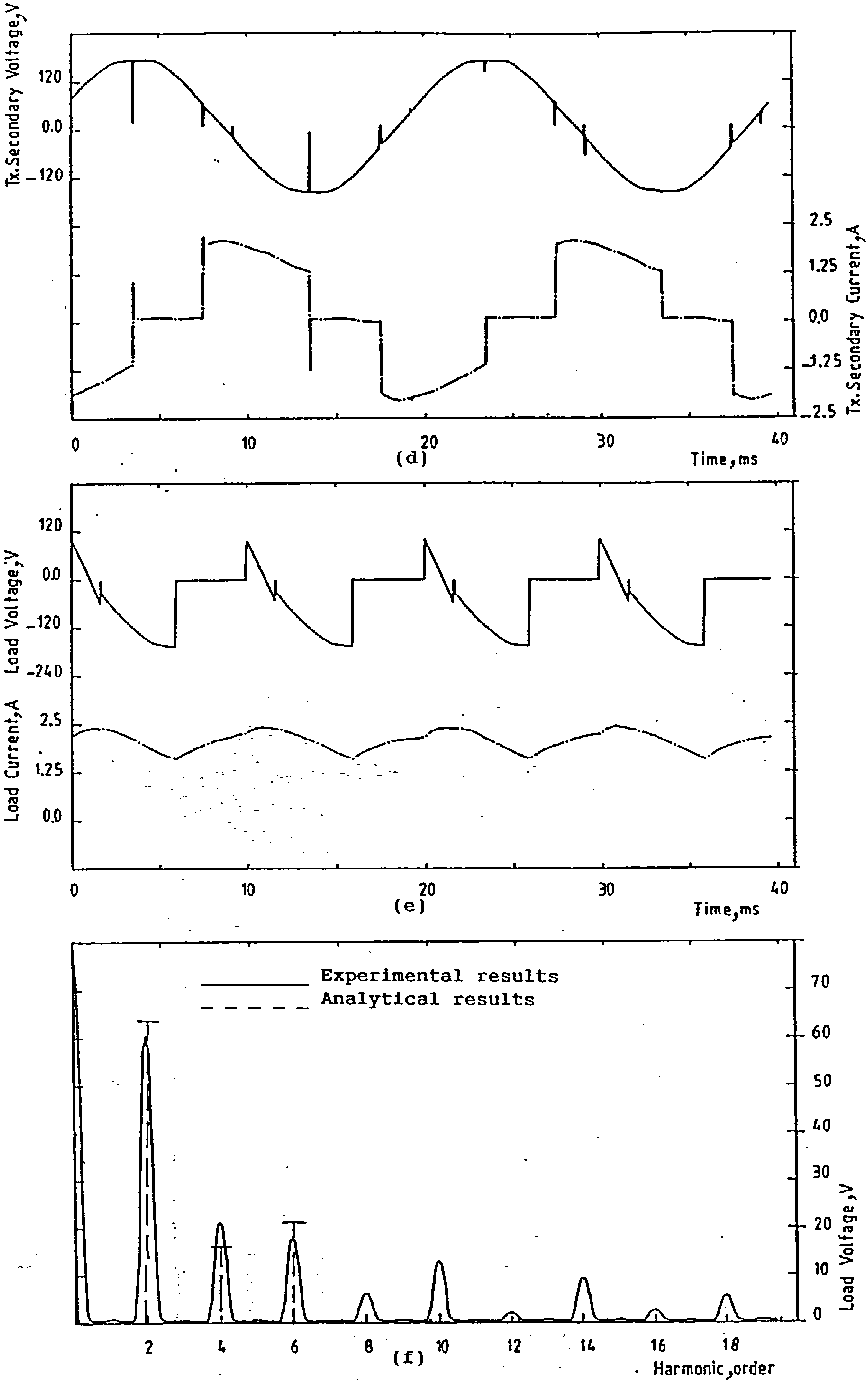

Figure6.17 Continued.
(d) Transformer secondary voltage and current of Br.2.
(e) Load voltage and current.
(f) Load voltage spectrum.

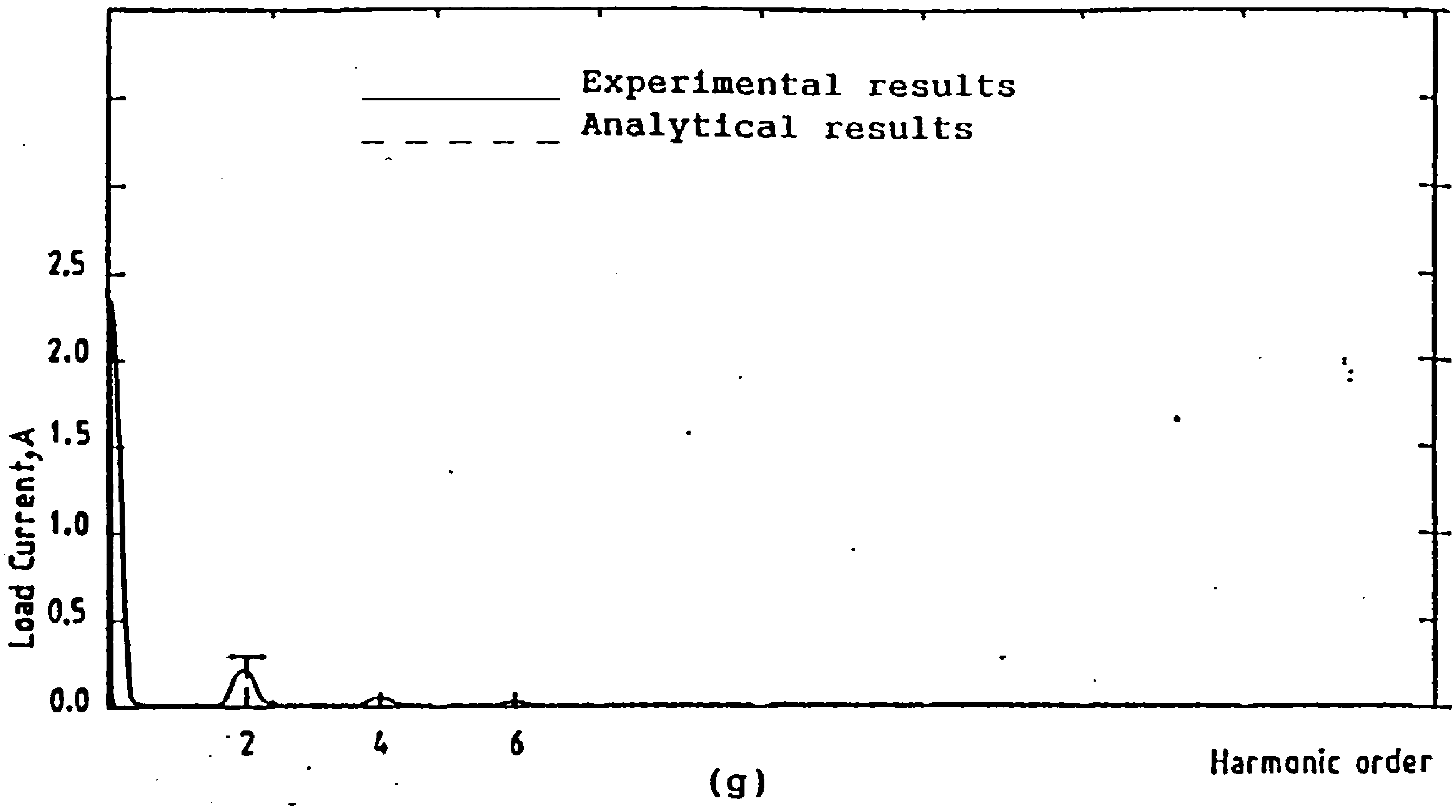

Figure6.17 Continued.
(g) Load current spectrum.

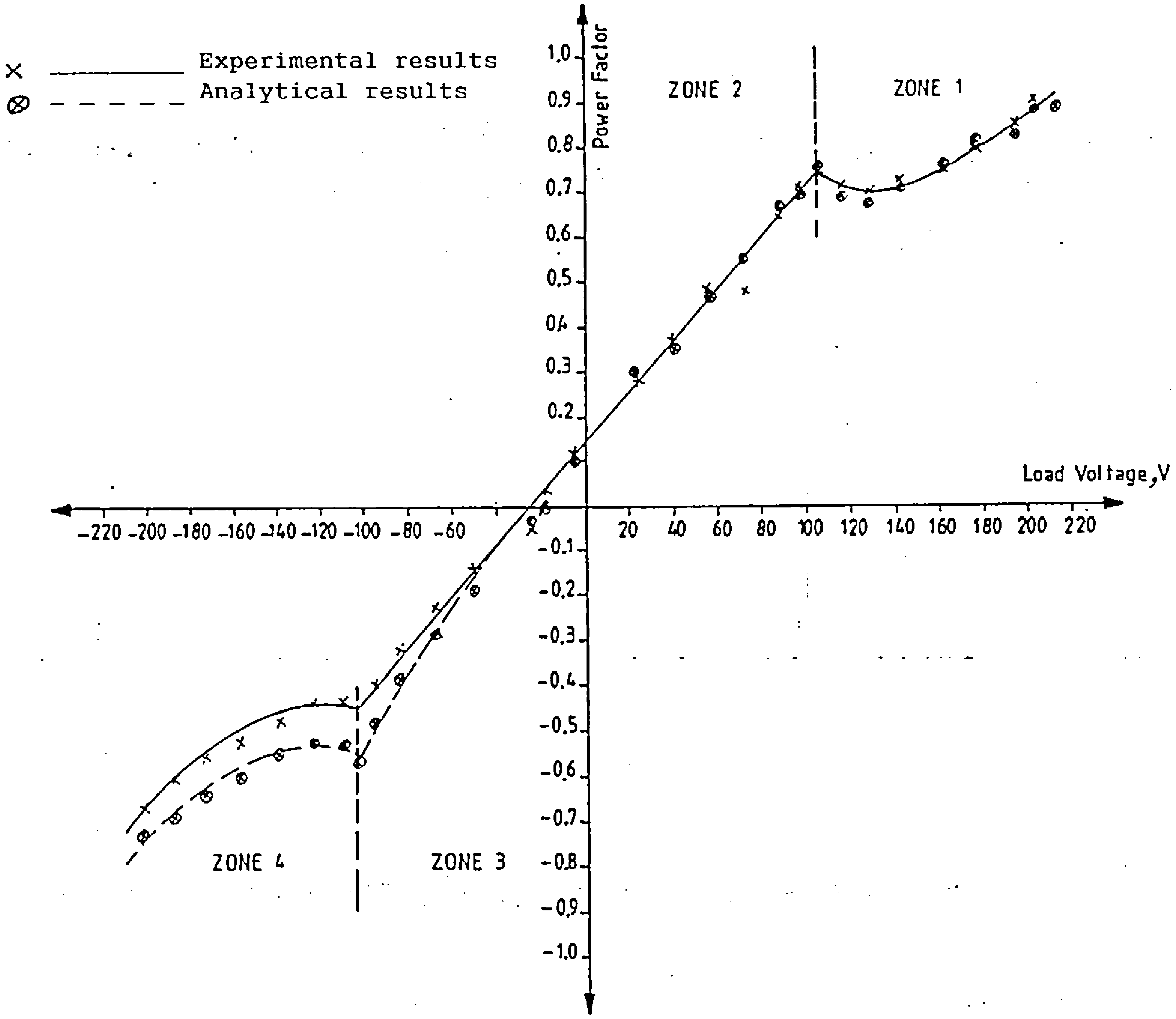

Figure6.18 Experimental and analytical variation of power factor with load voltage for sequence controlled double-bridge.

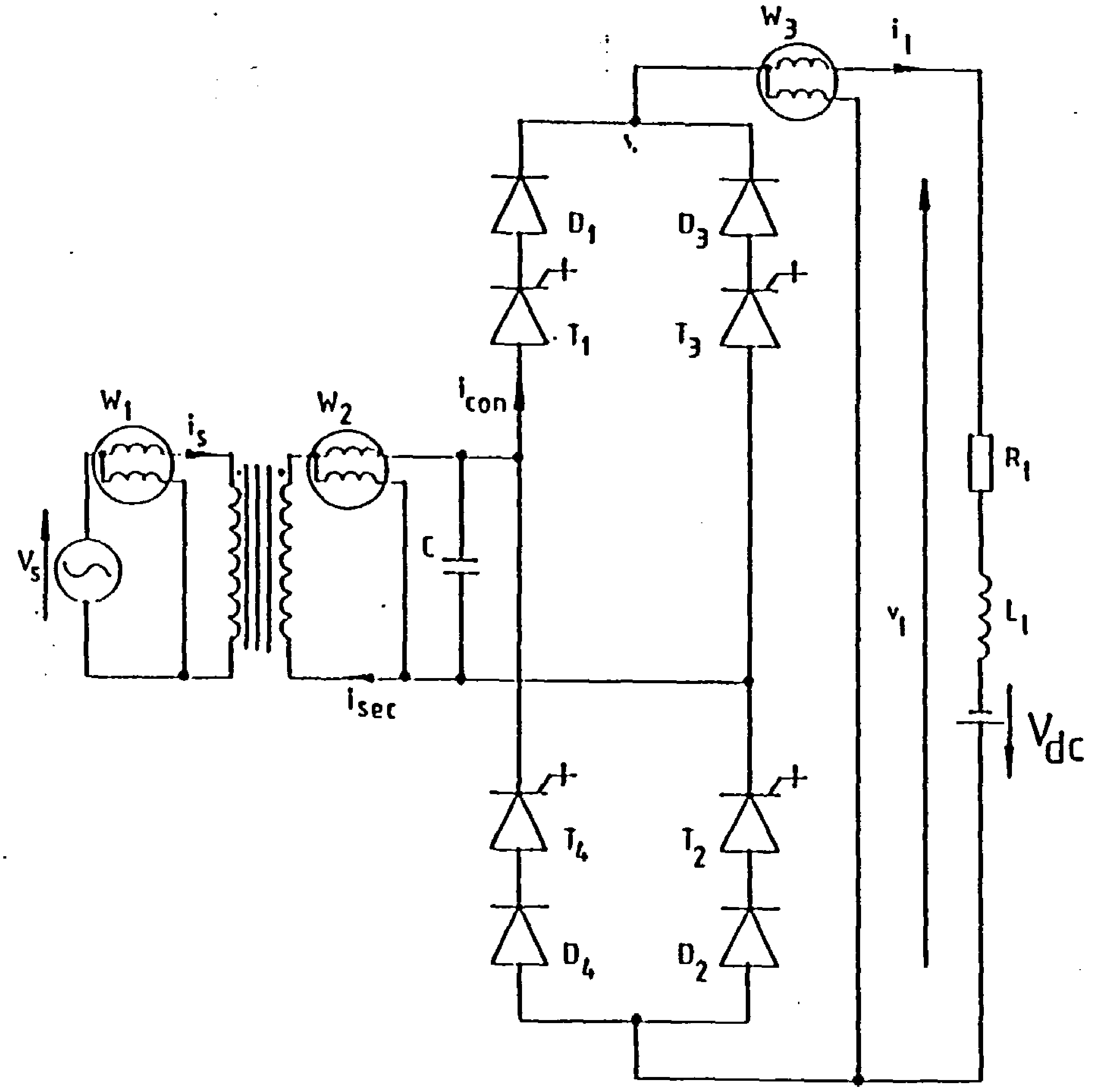

Figure6.19 Fully-controlled PWM bridge converter connected to a passive load.

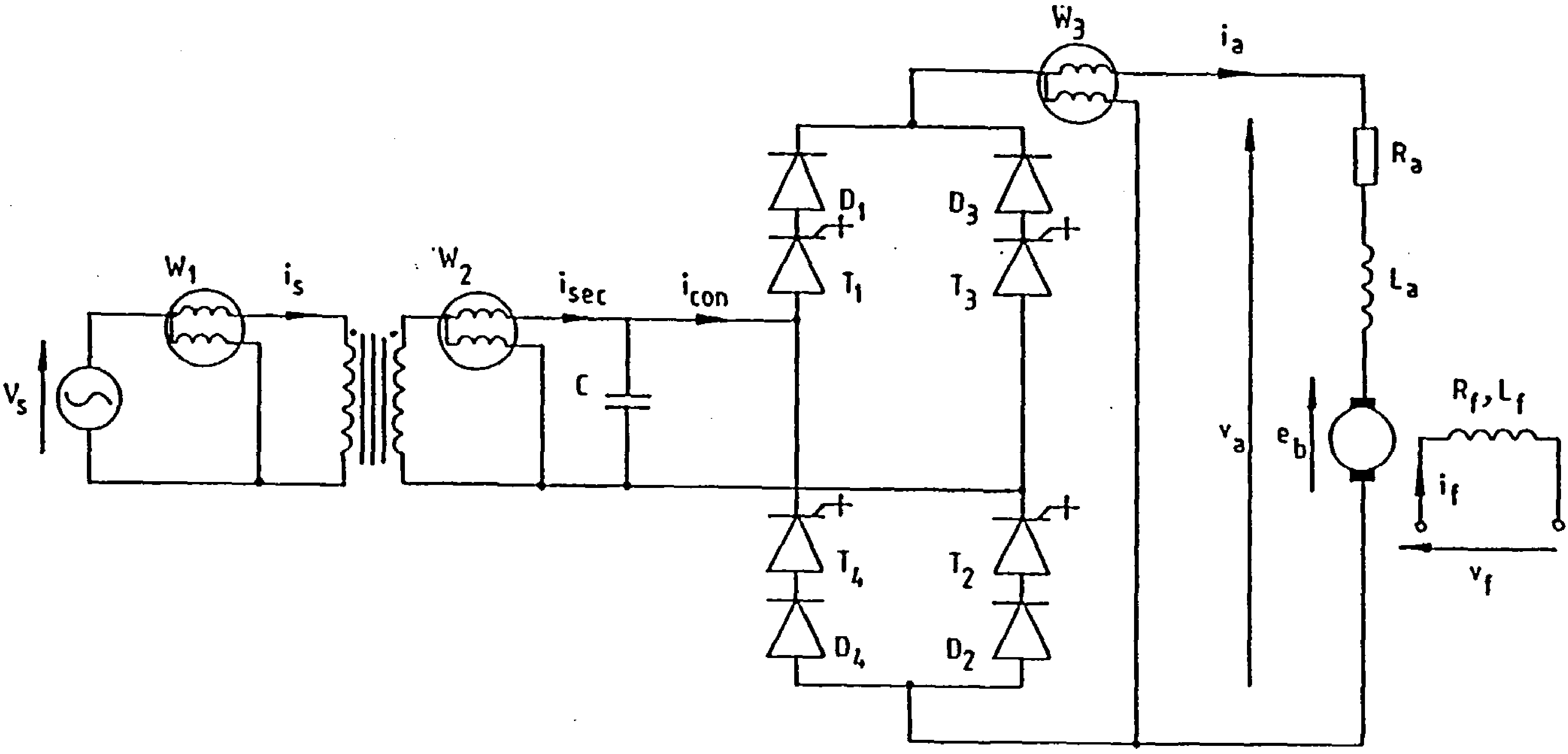

Figure6.20 Fully-controlled PWM bridge converter connected to a dc

Figure6.21 Experimental results for PWM bridge converter connected to a passive load.
(a) Supply voltage and current.
(b) Transformer secondary voltage and current.
(f_c=2kHz,R_1=80Ω,L_1=0.3H,V_1=159V)

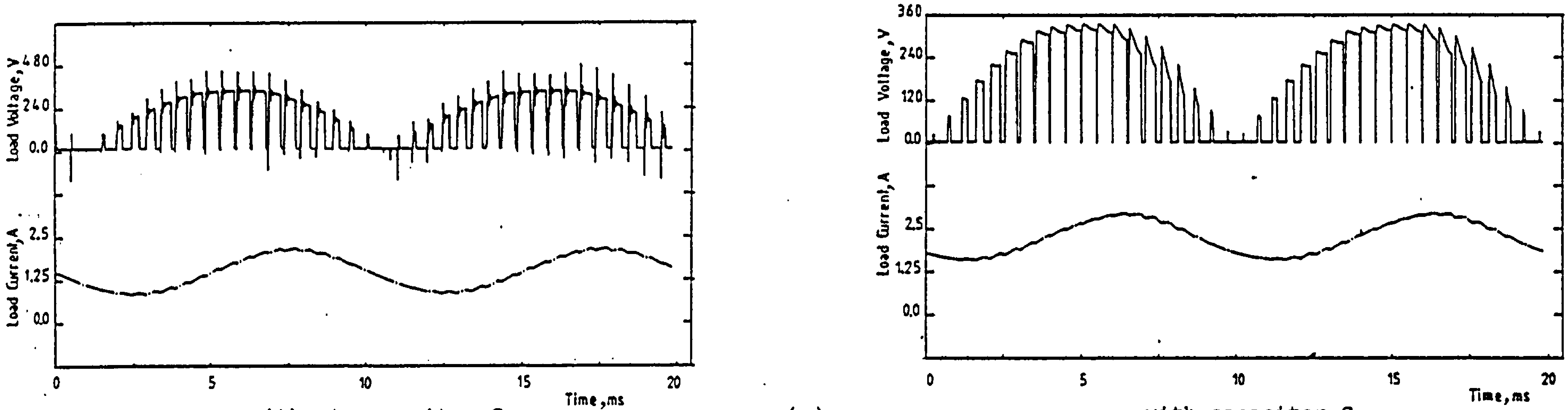

without capacitor C

(c)

with capacitor C

Figure6.21 Continued.
(c) Load voltage and current.

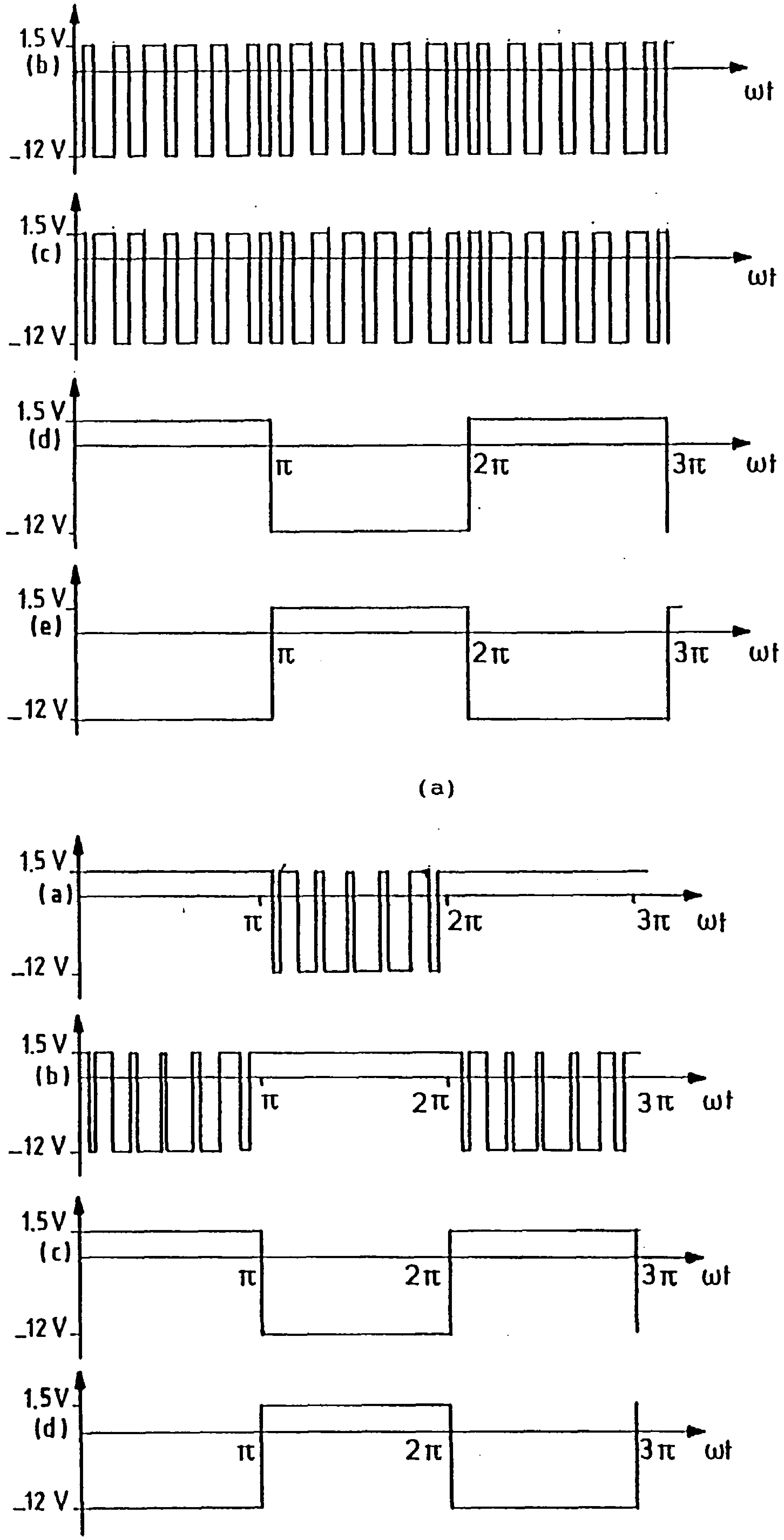

Figure6.22 Gate drive signals applied to GTO thyristors T_1toT_4.
(a) Original gate drive signals.
(b) Modified gate drive signals.

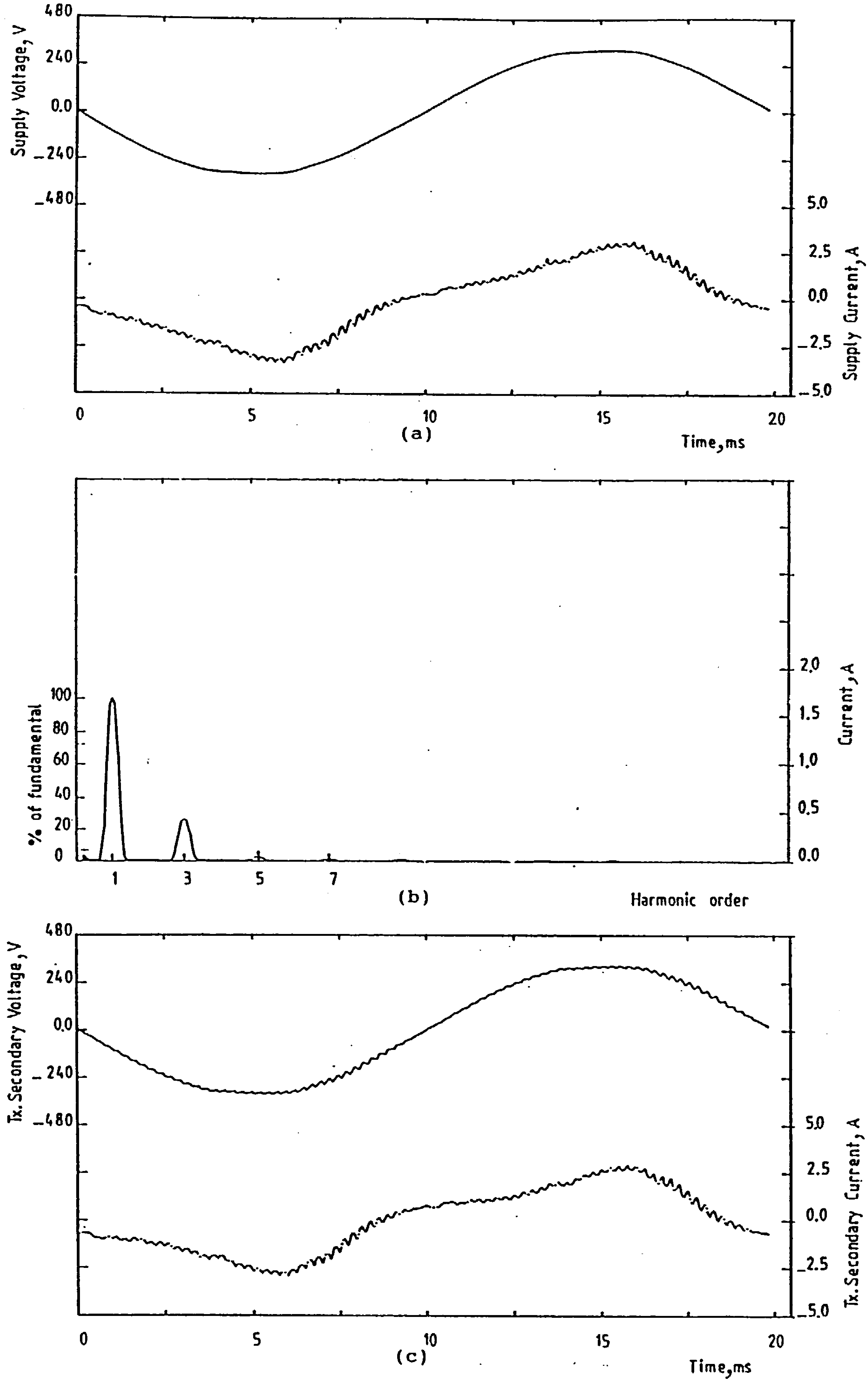

Figure6.23 Experimental results for PWM bridge converter connected to a passive load.
(a) Supply voltage and current.
(b) Supply current spectrum.
(c) Transformer secondary voltage and current.
(f_c=4kHz, R_1=80Ω, L_1=0.3H, V_1=159V)

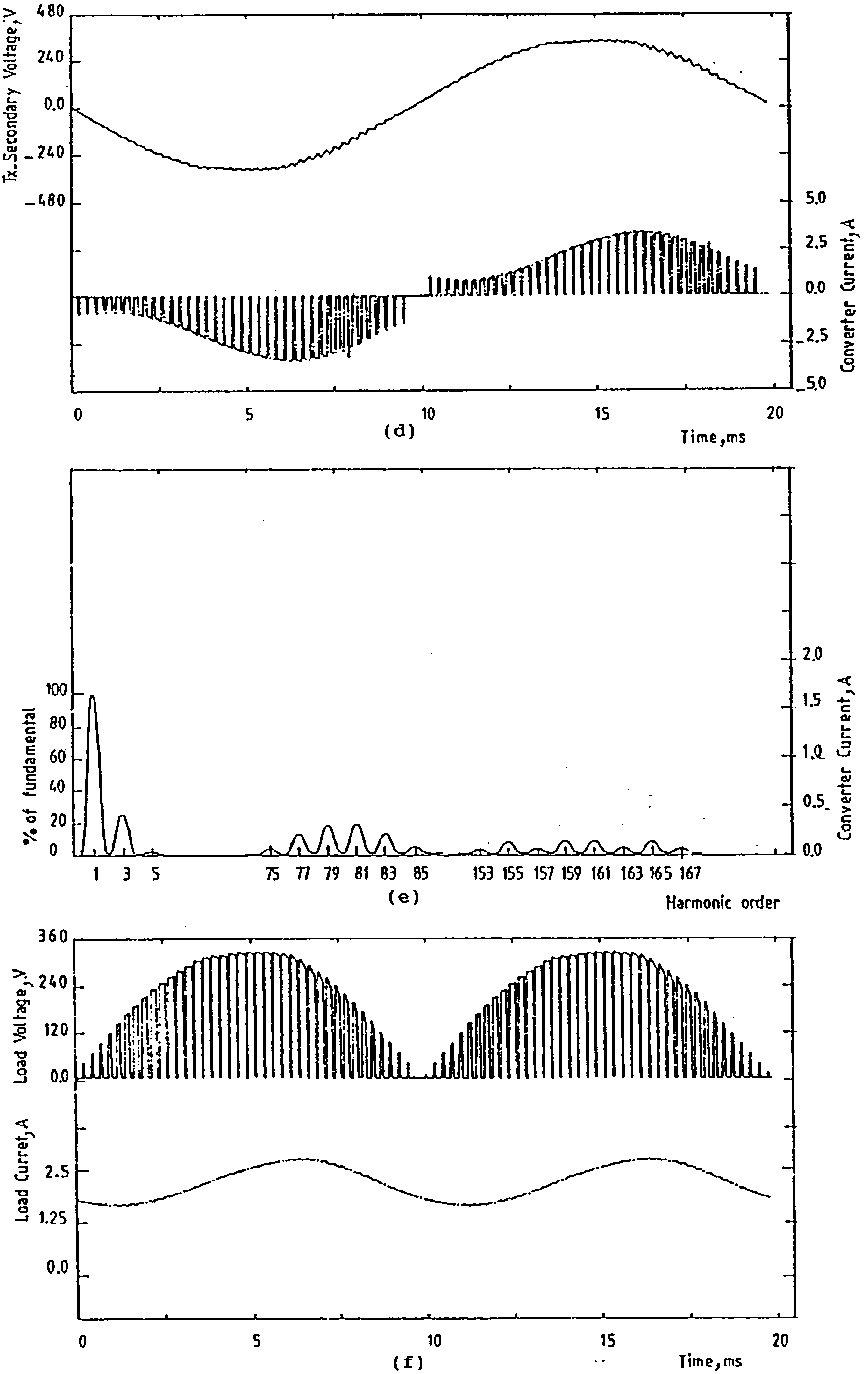

Figure6.23 Continued.
(d) Transformer secondary voltage and converter current.
(e) Converter current spectrum.
(f) Load voltage and current.

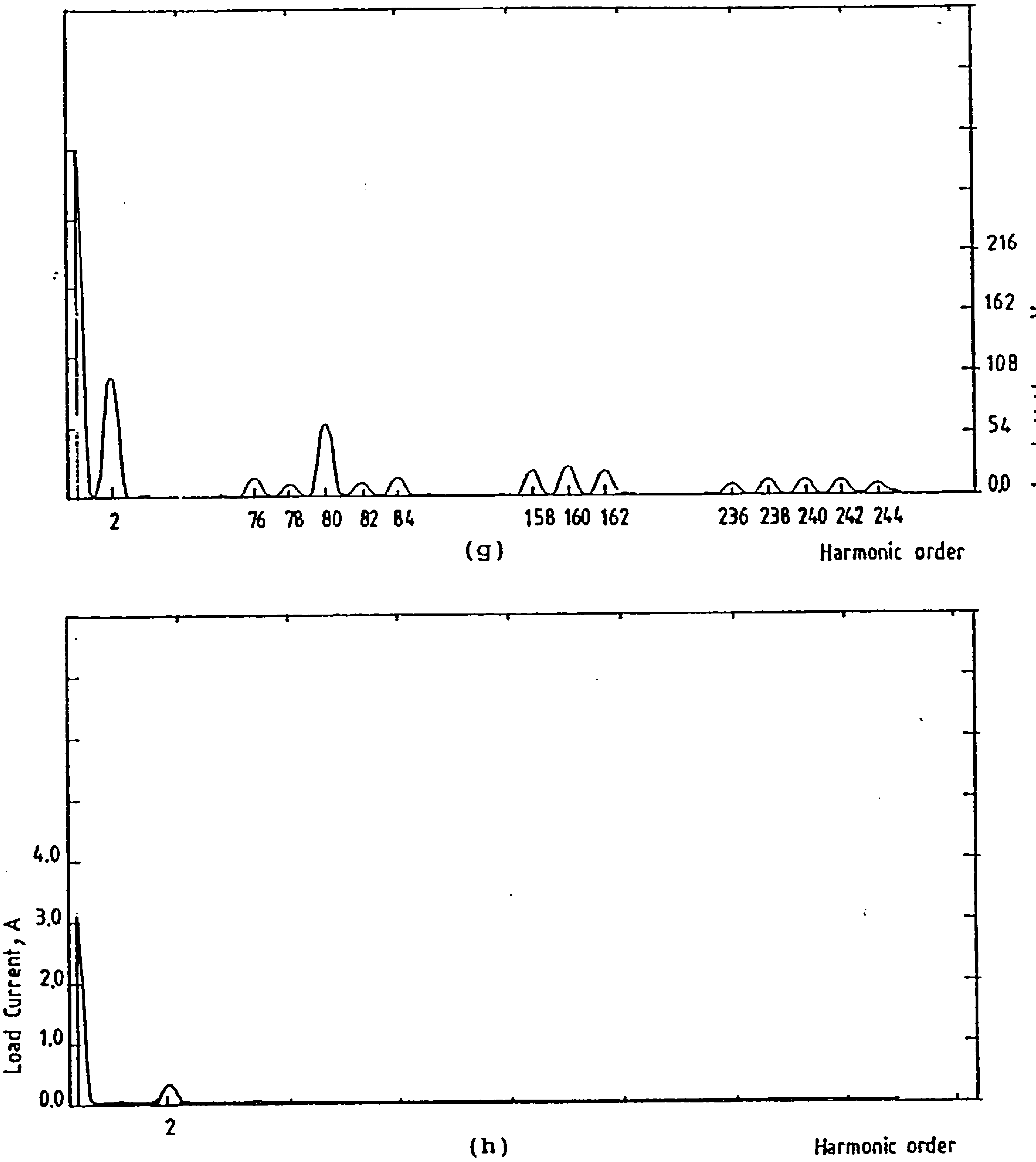

Figure6.23 Continued.
(g) Load voltage spectrum.
(h) Load current spectrum.

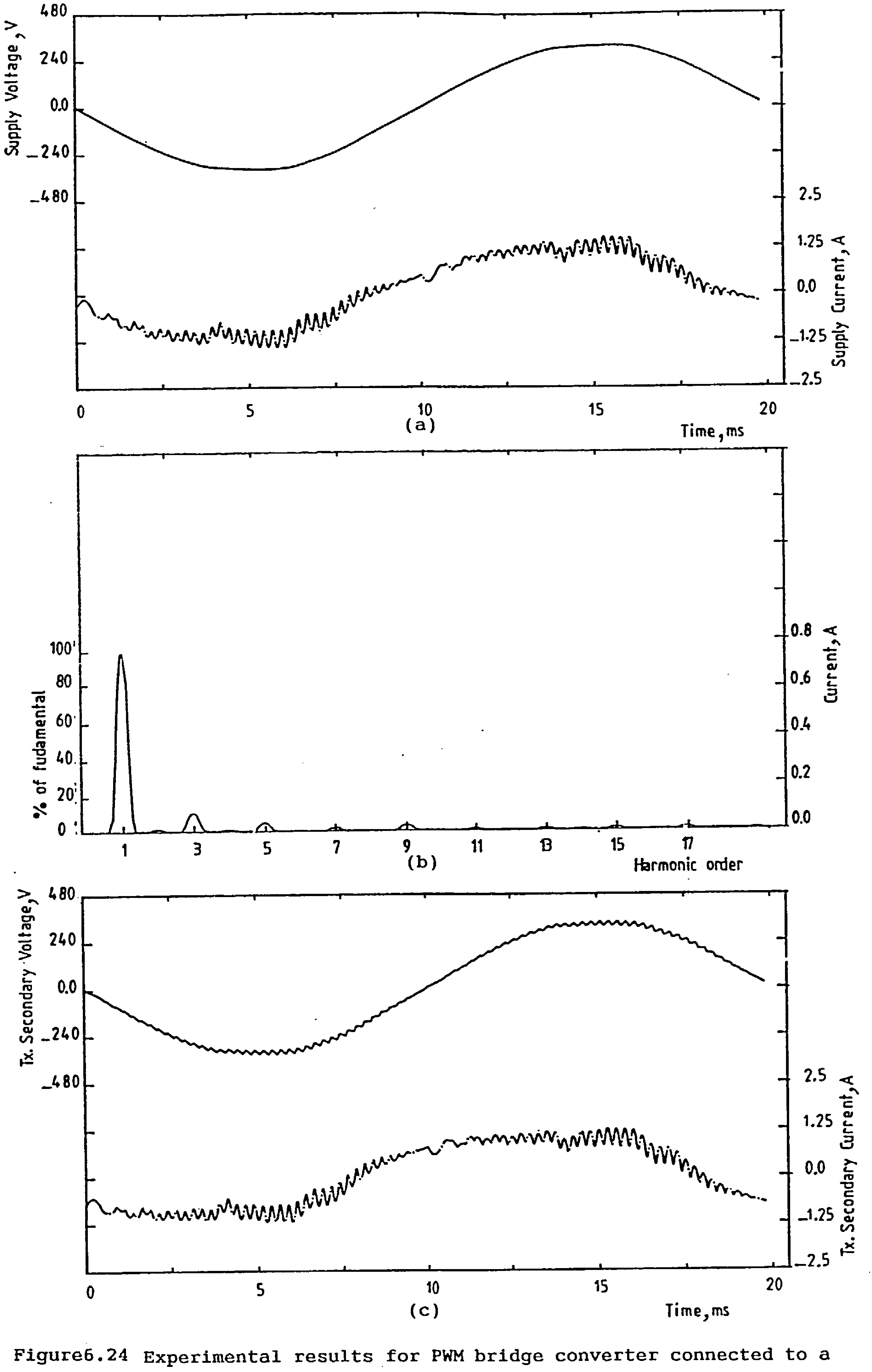

Figure6.24 Experimental results for PWM bridge converter connected to a passive load.

(a) Supply voltage and current.

(b) Supply current spectrum.

(c) Transformer secondary voltage and current.

(f_c=4kHz,R_1=27Ω,L_1=0.3H,V_1=55V)

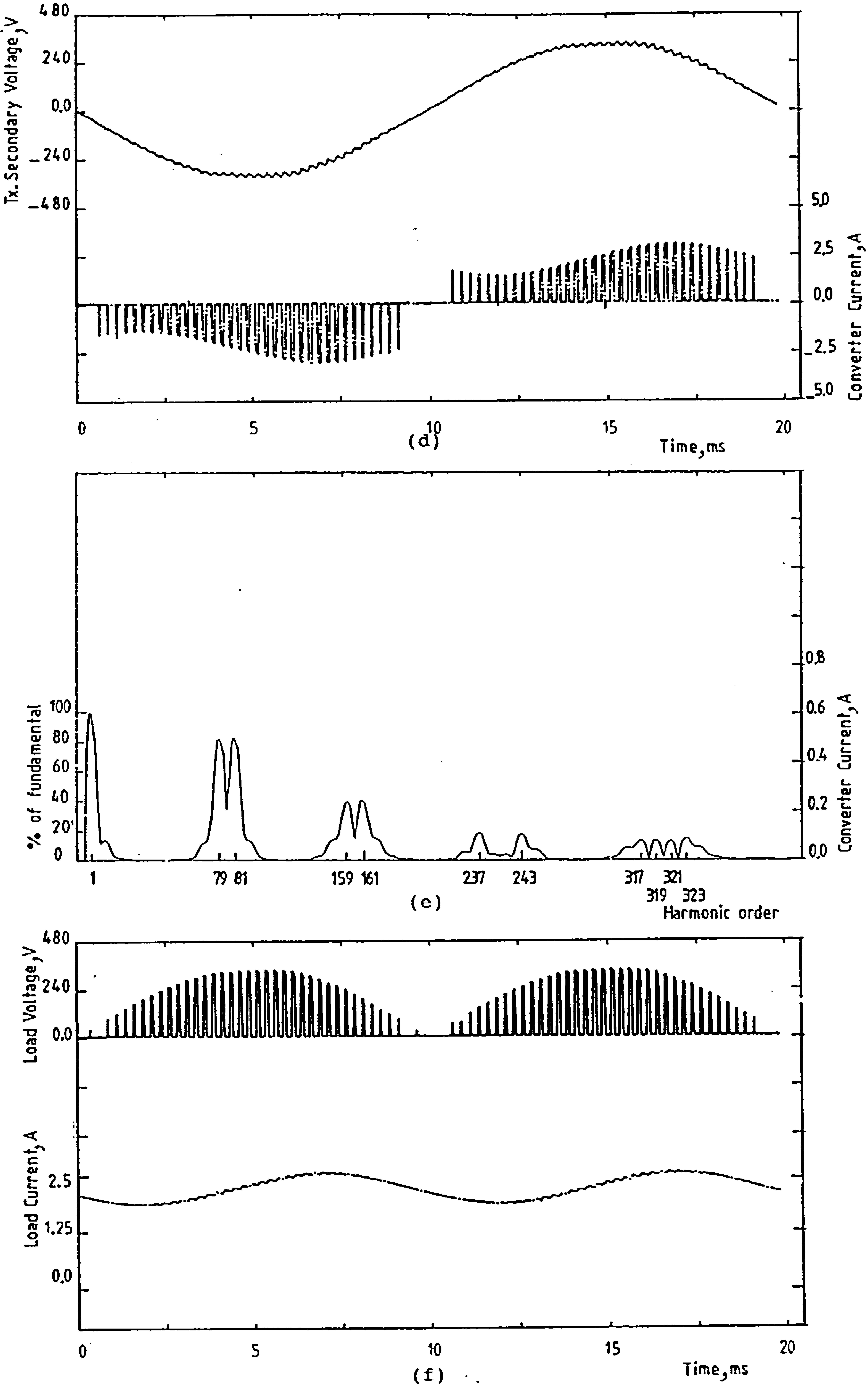

Figure6.24 Continued.
(d) Transformer secondary voltage and converter current.
(e) Converter current spectrum.
(f) Load voltage and current.

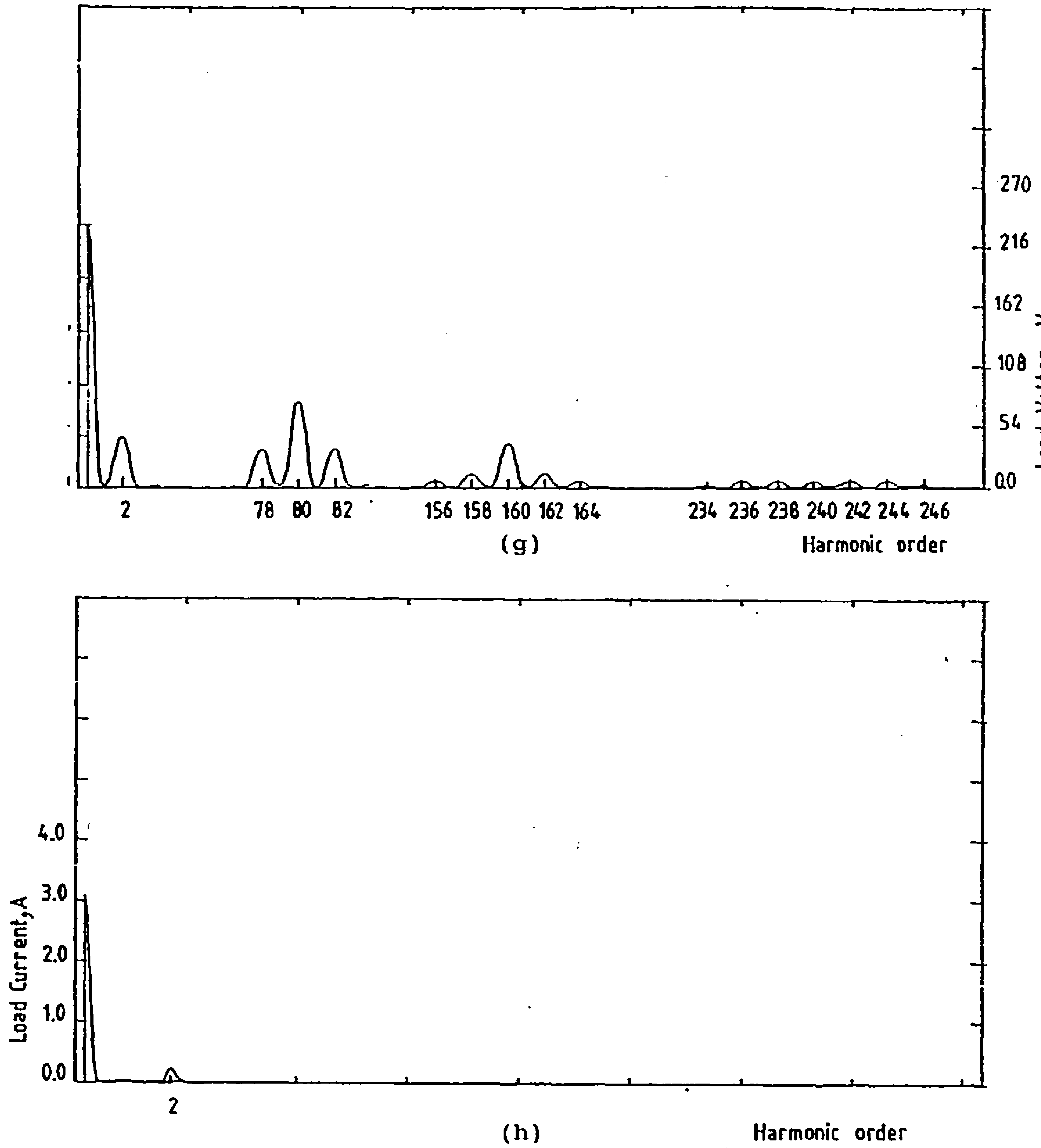

Figure6.24 Continued.
(g) Load voltage spectrum.
(h) Load current spectrum.

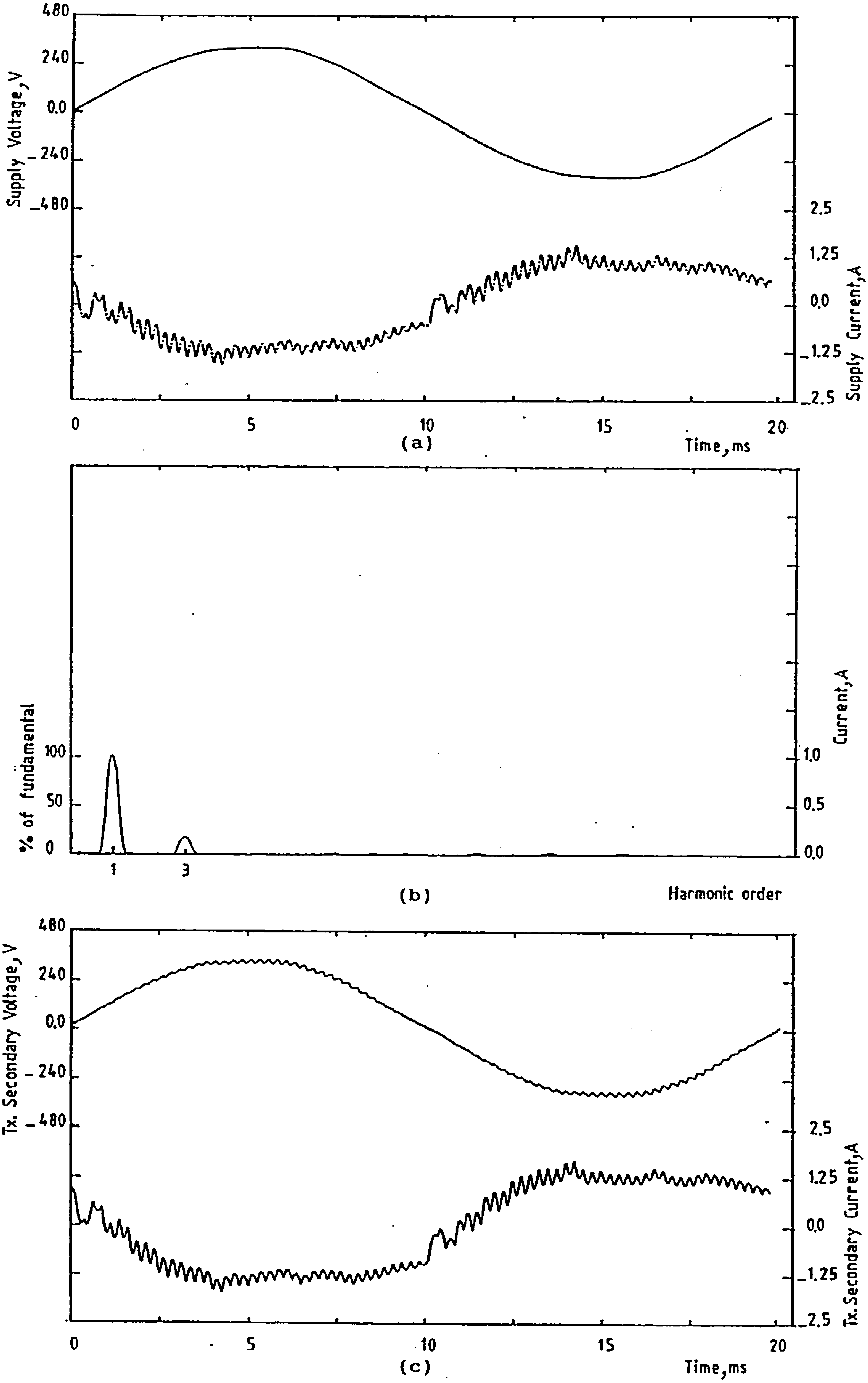

Figure6.25 Experimental results for PWM bridge converter connected to a passive load.
(a) Supply voltage and current.
(b) Supply current spectrum.
(c) Transformer secondary voltage and current.
(f_c=4kHz, R_1=34Ω, L_1=0.3H, V_1=-152V, V_{dc}=220V)

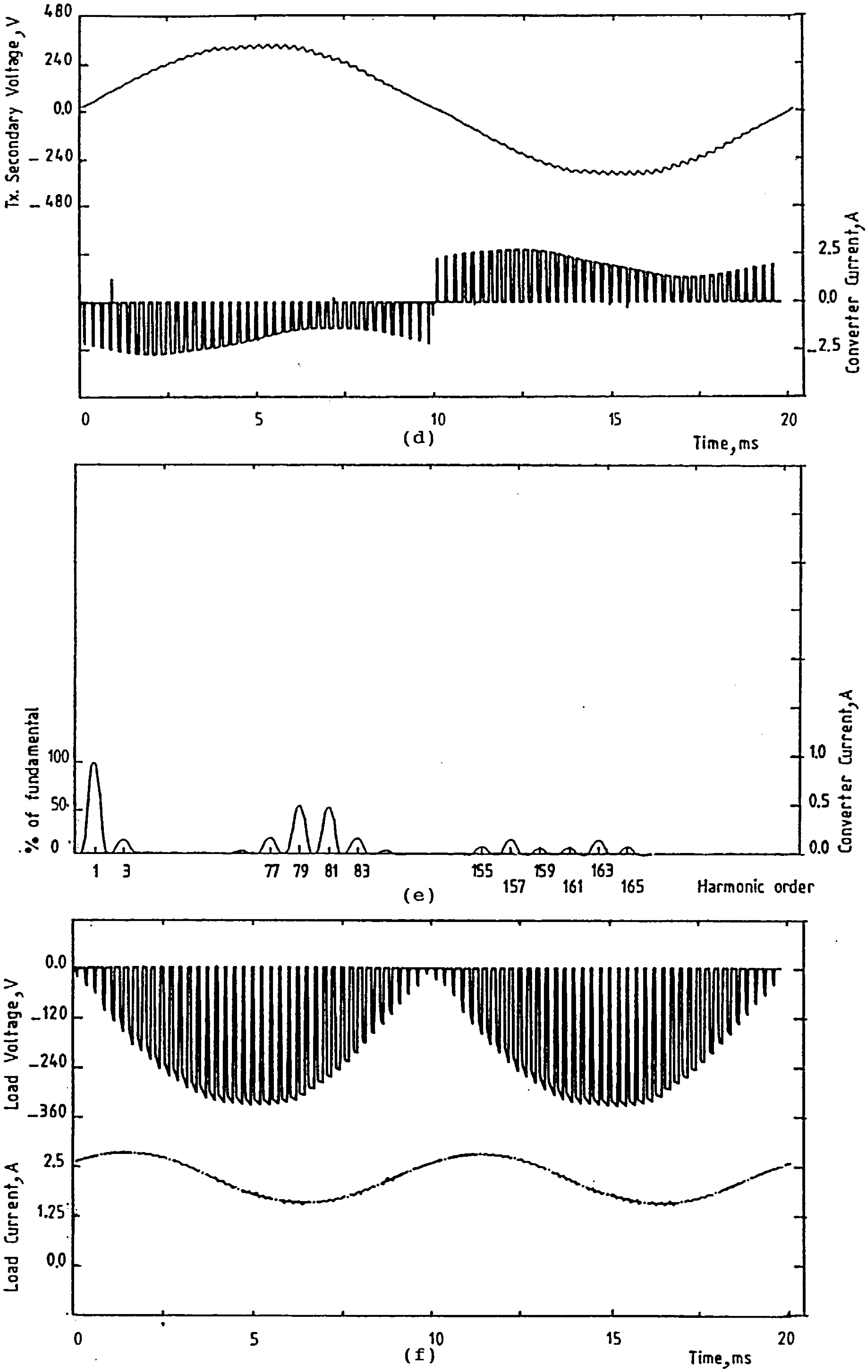

Figure6.25 Continued.
(d) Transformer secondary voltage and converter current.
(e) Converter current spectrum.
(f) Load voltage and current.

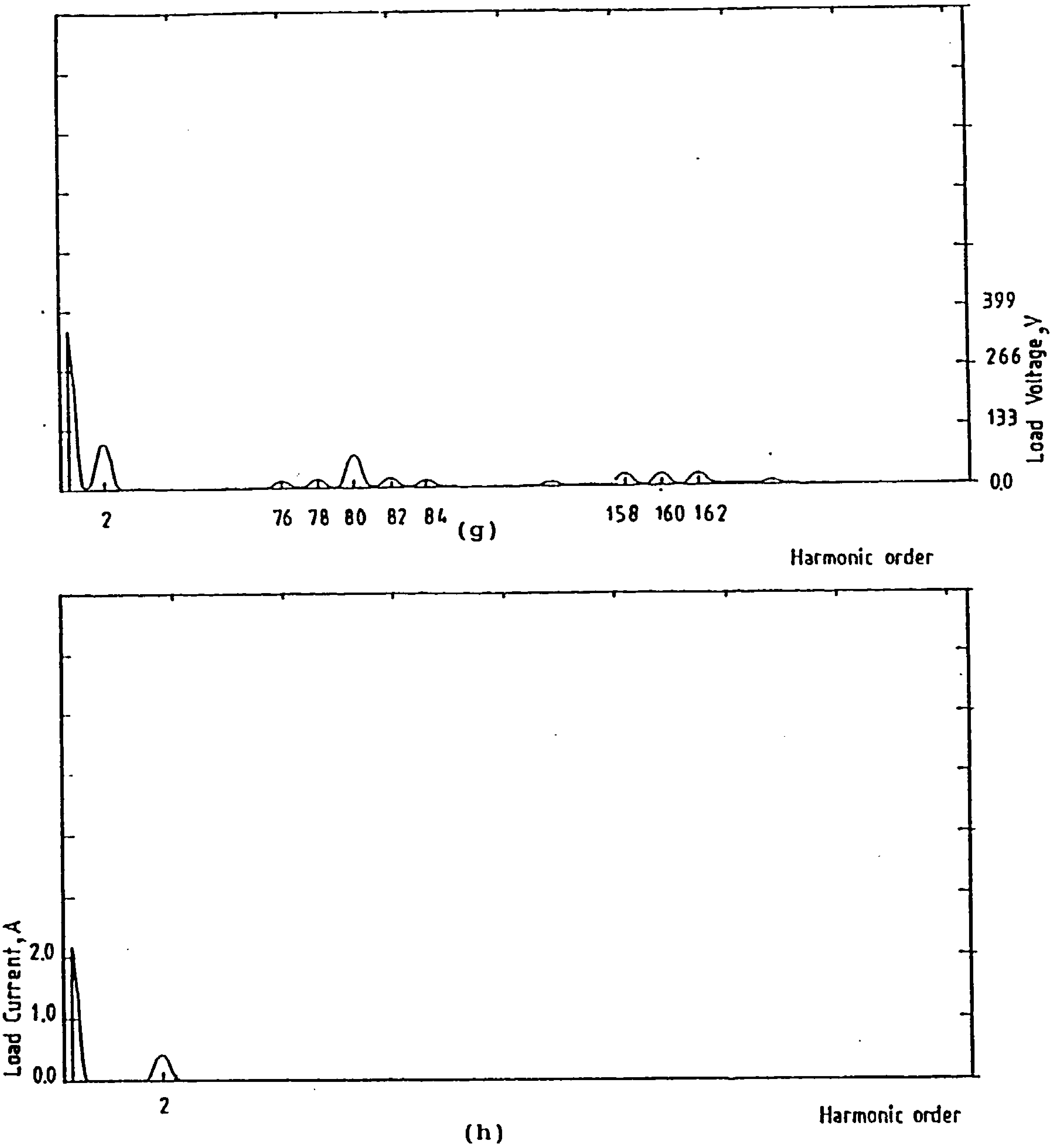

Figure6.25 Continued.
(g) Load voltage spectrum.
(h) Load current spectrum.

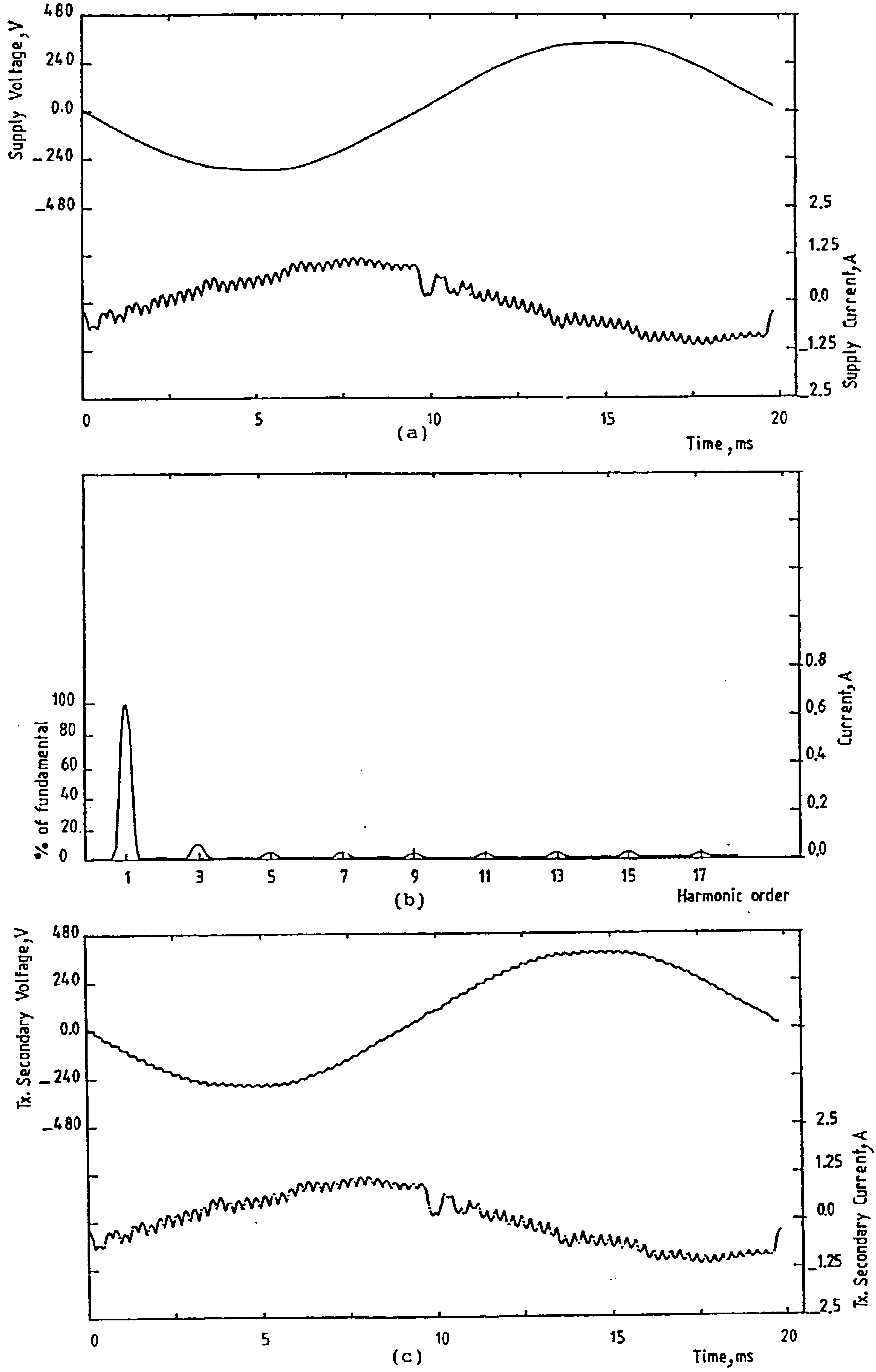

Figure6.26 Experimental results for PWM bridge converter connected to a passive load.
(a) Supply voltage and current.
(b) Supply current spectrum.
(c) Transformer secondary voltage and current.
(f_c=4kHz,R_l=27Ω,L_l=0.3H,V_l=-48V, V_{dc}=102V)

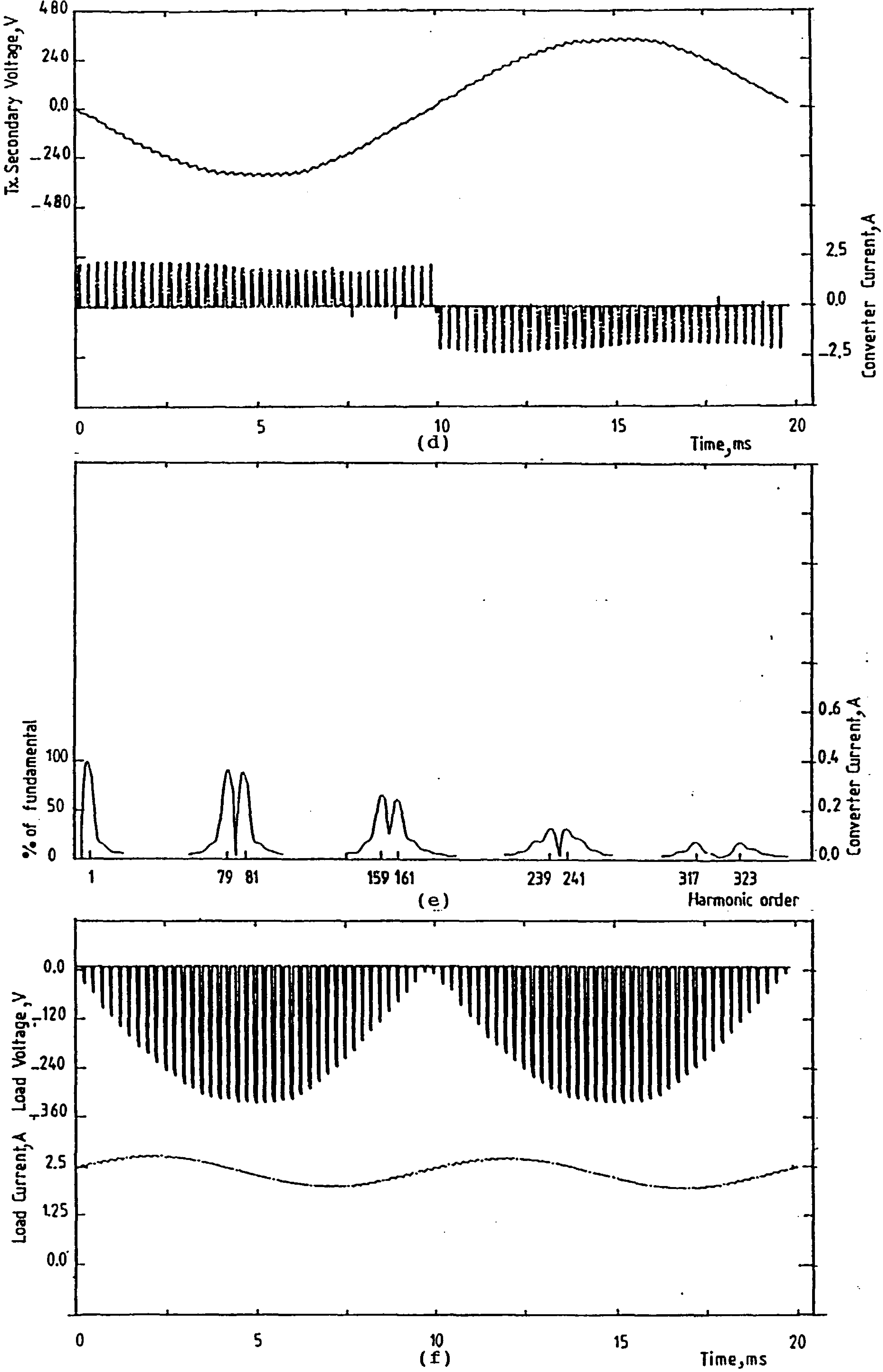

Figure6.26 Continued.
(d) Transformer secondary voltage and converter current.
(e) Converter current spectrum.
(f) Load voltage and current.

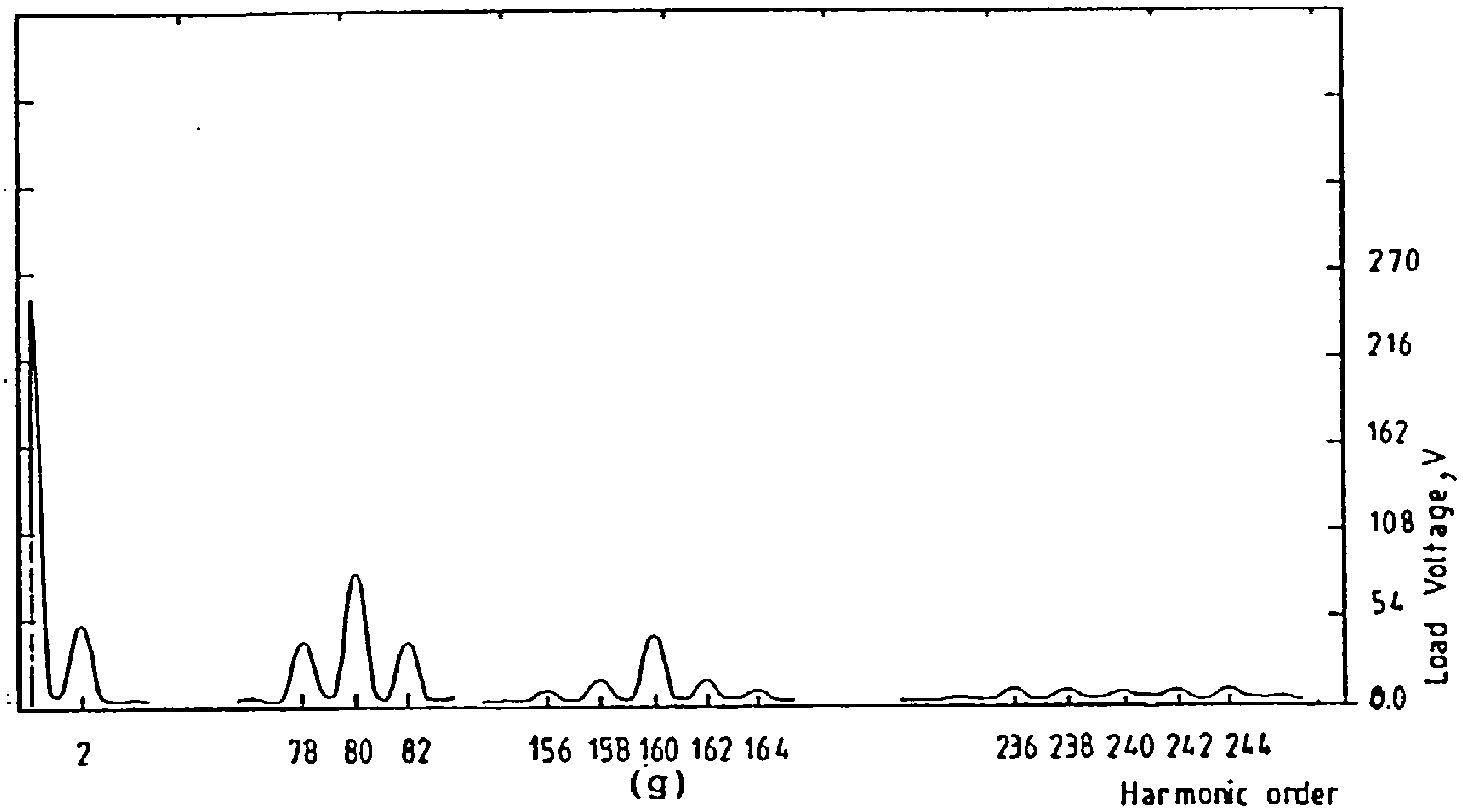

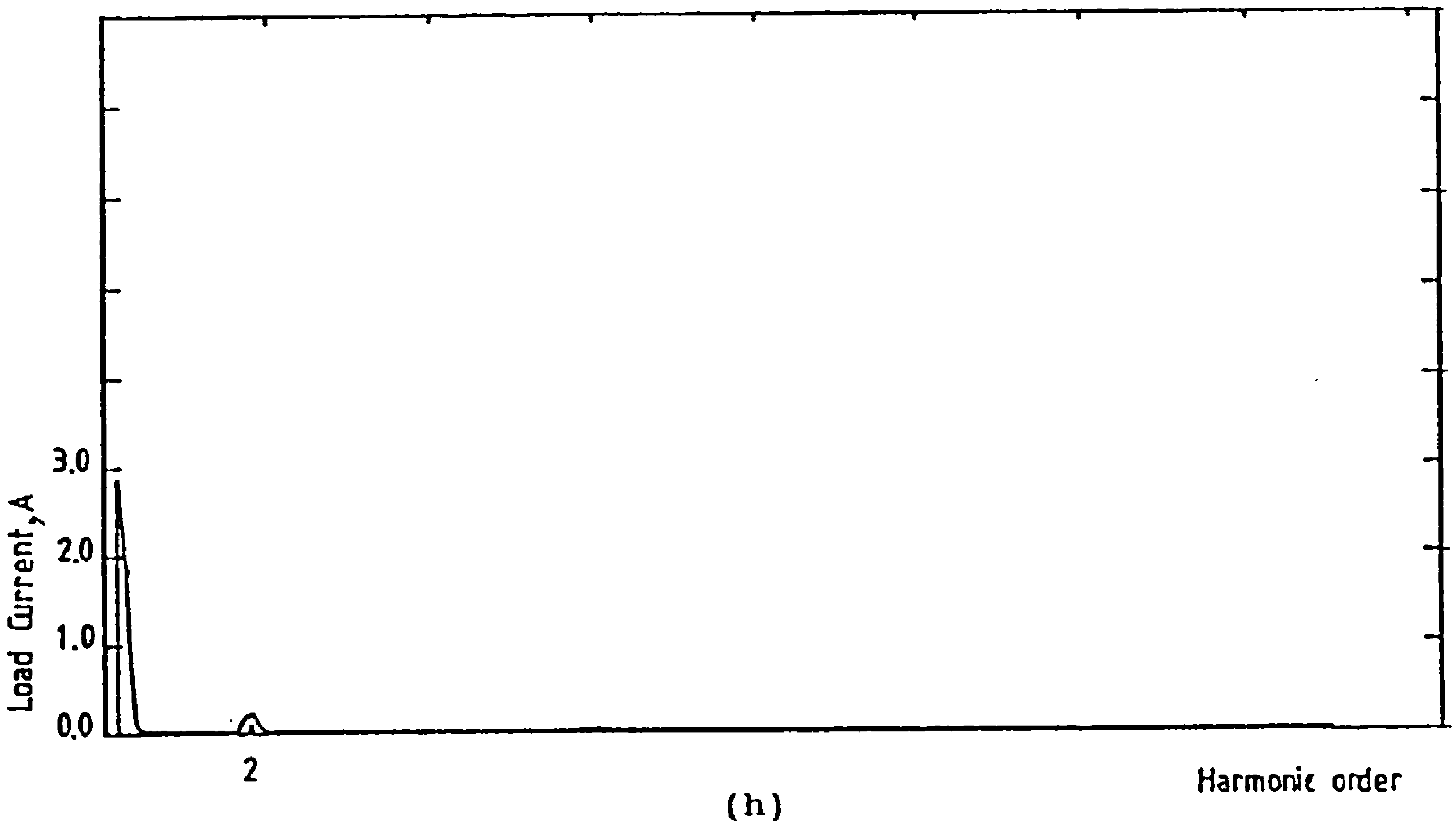

Figure6.26 Continued.
(g) Load voltage spectrum.
(h) Load current spectrum.

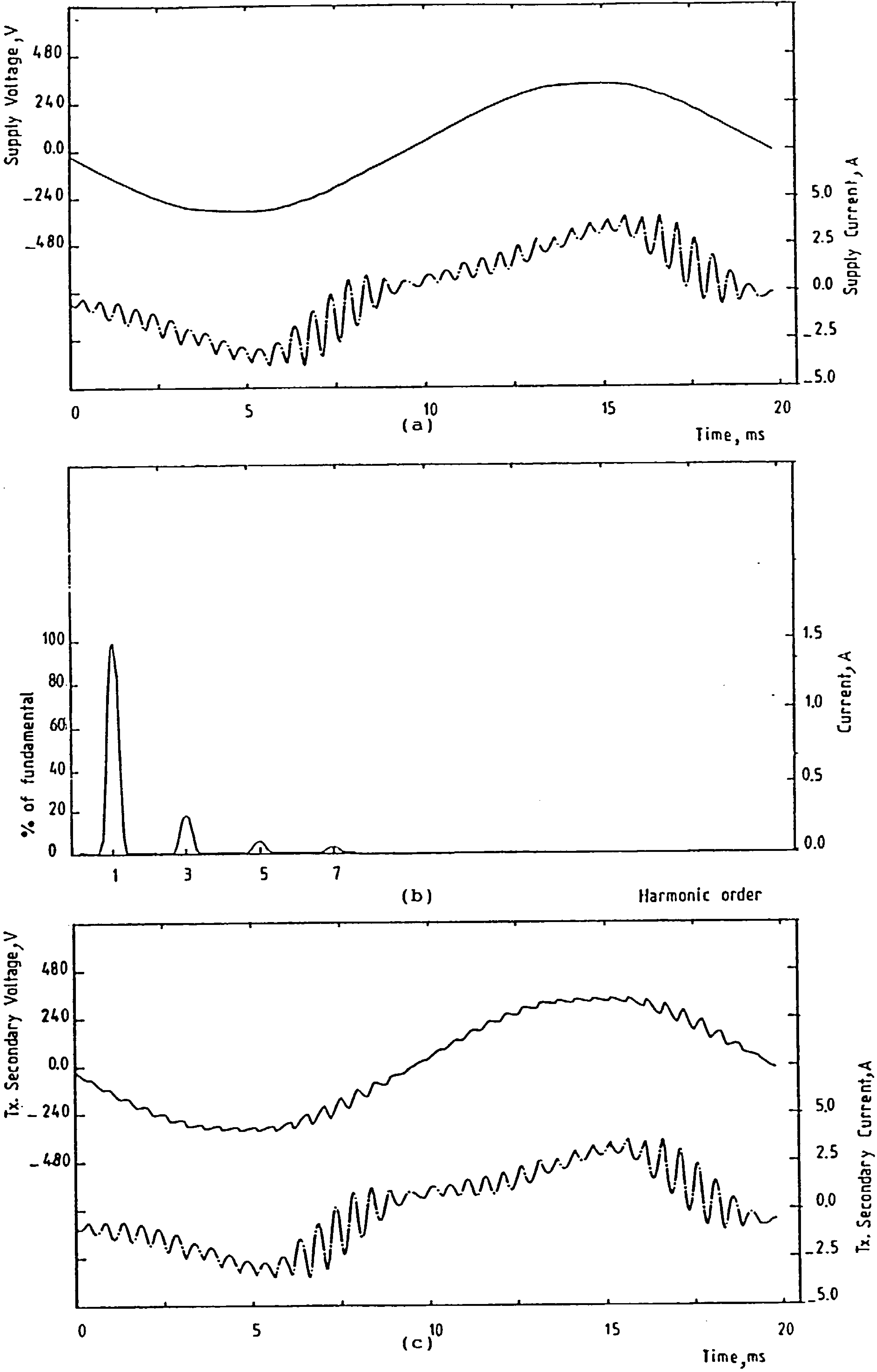

Figure6.27 Experimental results for PWM bridge converter connected to a passive load.
(a) Supply voltage and current.
(b) Supply current spectrum.
(c) Transformer secondary voltage and current.
(f_c=2kHz, R_1=80Ω, L_1=0.3H, V_1'=159V)

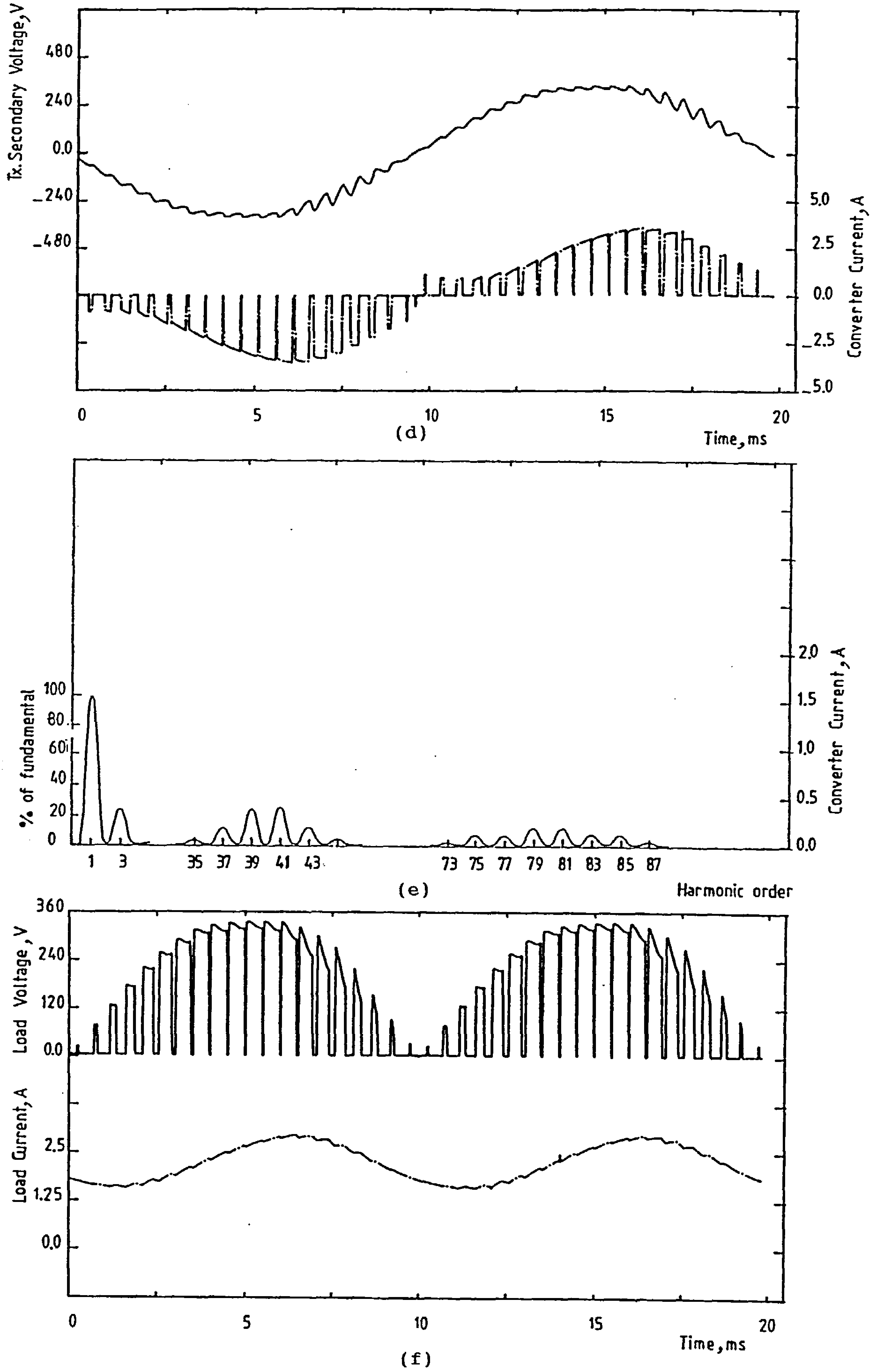

Figure6.27 Continued.
(d) Transformer secondary voltage and converter current.
(e) Converter current spectrum.
(f) Load voltage and current.

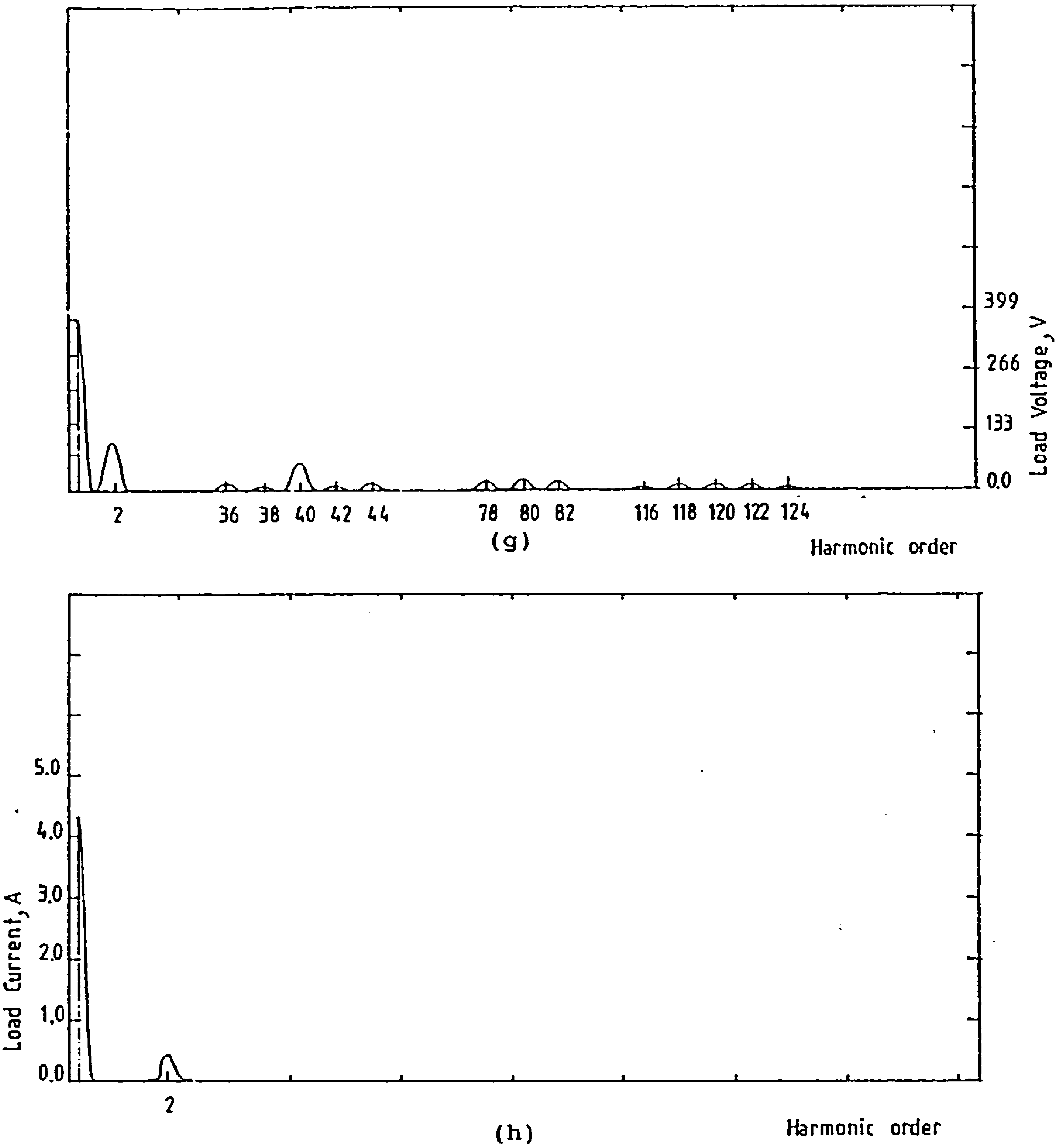

Figure6.27 Continued.
(g) Load voltage spectrum.
(h) Load current spectrum.

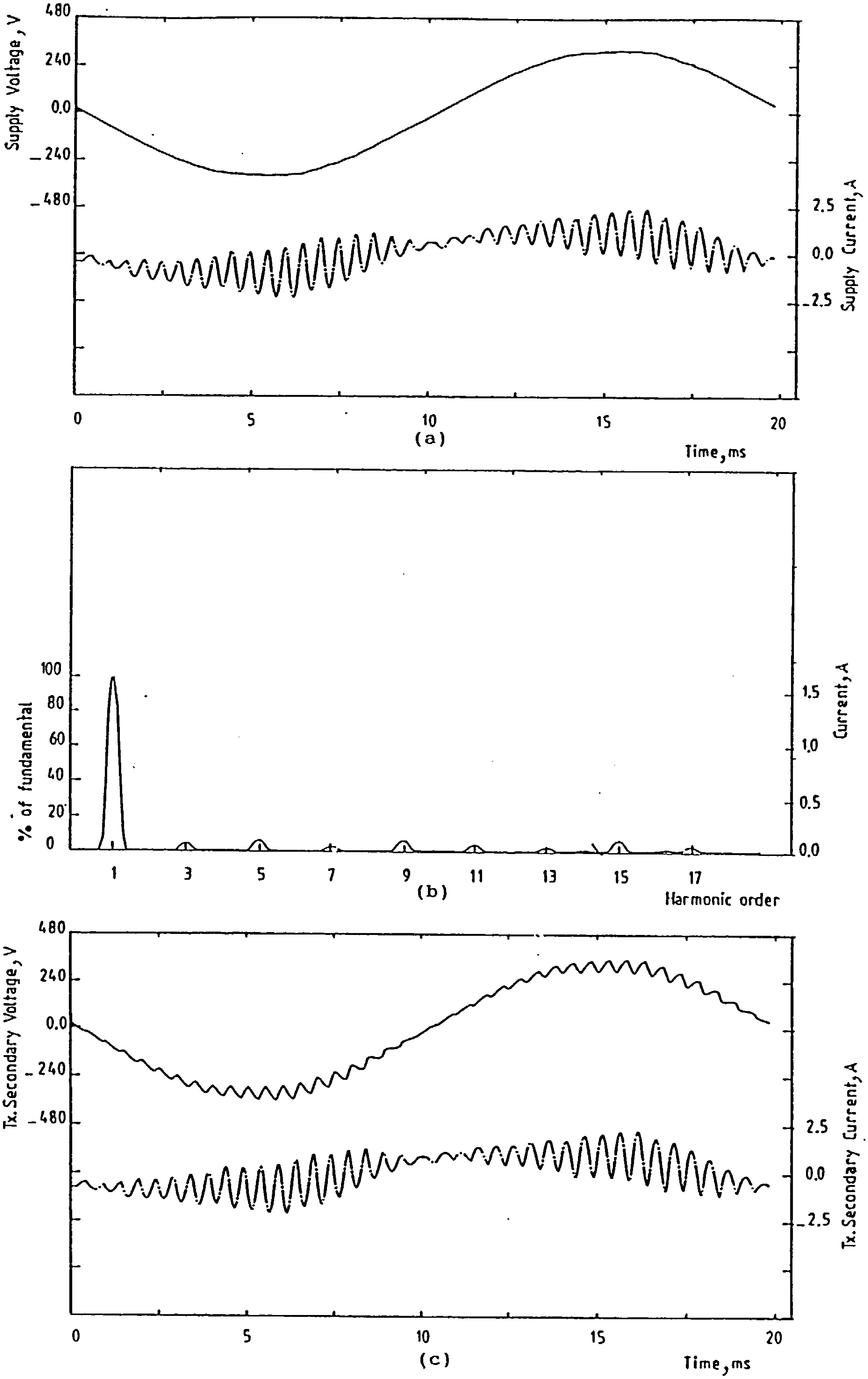

Figure6.28 Experimental results for PWM bridge converter connected to a passive load.
(a) Supply voltage and current.
(b) Supply current spectrum.
(c) Transformer secondary voltage and current.
($f_c=2\text{kHz}, R_1=27\Omega, L_1=0.3\text{H}, V_1=55\text{V}$)

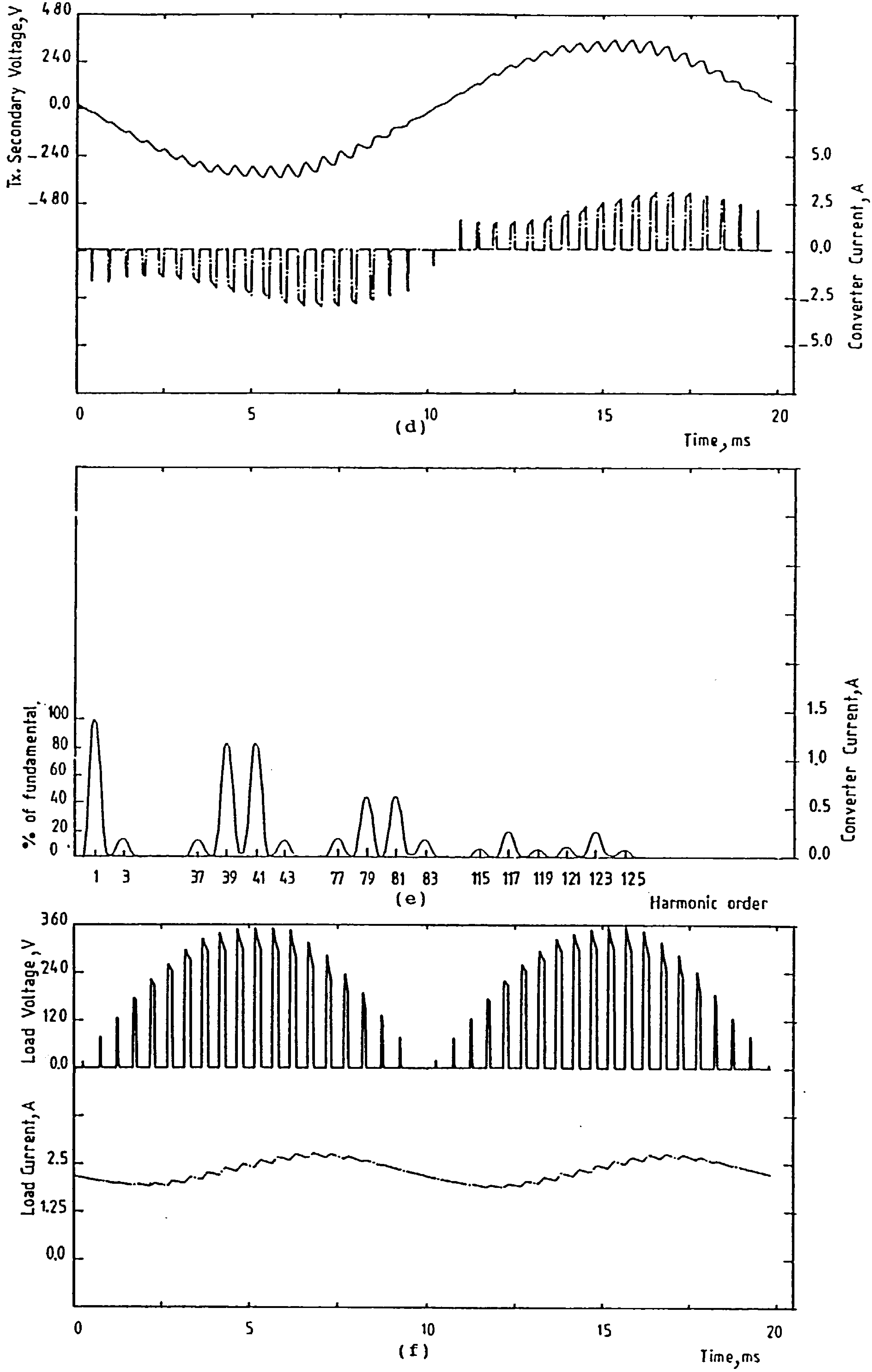

Figure6.28 Continued.
(d) Transformer secondary voltage and converter current.
(e) Converter current spectrum.
(f) Load voltage and current.

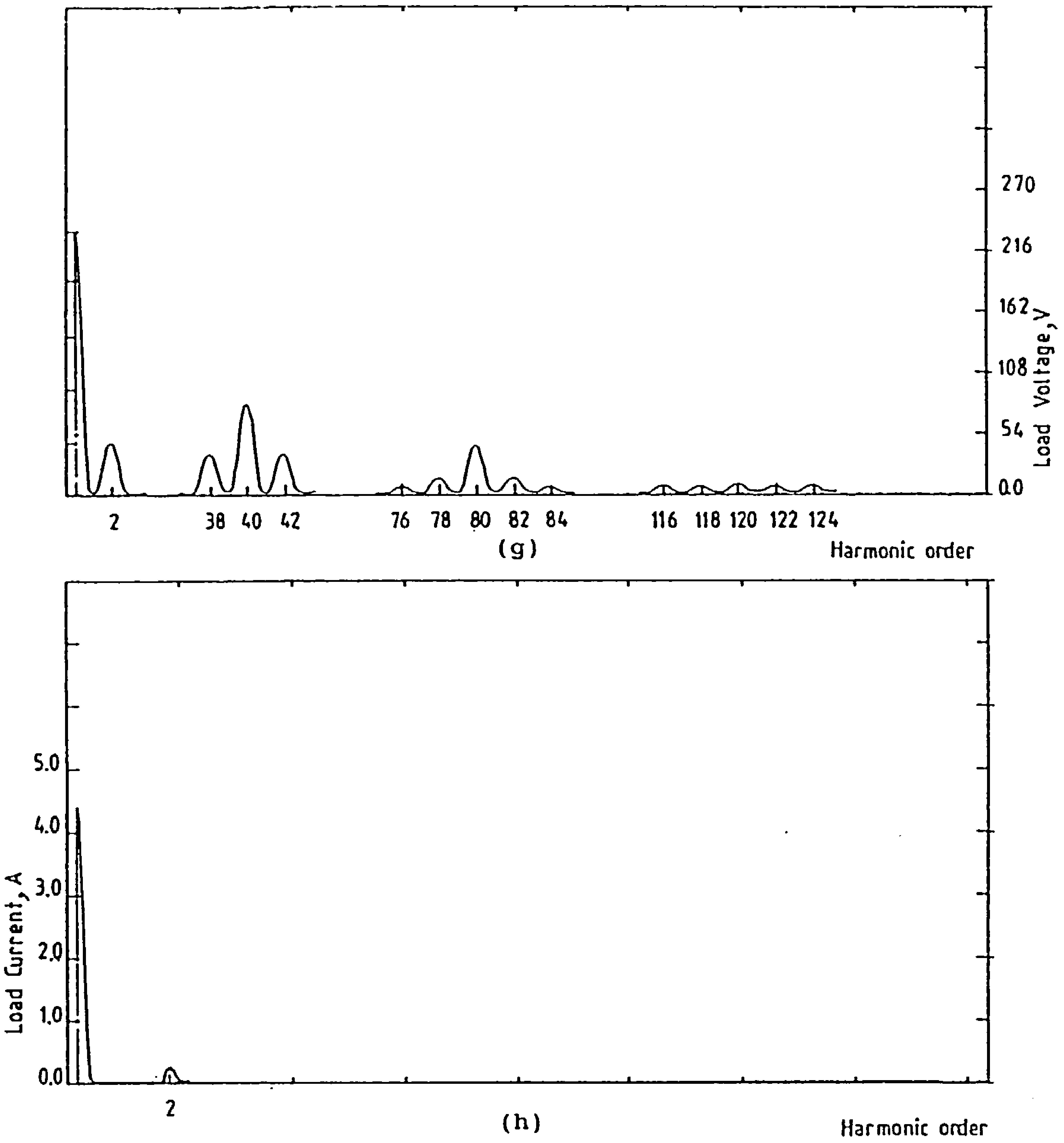

Figure6.28 Continued.
(g) Load voltage spectrum.
(h) Load current spectrum.

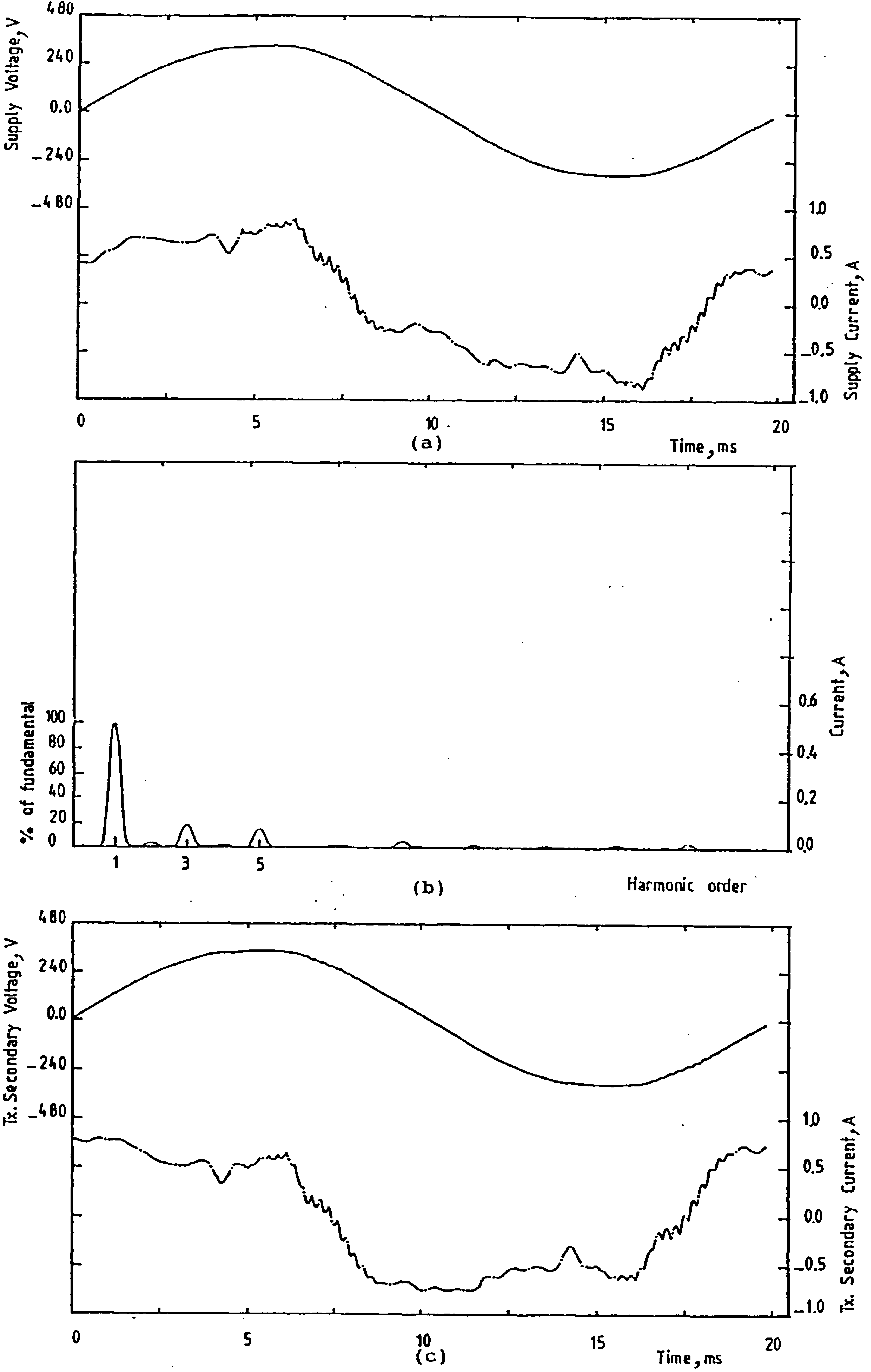

Figure6.29 Experimental results for PWM bridge converter connected to a dc machine.
(a) Supply voltage and current.
(b) Supply current spectrum.
(c) Transformer secondary voltage and current.
(f_c=4kHz, L_1=0.15H, V_a=225V, I_a=0.3A)

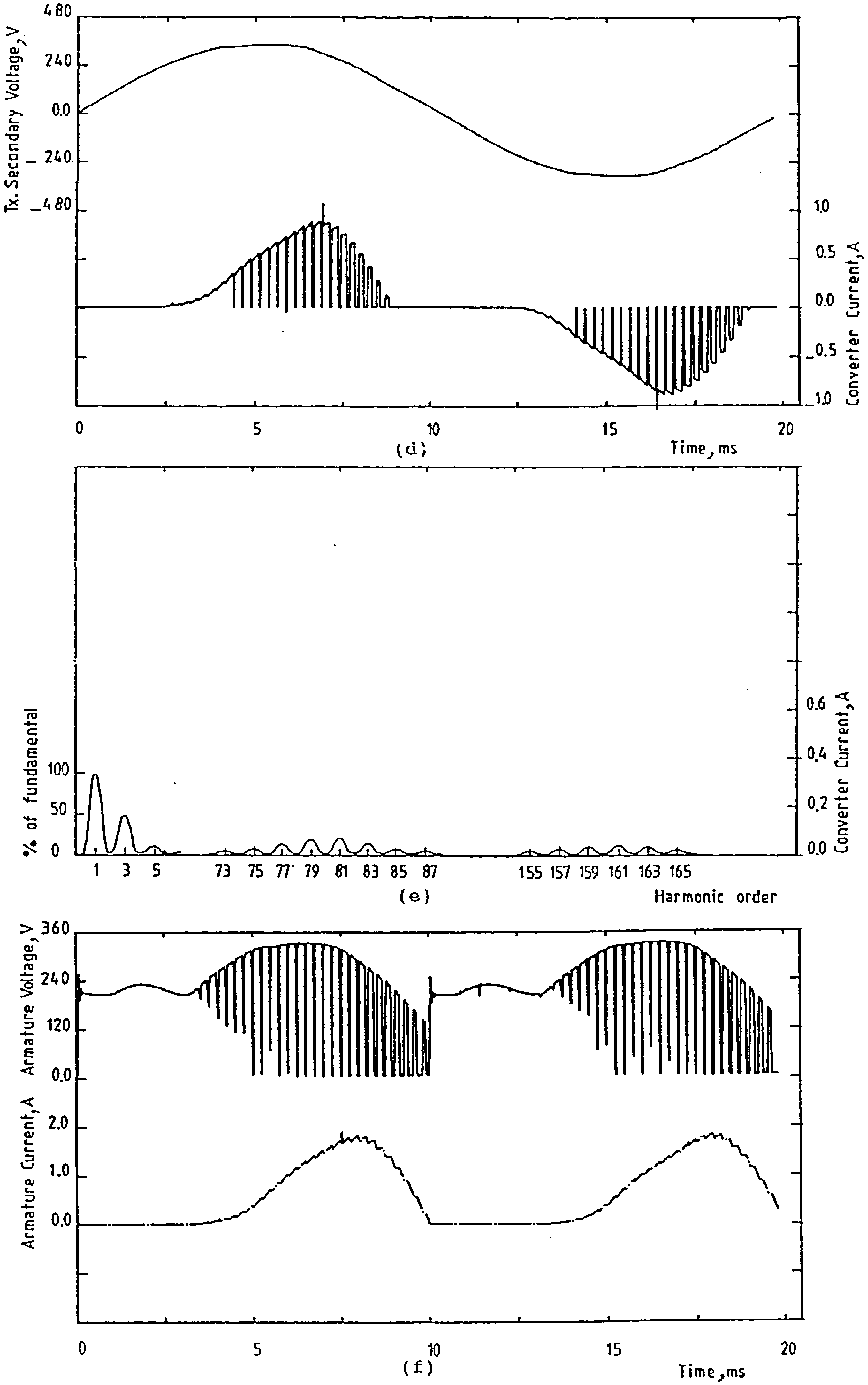

Figure6.29 Continued.
(d) Transformer secondary voltage and converter current.
(e) Converter current spectrum.
(f) Armature voltage and current.

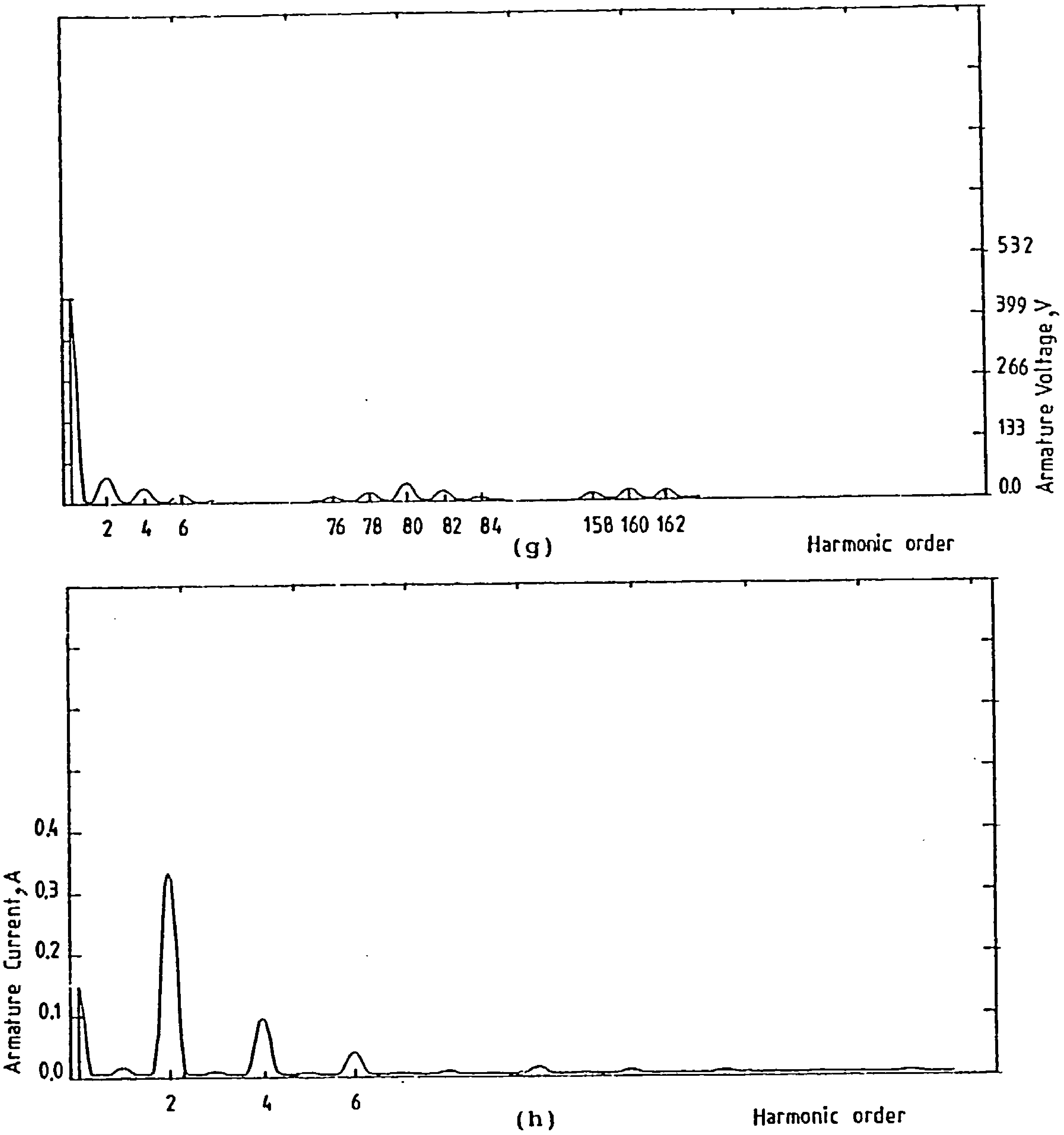

Figure6.29 Continued.
(g) Armature voltage spectrum.
(h) Armature current spectrum.

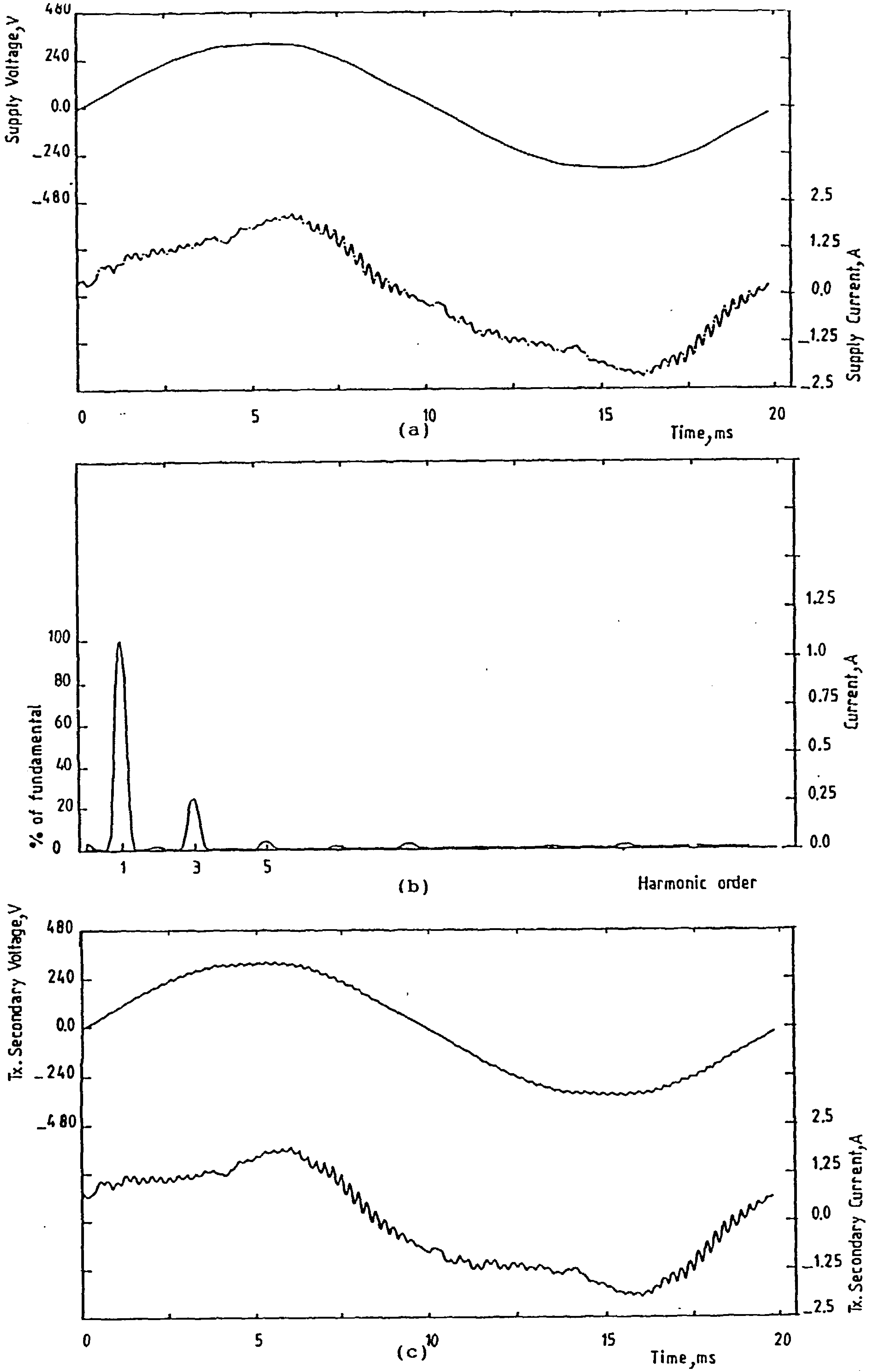

Figure6.30 Experimental results for PWM bridge converter connected to a dc machine.

(a) Supply voltage and current.

(b) Supply current spectrum.

(c) Transformer secondary voltage and current.

(f_c=4kHz, L_1=0.15H, V_a=159V)

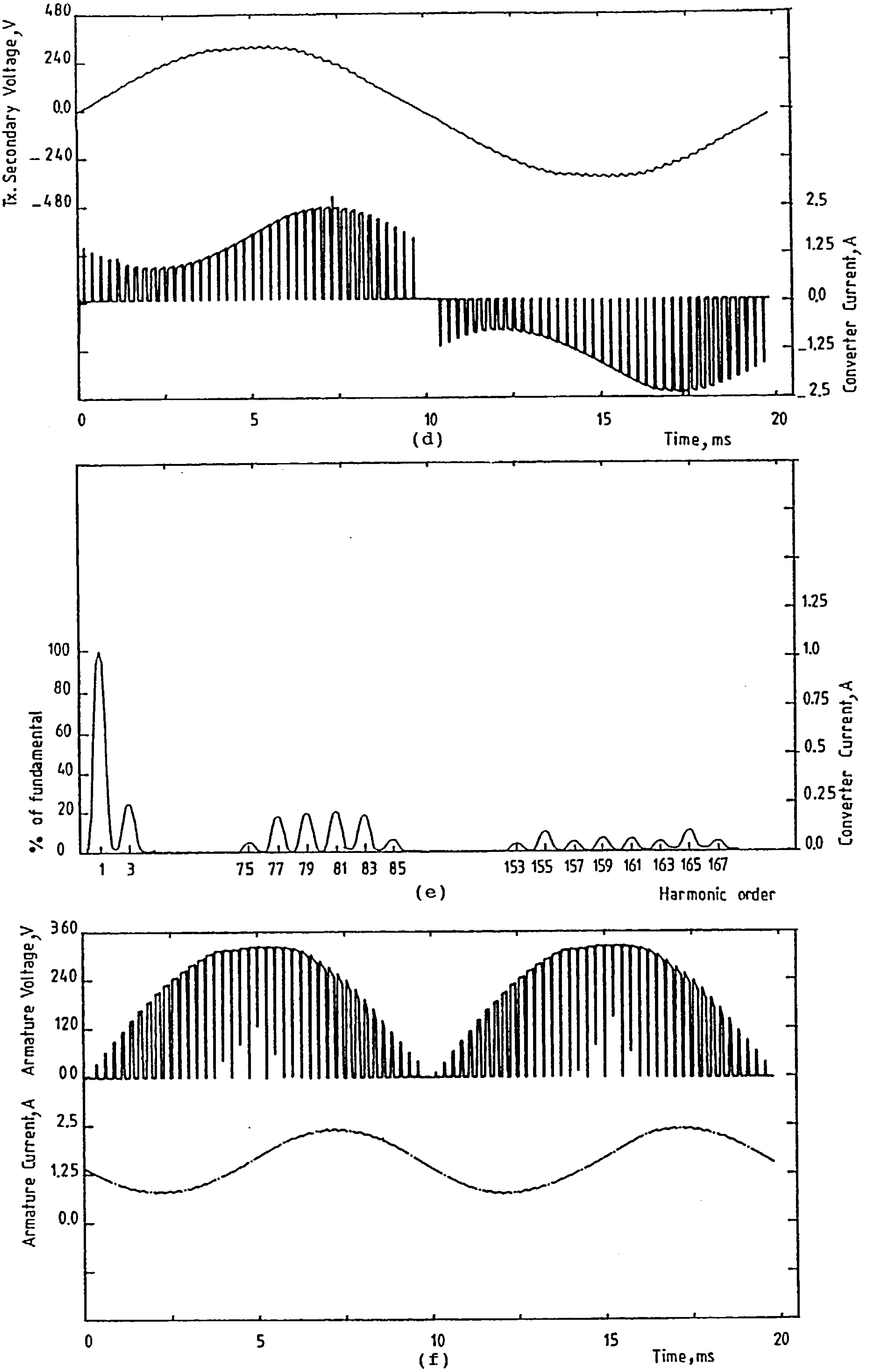

Figure6.30 Continued.
(d) Transformer secondary voltage and converter current.
(e) Converter current spectrum.
(f) Armature voltage and current.

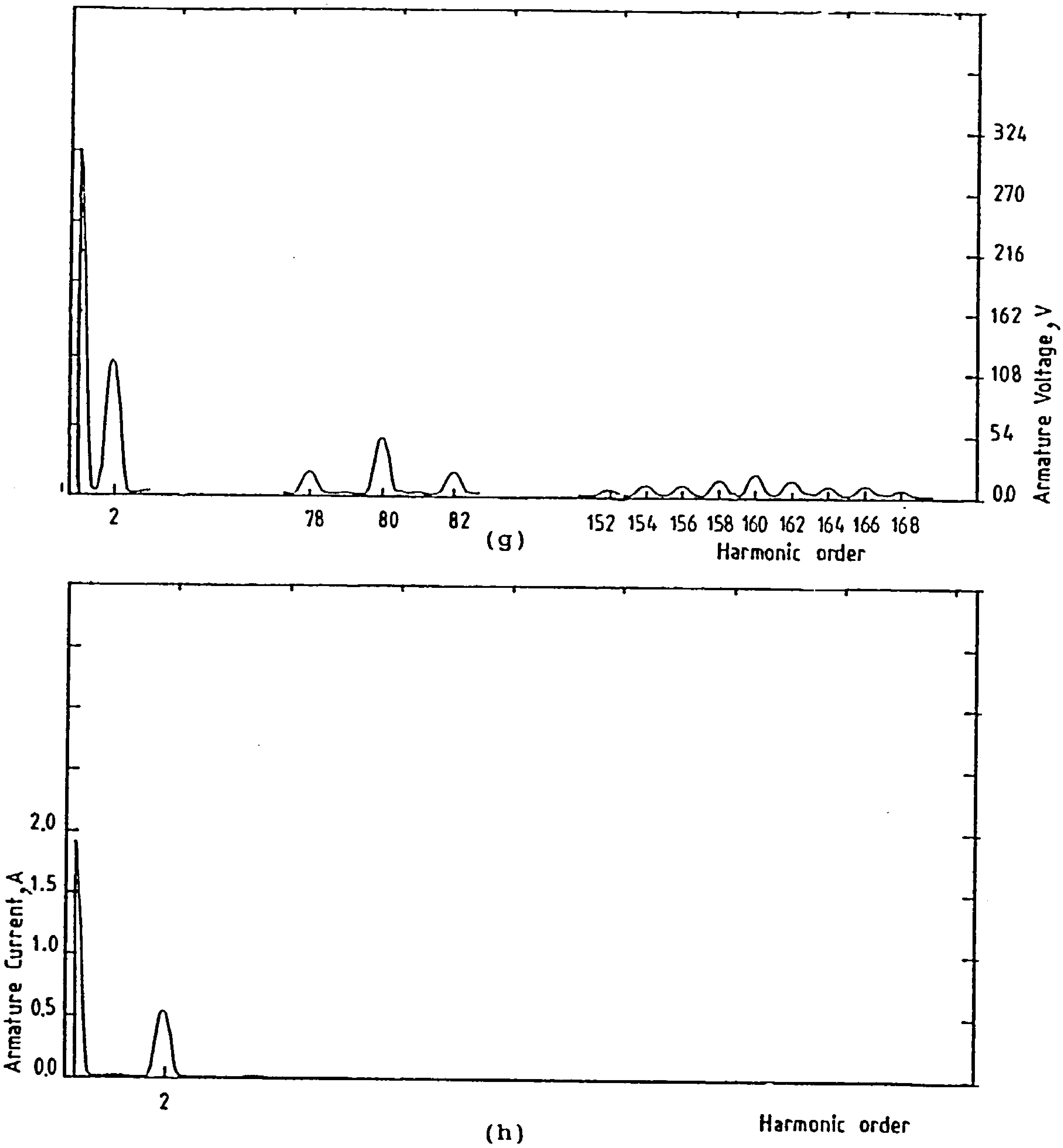

Figure6.30 Continued.
(g) Armature voltage spectrum.
(h) Armature current spectrum.

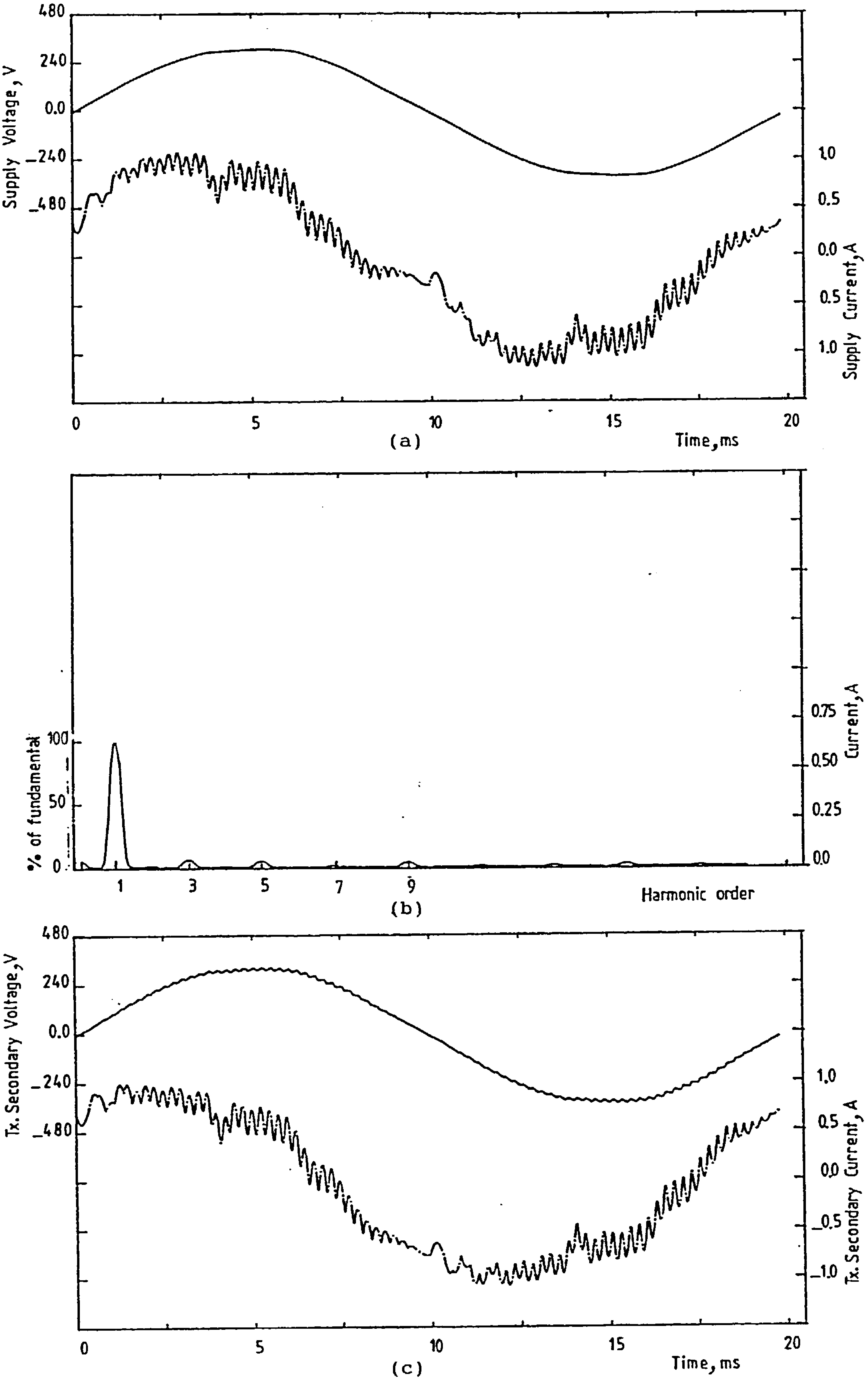

Figure6.31 Experimental results for PWM bridge converter connected to a dc machine.

(a) Supply voltage and current.

(b) Supply current spectrum.

(c) Transformer secondary voltage and current.

(f_c=4kHz, L_1=0.15H, V_a=55V)

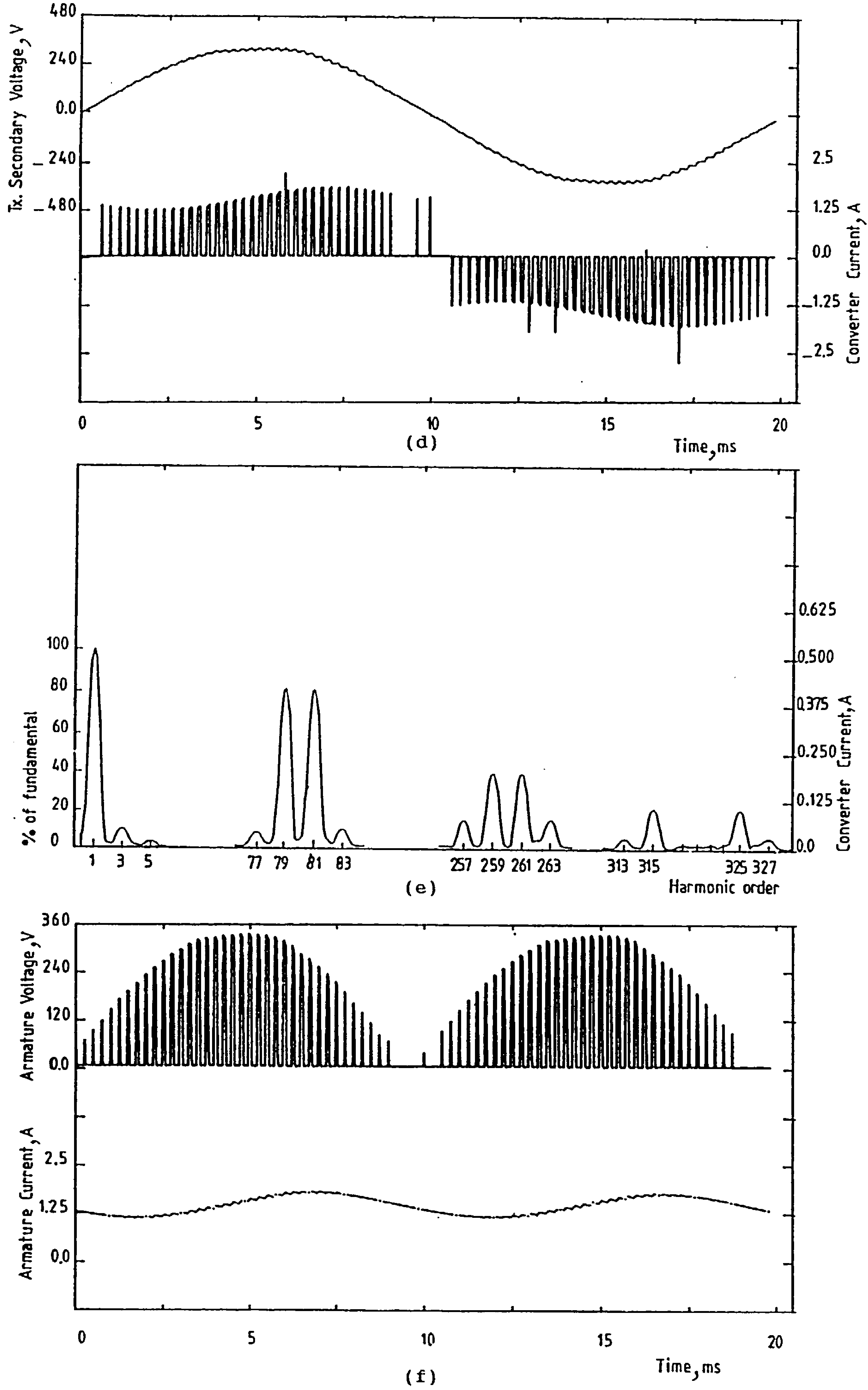

Figure6.31 Continued.
(d) Transformer secondary voltage and converter current.
(e) Converter current spectrum.
(f) Armature voltage and current.

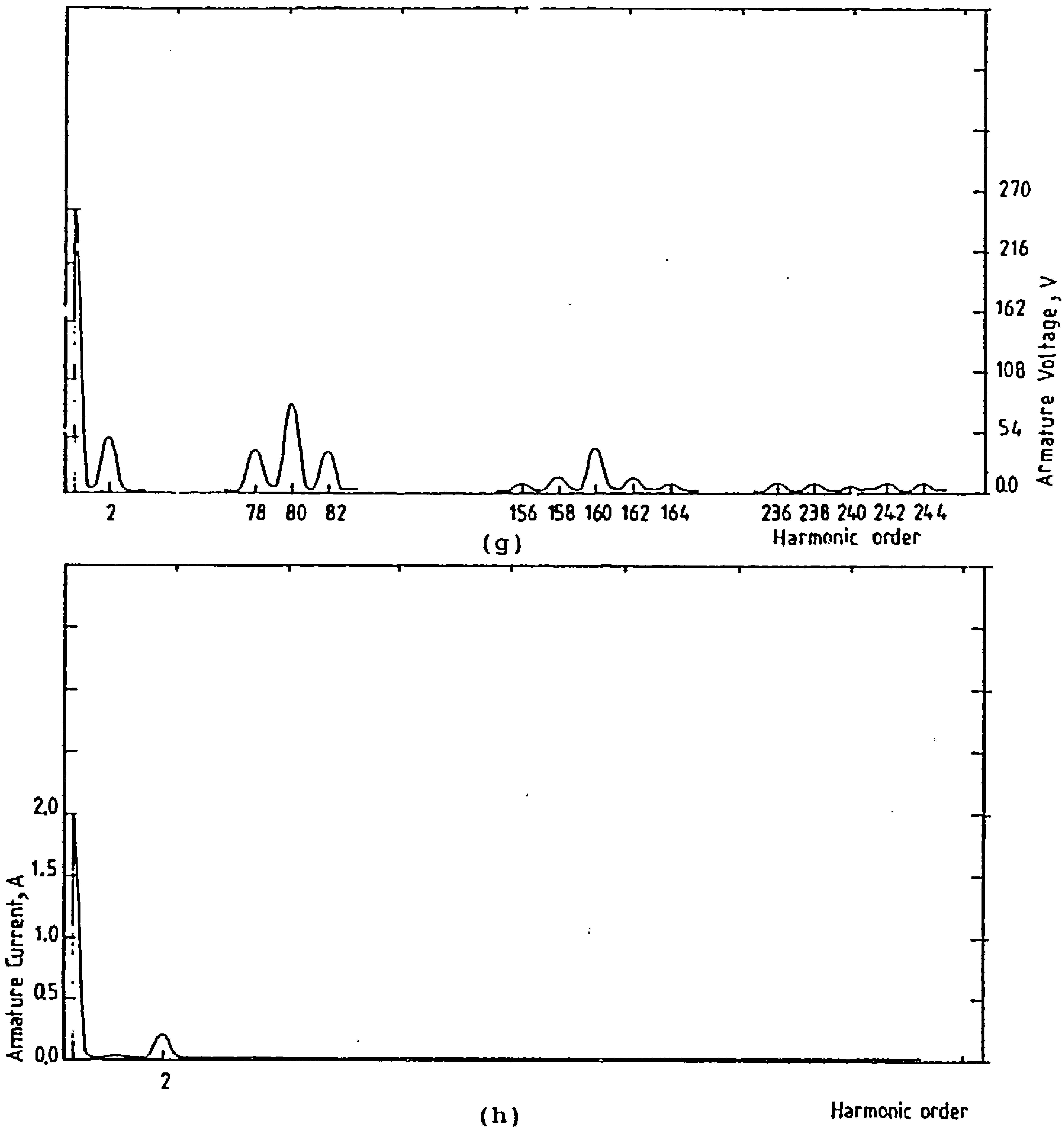

Figure6.31 Continued.
(g) Armature voltage spectrum.
(h) Armature current spectrum.

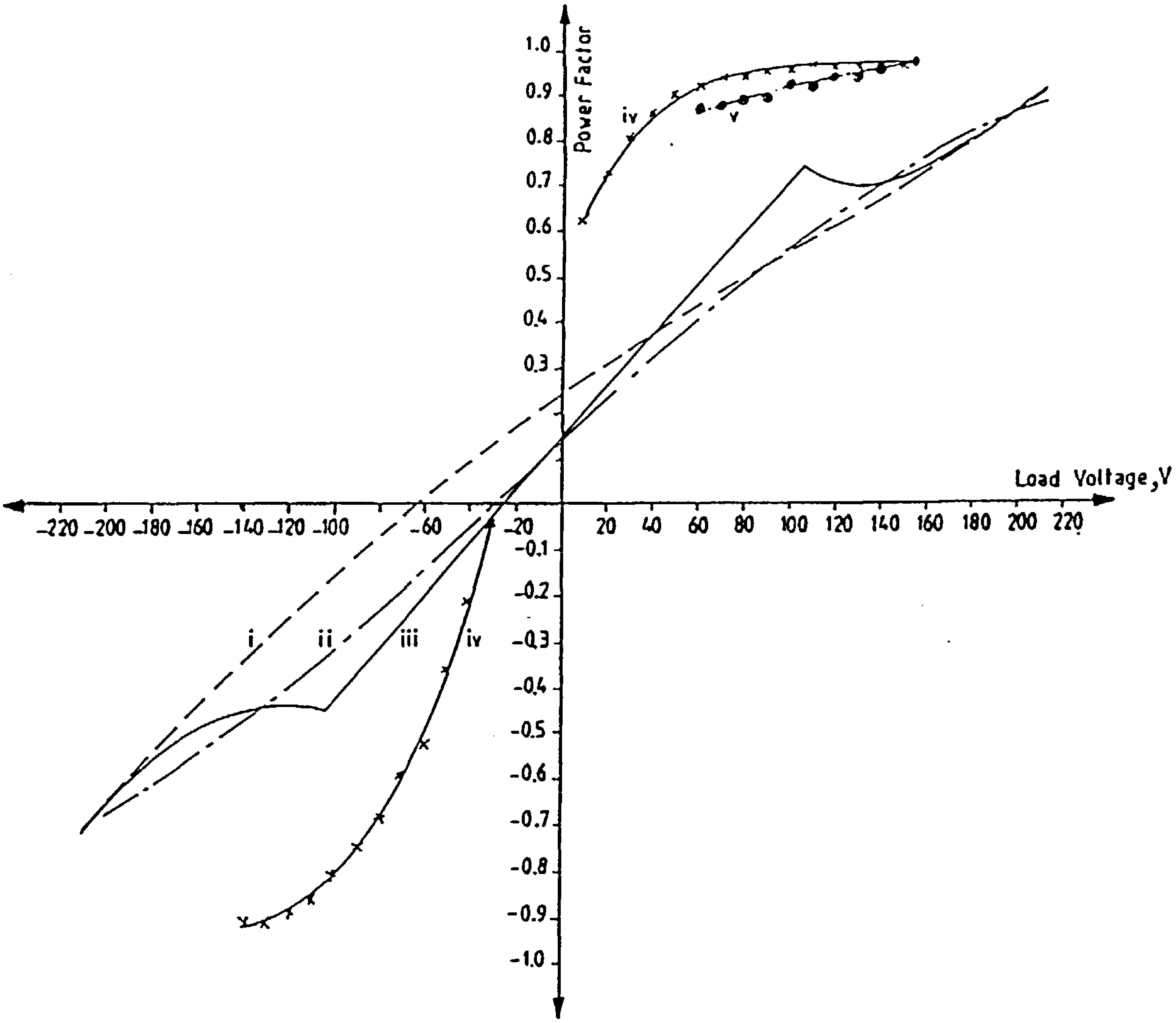

Figure6.32 Experimental variation of input power factor with load voltage for different controllers.

(i) Conventional controlled single-bridge on a passive load.

(ii) Sequence-controlled single-bridge on a passive load.

(iii) Sequence-controlled double-bridge on a passive load.

(iv) PWM bridge converter on a passive load.

(v) PWM bridge converter on a dc machine load.

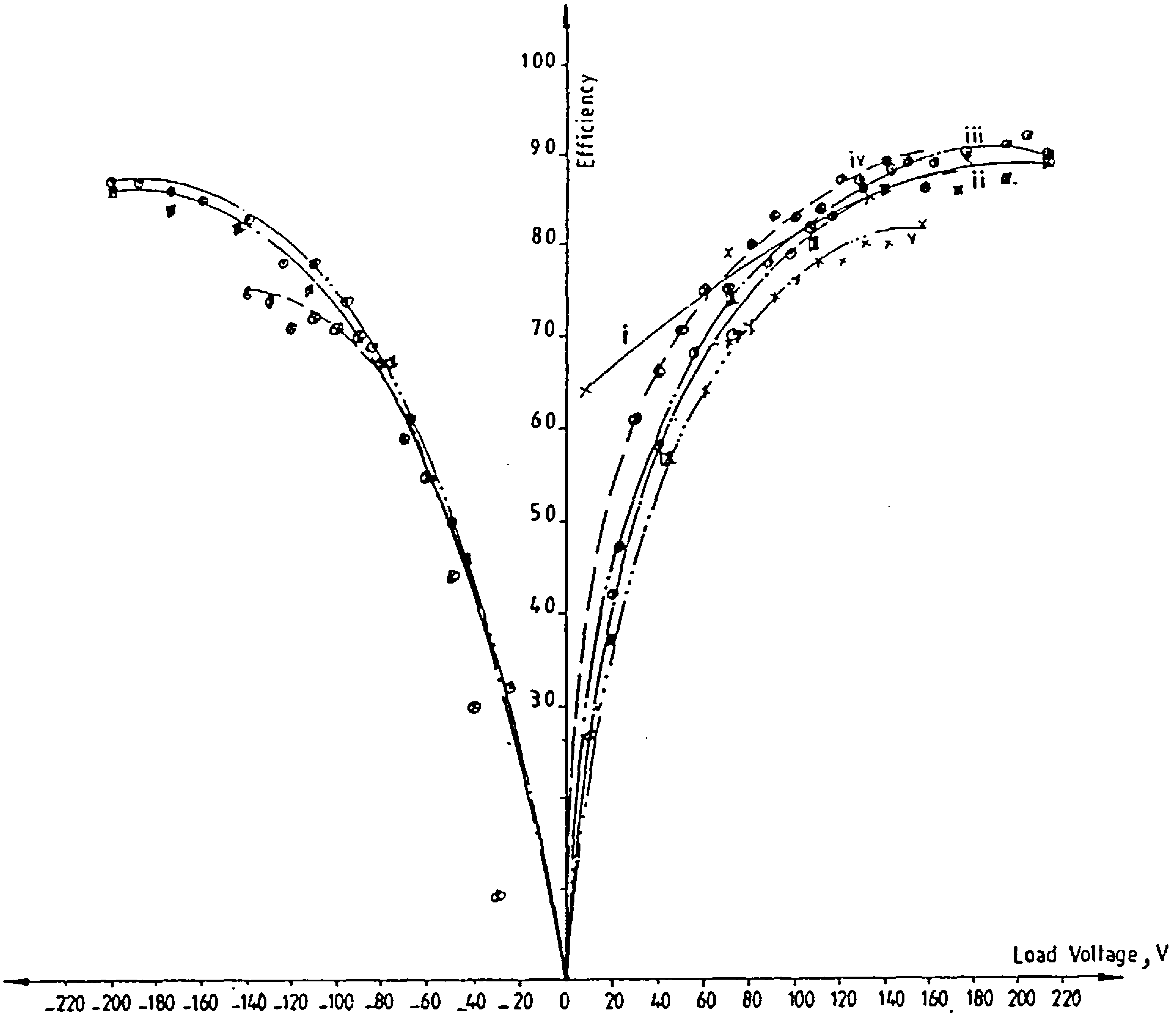

Figure6.33 Experimental variation of efficiency with load voltage for different controllers.

(i) Conventional controlled single-bridge on a passive load.
(ii) Sequence-controlled single-bridge on a passive load.
(iii) Sequence-controlled double-bridge on a passive load.
(iv) PWM bridge converter on a passive load.
(v) PWM bridge converter on a dc machine.

CHAPTER 7

CONCLUSION

This chapter presents a summary of the important features of the work described in the thesis and concludes with suggestions for further research.

In order to investigate fully the performance of various converter configurations and switching strategies, a number of laboratory-scale converters were designed and built. The commutation phenomenon, which is inevitable with line commutated ac-to-dc converters, was fully investigated. It was found that the commutation angle increases with an increase in the load current and supply reactance and decreases as the commutating voltage increases. As shown in figure 6.10, the commutation angle is a minimum at a firing delay angle of 90^o, where the commutating voltage is a maximum. One effect of commutation is to severely distort the supply voltage waveform, a process that is termed 'notching' and can cause mal-operation and misfiring of thyristors. This distortion is more severe with sequence control, since there are two commutation notches (at the firing delay angles α_v and α_f), whereas with conventional control there is only one. Another effect of commutation is that it reduces the mean load voltage. However, with sequence control the commutation angle produced at a firing delay angle α_f has no effect on the mean load voltage during either rectification or inversion, since the load voltage is already zero due to free-wheeling.

Harmonic analysis of the load voltage shows that it contains a dc component together with even harmonics whose magnitudes decrease with increasing harmonic order, with the second harmonic therefore being predominant. These voltage harmonics produce load current harmonics at the same frequency, the addition of which determines the peak-to-peak load current ripple. A comparison between different controllers indicates that the r.m.s. value of the second harmonic of the load voltage produced by the sequence-controlled double-bridge converter is 44% of that produced with a sequence-controlled single-bridge converter when the load voltage is 106V and 50% when the load voltage is -106V. This substantial improvement in the load voltage harmonics results in a corresponding improvement in the peak-to-peak load current ripple and consequently in a substantial savings in the cost of the output smoothing inductor. The harmonic analysis of the supply current waveform reveals that it contains odd harmonics whose magnitudes primarily depend on the firing delay angle and the type of the controller used. A comparison between different controllers shows that the sequence-controlled double-bridge converter produces smaller supply current harmonics resulting in lower losses and a better efficiency than that of conventional and sequence-controlled single-bridge converters. The variation of input power factor with firing delay angle presented in chapter 6 shows that the sequence-controlled double-bridge converter has a better power factor than either the conventional or sequence controlled single-bridge converters. To improve conditions even further, a pulse-width modulation (PWM) switching strategy was considered for a single-bridge converter. Since the switching devices have to turn-on and turn-off when required, and also withstand high voltage and current, gate turn-off (GTO) thyristors were selected. The switching frequency adopted for this converter was either 2kHz or 4kHz. The low-order supply current and load voltage harmonics produced at the higher frequency is almost the same as that produced at the lower frequency. However, the size and the cost of the filter elements to eliminate the high-order harmonics, which are located at the switching frequency and multiples of it, is smaller at 4kHz than that at 2kHz, but has the disadvantage of increased switching losses. A comparison between PWM and sequence-controlled double-bridge converters shows clearly an improvement in the low-order supply current harmonics with the PWM switching strategy, but no change in the load voltage harmonics. This improvement obtained is at the expense of producing high-order harmonics, but these can easily be filtered. Since the input displacement and distortion factors are improved with the PWM scheme, its power factor is considerably better than that of the sequence-controlled double-bridge converter. Another reason for this improvement is that the capacitor connected across the transformer secondary winding to eliminate the ringing on transformer voltage waveforms, also functions to some extent as a power factor correction capacitor.

A major disadvantage with the phase-controllers is a low input power factor particularly at low output voltages. This is improved substantially with the PWM controller and, in addition, the supply current and load voltage harmonics are also improved, which results in an important savings in the cost and size of the input and output filtering components.

With a supply voltage of 240V and a load current of 2A, the maximum mean load voltage available from the phase-controllers was 212V, compared to the 158V obtained from the PWM controller i.e. a reduction of 25%, which is clearly a disadvantage. Another disadvantage is the increased switching losses caused by more frequent device switching. In addition, GTOs are substantially more expensive than conventional thyristors and the gate drive circuits for GTOs are both more complex and expensive.

Mathematical models were developed for the PWM bridge converter and the sequence-controlled single and double-bridge converters, and computer programmes were written in Fortran 77 to be run on a mainframe computer. The circuit parameters for these models can easily be changed, in order to study converters of different power ratings or switching frequencies. The ripple content of the load current can be varied relative to its mean level, simply by altering the value of the load inductance, and so the programmes can be used to simulate situations from an almost ripple-free load current to the case where the load is purely resistive. The firing delay angles of each thyristor can be adjusted individually, in order to investigate different switching strategies. Computed and experimental results were in close agreement, which verifies the tensor and model-subroutine techniques in developing the digital models.

Analytical models were developed for sequence-controlled single and double-bridge converters and for a conventional controlled single-bridge converter. The models were developed by performing a Fourier analysis on the supply current and load voltage waveforms, as described in Appendix A2. Mathematical expressions were then derived for the Fourier coefficients, and from these the r.m.s. value of the n-th harmonic and the corresponding phase displacement angle were calculated on the assumption of a completely smooth load current. However, such an assumption is not justifiable with ac-to-dc converters and consequently the technique of Chapter 5 was developed to include the load current ripple in calculating the supply current harmonics. The results obtained from the analytical models agree very closely with the experimental and computed results which substantiates the techniques used in developing the models. These simple but effective models may supplement the digital ones in predicting the performance of the converter circuits. The major advantage of an analytical model over a digital one is that it allows the designer to assess which circuit parameters influence the converter characteristics, such as the input power factor, peak-to-peak load current ripple, harmonic content of the supply current and load voltage waveforms.

7.1 Suggestions for Further Work

The optimal PWM switching techniques used in ac inverters may be implemented to eliminate/or reduce low-order supply current harmonics, including those injected into the supply due to the load-side current ripple. This may be achieved by off-line calculation of the turn-on and turn-off angles, such that a predetermined number of low-order supply current harmonics are eliminated. These calculations may be repeated to provide switching angles for a complete range of output voltages and these angles may be stored in look-up tables. All that is then required is to retrieve the set of switching angles corresponding to the desired output voltage. These are then applied to the gates of the GTOs to turn them on and off, according to the required sequence. The advantages of an optimal PWM switching strategy is the total elimination/or minimisation of low-order supply current harmonics, leading to a substantial reduction in the cost and size of the input-side current filters. An increase in both the input displacement factor and the distortion factor results in a better power factor than either phase-controllers or conventional PWM switching strategy. A reduction in the peak-to-peak load current ripple results in a reduction in the size and cost of the output smoothing inductance.

REFERENCES

1)R.A. Van Eck, "The Separately Excited DC Traction Motor Applied to DC and Single-phase AC Rapid Transit Systems and Electrified Railroads, Part I", IEEE Transactions on Industry and General Applications., Vol. IGA-7, No. 5, Sep/Oct. 1971, pp. 643-649.

2)P.C. Sen, Thyristor DC Drives, J. Wiley,1981, Chapter 1.

3)R.A. Van Eck, "The Separately Excited DC Traction Motor Applied to DC and Single-phase AC Rapid Transit Systems and Electrified Railroads, Part II - Applications", IEEE Transactions on Industry and General Applications, Vol. IGA-7, No. 5, Srp/Oct. 1971, pp. 650-657.

4)F.T. Bennell, "Rectifiers for Railway-traction Substations", IEE. Elec. Power App., Vol.2, No. 1, 1979, pp. 22-26.

5)L.R. Denning, "Influence of Commutating Reactance on the Design of DC Power Supply Converters", Power Engineering Journal, 1987, pp. 181-187.

6)J. Schaefer, Rectifier Circuits Theory and Design, John Wiley and Sons inc., 1965, Chapter 4.

7)C.W. Lander, Power Electronics, McGraw Hill, 1981, Chapters 2, 3 and 8.

8)K.L. Briggs, "Harmonics from Thyristor Drives and Their Effect on Electricity Supplies", Published by KTK (Newtown) Ltd, 1979, pp. 1-6.

9)Karl-Heinz Bezold, Johannes Foster and Hilmar Zander, "Thyristor Converters for traction DC Motor Drives", IEEE Transactions on Industry Applications, Vol. IA-9, No. 5, Sep/Oct. 1973, pp. 612-617.

10)H.K. Patel and G.K. Dubey, "Modified Sequence-control Technique for Improving Performance of Regenerative Bridge Converters", IEEE Transactions on Industry Applications, Vol. IA-19, No. 5, Sep/Oct. 1983, pp. 683-688.

11)W. Drury, W. Farrer and B.L. Jones, "Performance of Thyristor Bridge Converters Employing Flywheeling", IEE Proceedings, Vol. 127, Pt. B, No. 4, July 1980, pp. 268-276.

12)W. Farrer and D.F. Andrew, "Fully Controlled Regenerative Bridges with Half-controlled Characteristics", IEE Proceedings, Vol. 125, No. 2, Feb. 1978, pp. 109-112.

13)M.H. Rashid, Power Electronics: Circuits, Devices and Applications, Prentice-Hall, 1988, Chapter 4.

14)Mohan, Undeland and Robbins, Power Electronics: Converters, Applications and Design, J. Wiley, 1989, Chapter 6.

15)Teruo Kataoka, Kazuhiro Mizumachi and Sota Miyairi, "A Pulsewidth Controlled AC-to-DC converter to Improve Power Factor and Waveform of AC Line Current", IEEE Transactions on Industry Applications, Vol. IA-15, No. 6, Nov/Dec. 1979, pp. 670-675.

16)K.A. Krishnamurthy, G.K. Dubey and Prof. G.N. Revankar, "Convertor Control with Selective Reduction of Line Harmonics", IEE Proceedings, Vol. 125, No. 2, Feb. 1978, pp. 141-145.

17)G.R. Selmon and A. Straughen, Electric Machines, Addison-Wesley, 1980, Chapter 4.

18)P.C. Sen, Principles of Electric Machines and Power Electronics, John Wiley & Sons, 1989, Chapter 4.

19)V.R. Stefanovic, "Power Factor Improvement with a Modified Phase-controlled Converter", IEEE transactions on Industry Applications, Vol. IA-15, No. 2, March/April 1979, pp. 193-201.

20)J.M.D. Murphy and F.G. Turnbull, Power Electronic Control of AC Motors, Pergamon Press, 1988, Chapter 3.

21)P. Horowitz, and W. Hill, The Art of Electronics, Cambridge University Press, 1980, Chapters 3 and 9.

22)A.P. Malvino, Electronic Principles, Second Edition, Tata McGraw-Hill, 1979, Chapter 21.

23)B. Ilango, et al, "Firing Circuit for Three-phase Thyristor-bridge Rectifier", IEEE Transactions, Vol. IECI-25, No. 1, 1978, pp. 45-49.

24)F. Burgum, E.B.G. Nijhoh and A. Woodworth, "Gate Turn-off Switch", Mullard Technical Publication, 1981, M81-0075.

25)A. Woodworth and F. Burgum, "Simple Rules for GTO Circuit Design", Mullard Technical Publication, 1981, M83-0137.

26)F.J. Burgum, "Basic GTO Drive Circuits", Mullard Technical Publication, 1982, M81-0128.

27)J.A. Houldsworth and W.B. Rosink, "Introduction to PWM Speed Control System for 3-phase AC Motors", Mullard Technical Publication, 1981, M81-0050.

28)The Gate Turn-off Switch in PWM ac Motor Control, Mullard Technical Publication, 1981, M81-0057.

29)Howard M. Berlin, Design of Phase-lock Loop circuit with Experiments, H.W. Sams, 1979.

30)A. Barno and D.I. Porat, Operational Amplifiers, Second Edition, John Wiley & Sons, 1989, Chapter 11.

31)W.G. Jung, IC Op-amp Cook book, Second Edition, H.W. Sams, 1986.

32)S. Williams and I.R. Smith, "SCR Bridge Converter Computation Using Tensor Methods", IEEE Transactions on Computers, Vol. C-25, 1976, pp. 1-6.

33)J.G. Kettleborough, I.R. Smith and B.A. Fanthome, "Simulation of a dedicated Aircraft Generator Supplying a Heavy Rectified Load", IEE Proceedings, Vol. 130, Pt. B, No. 6, 1983, pp. 431-435.

34)J.G. Kettleborough, I.R. Smith and B.A. Fanthome, "Simulation of a Transformer/Rectifier Unit for Aircraft Power-supply Systems", IEE Proceedings, Vol. 129, Pt. B, No. 6, 1982, pp. 323-329.

35)J.K. Hall, J.G. Kettleborough and A.B.M.J. Razak, "Parallel Operation of Bridge Rectifiers Without an Interbridge Reactor", IEE Proceedings, Vol. 137, Pt. B, No. 2, 1990, pp. 125-140.

36)J.L. Hay and N.G. Hingorani, "Dynamic Simulation of Multiconverter HVDC Systems by Digital Computer Part I: Mathematical Model", IEEE Transactions on Power Apparatus and Systems, Vol. PAS-89, No. 2, 1970, pp. 218-222.

37)J.L. Hay and N.G. Hingorani, "Dynamic Simulation of Multiconverter HVDC Systems by Digital Computer Part II: Computer Program", IEEE Transactions on Power Apparatus and Systems, Vol. PAS-89, No. 2, 1970, pp. 222-228.

38)H.H. Happ, Diakoptics and Networks, Academic Press, 1971, Chapter 1.

39)P.A. Stark, Introduction to Numerical Methods, Macmillan, 1971, Chapters 2 and 3.

40)C.F. Gerald, Applied Numerical Analysis, Second Edition, Addison Wesley, 1980, Chapters 1 and 5.

41)T.M.R. Ellis, Structured Fortran, University of Sheffield Computing Services, 1980.

42)Y.C. Chan, Mathematical Modelling of a PWM controlled ac-to-dc converter, Final Year Undergraduate Project, Department of Electronic and Electrical Engineering, Loughborough University of Technology, 1988.

43)High Speed 'H.R.C.' Fuse Links, A350 Series, International Rectifier, Bulletin E2808A.

Appendix A1

Derivation of Mean Armature Voltage

In deriving the expressions presented in this section, the following assumptions were made:

a) The armature current is smooth and continuous.
b) Thyristor voltage drops are negligible.

The circuit diagram and armature voltage waveforms for a series connected double-bridge converter are given in figures A1.1(a) and (b) respectively. The mean armature voltage is obtained from the unshaded area of figure A1.1(b) as

$$V_a = \frac{1}{\pi}\left[\int_0^{\alpha_{f2}} -V_m \sin(\omega t)d(\omega t) + \int_{\alpha_{f2}}^{\alpha_{f1}} -\frac{V_m}{2}\sin(\omega t)d(\omega t) + \int_{\alpha_{v2}+\delta_{v2}}^{\alpha_{v1}+\delta_{v1}} \frac{V_m}{2}\sin(\omega t)d(\omega t) + \int_{\alpha_{v1}+\delta_{v1}}^{\pi} V_m \sin(\omega t)d(\omega t)\right] \quad (A1.1)$$

where V_m is the peak value of the supply voltage and δ_{v1}, δ_{v2} are the commutation angles defined in figure A1.1(b).

Integrating equation (A1.1) gives

$$V_a = \frac{1}{4} V_{d0}[\cos \alpha_{f1} + \cos \alpha_{f2} + \cos(\alpha_{v1}+\delta_{v1}) + \cos(\alpha_{v2}+\delta_{v2})] \quad (A1.2)$$

where α_{f1}, α_{v1}, α_{f2} and α_{v2} are the firing delay angles and

$$V_{d0} = \frac{2V_m}{\pi} \quad (A1.3)$$

It follows from equation (2.12) of Chapter 2 that,

$$\cos(\alpha_{v1} + \delta_{v1}) = \cos \alpha_{v1} - \frac{2I_aX_t}{V_m} \quad (A1.4)$$

and

$$\cos(\alpha_{v2} + \delta_{v2}) = \cos \alpha_{v2} - \frac{2I_aX_t}{V_m} \quad (A1.5)$$

Substituting these results in equation (A1.2) yields

$$\begin{aligned} V_a = \frac{1}{4} V_{d0}[\cos \alpha_{f1} + \cos \alpha_{v1} + \\ \cos \alpha_{f2} + \cos \alpha_{v2} - \frac{4I_aX_t}{V_m}] \end{aligned} \quad \text{(A1.6)}$$

where X_t is the combined supply and transformer leakage reactance.

The commutation angles δ_{f1} and δ_{f2} included in figure A1.1(b) have no effect on the mean output voltage for this control strategy, since commutation occurs during the free-wheeling period. The mean armature voltage for a sequence-controlled single-bridge converter is obtained by substituting $\alpha_{v1}=\alpha_{v2}=\alpha_v$, $\alpha_{f2}=\alpha_{f2}=\alpha_f$ and $\delta_{v1}=\delta_{v2}=\delta_v$ in equation (A1.2) as

$$V_a = \frac{1}{2} V_{d0}[\cos \alpha_f + \cos(\alpha_v + \delta_v)] \quad \text{(A1.7)}$$

From equation (2.12) of Chapter 2,

$$\cos(\alpha_v + \delta_v) = \cos \alpha_v - \frac{I_aX_t}{V_m} \quad \text{(A1.8)}$$

and substituting in (A1.7) gives:

$$V_a = \frac{1}{2} V_{d0}[\cos \alpha_f + \cos \alpha_v - \frac{I_aX_t}{V_m}] \quad \text{(A1.9)}$$

It follows from equation (A1.8) that,

a) For a conventional controlled single-bridge converter $\alpha_v=\alpha_f=\alpha$, hence

$$V_a = \frac{1}{2} V_{d0}[2\cos \alpha - \frac{I_aX_t}{V_m}] \quad \text{(A1.10)}$$

b) For a half-controlled bridge converter $\alpha_f=0$, $\alpha_v=\alpha$, so that

$$V_a = \frac{1}{2} V_{d0}[1 + \cos \alpha - \frac{I_aX_t}{V_m}] \quad \text{(A1.11)}$$

If commutation is neglected (X_t=0) equations (A1.6), (A1.9), (A1.10) and (A1.11) reduce respectively to

$$V_a = \frac{1}{4} V_{d0}[\cos \alpha_{f1} + \cos \alpha_{v1} + \cos \alpha_{f2} + \cos \alpha_{v2}] \quad (A1.12)$$

$$V_a = \frac{1}{2} V_{d0}[\cos \alpha_f + \cos \alpha_v] \quad (A1.13)$$

$$V_a = V_{d0} \cos \alpha \quad (A1.14)$$

and $$V_a = \frac{1}{2} V_{d0}[1 + \cos \alpha] \quad (A1.15)$$

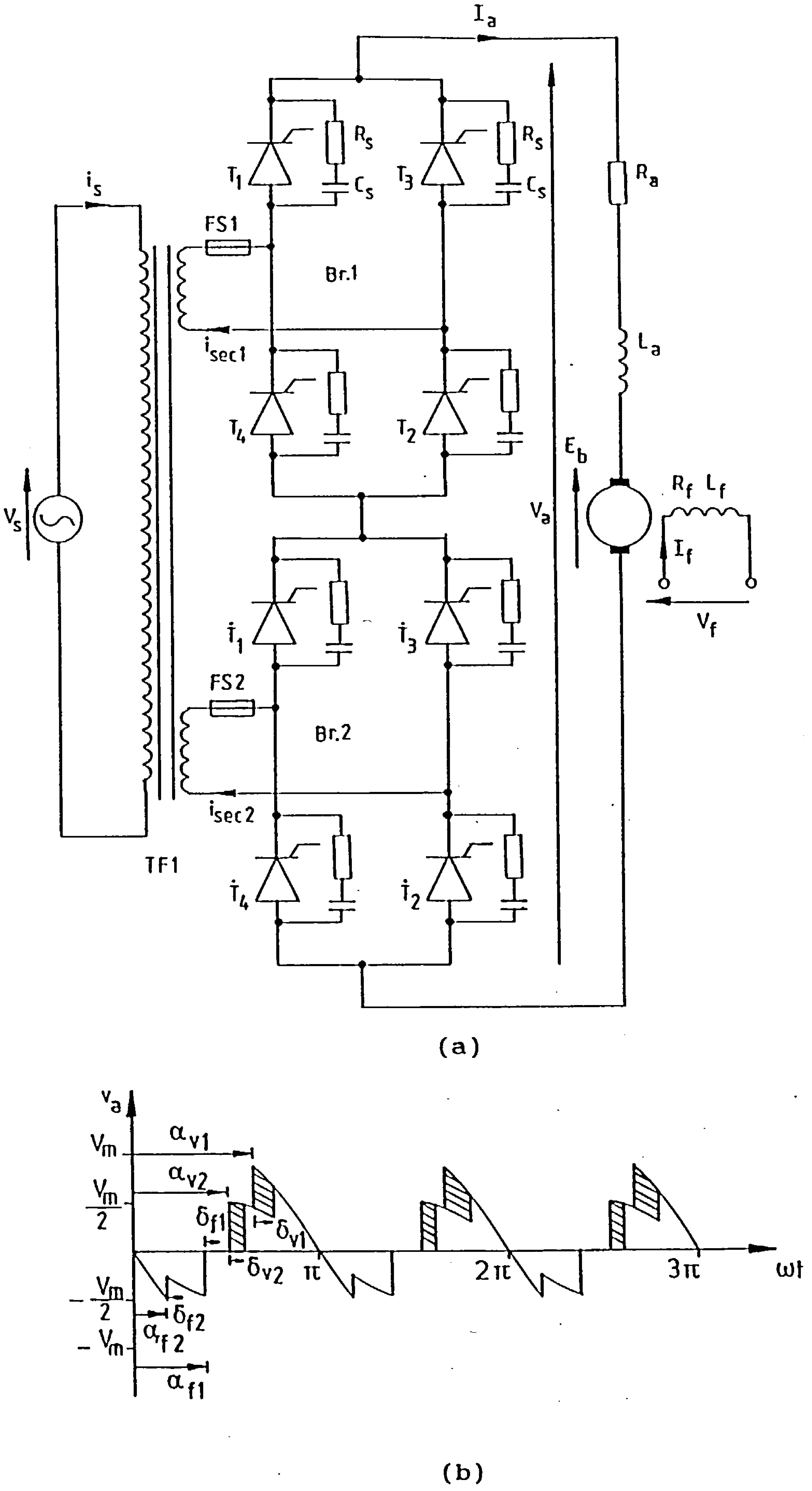

FigureA1.1 Series connected double-bridge converter.

(a) Connection.

(b) Armature voltage waveform.

Appendix A2

Power Factor and Harmonic Analysis of the Supply Current and Armature Voltage Waveforms

A2.1 Power Factor and Harmonic Analysis of the Supply Current Waveform

Figure A2.1 shows a series connected double-bridge converter employing sequence control. Neglecting commutation, the supply current and armature voltage waveforms for a smooth and continuous armature current are as shown in figures A2.1(b) and (c). Inspection of the supply current waveform reveals that the dc component is zero and only odd harmonics exist. The Fourier series for this waveform can be represented by

$$i_s = \sum_{n=1}^{\infty} [a_n \cos(n\omega t) + b_n \sin(n\omega t)] \qquad n=1,3,.. \qquad (A2.1)$$

where i_s is the supply current waveform. The coefficients a_n and b_n are obtained from,

$$a_n = \frac{1}{\pi}\left[\int_0^{2\pi} i_s \cos(n\omega t)d(\omega t)\right] \qquad (A2.2)$$

$$\text{or } a_n = \frac{1}{\pi}\left[\int_0^{\alpha_{v2}} -I_a\cos(n\omega t)d(\omega t) + \int_{\alpha_{v2}}^{\alpha_{f2}} -\frac{I_a}{2}\cos(n\omega t)d(\omega t) + \int_{\alpha_{f1}}^{\alpha_{v1}} \frac{I_a}{2}\cos(n\omega t)d(\omega t) + \int_{\alpha_{v1}}^{\pi+\alpha_{v2}} I_a\cos(n\omega t)d(\omega t) + \int_{\pi+\alpha_{v2}}^{\pi+\alpha_{f2}} \frac{I_a}{2}\cos(n\omega t)d(\omega t) + \int_{\pi+\alpha_{f1}}^{\pi+\alpha_{v1}} -\frac{I_a}{2}\cos(n\omega t)d(\omega t) + \int_{\pi+\alpha_{v1}}^{2\pi} -I_a\cos(n\omega t)d(\omega t)\right] \qquad (A2.3)$$

giving

$$a_n = -\frac{I_a}{n\pi}[\sin(n\alpha_{v2})+\sin(n\alpha_{f2})+\sin(n\alpha_{v1})+\sin(n\alpha_{f1})] \qquad (A2.4)$$

and

$$b_n = \frac{1}{\pi}\left[\int_0^{2\pi} i_s \sin(n\omega t)d(\omega t)\right] \qquad (A2.5)$$

$$\text{or } b_n = \frac{1}{\pi}\left[\int_0^{\alpha_{v2}} -I_a\sin(n\omega t)d(\omega t) + \int_{\alpha_{v2}}^{\alpha_{f2}} -\frac{I_a}{2}\sin(n\omega t)d(\omega t) + \right.$$

$$\int_{\alpha_{f1}}^{\alpha_{v1}} \frac{I_a}{2}\sin(n\omega t)d(\omega t) + \int_{\alpha_{v1}}^{\pi+\alpha_{v2}} I_a\sin(n\omega t)d(\omega t) +$$

$$\int_{\pi+\alpha_{v2}}^{\pi+\alpha_{f2}} \frac{I_a}{2}\sin(n\omega t)d(\omega t) + \int_{\pi+\alpha_{f1}}^{\pi+\alpha_{v1}} -\frac{I_a}{2}\sin(n\omega t)d(\omega t) +$$

$$\left.\int_{\pi+\alpha_{v1}}^{2\pi} -I_a\sin(n\omega t)d(\omega t)\right] \qquad (A2.6)$$

giving

$$b_n = \frac{I_a}{n\pi}\,[\cos(n\alpha_{v2})+\cos(n\alpha_{f2})+\cos(n\alpha_{v1})+\cos(n\alpha_{f1})] \qquad (A2.7)$$

The nth-harmonic rms current I_n is

$$I_n = \sqrt{\frac{a_n^2 + b_n^2}{2}} \qquad (A2.8)$$

Using equations A2.4 and A2.7 yields

$$\begin{aligned} I_n = \frac{\sqrt{2}I_a}{n\pi} \Bigg[& \frac{2+\cos n(\alpha_{v2}-\alpha_{f2})+\cos n(\alpha_{v2}-\alpha_{v1}) +}{2} \\ & \frac{\cos n(\alpha_{v2}-\alpha_{f1})+\cos n(\alpha_{f2}-\alpha_{v1}) +}{2} \\ & \frac{\cos n(\alpha_{f2}-\alpha_{f1})+\cos n(\alpha_{v1}-\alpha_{f1})}{2}\Bigg]^{1/2} \end{aligned} \qquad (A2.9)$$

Operating in zone 1 $\alpha_{f1}=\alpha_{v2}=\alpha_{f2}$, which when substituted in equation A2.9 gives

$$\frac{I_n}{I_a} = \frac{\sqrt{2}}{n\pi}\sqrt{\frac{5 + 3\cos n(\alpha_{v1} - \alpha_{f1})}{2}} \qquad (A2.10)$$

and in zone 2 $\alpha_{v2}=\alpha_{f1}$ so that

$$\frac{I_n}{I_a} = \frac{\sqrt{2}}{n\pi}\sqrt{\frac{3+2\cos n(\alpha_{v2}-\alpha_{v1})+ 2\cos n(\alpha_{v2}-\alpha_{f1})+ \cos n(\alpha_{v1}-\alpha_{f1})}{2}} \qquad (A2.11)$$

For a sequence controlled single-bridge $\alpha_{v1}=\alpha_{f1}=\alpha_v$ and $\alpha_{v2}=\alpha_{f2}=\alpha_f$. Substituting in equation A2.9 yields

$$\frac{I_n}{I_a} = \frac{2\sqrt{2}}{n\pi}\sqrt{\frac{1 + \cos n(\alpha_v - \alpha_f)}{2}} \qquad (A2.12)$$

For a conventional controlled single-bridge in which $\alpha_{v1}=\alpha_{v2}=\alpha_{f1}=\alpha_{f2}=\alpha$ which gives

$$\frac{I_n}{I_a} = \frac{2\sqrt{2}}{n\pi} \qquad (A2.13)$$

The input displacement angle for the nth-harmonic is

$$\phi_n = \tan^{-1}\frac{a_n}{b_n} \qquad (A2.14)$$

Using equations A2.4 and A2.7 yields

$$\phi_n = -\tan^{-1}\frac{\sin n\alpha_{v2} + \sin n\alpha_{f2} + \sin n\alpha_{v1} + \sin n\alpha_{f1}}{\cos n\alpha_{v2} + \cos n\alpha_{f2} + \cos n\alpha_{v1} + \cos n\alpha_{f1}} \qquad (A2.15)$$

where the minus sign indicates that the supply current lags the supply voltage. The displacement angle for the fundamental component is obtained by putting n=1 in equation A2.15 as

$$\phi_n = -\tan^{-1}\frac{\sin \alpha_{v2} + \sin \alpha_{f2} + \sin \alpha_{v1} + \sin \alpha_{f1}}{\cos \alpha_{v2} + \cos \alpha_{f2} + \cos \alpha_{v1} + \cos \alpha_{f1}} \qquad (A2.16)$$

When operating in zone 1

$$\phi_1 = -\tan^{-1}\left(\frac{3\sin \alpha_{f1} + \sin \alpha_{v1}}{3\cos \alpha_{f1} + \cos \alpha_{v1}}\right) \qquad (A2.17)$$

and in zone 2

$$\phi_1 = -\tan^{-1}\left(\frac{2\sin \alpha_{v2} + \sin \alpha_{v1} + \sin \alpha_{f1}}{2\cos \alpha_{v2} + \cos \alpha_{v1} + \cos \alpha_{f1}}\right) \qquad (A2.18)$$

For a sequence-controlled single-bridge

$$\phi_1 = -\tan^{-1}\frac{\alpha_v + \alpha_f}{2} \qquad (A2.19)$$

and with conventional control,

$$\phi_1 = -\tan^{-1}\alpha \qquad (A2.20)$$

The supply power factor is,

$$P.F. = \frac{I_1}{I_s}\cos\phi_1 \qquad (A2.21)$$

where I_1 is the rms value of the fundamental component and I_s is the rms value of the supply current.

Referring to figure A2.1(b), it follows that

$$I_s = \sqrt{\frac{1}{2\pi}\int_0^{2\pi} i_s^2 d(\omega t)} \qquad (A2.22)$$

or

$$I_s = \frac{I_a}{2}\sqrt{\frac{3\alpha_{v2}+\alpha_{f2}-3\alpha_{v1}-\alpha_{f1}+4\pi}{\pi}} \qquad (A2.23)$$

Operating in zone 1

$$I_s = \frac{I_a}{2}\sqrt{\frac{3(\alpha_{f1}-\alpha_{v1})+4\pi}{\pi}} \qquad (A2.24)$$

and in zone 2

$$I_s = \frac{I_a}{2}\sqrt{\frac{4\alpha_{v2}-3\alpha_{v1}-\alpha_{f1}+4\pi}{\pi}} \qquad (A2.25)$$

For sequence controlled single-bridge

$$I_s = I_a\sqrt{\frac{\pi-\alpha_v+\alpha_f}{\pi}} \qquad (A2.26)$$

and for a conventional-controlled single-bridge

$$I_s = I_a \qquad (A2.27)$$

The supply power factor for a sequence-controlled double-bridge converter operating in zone 1 is

$$P.F. = 0.9 \sqrt{\frac{\pi[5 + 3\cos(\alpha_{v1}-\alpha_{f1})]}{6(\alpha_{f1}-\alpha_{v1}) + 8\pi}}$$

$$\cos \tan^{-1}\left(\frac{3\sin \alpha_{f1}+\sin \alpha_{v1}}{3\cos \alpha_{f1}+\cos \alpha_{v1}}\right) \qquad (A2.28)$$

and when operating in zone 2

$$P.F.=0.9\sqrt{\frac{\pi[3+2\cos(\alpha_{v2}-\alpha_{v1})+ 2\cos(\alpha_{v2}-\alpha_{f1})+ \cos(\alpha_{v1}-\alpha_{f1})]}{8\alpha_{v2}-6\alpha_{v1}-2\alpha_{f1}+8\pi}}$$

$$\cos \tan^{-1}\left(\frac{2\sin \alpha_{v2} + \sin \alpha_{v1} + \sin \alpha_{f1}}{2\cos \alpha_{v2} + \cos \alpha_{v1} + \cos \alpha_{f1}}\right) \qquad (A2.29)$$

For a sequence-controlled single-bridge

$$P.F. = 0.8 \left[\frac{\cos \alpha_v + \cos \alpha_f}{\sqrt{(\pi - \alpha_v + \alpha_f)}}\right] \qquad (A2.30)$$

and for a conventional controlled single-bridge

$$P.F. = 0.9 \cos \alpha \qquad (A2.31)$$

A2.2 Harmonic Analysis of Armature Voltage Waveform

Neglecting commutation, the armature voltage waveform of figure A2.1(c) may be represented by the Fourier series

$$V_a = V_{dc} + \sum_{n=2}^{\infty} [a_{nv}\cos(n\omega t) + b_{nv}\sin(n\omega t)] \quad n=2,4,.. \qquad (A2.32)$$

where

$$V_{dc} = \frac{1}{\pi} \int_0^{\pi} V_m \sin(\omega t)\, d(\omega t) \qquad (A2.33)$$

$$a_{nv} = \frac{2}{\pi} \int_0^{\pi} V_m \sin(\omega t) \cos(n\omega t)\, d(\omega t) \qquad (A2.34)$$

$$b_{nv} = \frac{2}{\pi} \int_0^{\pi} V_m \sin(\omega t) \sin(n\omega t)\, d(\omega t) \qquad (A2.35)$$

The dc component V_{dc} is the average value of the armature voltage waveform, as is evident from equation A2.33.

Equation A2.32 can also be expressed as

$$V_a = V_{dc} + \sum_{n=2}^{\infty} \sqrt{2}V_n \sin(n\omega t+\phi_n)) \quad n=2,4,. \tag{A2.36}$$

$$V_n = \pm \sqrt{\frac{a_{nv}^2+b_{nv}^2}{2}} \tag{A2.37}$$

$$\phi_n = \tan^{-1} \frac{a_{nv}}{b_{nv}} \tag{A2.38}$$

where V_n is the rms value of the nth-harmonic and ϕ_n is the phase angle.

The coefficients a_{nv} and b_{nv} for the armature voltage waveform of figure A2.1(c) are

$$a_{nv}=\frac{2}{\pi}\left[\int_0^{\alpha_{v2}} -V_m\sin(\omega t)\cos(n\omega t)d(\omega t) + \int_{\alpha_{v2}}^{\alpha_{f2}} -\frac{V_m}{2}\sin(\omega t)\cos(n\omega t)d(\omega t) + \int_{\alpha_{f1}}^{\alpha_{v1}} \frac{V_m}{2}\sin(\omega t)\cos(n\omega t)d(\omega t) + \int_{\alpha_{v1}}^{\pi} V_m\sin(\omega t)\cos(n\omega t)d(\omega t)\right] \tag{A2.39}$$

and

$$b_{nv}=\frac{2}{\pi}\left[\int_0^{\alpha_{v2}} -V_m\sin(\omega t)\sin(n\omega t)d(\omega t) + \int_{\alpha_{v2}}^{\alpha_{f2}} -\frac{V_m}{2}\sin(\omega t)\sin(n\omega t)d(\omega t) + \int_{\alpha_{f1}}^{\alpha_{v1}} \frac{V_m}{2}\sin(\omega t)\sin(n\omega t)d(\omega t) + \int_{\alpha_{v1}}^{\pi} V_m\sin(\omega t)\sin(n\omega t)d(\omega t)\right] \tag{A2.40}$$

which reduce to

$$a_{nv} = \frac{V_m}{\pi}\left[\frac{1}{n+1}\cos A\cos B - \frac{1}{n-1}\cos C\cos D + \frac{1}{n+1}\cos E\cos F - \frac{1}{n-1}\cos G\cos H\right] \tag{A2.41}$$

and

$$b_{nv} = \frac{V_m}{\pi}\left[\frac{1}{n+1}\sin A\cos B - \frac{1}{n-1}\sin C\cos D + \frac{1}{n+1}\sin E\cos F - \frac{1}{n-1}\sin G\cos H\right] \tag{A2.42}$$

where $$A = \frac{(n+1)(\alpha_{f2}+\alpha_{v2})}{2} \tag{A2.43}$$

$$B = \frac{(n+1)(\alpha_{f2}-\alpha_{v2})}{2} \tag{A2.44}$$

$$C = \frac{(n-1)(\alpha_{f2}+\alpha_{v2})}{2} \tag{A2.45}$$

$$D = \frac{(n-1)(\alpha_{f2}-\alpha_{v2})}{2} \tag{A2.46}$$

$$E = \frac{(n+1)(\alpha_{v1}+\alpha_{f1})}{2} \tag{A2.47}$$

$$F = \frac{(n+1)(\alpha_{v1}-\alpha_{f1})}{2} \tag{A2.48}$$

$$G = \frac{(n-1)(\alpha_{v1}+\alpha_{f1})}{2} \tag{A2.49}$$

$$H = \frac{(n-1)(\alpha_{v1}-\alpha_{f1})}{2} \tag{A2.50}$$

The Fourier coefficients a_{nv} and b_{nv} for a sequence controlled single-bridge converter are obtained by substituting $\alpha_{v1}=\alpha_{f1}=\alpha_v$ and $\alpha_{v2}=\alpha_{f2}=\alpha_f$ in equations A2.43 to A2.50, which gives

$$a_{nv} = \frac{V_m}{\pi} \left[\frac{1}{n+1}\cos A - \frac{1}{n-1}\cos C + \frac{1}{n+1}\cos E - \frac{1}{n-1}\cos G\right] \tag{A2.51}$$

$$b_{nv} = \frac{V_m}{\pi} \left[\frac{1}{n+1}\sin A - \frac{1}{n-1}\sin C + \frac{1}{n+1}\sin E - \frac{1}{n-1}\sin G\right] \tag{A2.52}$$

where $$A = (n+1)\alpha_f \tag{A2.53}$$

$$C = (n-1)\alpha_f \tag{A2.54}$$

$$E = (n+1)\alpha_v \tag{A2.55}$$

$$G = (n-1)\alpha_v \tag{A2.56}$$

For a conventional controlled single-bridge converter $\alpha_{v1}=\alpha_{f1}=\alpha_{v2}=\alpha_{f2}=\alpha$, so that

$$a_{nv} = \frac{2V_m}{\pi}\left[\frac{1}{n+1}\cos A - \frac{1}{n-1}\cos C\right] \tag{A2.57}$$

$$b_{nv} = \frac{2V_m}{\pi}\left[\frac{1}{n+1}\sin A - \frac{1}{n-1}\sin C\right] \tag{A2.58}$$

where $$A = (n+1)\alpha \tag{A2.59}$$

$$C = (n-1)\alpha \tag{A2.60}$$

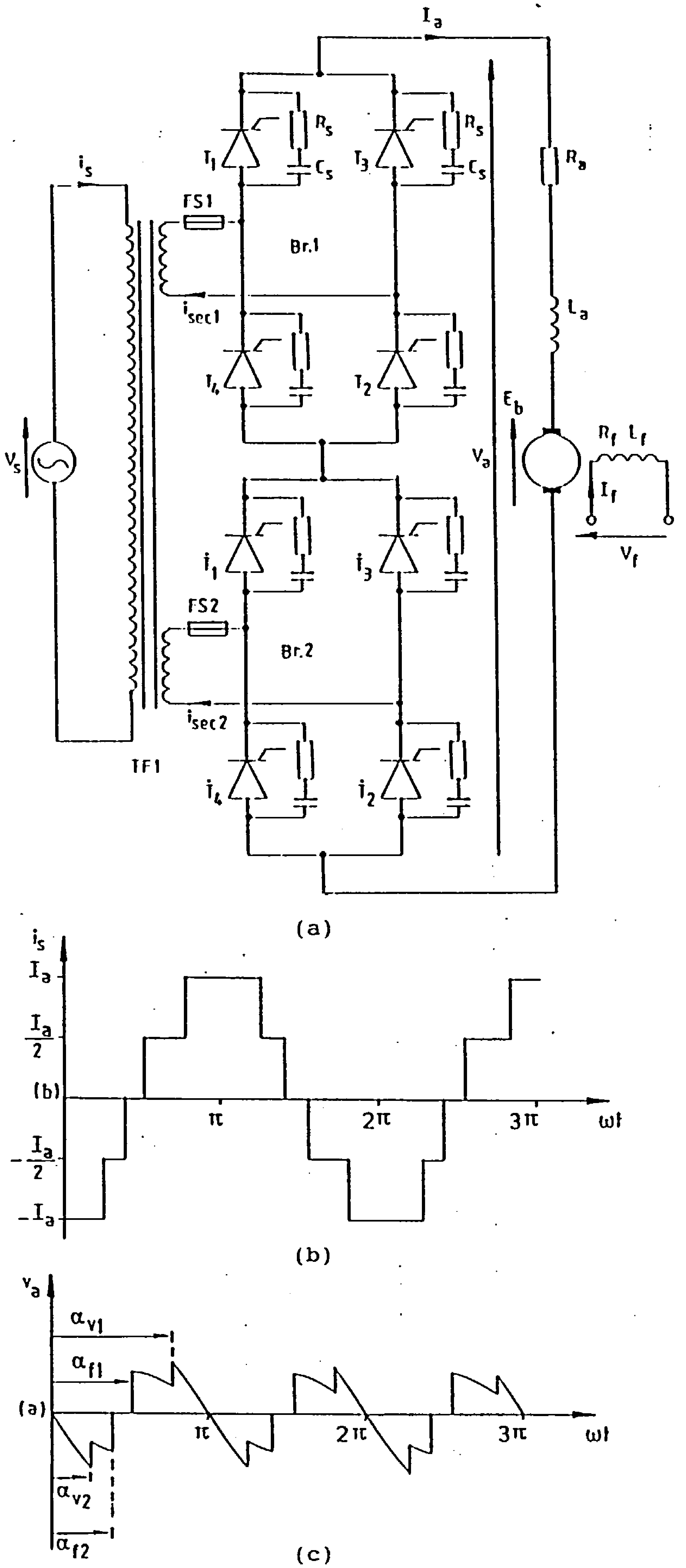

(a)

(b)

(c)

FigureA2.1 Series connected double-bridge converter.
(a) Connection.
(b) Supply current waveform.
(c) Armature voltage waveform.

Appendix A3

Snubber-circuit Design

The snubber circuit configuration is shown in figure A3.1. The design data for the converter grade thyristor CR24U quotes a maximum continuous on-state current I_T of 36A and a maximum $\frac{dv}{dt}$ of 200V/μs. It follows that

$$C_S = \frac{I_T}{\left[\frac{dv}{dt}\right]} = 0.18\mu F \qquad (A3.1)$$

A standard 0.22μF, 250V ac capacitor was chosen. The resistor R_S was selected to limit the peak anode current at turn-on to about 1.5A for a supply voltage of 240V. This yields a value of R_S = 220Ω.

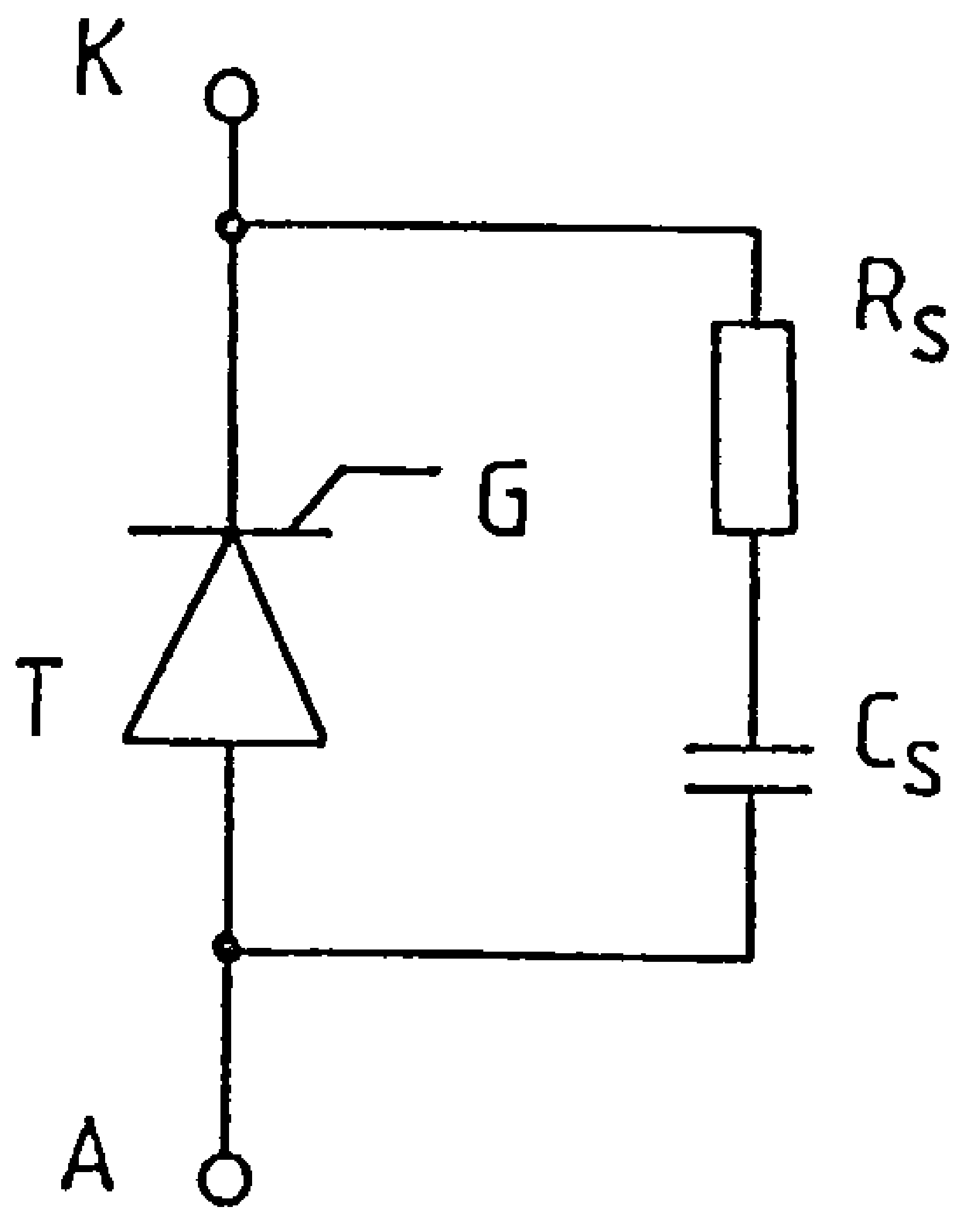

FigureA3.1 Snubber circuit configuration

Appendix A4

Selection of Fuse Links FS1 and FS2

Assuming a continuous armature current of 11A and referring to figure A4.1, $I_{sec1}=I_{sec2}=11A$.
The impedance of the power transformer TF1 is 2.4% which gives a prospective fault current of

$$I_{fault} = \frac{11\times100}{2.4} = 459A$$

Since the fuses must carry the transformer secondary current of 11A, International Rectifier fuse links A350-12 [43] were selected. From the fuse characteristics presented in the reference, I^2t and the cut-off current I_{co} were obtained as

$$I^2t=25\ A^2\text{-}s$$
$$I_{co}=200\times0.8=160\ A$$

From the thyristor specifications

$$I_{TSM}=375\times1.4=525\ A$$
$$I^2t=700\ A^2\text{-}s$$

Since the cut-off current and I^2t let through of the fuse are smaller than the I_{TSM} and I^2t of the thyristor, the fuse link A350-12 is clearly suitable for this duty.

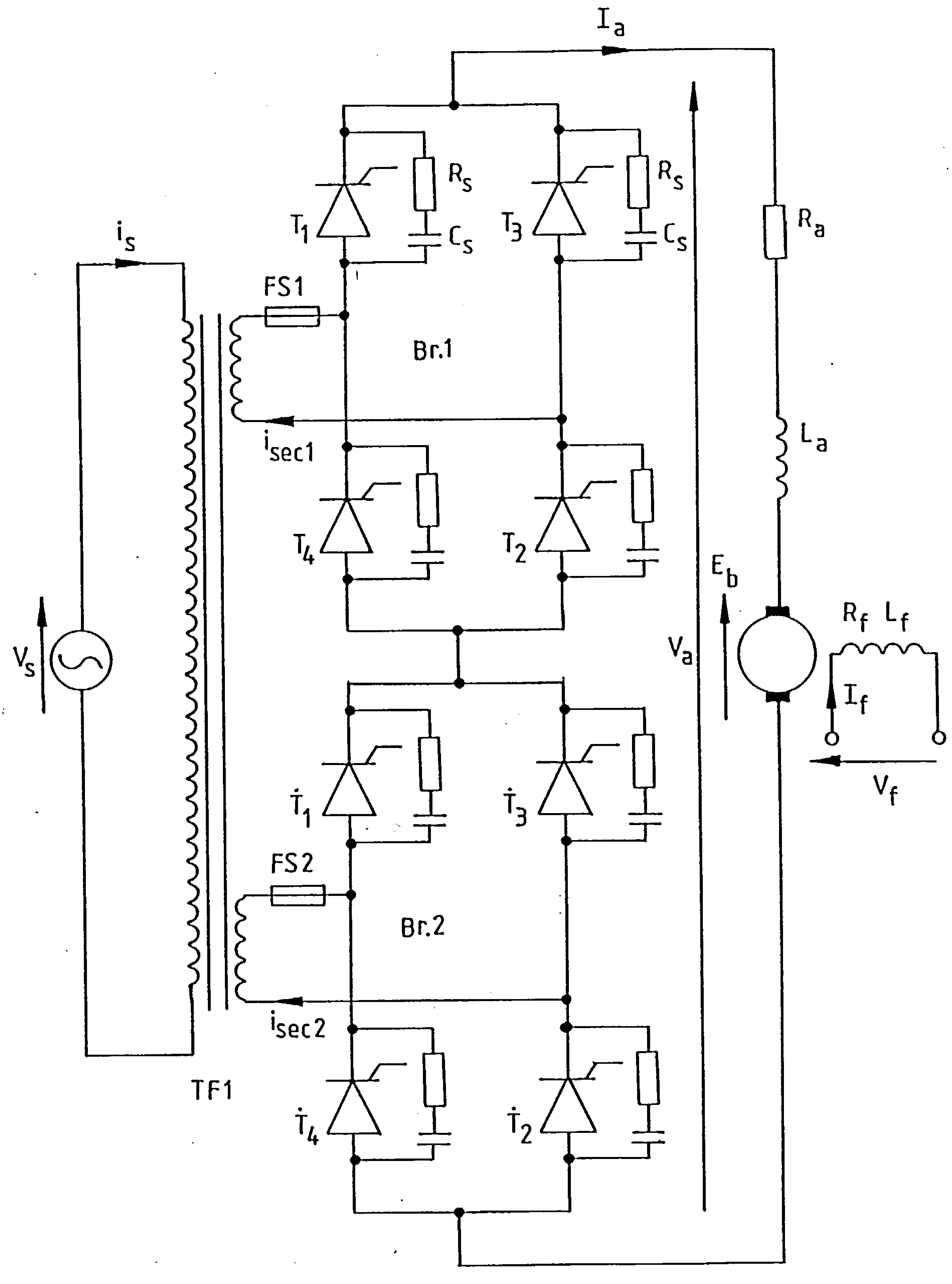

FigureA4.1 Series connected double-bridge converter.

Appendix A5

Choice of Heat Sink

The maximum allowable on-state power loss in a thyristor is given by $V_F I_F$ where I_F is the maximum anode current and V_F the forward voltage drop corresponding to this current. For thyristor type CR24U the maximum allowable loss is therefore 66.6W. The heat P transferred to the surroundings is proportional to the temperature difference between the junction and the surroundings, with the constant of proportionality being known as the thermal resistance. The overall thermal resistance from junction to ambient R_{ja} is then

$$R_{ja} = \frac{T_j - T_a}{P} \qquad \text{(A6.1)}$$

where $T_j = 135^{o}C$ is the maximum junction temperature defined in the specifications for thyristor CR24U. If the surrounding temperature T_a is taken as $20^{o}C$ then, from equation A6.1, $R_{ja} = 1.72^{o}C/W$. However

$$R_{ja} = R_{jh} + R_{ha} \qquad \text{(A6.2)}$$

where R_{jh} is the junction-to-heat sink thermal resistance and R_{ha} is the heat sink-to-ambient thermal resistance.

With R_{jh} taken from the thyristor specifications as $1.1^{o}C/W$, it follows from equation A6.2 that R_{ha} is $0.62^{o}C/W$. A heat sink having a thermal resistance lower than this figure is required.

Appendix A6

Pulse-transformer Design

Consideration of figure A6.1 shows that the base current of TR3(i_{b3}) can be calculated from:

$$V_{c2} + R_4 i_{b3} + V_{be3} + \beta_3 i_{b3} R_5 = 10 \qquad \text{(A9.1)}$$

Assuming a collector voltage drop V_c of 1V, a base-emitter voltage drop V_{be} of 0.7V and a current gain β_3 of 70, it follows from equation A9.1 that i_{b3}=4mA. The input voltage V_i to transformer TF1 is,

$$V_i = 10 - V_{c3} - \beta i_{b3} R_5 \qquad \text{(A9.2)}$$

which enables V_i to be calculated as 4.8V.
The input voltage, the rate-of-change of flux and the number of turns N on the 1:1 ratio pulse transformer of figure A6.1 are related by the equation,

$$N = \frac{V_i}{\left(\frac{d\phi}{dt}\right)} \qquad \text{(A9.3)}$$

From figure A6.3, the number of turns is

$$N = \frac{V_i t_{on}}{\phi_{max}} \qquad \text{(A9.4)}$$

If B_{max} is the maximum permissible flux density in the transformer core and A_e is the magnetic cross-sectional area, then

$$N = \frac{V_i t_{on}}{B_{max} A_e} \qquad \text{(A9.5)}$$

The core of the pulse transformer has a magnetic cross-sectional area of 224mm^2 and for an operating frequency of 2kHz with a 50% duty cycle, t_{on} = 250µs. From equation A9.5 the number of turns was calculated as 40 for a maximum flux density of 0.13T. The wire diameter required is dependent on the rms current, and is

$$I_{rms} = I_p\sqrt{D} \tag{A9.6}$$

where I_p is the peak winding current and D the duty cycle. For $D=0.5$ and $I_p=\beta_3 i_{b3}=0.28A$, $I_{rms}=0.2A$.
The current density J is

$$J = \frac{I_{rms}}{\left(\frac{\pi d^2}{4}\right)} \tag{A9.7}$$

giving

$$d = \sqrt{\frac{4I_{rms}}{J\pi}} \tag{A9.8}$$

Assuming a current density of $2A/mm^2$, $d=0.36mm$. The nearest available wire size is 0.4mm and this was used for both primary and secondary windings.

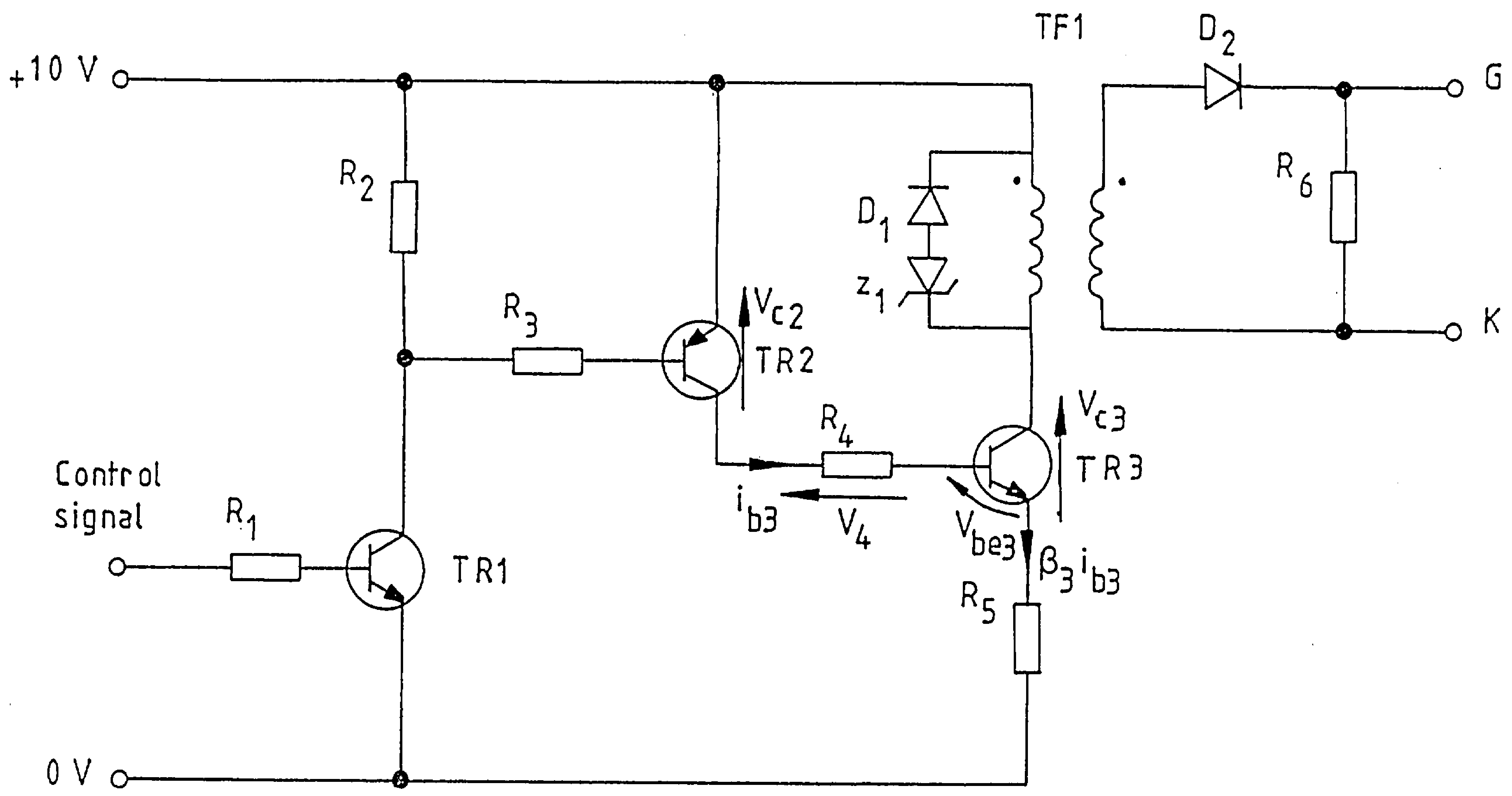

FigureA6.1 Conventional thyristor gate-drive circuit.
(Component values given in Appendix A10)

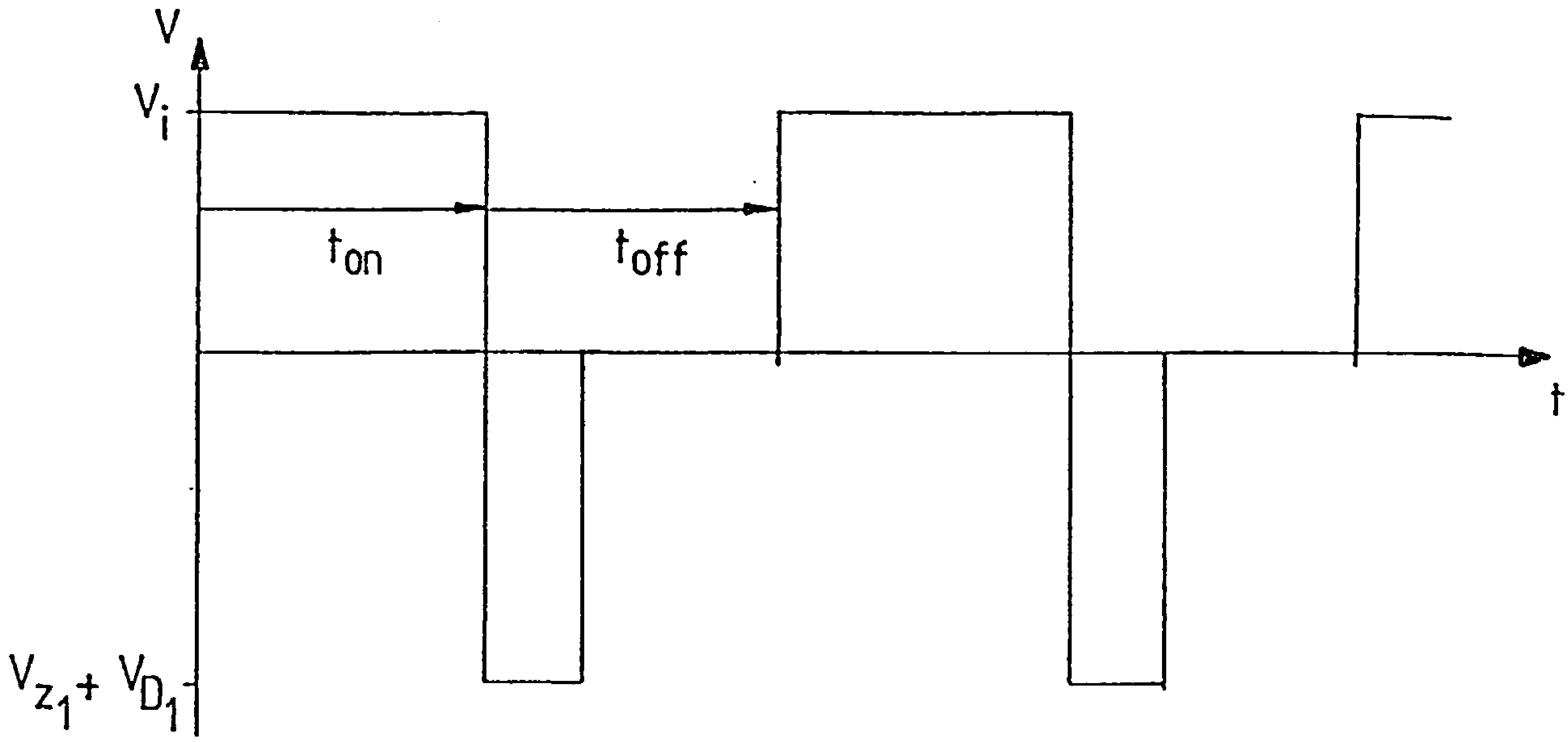

FigureA6.2 Pulse-transformer primary voltage waveform.

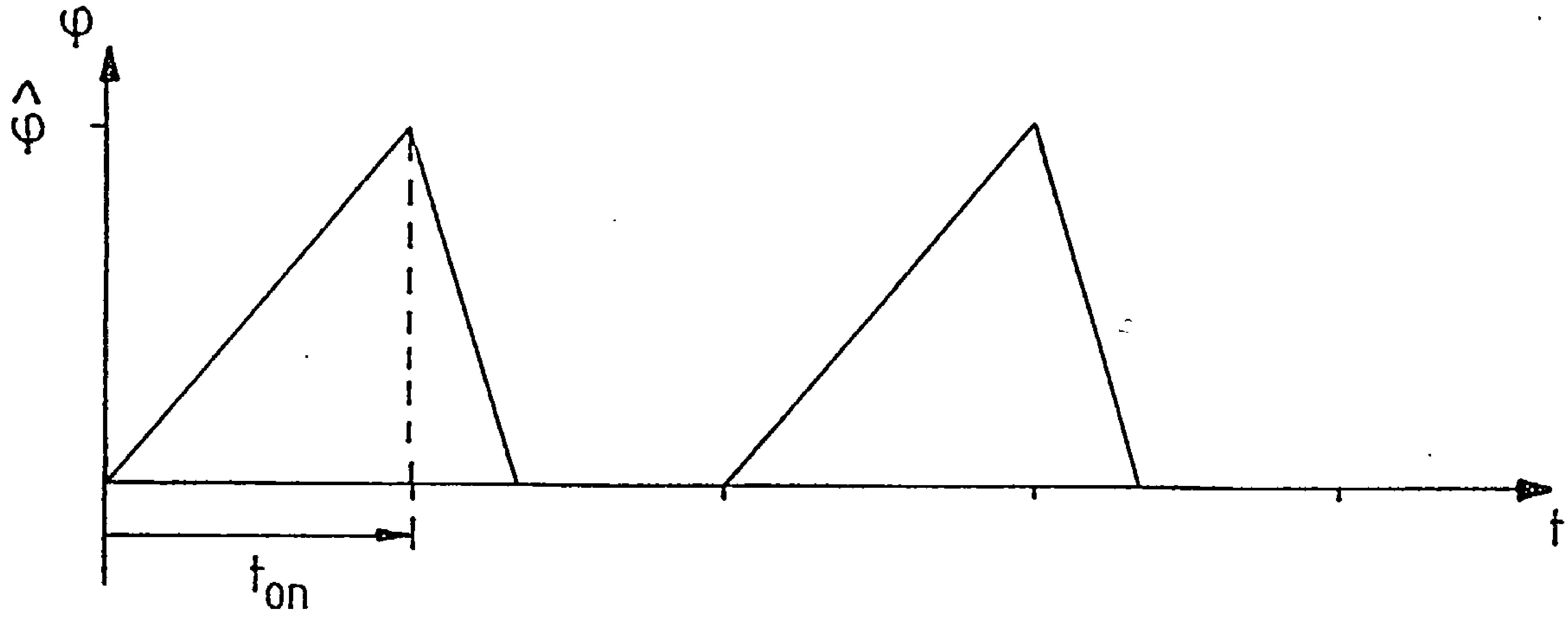

FigureA6.3 Pulse-transformer flux waveform.

Appendix A7

Choice of Heat Sink

The GTO thyristor and its series diode of figure A7.1 are mounted on the same heat sink and the heat flow diagram for the assembly is shown in figure A7.2. The forward conduction power loss of the diode P_d calculated from the product of the forward current and the forward voltage is 20W and that of the GTO P_g is precisely the same. The diode base temperature at the heat sink T_{hd} is given by

$$T_{hd} = T_{jd} - P_d R_{jhd} \qquad \text{(A13.1)}$$

where T_{jd} is the diode junction temperature. Although the maximum temperature quoted in the data sheet is 150°C, a limit of 120°C was used in the present application to provide a safety margin of 30°C. The junction to heat sink thermal resistance of the diode R_{jhd} is 3.3°C/W hence,

$$T_{hd} = 120 - 66 = 54^{o}$$

The GTO base temperature at the heat sink T_{hg} is given by

$$T_{hg} = T_{jg} - P_g R_{jhg} \qquad \text{(A13.2)}$$

where T_{jg} is the GTO junction temperature. Although this has a quoted maximum of 120°C in the data sheet, a limit of 90°C was used in the present application. R_{jhg} is the junction to heat sink thermal resistance of 1.8°C/W so that

$$T_{hg} = 90 - 20\times1.8 = 54^{o}C$$

Since the diode and the GTO are mounted on the same heat sink, the total power dissipated is 40W. If the heat sink temperature is taken as the average base temperature T_{ab} of the diode and the GTO, then:

$$T_{ab} = \frac{54 + 54}{2} = 54^{o}C$$

and the heat sink should have a thermal resistance of

$$R_h = \frac{T_{ab} - T_{amb}}{P_{tot}} = \frac{54 - 20}{40} = 0.85^{o}C/W$$

where T_{amb} is the assumed ambient temperature of 20°C.

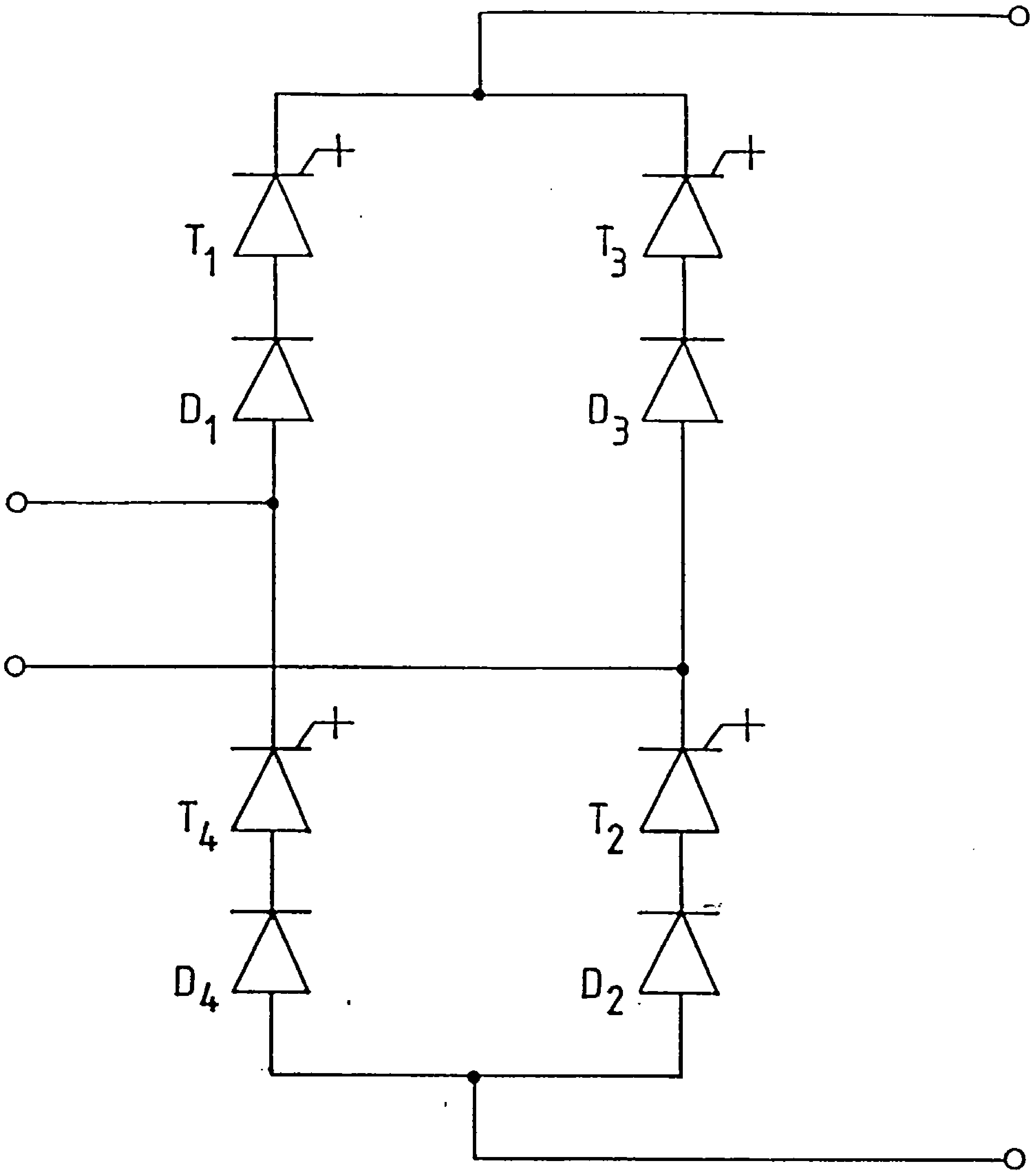

FigureA7.1 Single-phase GTO thyristor bridge converter.

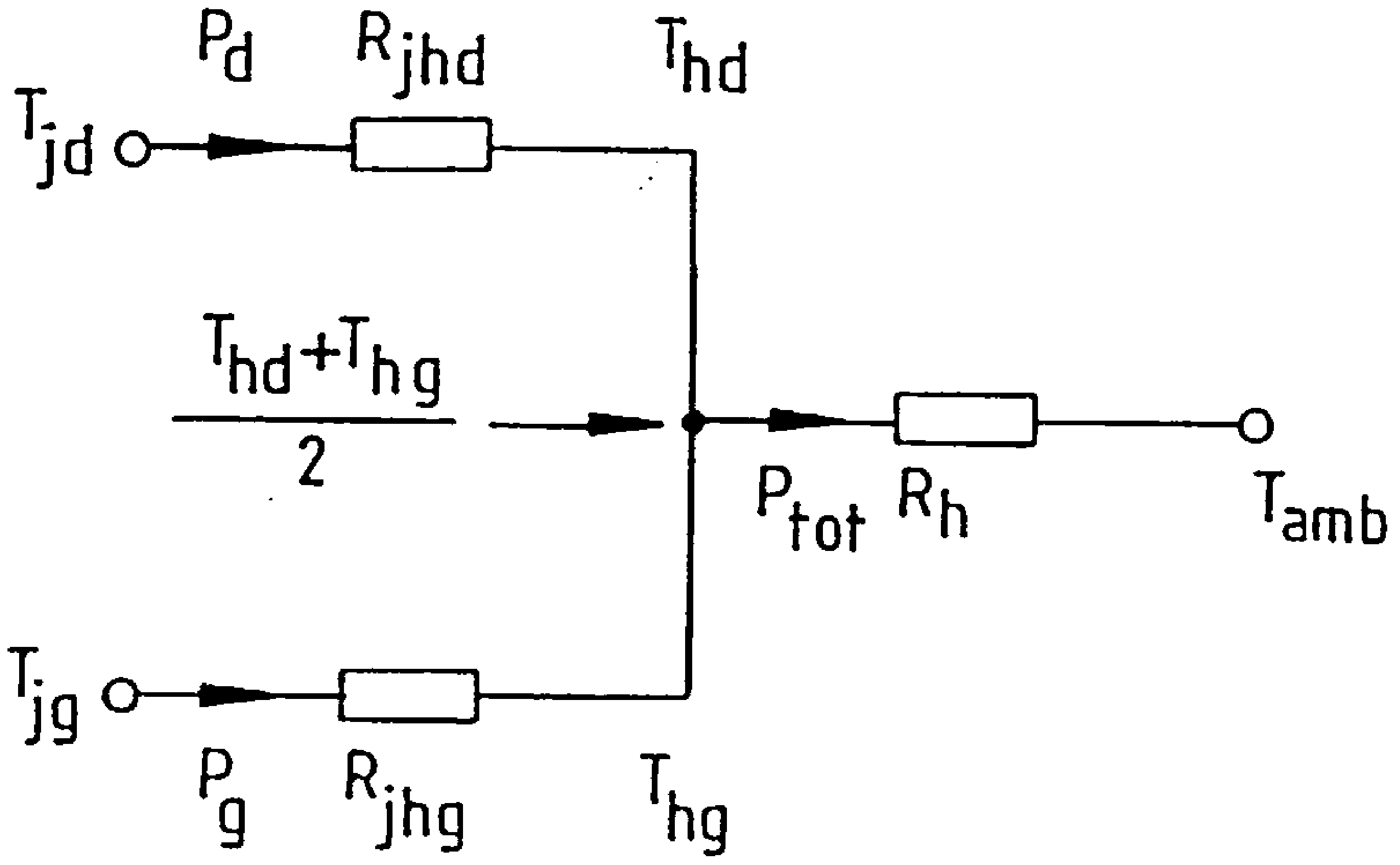

FigureA7.2 Heat flow diagram.

Appendix A8

Snubber-circuit Design

The snubber circuit configuration is shown in figure A8.1. Assuming a switching anode current I_p of 10A and a reverse gate voltage V_{GR} of 10V, from the GTO data sheet $\frac{dv}{dt}$ should be limited to 350V/μs. Since

$$C_S = \frac{I_P}{\left(\frac{dv}{dt}\right)} \qquad (A14.1)$$

a snubber capacitor of 0.047μF with an ac voltage rating of 1500V was chosen. The high speed diode D_S must be capable of conducting I_P for several microseconds, for which duty the Mullard device BY329-1000 is suitable. Resistor R_S was selected as 47Ω, to limit the peak anode current at turn-on to 7.2A with a supply voltage of 240V. In addition, the requirement that

$$R_S C_S < \frac{T_{on(min)}}{5} \qquad (A14.2)$$

limits the minimum turn-on time to 7μs. The power rating of the snubber resistor is,

$$R_S = 0.5 C_S V_m^2 f_S = 11W$$

where V_m is the peak supply voltage and f_S is the worst case switching frequency which is 4kHz.

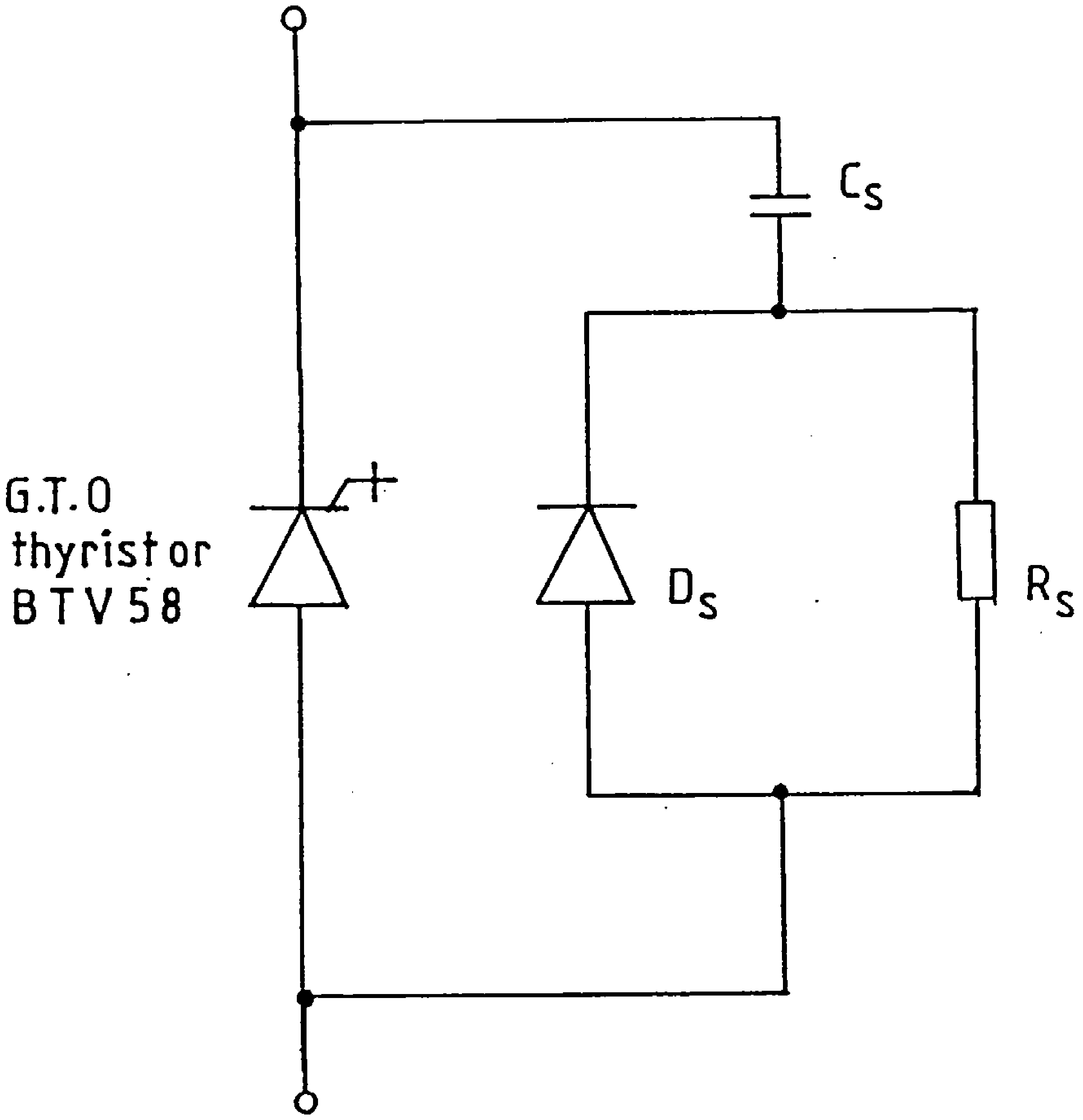

FigureA8.1 Snubber circuit configuration.

Appendix A9

Design of the Frequency Synthesizer

A CMOS 4046 phase-locked loop, PLL, was used in the frequency synthesizer circuit of section 4.5.1 of chapter 4. The design of the external circuitry of the phase-locked loop shown in figure A9.1 is outlined in this Appendix.

A9.1 VCO Component Selection

The operating frequency range of the voltage controlled oscillator(VCO), which is from 40Hz to 4kHz, is determined by the external capacitor C_1 and the two external resistors R_1 and R_2 of figure A9.1. Given a minimum frequency of 40Hz, R_2 and C_1 were determined from PLL data sheet as 1MΩ and 0.047μF respectively. However resistor R_1 was determined as 1kΩ by trial and error [29], in which, with VCO_{in}(pin 9) of 4046 connected to V_{DD}, R_1 was varied until the output frequency at pin 4 was 4kHz.

A9.2 Low-pass Filter Component Selection

In the low-pass filter configuration of figure A9.2, the damping ratio is $\sigma=0.2$ [21]. It follows that $\frac{R_4}{R_3} = 0.2$ and with $R_3=27k\Omega$, $R_4=5.4k\Omega$, or 5.6kΩ to the nearest standard value. If the break point frequency f_z of the low-pass filter (i.e. its zero) is 10Hz, it follows from $R_4C = \frac{1}{2\pi f_z}$ that $C=3.1\mu F$ or 3.3μF to the nearest standard value.

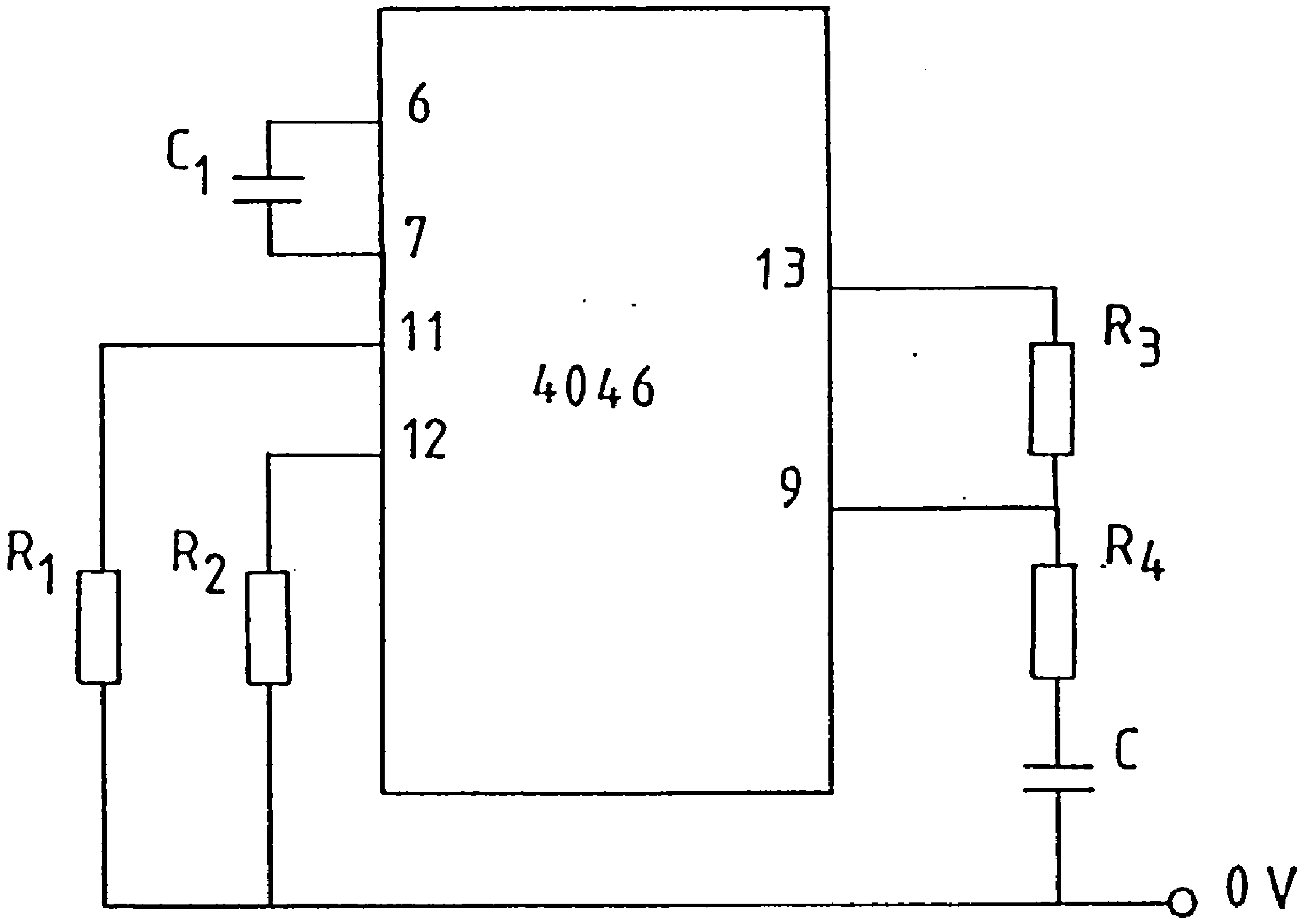

FigureA9.1 External circuitry of Phase-locked loop.

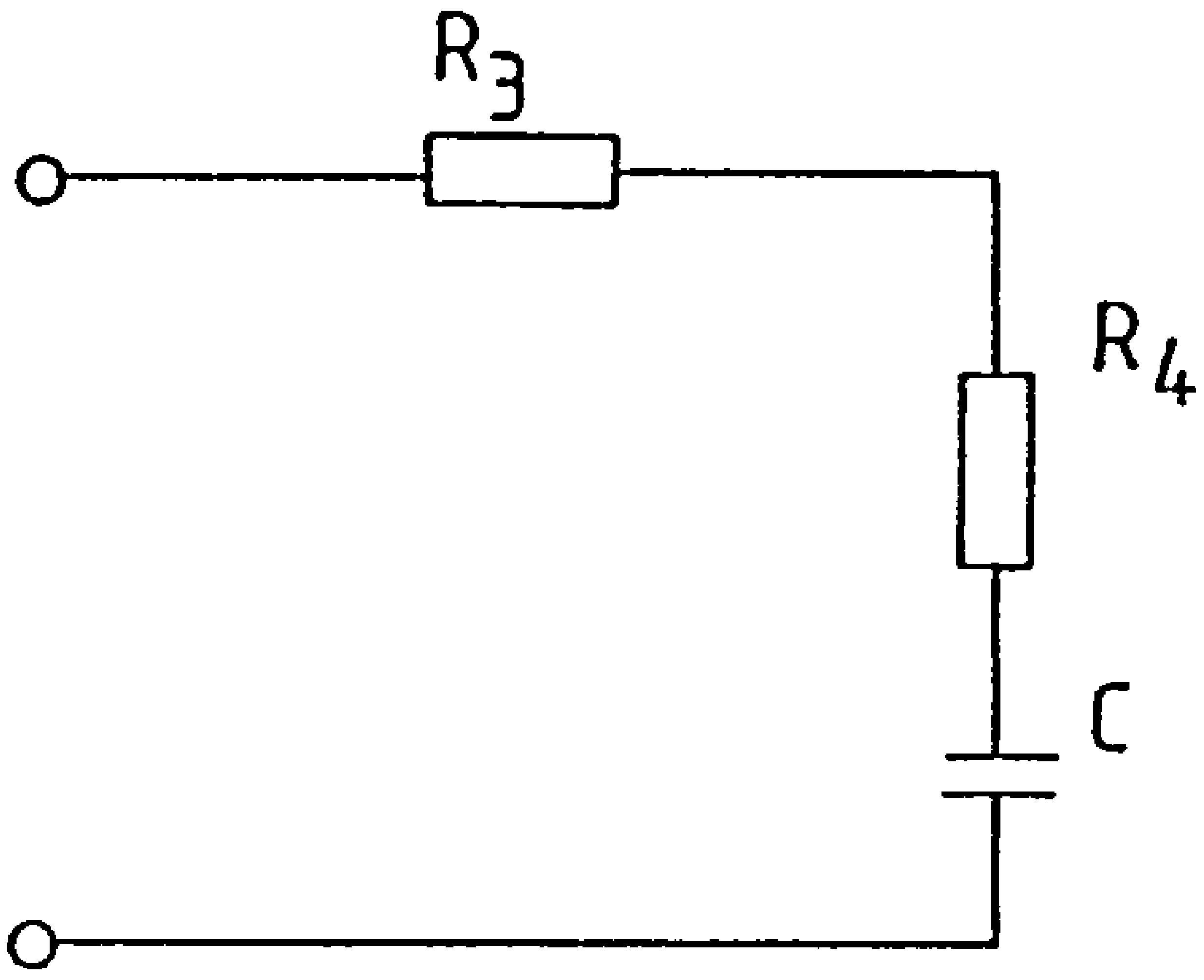

Figure A9.2 Circuit diagram of low-pass filter.

Appendix A10

List of Components Used in the Experimental Work

List of components used in the experimental work of chapters 3 and 4.

CHAPTER 3

Figure 3.1

TF1 Primary winding 250V,50Hz,1.5kVA
Two secondary windings
Sec1 125V,50Hz,750VA
Sec2 125V,50Hz,750VA

FS1,FS2	A350-12
T_1toT_4	CR24U
$\dot{T}_1$to$\dot{T}_4$	CR24U
R_s	220Ω,2.5W
C_s	0.22μF,250V

Figure 3.3

TF1 Primary 240V,50Hz,12VA
Secondary 5V,50Hz,12VA

All resistors 0.5W,5%

R_1toR_4	10k
R_5,R_7	470Ω
R_6,R_8	4.7k
R_9,R_{11}	2.2k
R_{10}	220Ω

Capacitors

C_1,C_2	2.2μF

Semiconductors

TR1,TR2	ZTX451
IC1toIC4	Op.Amp.741 series

Figure 3.4

All resistors 0.5W,5%

R_l	4.7k
R_u	100k
PS1toPS4	47k
R_1toR_8	4.7k

R_9toR_{12}	150Ω

Semiconductors

IC1	Voltage regulator LM7805
IC2toIC5	Operational Amplifier 741 series
IC6,IC7	7414
IC8,IC9	74123
Z_1toZ_4	BZX79C4V7

Figure 3.5

R_1,R_2	150Ω,0.5W,5%

Semiconductors

Z_1,Z_2	BZX79C4V7
IC1,IC2	7408

Figure 3.6

IC1	555 timer
IC2,IC3	7408

Figure 3.7

TF1 Core FX2242

Primary and secondary windings of 40 turns with 0.4mm diameter wire.

R_1	10k,0.5W,5%
R_2,R_4	1k,0.5W,5%
R_3	2.2k,0.5W,5%
R_5	15Ω,2.5W,5%
R_6	4.7Ω,2.5W,5%

Semiconductors

TR1,TR3	ZTX451
TR2	ZTX551
D_1,D_2	IN5399
Z_1	BZX79C10

Figure 3.9

All resistors 0.25W,5%

R_1toR_8	10k
R_9toR_{20}	1k
R_{21}toR_{26}	10k

Semiconductors

IC1toIC4	74LS374
IC5toIC12	74LS85
IC13,IC14	74LS93
IC15	7404

Miscellaneous

pb1 to pb4 Push button SPNO switch,1.5A @ 12Vdc

SW1 to SW8 End stackable single throw 8 way switch

Figure 3.10

TF1 Primary 240V,50Hz,12VA
Secondary 5V,50Hz,12VA

All resistors 0.25W,5%

R_1toR_4	10k
R_5,R_6	1k

Semiconductors

Z_1,Z_2	BZX79C4V7
IC1,IC2	Operational amplifier 741 series
IC3,IC4	74123
IC5	7432

Figure 3.11

IC1 to IC4 7411

CHAPTER 4

Figure 4.1

TF1	Primary winding 250V,50Hz,1.5kVA Secodondary winding 250V,50Hz,1.5kVA
FS1	A350-5
T_1 to T_4	BTV58-1000R
D_1 to D_4	BY329-1000
R_s	47Ω, 10W, 5%
C_s	0.047µF,1500V
D_s	BY329-1000

Figure 4.2

All resistors are 0.5W, 5%

R_1,R_{10} 10k

Capacitors

C_1,C_2 220pF

R_2	2.2k
R_3	390Ω
R_4toR_6	4.7k
R_7	270Ω
R_8	1k
R_9	39Ω

C_4,C_6	150µF,16V
C_3	22nF
Semiconductors	
TR1	BC548
TR2	BD645
TR3	BD675
INV$_a$toINV$_f$	HEF40106B

Figure 4.3

TF1 Primary 240V,50Hz,50VA
    Secondary 30V,center tap,50Hz,50VA
C_1,C_2 470µF,40V
Br1 BY225
VR1 LM7812CT
VR2 LM7912CT

Figure 4.4

TF1 to TF4	AT4043/48
R_1	18k,0.5W,5%
R_2	12k,0.5W,5%
R_3	100Ω,0.5W,5%
R_4	6.8Ω,11W,5%
R_5	470Ω,0.5W,5%
Capacitors	
C_1	560pF
C_2	10nF
C_3	22nF
C_4	150µF,25V

Semiconductors	
IC1	555 timer
D_1toD_3	BAW62
D_4	BZX87-C33
TR1	BDX35
D_5toD_{12}	BAV10
D_{13}toD_{15}	BZX79-C12

Figure 4.5

TF1 Primary 240V,50Hz,12VA
    Secondary 5V,50Hz,12VA
All resistors 0.25W,5%
R_1,R_2 10k
R_3,R_4 1k

Capacitors	
C_1	0.047µF
C_2	3.3µF

R_5	1MΩ	C_3toC_5	0.1µF
R_6	27k	C_6	0.15µF
R_7	5.6k		
R_8,R_9	1k		

Semiconductors

D_1	BZY88C5V6
D_2	BZY88C3V9
IC1	Operational amplifier 741 series
IC2	4046
IC3,IC4	4018
IC5	4029
IC6	4069
IC7	TL071

Figure 4.6

All resistors 0.25W,5%		C_1	0.047µF
R_1	10k		
R_2	220k		
R_3,R_5	1k		
R_4	10k		

Semiconductors

IC1,IC2 Operational amplifier 741 series

Figure 4.7

All resistors 0.25W,5%		Semicondutors	
R_1,R_4,R_5,R_7,R_8,R_{10},R_{11}	10k	IC1toIC4	TL071
R_2	15k		
R_3	20k		
R_6	6.2k		
R_9	50k		

Figure 4.7 and 4.8

IC1,IC2,IC4	4069
IC3	4081

Appendix A11

Parameters Used in the Computer Model

A11.1 Sequence-controlled Single-bridge Converter

Referring to figure A11.1, the parameters of the source impedance, power transformer and thyristors together with the mutual inductance between the windings are respectively:

$R_{11} = 0.1\Omega$ $L_{11} = 0.01H$
$R_{22} = 0.5\Omega$ $L_{22} = 5.4005H$
$R_{33} = 0.5\Omega$ $L_{33} = 5.4005H$
$R_{44} = R_{55} = R_{66} = R_{77} = 0\Omega$
$L_{44} = L_{55} = L_{66} = L_{77} = 10^{-6}H$
$M_{23} = M_{32} = 5.4H$

A11.2 Sequence-controlled Double-bridge Converter

With reference to figure A11.2, the parameters of the source impedance and power transformer together with the mutual inductance among the windings are:

$R_{11} = 0.1\Omega$ $L_{11} = 0.01H$
$R_{22} = 0.5\Omega$ $L_{22} = 5.4005H$
$R_{33} = 0.125\Omega$ $L_{33} = 1.35H$
$R_{44} = 0.125\Omega$ $L_{44} = 1.35H$
$M_{23} = M_{32} = 2.7H$
$M_{24} = M_{42} = 2.7H$
$M_{34} = M_{43} = 1.35H$

The thyristor parameters R_{55} to R_{1010} and L_{55} to L_{1010} are equal to,

$R_{55} = 0\Omega$ $L_{55} = 10^{-6}H$

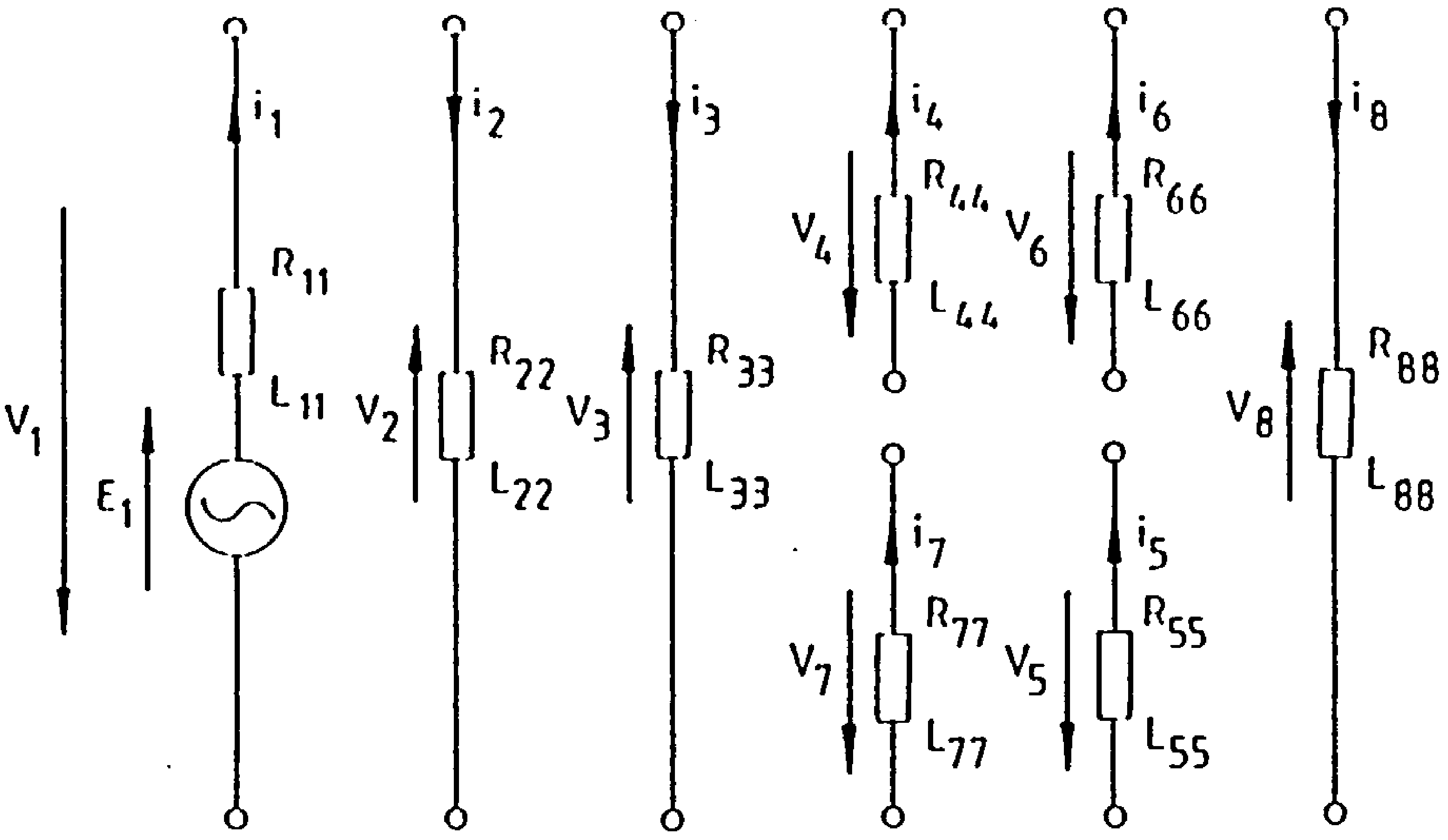

FigureA11.1 Branch reference frame for single-bridge converter.

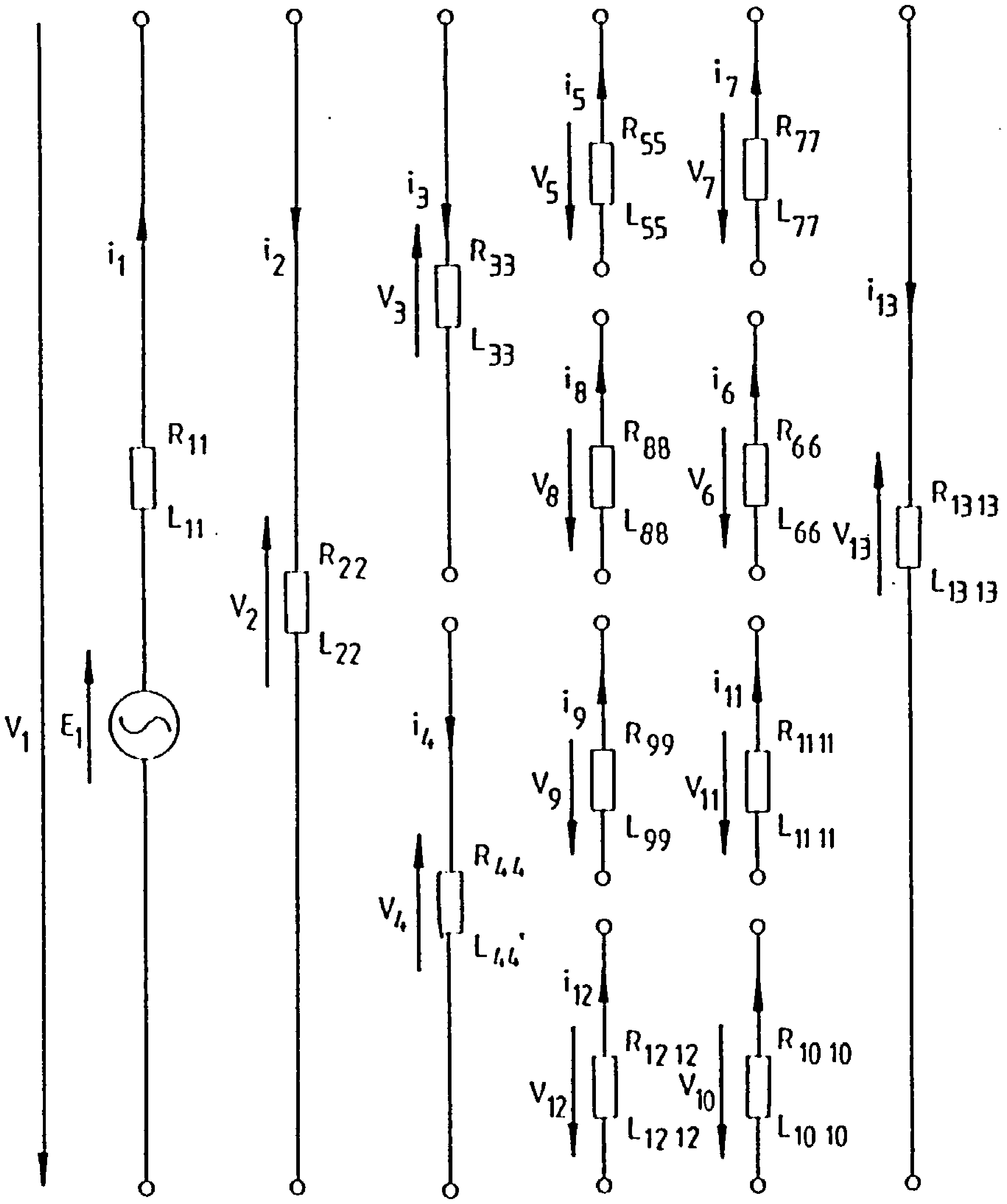

FigureA11.2 Branch reference frame for double-bridge converter.